THESIS IN PHYSICS

Development of magnetic tunnel junction (MTJ) sensors for the detection of single magnetic particles

written by

Monika Brzeska
born on September 23rd, 1976
in Gdynia, Poland
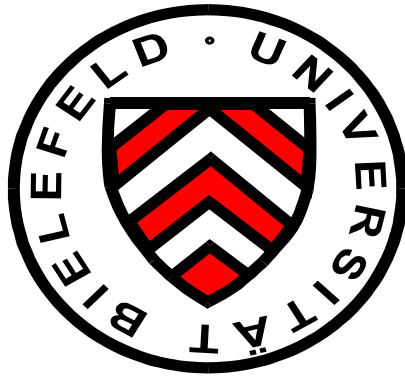
Department of Physics
University of Bielefeld

October 2009

Declaration

I wrote this thesis by myself and used only the indicated resources.

Bielefeld, October 15th, 2009

(Monika Brzeska)

Reviewers:
Prof. Dr. Günter Reiss
Univ. Doz. Dr. Hubert Brückl

Date of submission: October 15th, 2009

Abstract

In the last few years, magnetoresistive transducers, such as giant magnetoresistances, have become potential sensing elements in various biosensors for the detection or identification of biomolecules [80-83, 84]. In these biosensors, magnetic microsized and nanosized particles have been used as markers of biomolecules.

Actually, magnetoresistive biosensors hold great innovative potential in biosensing through their small size, high sensitivity, low cost, and portability. Traditional methods for detection of biomolecules have employed laboratory techniques such as fluorescence, preceded by using commercially available fluorescent markers, which bind specifically to the biological target and are easily detected using optical transducers [75]. In comparison to the old technique, the new trend required highly qualified personnel, expensive equipment, and was time consuming. Additionally, the advantage of using magnetoresistive biosensors compared to the fluorescence detection method results in higher sensitivity, even to small magnetic fields.

The concept of combining magnetic particles with the sensitivity of magnetoresistive transducers was developed initially by Baselt et al. from the Naval Research Laboratory in Washington in 1998. Since then, many fundamental and application studies on magnetoresistive biosensor have been conducted [80].

Currently, magnetoresistive biosensor laboratory development is taking a turn toward a higher sensitivity of sensing elements and employment of the nanosize magnetic particles for detection [84]. In 2003, companies such as Philips and IBM began to work on commercialized magnetoresistive biosensors based primarily on giant magnetoresistance (GMR) transducers. The challenge for future work is to integrate a setup with microfluid systems and miniaturized detection methods into a portable, hand-held device for application in medical diagnostic tests [82, 84].

Spin valve-type biosensors and GMR biosensors are the most common biosensor types used in the detection of magnetic particles; Magnetic tunnel junction (MTJ) sensors and the detection of single magnetic particles are still very new. Compared to the spin valve sensors, MTJ sensors have larger values of magnetoresistance MR, and they are high impedance devices. This means that one can achieve larger output levels with MTJ sensors than with spin valves. For this reason, MTJ sensors are very interesting for the biosensor industry [134,139].

There are few publications on magnetoresistive biosensors and very little work that has been conducted based on magnetic tunnel junction [75]. For this reason, this biosensor has been developed and tested in a laboratory at the University of Bielefeld [75]. Recently, small size MTJ sensors have been developed for the detection of single small size magnetic particles, and this is the subject of the present PhD thesis.

This work is organized into two parts. The first part, Theoretical Background, addresses motivation, introduces the subject, and presents the state of the art of magnetoresistive biosensor technology. This part is divided into three chapters. The first chapter discusses the biosensor concept and the key opportunities for biosensor development in current and future technology. The second chapter gives an overview of magnetic particles and their application in medicine and biosensor technology. The last chapter introduces the magnetoresistive technology and provides information on recent developments in the field.

The second part, Experimental and Methodical Part, presents the techniques used to fabricate and characterize the MTJ sensor. The fifth, sixth and the seventh chapters describe the methodology used to present the detection capability of MTJ sensors down to the single magnetic particle level.

The method for hysteresis free MTJ sensor fabrication is also presented in this part. Some aspects of single magnetic particle positioning and transporting on the sensor are discussed in the last chapter as well. This section ends with a conclusion and recommendations for further work.

Publications

M.Brzeska, J.Godlewski, Theoretical analysis of current induced by high-energetic radiation in dielectric materials, Molecular Physics Reports, 36: 179-182, 2002

M.Brzeska, M.Panhorst, P.B. Kamp, J.Schötter, G.Reiss, A.Pühler, A.Becker, and H.Brueckl. Detection and manipulation of biomolecules by magnetic carriers. Journal of Biotechnology, 112: 25-33, 2004

M.Brzeska, M. Justus, J.Schotter, K.Rott, G.Reiss and H. Brueckl, Development of Magnetoresistive Sensors for the identification of single molecule by magnetic markers, Molecular Physics Reports 39: 32-38, 2004

H. Brueckl, M. Brzeska, D. Brinkmann, J.Schotter, G.Reiss, W. Schepper, P. B. Kamp, A. Becker, Magnetoresistive logic and biochip, Journal of Magnetism and Magnetic Materials, 282: 219-224, 2004

G. Reiss, H. Brueckl, A. Huetten, H.Koop, D.Meyners, A.Thomas, S.Kämmerer, J. Schmalhorst and M.Brzeska, New materials and application for magnetic tunnel junctions, Physics Status Solidies, Journal of Physics C, (a) 201, no.8: 1628-1634, 2004

G. Reiss; H. Brückl; A. Hütten; H. Koop; D. Meyners; A. Thomas; S. Kämmerer; J. Schmalhorst, M. Brzeska: Impact of geometry and material stacking on the properties of magnetic tunneling junctions, Nanostructured Magnetic Materials and their Application, Edi.: B. Aktas et al. , S. 57-70 . Kluwer Academic Publisher, 2004

G. Reiss, H.Brueckl, A.Huetten, J.Schotter, M.Brzeska, M.Panhorst, D.Sudfeld, A.Becker,P.B. Kamp, A.Pühler, K.Wojczykowski and P. Jutzi, Magnetoresistive sensors and magnetic nanoparticles for biotechnology, Journal of Materials Research, Vol. 20, No.12: 3294-3302, 2005

U. Neuhäusler, J. Lin, A. Oelsner, M. Schicketanz, D. Valdaitsev, J. Slieh, N. Weber, M. Brzeska, A. Wonisch, T. Westerwalbesloh, A. Brechling, H. Brückl, M. Escher, M. Merkel, G. Schönhense, U. Kleineberg and U. Heinzmann
A new approach for actinic defect inspection of EUVL multilayer mask blanks: Standing wave photoemission electron microscopy, Microelectronic Engineering, Vol.83 (4-9): 680-683, 2006

U. Neuhäusler, A. Oelsner†, M. Schicketanz, J. Slieh, N. Weber, M. Brzeska, A. Wonisch, T. Westerwalbesloh, H. Brückl, M. Escher, M. Merkel, G.Schönhense, U. Kleineberg and U. Heinzmann, High resolution actinic defect inspection for EUVL multilayer mask blanks by photoemission electron microscopy, Applied Physics Letters, Vol.88 (5): 053113.1-053113.3, 2006

J. Schotter, M. Panhorst, M. Brzeska, P.B. Kamp, A. Becker, A, Pühler, G. Reiss, H. Brückl: Molecular Detection with Magnetic Labels and Magnetoresistive Sensors, In Nanoscale Devices - Fundamentals and Applications, Springer 2006 (R. Gross et. al. edt.) p 35 – 46

x

Conferences

Poster at the Nanobionics 2 conference (293th Wilhelm and Else Heraeus Seminar) in Marburg (2002):"Manipulation of biomolecules with magnetic carriers and their detection"

Poster at the DPG Früjahrstagung (AK Festkörperphysik) in Dresden (2003): Development of micrometer-sized magnetic tunnel junctions for the detection of single molecules by magnetic markers

Poster at the SFB613- Workshop in Bielefeld (2003): Manipulation and detection of biomolecules by magnetic carrier

Talk at the 7th International Conference on Intermolecular Interaction in Matter in Miedzyzdroje (2003), Development of magnetoresistive sensors for detection of single molecules by magnetic markers

Poster at the Fifth International Conference on the Scientific and Clinical Applications of Magnetic Carriers (2004) in Lyon, Model experiments for the detection of single magnetic particles/molecules with a force microscope

Contents

7. Model experiments for single magnetic particle detection

8. Hysteresis-free MTJ sensor

9. Single magnetic particle positioning

1. Biosensors

Biosensors are currently one of the key technologies in biology and medical research. They are devices that utilize a biochemical reaction to determine a specific compound [1-2]. Using biosensors, many biological and medical tests can be performed automatically, speedily and inexpensively. They also play an important role in the health-care industry because both patients and healthcare providers can receive tailored summaries of the data and this can improve treatment [3-4].

Historically biosensors were invented in 1956 by Prof Leyland D. Clark. In 1962 he demonstrated at a New York Academy of Sciences symposium an enzyme electrode as a new electrochemical sensor. This electrode was made by polymerizing a gelatinous membrane of immobilized enzyme over a polarographic oxygen electrode. The electrode was built up to measure the diffusion flow of oxygen through a plastic membrane. The current output was a linear function of oxygen concentration. When the enzyme electrode was placed in contact with a biological solution or tissue, glucose and oxygen diffused into the gel layer. The flow of oxygen to the electrode was reduced in the presence of glucose oxidase and glucose. The electrode was built up from two platinum cathodes and one reference silver chloride electrode. The glucose concentration was determined as a function of oxygen concentration by recording the difference between the output of the two Pt-electrodes against the silver electrode [5-6]. Since then a lot of works have been published on enzyme electrodes. The first enzyme biosensor based on potentiometry was reported in 1969 by Guilbault and Montalvo [7]. Today, numerous types of biosensor have been developed and reported in the literature [8-10]. This type of instrumentation is now available for use in medicine, military and environmental diagnostic. However, there are still many opportunities for the development of biosensors which could be more sensitive, selective, miniaturized and unexpensive. This chapter discusses the biosensor concept and current and future technology trends.

1.1 Definition, application and classification

Different component of a biosensor are shown in Figure 1.1. It is commonly known that a biosensor is an analytical device that incorporates a biological receptor such as biologically active molecules, cell fragments, whole cells or tissue as part of a biotransducer that converts the binding events between the receptor and the target analyte into an

analytically useful signal [11-13]. The biosensors are characterized by a high degree of selectivity and sensitivity [14]. These devices provide a rapid access to the measurement data and in many cases give a reproducible results. Some of the advantages of these recent tools are easy preparation of the sample, relatively low cost, rapid time of response, long half life and easy storage [15]. The classification of biosensor depends on the transducers, bioactive components and different types of interaction. The transducing microsystem may be optical, electrochemical, thermoelectric, piezoelectric or magnetic. Biosensor usually gives a digital electronic signal that is proportional to the concentration of a specific analyte or some groups of analytes [13, 15].
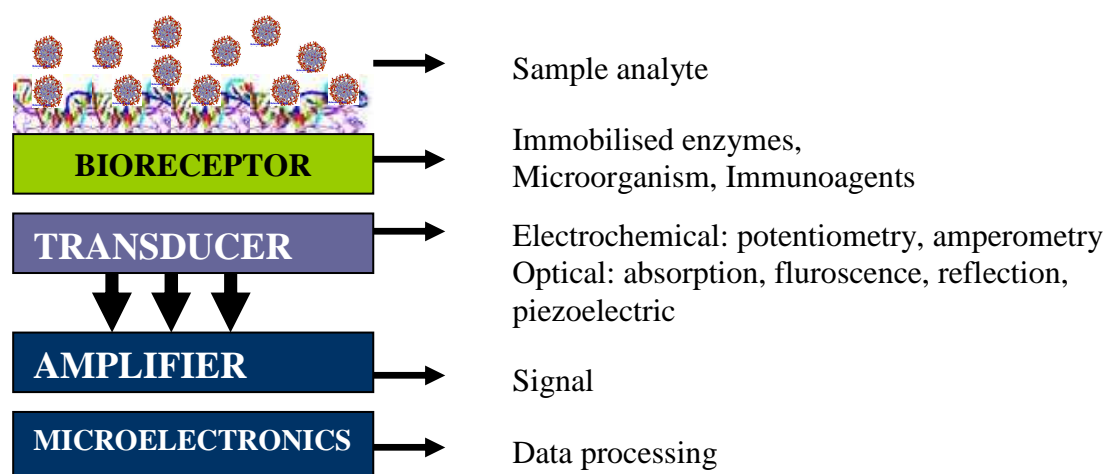
Figure 1.1 Different components of a biosensor [16].

With recent advances in biosensor technology there evolved a need for a miniaturization. This type of device has many advantages: small sample volume, lower sensor cost and portability. The miniaturizations allow biosensors to penetrate several untapped markets especially in medicine [17-18]. The biosensor has to be also fast, easy to use, specific and inexpensive.
Many of currently produced sensors are not very stable, that means that many of them are based on a biological element that is characterized by a poor stability in a specific environment condition. This is the key challenge faced by manufacturers and the reason why many of the biosensors are not commercialized up to now. However, many of the designed biosensors have found application in markets comprising home diagnostics, point-of-care, research laboratories, process industries, environment and bio-defense technology.

One of the most important applications is the biomedical sector because this area represents the largest market opportunity. Many biosensors are used in an emergency room for example to test blood chemistry or for in vitro diagnostic. A schematic diagram presented in figure 1.2 shows main applications for the in vitro diagnostic.
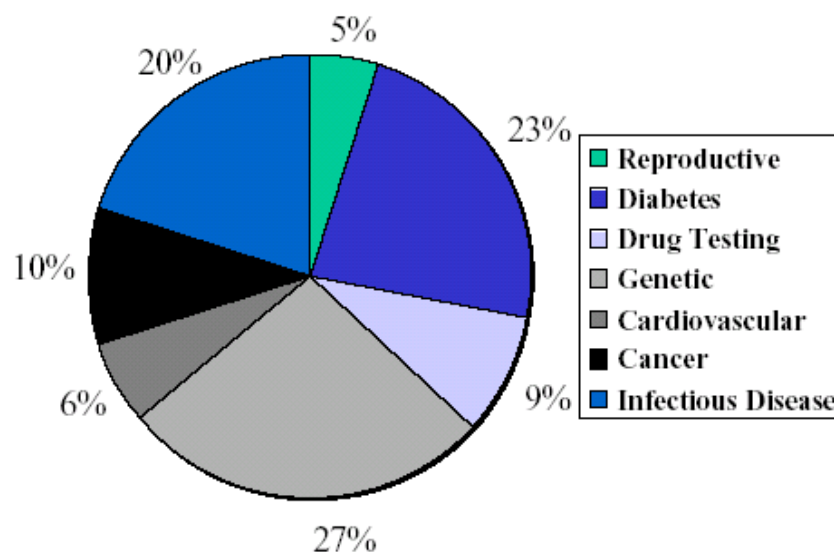
Figure 1.2 A schematic diagram showing various application of biosensor in in-vitro diagnostic [23].

Biosensors are used in medical diagnostic to detect almost everything what is needed. They are developed to test for diabetes, drugs, infectious diseases, DNA, AIDS and many other molecules [24-25]. In a disease like the diabetes the human body is not able to control the amount of glucose in the blood. The diabetes develops when there is a relatively insufficient amount of the natural hormone insulin. Diabetes usually cannot be cured, but it can be controlled. In a standard procedure glucose is controlled by pricking a finger to obtain a blood sample, which is then

Figure 1.3. Optical chemical sensors that operate on induced fluroscence changes [31].

collected on a test strip and analyzed by a glucometer [26-28].   This   test   is uncomfortable for a patient and as a routine diabetes control must be customarily repeated for a minimum of four times a day. For this reason the group from SMSI (Sensor for Medicine and Science, Inc) is developing glucose sensor (see Figure 1.3). This is a minimally invasive glucose monitoring system, consisting of an implantable sensor and a watch reader [29-30].

It is designed to measure and display glucose level every few minutes without any user intervention. This product is already in pre-clinical studies. Advantage of this sensor is, that primarily it is non-invasive- the implant can be placed into the body for up to one year, secondly it is accurate and is designed to reduce the risk of a user error and finally, most important, patients and health care providers can receive tailored summaries of the data and this can improve treatment [29-30].

The biosensors have also the potential to be used in a pharmaceutical process control, hospital –associated infection control and infectious disease diagnostics [4,32]. Using this device, the bacteria responsible for an infection can be identified very quickly. The stored information usually can be used to monitor the spread of an epidemic and can help to facilitate rapid intervention.

A remarkable progress has also been accomplished in genetical diagnostics. Thanks to many genetic tests, doctors now have a device which enable them to analyze how certain illnesses, or increased risks for certain illnesses, pass from generation to generation. Actually many diseases are diagnosable by a molecular analysis of nucleic acids and still many of them will be in future recognized due to a research project called the Human Genome Project. Up to now it has been recognized, that humans are in more then 99% identical in their DNA sequence [33]. The minimal differences between human organisms are, however, relevant for health and healthcare. Knowledge of a particular variation can help to understand a disease history of the population and can also estimate a treatment outcome. Still there is a need for a new DNA analysis system that can open up a new genetic testing market. This is the main reason why biosensor technology is involved in genetical diagnostics. The other reason is that many of new generation devices are produced using photolithographic microfabrication. The modern biosensors are mainly silicon-based, produced together with integrated electronics and this provides a system that is accurate, deals with a low sample volume and is cost-efficient [34-35]. Other promising markets for biosensors are the environmental analysis and the food industry market. The main potential for such devices lies in the land pollution mapping or

monitoring of pollution in the oil and gas industry. The sensors can be also used in the case of any epidemy emerging due to a natural disaster as well as for a in situ monitoring of contaminated water. In addition to the pollution, the sensitivity and selectivity of the biosensor can be very helpful in controlling food processing. The use of biosensors in environmental monitoring has a strong advantage compared to classical methods such as spectrometry and chromatography. The old techniques required a highly trained personnel, expensive devices and were time consuming [2].

The biosensor market has been significantly increasing and will continue to grow in the next decades. A potential client has to deal with different classes of biosensors that depend on the biological receptor and the transducer used. In many cases the immobilization method of the biological molecule plays an important role in the selection of devices.

1.2 Biological Receptors

Biological receptors are an integral part of the biosensor technologies. For the measurement they are binding the analyte of interest to the sensor. There are specific interactions between the target analyte and bioreceptors that produce a physico-chemical change, which is detected and than measured by transducer [8]. Bioreceptors can be classified into five different class: antibody/ antigen, enzymes, nucleic acids/DNA, cellular structures/cells, and biomimetic. Typically used bioreceptors are enzymes, antibodies and nucleic acids [8].

1.2.1 Enzymes

Enzymes are substances that catalyse and speed up a chemical reaction in organisms. Enzymes usually rank among proteins. These particles can bind to one or more ligands, called substrates and transform them into chemically modified products. They are catalyst molecules, i.e.they increase the rate of a reaction but they are not the substrate of the reaction. To put it another way a substrate is a molecule upon which an enzyme acts to yield a product. Every enzyme has two important regions: one that recognizes and binds the substrate, and one that catalyzes the reaction once the substrates have been
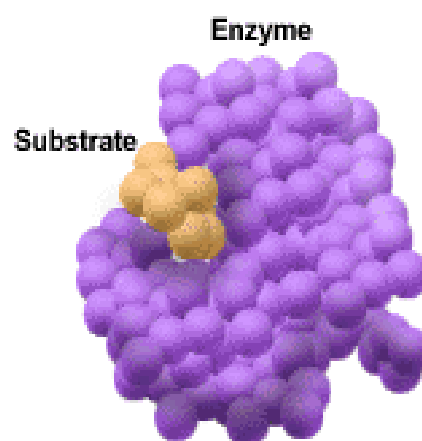
Figure 1.4 Picture of enzymes structural models together with binding substrate [39].

bound. Fig. 1.4 shows an enzyme model [36-38]. There is a large number of enzymes available commercially and applied broadly in biotechnology, e.g. glucose oxidase and urase. Enzymes can also be extracted directly from biological materials and used together with cofactors such as NAD or NADP, which are however very unstable [8]. For these reason, the commercialized enzymes are commonly used in biosensor technology [36-38].

1.2.1.1 Chemical structure of enzymes

Chemically, enzymes are made up of chains of amino acids connected together by peptide bonds [40]. Figure 1.5 shows the chemical structure of an enzyme.
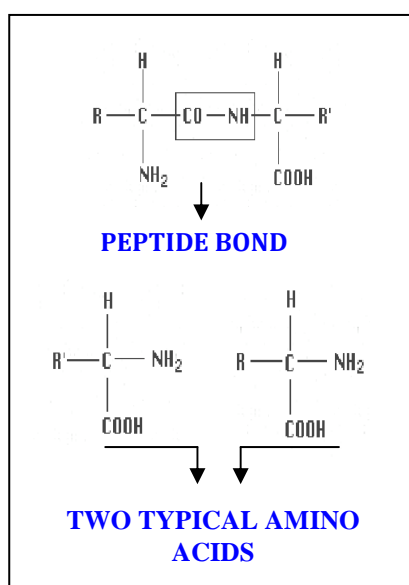
Figure 1.5 Chemical structures of an enzyme: two amino acids are linked
by a peptide bond [41].

An enzyme requires the presence of other compounds-cofactors before its catalytic activity is started. Enzymes composed only of proteins are known as simple enzymes in contrast to complex enzymes, which are composed of proteins and small organic non-protein molecules. In biological terminology complex enzymes are known as holoenzymes [40]. Holenzymes have usually two components: the protein component is known as apoenzyme and non-protein component is called coenzyme or prosthetic group. The prosthetic group is bound to the organic molecule to the apoenzyme via a covalent bound. When the binding is non-covalent then the organic molecule is called coenzyme. Some enzymes require metals as non-protein components and thus these enzymes are called metalloenzymes. The functional role of coenzymes is to transport a chemical group from one reactant to another.

6

During the enzymatic actions coenzymes undergo chemical changes, for this reason many coenzymes are regarded as a type of substrate or a second substrate (see Fig.1.6) [40].

APOENZYME	APOENZYME	APOENZYME
↓	↓	↓
COENZYME	PROSTHETIC GROUP	METAL ION

HOLOENZYMES: APOENZYMES + COFACTORS
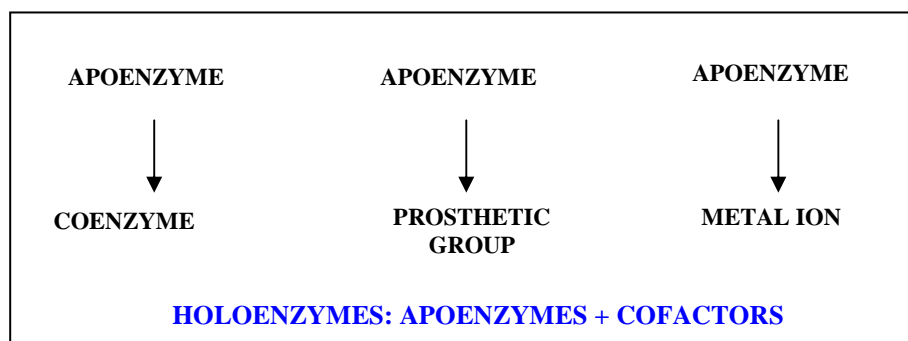
Figure 1.6 Diagram presenting the structure of a holoenzyme [41].

1.2.1.2 The specificity of enzymes

The properties of enzymes depend on their specificities, i.e. a specific enzyme will catalyze only one reaction and will act only on molecules that have specific functional groups, such as amino, phosphate and methyl groups. By linkage specificity the enzyme will act on a particular type of chemical bond regardless of the rest of the molecular structure [40]. Enzymes are also specific for a particular sterochemical configuration of the substrate. An enzyme that binds to a D-sugar will not attack the corresponding L-isomer, this is called sterochemical specificity. Because of their specificity, selectivity and efficiency enzymes are excellent analytical reagents. They are used to determine the concentration of their substrates (as analytes) by calculation of reactions rates. In biochemistry the rate of chemical reaction is described by the number of molecules of reactant(s) that are converted into product(s) in a specified time period. If the reaction condition and enzyme concentration are kept constant, the rate of reaction (V) is proportional to the substrate concentration (S), at low substrates concentrations. This is commonly calculated from the difference in optical absorbance between the reactants and products [40]. For this reasons enzymes are commonly used in analytical laboratories, especially when a relatively small number of samples need to be investigated. For a large number of samples this technology using large amounts of molecules is usually unprofitable because of an expensive enzyme and coenzyme usage, time consumption, laboratory intensiveness and a need of reproducible procedure with properly equipped analytical laboratories. For this reason the production of enzyme based biosensors is associated with micro-fluids technology [42].

1.2.2 Antibodies

Antibodies are proteins produced by the immune system to help recognizing a wide range of foreign substance and unhealthy cells, such as tumor cells. The antibody production is usually induced by agents called antigens. Antibodies belong to the protein class immunoglobulins. Antibodies are made of two types of polypeptides: heavy chains and light chains (see figure 1.7). An antibody has three parts: two parts are identical and are corresponding to two "arms" and the third part builds the "stem". Every arm of the antibody contains a single light chain linked to a heavy chain by disulfidebonds. This is very strong covalent bond between two sulhydryl groups (-SH), where after oxidation of the thiol group, disulfide S-S bond are formed (see figure 1.7) [36-38].

(a)   **(b)**
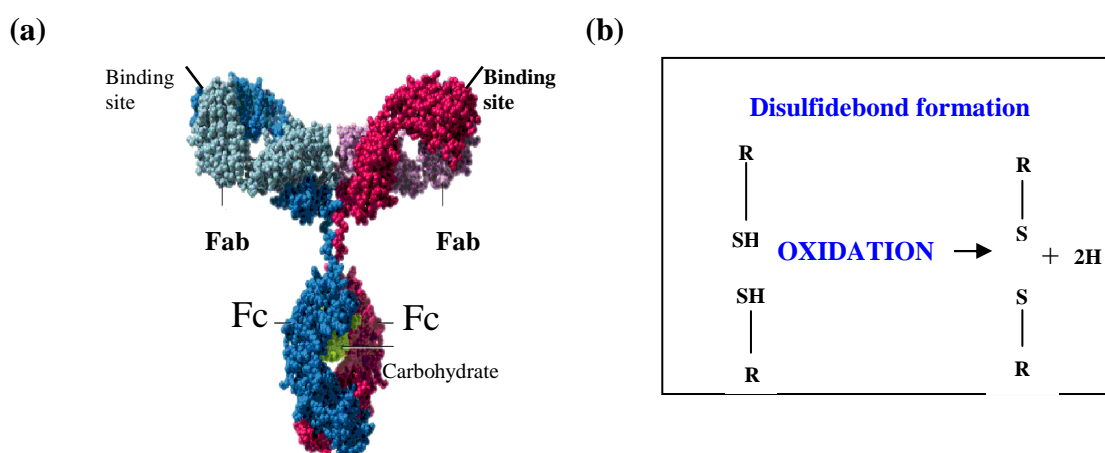
Figure 1.7 (a) A model of an antibody. The heavy chains are   coloured dark red and dark blue; the corresponding light chains are light red and light blue (b) Formation of disulfidebond [39].

1.2.2.1 Production of antibodies

The injection of a foreign molecule into an organism can cause an immunological reaction - the formation of both antibodies and immune cells that can bind to this particle. Only large molecules such as polysaccharides, proteins or factors such as infectious agents, or insoluble foreign matter can elicit an immune response in the body. A substance that provokes antibody or immune-cell formation to be recognized by an immune system is called an antigen. A hapten is a small molecule which can elicit an immune response only when attached to a large carrier such as a protein; the carrier may be one which also does not elicit an immune response by itself [36-38].

Each molecule of an antibody has affinity to bind two identical antigen molecules at the end of each arm [36-38]. The contact between antigen and antibody is stabilized by non-covalent bonds. This very important property of antibodies finds application in biosensor technology. The immunosensors or antibodies based biosensor usually use an antigen-antibody reaction to produce a transducer signal change [43]. Antigens are bound to antibodies by hydrophobic, ionic and van der Waals forces. The antigens have a special site called a determinant that binds to antibodies. Some proteins have many determinants to which antibodies might bind. When a small molecule is attaching to the surface of protein, a new determinant can be created [36-38] (see Figure 1.8).
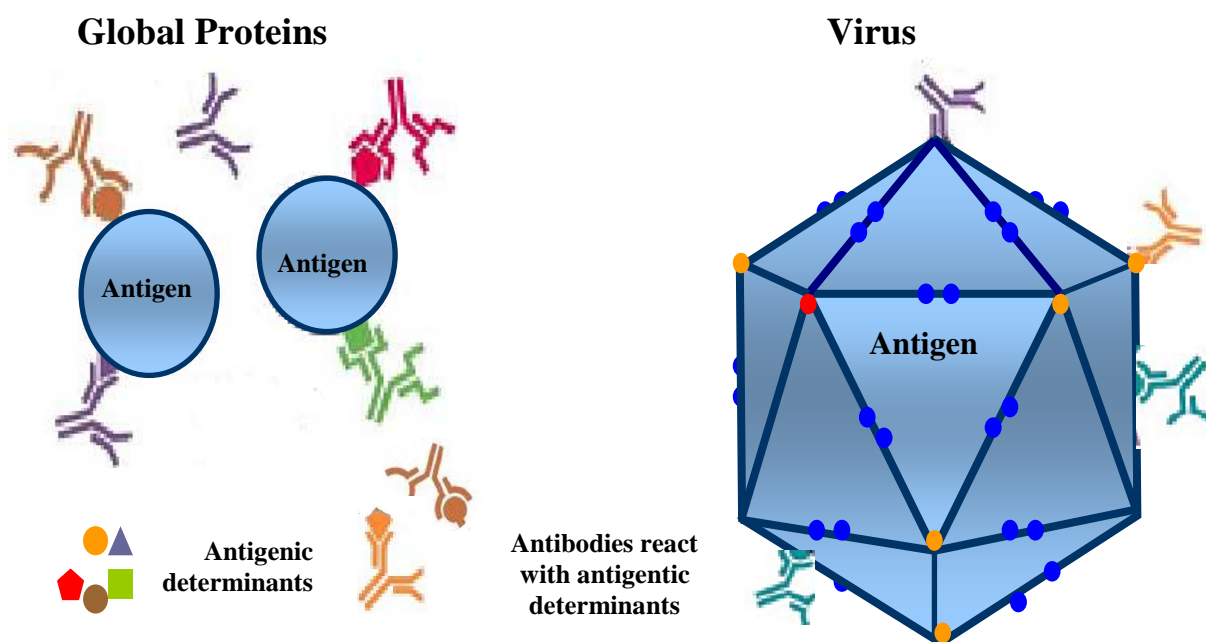
Figure 1.8 Antibodies can bind to single or multiple determinants on antigen. Viruses have multiple determinants on a single particle, for this reason antibodies form large groups when reacting with such antigens [38] (Images taken from the ref. [44]).

1.2.2.2 Affinity and avidity of antibodies

The measure of the strength of the binding between an antigen and an antibody is the affinity. The equilibrium of the interaction antigen-antibody is calculated with the affinity constant K_A (see equation 1 and 2).

$$A_b + A_g \quad \longleftrightarrow \quad A_b \text{——} A_g \qquad (1)$$

$$K_A = \frac{[A_b - A_g].}{[A_b].*[A_g].} \qquad (2)$$

where ,
A_b-represents antibody
A_g-represnts antigen
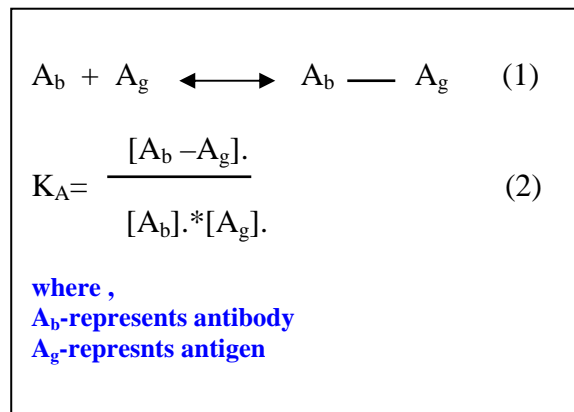
The time to obtain an equilibrium of the interaction does not directly depend on the affinity, but the higher the affinity shorter is the time. High affinity complexes are also much more stable [45].

The specification of immunosensors is determined by the affinity of their components. High affinity results in sensitive sensors, but too high affinity causes irreversibility.

 Avidity is a measure of the stability of the antibody-antigen complex. From a practical point of view avidity is more important than affinity because it gives information about the valence of the antibody and the geometric arrangement of the interacting compounds. The immobilized antigen has an influence on the avidity. High avidity is reached when all determinants are bound to the antibody. Under this condition the antigen-antibody complex is more stable [45].

1.2.3 Nucleic acids

Nucleic acid is a molecule that stores and transits information in cells. The information is processed in the form of a code. Cells have two information molecules: deoxyribonucleic acid (DNA) and ribonucleic acid (RNA).

DNA and RNA are built up of chemically linked chains of nucleotides, each of which consists of a sugar, a phosphate and   five kinds of nucleobases. In RNA molecules, the pentose is ribose and in DNA it is deoxyribose. The DNA and RNA contain also other nukleobases. Adenine and guanine belong to the double-ringed class of molecules called purines. Cytosine, thymine, and uracil are all pyrimidines (see Figure 1.9) [37-38].

Purines   **Pyramidines**

| Adenine | Guanine | Uracil | Thymine | Cytosine |
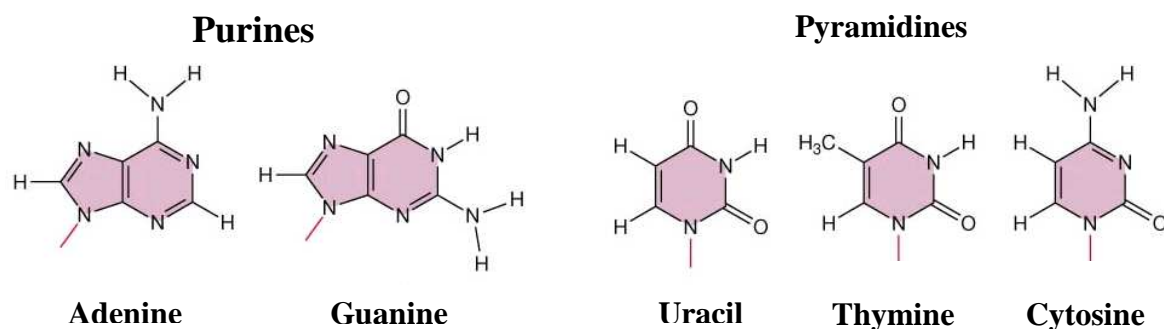
Figure 1 .9 The chemical structure of purines and pyrimidines [46].

The presence of a phosphate group in a chemical structure determines the acidic character of the bases. The bases: adenine, guanine and cytosine are typical for DNA and RNA. The thymine is specific for DNA and uracil for RNA. The names of the bases are usually abbreviated by A,G,C,T and U. The sugar component of a nucleotide is a connection between the base and the phosphate group. A combination of base and sugar without a phosphate group is called a nucleoside. Nucleosides that have one, two or three attached phosphate groups are called nucleoside phosphates. Nucleoside phosphates are divided in three groups: monophosphates with a single phosphat, diphosphates (two groups of phosphate) and triphosphates (three groups of phosphate). The nucleoside triphosphate is necessary for the synthesis of nucleic acids. The nucleotides are linked to each other by phosphodiester bonds [36-38].

Nucleic acids are formed by a reaction between a hydroxyl group, attached to the carbon of a sugar of one nucleotide, and the phosphate group of another nucleotide. From a chemical point of view, a nucleic acid strand is a phosphate –pentose polymer with purine and pyrimidine bases as side groups. Figure 1.10 shows the formation of nucleic acids.
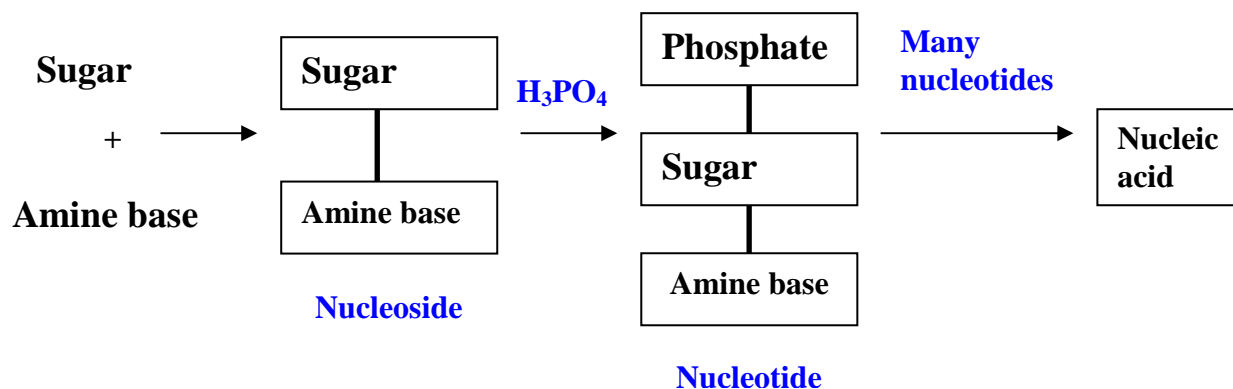
Figure 1.10 The scheme of the formation of nucleic acids [47].

1.2.3.1 DNA

The structure of the DNA was discovered by James Watson and Francis H.C. Crick in 1953 [48]. DNA molecule consists of two polynucleotide strands which are wound around each other to form the structure known as double helix (see

Figure 1.11). The two strands are linked to each other by hydrogen bonds and hydrophobic interactions. The sugar (deoxyribose) and phosphate form backbones while the base connects the two polynucleotide strands. Usually they are placed in a distance of 0.34 nm from the helix axis. The bases in two strands have their precise place. The base A is always paired with T by two hydrogen bonds and G is paired with C by three hydrogen bonds. This is called complementarity [36-38]. Another type of reaction such as G-A and A-G is also possible but only theoretically or in synthetic DNAs. DNA molecules exist in three forms called B, A and Z.

Figure 1.11 Structure of right-handed DNA molecule [50].

The B-form (the right-handed form) is the most common form of DNA in cells. In the B-form, the helix makes a complete turn every 3.4nm, i.e. there are 10 pairs per turn and the interwound strands make two grooves of different widths, referred to as the major and

the minor groove, which can facilitate bonding with specific proteins. The crystallographic structure of B-DNA form can change to the still right-handed A-form in a solution with higher salt concentrations or with alcohol added. In the A-form the helix makes a turn every 2.3 nm and there are 11 base pairs per turn [36-38]. The stacked bases are tilted. Another DNA structure is called the Z form. In this form, the bases seem to zigzag when viewed from the side and it has a left handed configuration. Here one turn spans 4.6 nm, comprising 12 base pairs. The both forms A and Z can also exist in cells. Figure 1.12 shows the DNA double helical structure and different forms of DNA [36-38].
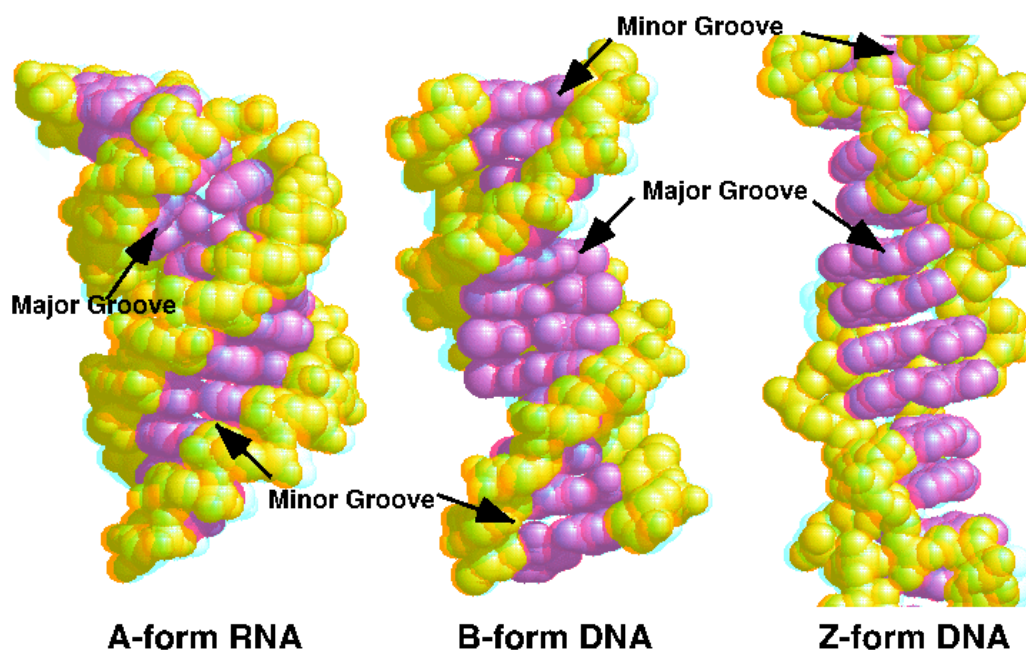
Figure 1.12 Comparison between A, B and Z form of DNA [50].

1.2.3.2 DNA Hybridization

The unwinding and separation of DNA strands is possible experimentally, this process is called denaturation. There are various methods with which DNA molecule can be denaturized. The thermal denaturation, also called melting, is the separation of the DNA by heating the double helix [36-38].The melting temperature T_m, is the temperature at which half of the DNA molecules are single and the other half double stranded (see Figure 1.13).
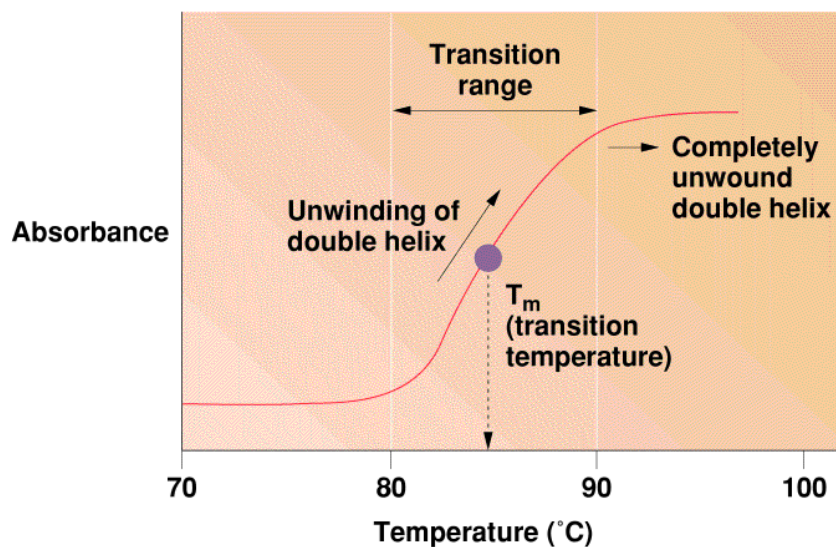
Figure 1.13 The T_m is the mid-temperature of the transition between and denatured states of the DNA molecule [51].

By lowering the temperature or increasing the ion concentration, the single stranded DNAs can bind again. This process is called renaturation [36-38]. Denaturation and renaturation of the DNA are the basis of nucleic acid hybridization techniques and for a DNA biosensor as well. The processes are schematically presented in Figure 1.14.
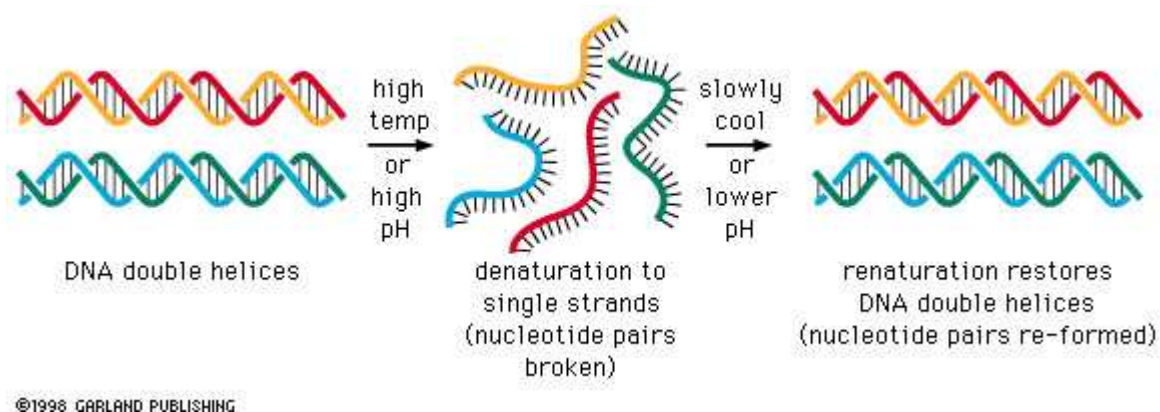
Figure 1.14 The denaturation and renaturation of two double-stranded DNA molecules [52].

1.3 Transducer

In the biosensor technology, a transducer converts the biological reaction into a measurable signal. The type of a transducer depends on the parameters that are measured. The commonly used transducers are based on optical, electrochemical or thermal changes. The signal that is measured by a transducer usually is converted to an electrical signal [8].

This section will focus only on optical transducers and especially on optical sensors based on fluorescence because this technology is the most commercialized on the market. Concerning other type of transducers, the reader is referred to the review articles or to the excellent book by Tran Minh Canh on biosensors [8].

1.3.1 Optical transducers

Many types of optical transducers are applied in biosensors. They are based on optical methods that include absorption, fluorescence, refractive index changes and light scattering. The optical methods are usually chosen according to the biosensor application and the anticipated sensitivity [3]. In practice, the optical transducer measures the changes in the intensity, frequency, phase shift and polarization of the light. The measurable parameters are correlated to changes in concentration, mass and number of biomolecules. This type of transducer is made up of electronics and standard optical components, such as fiber optics, wave guides, photodiodes, spectroscopes and interferometers [15]. The classical optical technique used in the biosensor technology was based on optical absorption and X-ray fluorescence spectroscopy and required a large apparatus. Since the miniaturized sensors are more interesting for a potential market, new techniques were applied to manufactured optical sensors, one of them is fiber optics [15]. The thin fiber itself is made of glass or plastic and is used for transmitting the light in optoelectronics. It's dimensions are similar to those of a human hair. In biosensor technology, fiber optics are used to transmit the light to and from the analyte [53,54]. These kinds of biosensors have usually a very simple construction. The light source can be light-emitting diodes (LEDs), a lamp (for example: halogen lamp), a laser or laser diodes. In case of a lamp and laser, the construction is supported by beam focus optics and holders for the fiber alignment. In the case of LEDs and laser diodes, the fiber optic is connected by commercial connectors [3,15].

The light intensity is detected by PN-type photodiodes and registered by a standard electronic circuit [3]. Fiber optics sensors are usually classified in two groups: extrinsic sensor with one single fiber or two fibers and an intrinsic sensor based on evanescent waves. The single fiber terminology means, that the same fiber is used for lighting and detection. In case of the two fiber technology, one of the fibers is used for lighting and the second for detection. In the first technique, the light from the source is transported along an optical fiber to the place where a biologic sensing element is located. Reflected, scattered or emitted light is then transported by a bifurcation of the same fiber or by the second fiber. The technique of Evanescent Wave (EW) is a special one in optical sensor technology and will be described in a separate section [3, 15].

Optical fiber sensing has in comparison to the other type of transducers many advantages like miniaturization, flexibility and brightness. Special geometrical properties of a fiber give a possibility to insert it into needles or catheters thereby enabling a measurement inside tissues or blood cells [3]. These sensors are made of materials that are non-toxic and biocompatible and for this reason they are mainly used for medical application. This kind of sensing requires for in vivo application a lower light power and thus is safer for the patient [55].

1.3.2 Optical Techniques: Evanescent Waves

An evanescent wave itself is an electromagnetic wave that is formed when incident light is reflected on an interface such as glass or quartz at an angle larger then the critical angle, causing total internal reflection [56]. The reflection and refraction process is predicted by Snell's law. When a light beam passes at oblique angle through the interface between two materials with different refractive indices both a reflected and a refracted light beam emerge. At the critical angle, the light passes through a medium with a higher into a medium with a lower n and will be refracted at 90°. In other words it will be refracted along the interface. For the angle of incidence larger   than   the critical angle, the light cannot pass
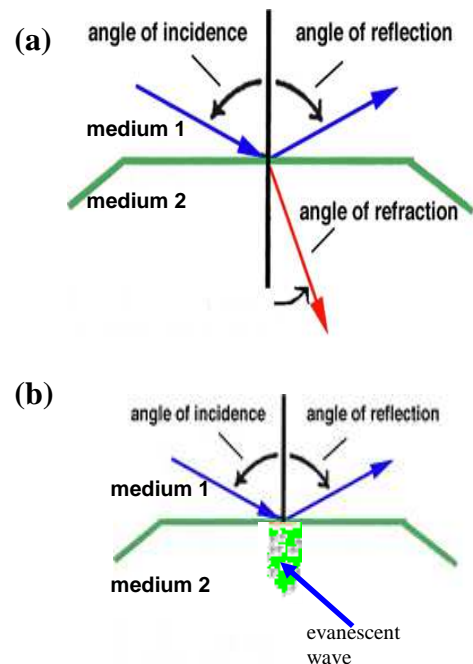
through the second medium but is reflected back into the **(c)**

first medium. This   process is known as total internal

reflection [57]. While the incident light is reflected, the

electromagnetic field component penetrates a short (tens

of nanometers) distance into the medium of lower

refractive index creating an evanescent wave (see figure

1.15 -b). The intensity of the wave decays exponentially

with the distance from   the   interface   at   which   they

Figure 1.15 Schematic diagram

are   formed [58]. The evanescent wave phenomena is

for (a) both reflection and

usually used together with optical fiber techniques [58].

refraction occur when the light
is incident on a more refractive

A cladding of the fiber has a larger refractive index then

medium (b) evanescent wave (c)
total   internal   reflection   in
optical fibre [59].

the core of the fiber. When   light   passes   through   the core-cladding interface, the total

internal reflection   takes   place   in the   core (see Figure 1.15c). At the same time, the

energy of the light waves in the core penetrates into the cladding, forming an evanescent

wave. In the biosensor technology, a cladding of a fiber is removed, so that   a sample is in

direct contact with the evanescent waves [58].

1.3.3 Optical Techniques: Surface Plasmon Resonance

Surface plasmon resonance (SPR) is an optical technique for determining refractive index

changes at surfaces. This surface is typically an interface between a metal such as gold or silver

and a dielectric material such as air or water [8]. The optical system of an SPR apparatus

consists of a dielectric substrate and a prism coated with a thin metal film, light emitting

diodes, and a detector [9]. The technique is also based on the total internal reflection

phenomenon, which induces the generation of surface plasmons in the metal film [9,60]. The

surface plasmons are quasiparticles, which are confined to surfaces and interact strongly with

incident light [61]. These particles are produced by the quantization of the density waves of the

charge carriers in the metal. The plasmons can be excited by light only at a well-defined angle

of incidence, which occurs when the wave vector of the light in the plane of the sensor is equal

to that of the surface plasmon, i.e. at a resonance condition [61].

The reflected light energy is thus reduced at this resonance angle, which is visible as a sharp minimum in the angle-dependent reflectance. The location of the minimum is determined by detecting the change in the angle or wave length. The resonance angle strongly depends on the refractive index or dielectric constant [9,60].
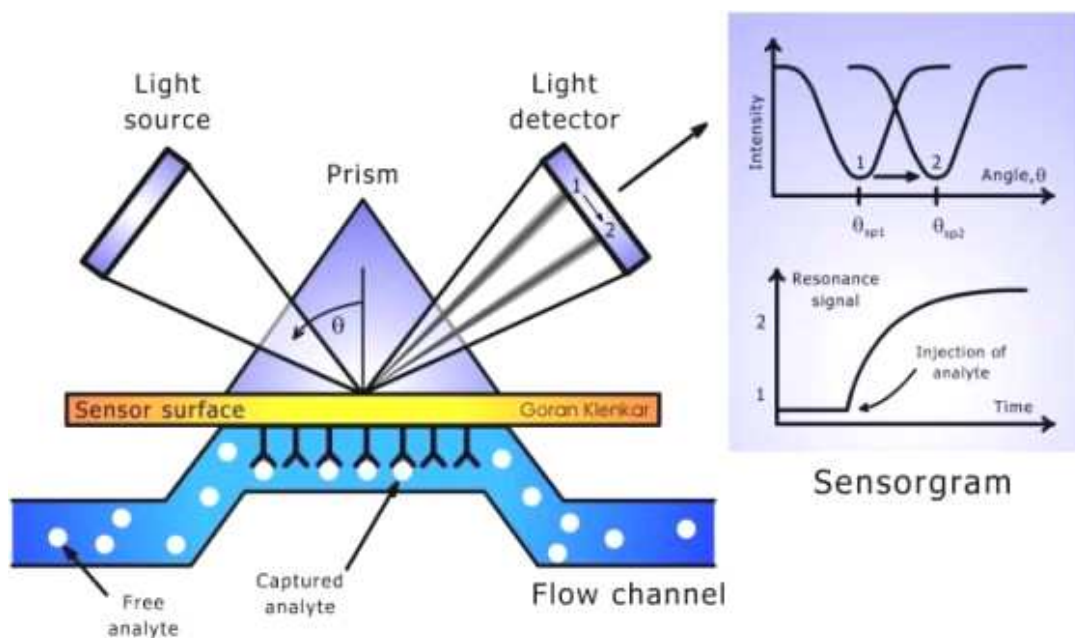
Figure 1.16 A schematic illustration of surface plasmon resonance [62].

A schematic illustration of surface plasmon resonance is presented in Figure 1.16. One of the binding molecules is immobilized on the surface of a sensor, for example in a flow cell. The other binding molecules are flowing over the surface of the sensor and thus interact with the immobilized molecules [9, 60]. A binding interaction on the surface of the sensor is determined by a change in the refractive index close to the surface of the sensor. When molecules in the sample bind to the sensor surface, the concentration and therefore the refractive index at the surface changes and this is detected as a shift of the resonant angle or the wave length. The changes are measured continuously to form a plot called sensogramm (the response against time during an interaction), which provides information about the progress of the interaction [63]. These methods are usually applied to measure an antigen-

antibody interaction or complementariness of a DNA strand. The technique is characterized by high sensitivity and non-specificity. It means that it is not sensitive to chemical changes, but it can be applied to measure the binding of any pair of molecules [60].

1.3.4 Optical techniques: Fluorescence

One of the most popular transducer techniques used in DNA arrays is the total internal reflection fluorescence TIRF which monitors changes in the fluorescence [9]. This method has been developed to investigate the interactions of arrays of biomolecules, for example DNA, immobilized on a sensing surface. The TIRF technique is also based on the principle of total internal reflection [9]. It is differs from the other techniques in that the evanescent wave generated under total internal reflection excites a fluorophore near the surface of the waveguide, and the resulting fluorescence is measured by the detector [9]. The TIRF instrumentation usually consists of the light source and a detector and also a variety of focusing lenses to improve the detector response. A coherent light from a laser is used as the excitation source for the fluorophores. There are two common fluorescent labels used in the measurement: fluorescein and cyanine dye (Cy5). The choice of the laser depends on the fluorescent label used. Usually an argon-ion (488nm) laser is used for fluorescein and a helium-neon (633nm) or diode laser (635nm) for the cyanine dye. To detect the fluorescence, emission CCD cameras, photomultipliter tubes (PMT), photodiodes or a single photomultiplier tube can be used. The antibody-antigen binding interactions are the best known system used in sensors based on TIRF [9].

One example can be the immunosensor produced at the research group Gauglitz Optical Spectroscopy at the University of Tübingen. The setup of the immunosensor consists of a laser diode, a transducer, a flow cell with an auto sampler, polymer fibers, filters, photo diodes (PD), a lock-in and a personal computer (PC) [64]. The scheme is presented in Figure 1.17.

This biosensor uses dye labeled antibodies to detect specific organic analytes in water samples without pre-treatment and pre-concentration [64].
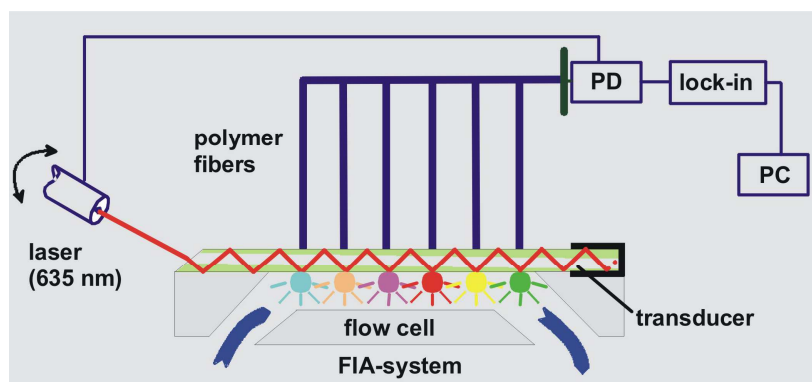
Figure 1.17 The scheme of fully automatic optical biosensor based on TIRF,
fabricated at the research group Gauglitz Optical Spectroscopy
at the University of Tübingen [64].

The procedure is as follows: in the first step a derivative analyte is covalently bound to the transducer. The sample, which contains the analyte is bound to the specifically labeled antibody by incubation. The process is finished when the equilibrium of the reaction is reached. When the sample is pumped over the sensor surface only the antibodies with free paratopes are bound to the surface (see Figure 1.18) [64].
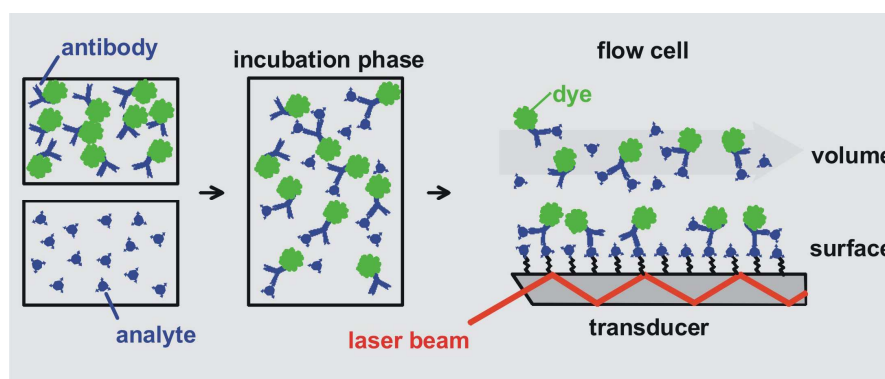
Figure 1.18 The binding of labeled antibody to the surface of transducer [64].

This type of detecting assay is called sandwich assay. The antigen, in this case analyte is bound to the immobilized capture antibody at one epitope and is detected by a fluorescent-labeled antibody. The assay produces a fluorescent signal that is directly proportional to the amount of the bound analyte [9].

The TIRF system can be also used for the detection of a DNA array. The principles for the detection are the same like in the case of immunosensors. A more detailed description of a DNA array detection can be found in reference [65].

1.4 Immobilization method

There are several techniques by which the biological component of a biosensing system can be immobilized at the surface of the transducer. These methods are divided into four groups: physical adsorption, covalent immobilization, physical entrapment, cross linking and membrane. Physical adsorption and covalent binding are the most common methods used in optical biosensor technology [8, 15].

1.4.1 Physical adsorption

Adsorption is a physical process, which occurs via dipole-dipole interaction or hydrogen bonding. The type of reaction depends on the nature of the substrate surface and the adsorbate. This method is very simple in application and has been used by several groups to immobilize enzymes or antibodies on the transducer (see Figure 1.19)   [9, 66].

Figure 1.19 Enzyme molecules adsorbed to the particle [66].

The enzymes are usually mixed with an appropriate adsorbent   under specific conditions of pH and ionic strength. When the incubation process is finished, the rest of loosely bound or unbound enzymes are washed away. The bonds are usually formed by a combination of hydrophobic effects and the formation of several salt links per enzyme molecule. The physical bond between the biological molecule and surface of the transducer is very strong, but in special conditions like introducing a substrate or changing the pH or ion strength the bond strenght can be reduced [66].

Antibodies are easily adsorbed on metal films such as gold or silver usually deposited on glass [8]. The link to the surface is usually formed by hydrophobic attraction. This process sometimes creates a number of constraints that have influence on epitope recognition and antigens–antibody interactions [67]. By optimizing the conditions of adsorption, one can minimize these technical problems.

The physisorption is a direct method for immobilization of biological molecules on the transducer surface. The disadvantage of using this method is that it is not a good technique to control the orientation of biomolecule on the transducer surface. Optical methods such as surface plasmon resonance need a highly developed technique of immobilization. In most cases, the proteins A and G or biotin are used to arrange the orientation of the molecules [68]. Other advanced techniques use functionalized self -assembled monolayers to attach molecules to the surface of a transducer [68].

1.4.2 Covalent binding

Covalent immobilization is based on the binding between functional groups of biomolecules and a support material via chemical groups such as $NH_2, CO_2, OH, C_6H_4OH, SH$ [15]. It mostly involves the activation of the surface using e. g. orsilane or thiol self -assembled monolayers. These advanced techniques are proper for attaching bio-molecules such as protein or nucleic acids [9, 15]. Organosilanes and thiol are compounds used for attaching an organic layer to an inorganic substrate. Organosilanes has the general formula RSiX3, where R is an organofunctional group selected according to the desired surface properties and X is a hydrolysable group, typically an alkoxy group, which is capable of reacting with the substrate [69]. Thiol contains a functional group composed of a sulfur and a hydrogen atom (-SH). This functional group is referred to either as a thiol or sulfhydryl group [70]. The method to form uniform layers of silane or thiol on inorganic substrate is called "self assembly".

Self Assembled Monolayers (SAMs) are usually formed from alkanthiolen on a gold surface and alkylsiloxanen on a glass surface. This section will be limited to the deposition of SAMs from chains of n-alkanethiols (CH3(CH2)n-1SH) on gold surfaces, since this shows so far the largest application potential. A thiols-self assembly layer is usually formed on metal surfaces such as gold, silver, platinum or copper [68]. The structure of a self-assembled monolayer relies on the morphology of the metal. Generally, Au (111) is employed for the growth of monolayers [71]. The preparation of SAM monolayers is very simply. The substrate, gold on silicon, is placed in a solvent, for example ethanol, which contains thiol groups. The functional ~SH group has a very strong absorption to the gold substrate, resulting in the formation of densly packed and ordered monolayers.

The adsorption of thiols on the substrate is very fast, but the molecule organization process takes more then 1 hour (see Figure 1.20) [71]. The thiol molecules are organized in a way that the tail group points away from the surface. The tail group is responsible for the SAMs functionalization and the covalent binding between material support and biomolecules [71, 68] (see figure 1.20).
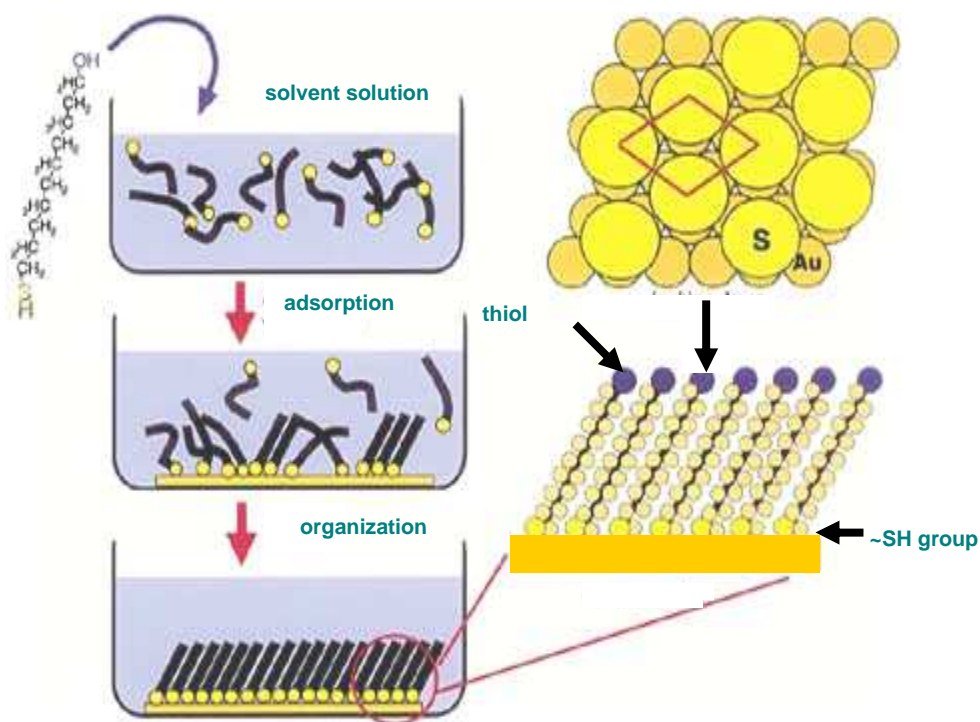
Figure 1.20 Formation of SEMs assembly monolayer on a Au(111) substrate [72].

An alkylsiloxane is often used for formation of silane –self assembled monolayers. Surface silanization involves a covalent binding of the silane molecule to the silicon oxide surface through the siloxane bond [73]. The method requires a solution of alkyltrichlorosilane in a hydrocarbon solvent. Silane SAMs are deposited on hydroxylated substrates such as silicon with a layer of native oxide, or glass. Generally, the preparation techniques are similar to those used for the formation of thiol self assembled monolayers. The substrate is immersed in the solution for a specified period of time and at a specified temperature. The biological molecules are covalently bound to the tail group of the silane monolayers.

1.5 Résumé

This chapter presented an overview on biosensor technology with detailed descriptions of biosensor components such as biological receptors and optical transducers. The optical sensing system is a well establish technology today. The implementation of fiber optics techniques made the optical biosensor technology more attractive for the market, providing a development of highly sensitive device, which may be used for detection of low-concentrations of an analyte. Advantages of the optical techniques involve also the speed and reproducibility of the measurement. The chemical detection is also a well established technology, but it is not presented in this chapter. It is a common method used in a transduction and readers can find a lot of information about this technology in the reference [74].The electrochemical transduction is a less expensive technology in comparison to that based on optical techniques. The last requires a huge instrumentation. The electrochemical biosensors involve advanced chemical engineering methods to transmit the electronic signals. The measurement can not be repeated many times and the system requires also a large volume of sample fluid [75].

The transduction technology (chemical and optical) requires a highly qualified personal and are still time consuming. The future of biosensor technology lies in the miniaturization, automatization, simplicity of the workload and the fabrication of low-cost devices. There are also tendencies to increase the sensitivity and the detection limits of the biosensor. Stability and reproducibility are also   key issues of a future technology.

Many of the developing biosensors are not commercialized yet and a lot of them will   never be used outside research laboratories. For the future technology, is important to develop communication between research laboratories and industry to speed up the commercialization of biosensors.

1.5.1 Commercial significance of biosensor

The report prepared by BBC research presents information   and analysis about developments of the biosensor technology in industry on   the worldwide market for the year 2009 [76]. The report says that the medical and life science sector was the most important application field for biosensor. The estimation presented there, shows that the market size in the year 2004 was about $6.1 billion and will grow to $8.2 billion in 2009 with a growth rate of about 6.3 per cent per year. 85 % of the total market in 2003 was spent on the glucose biosensor

product for patients with diabetes [76]. Additionally, a growth of the market has been observed in the pharmaceutical and military research industry. In the global research-driven pharmaceutical companies, there is a need for a new rapid assay biosensor that speeds up the progress of drug discovery. After the terrorism attack on the World Trade Center in USA, there is a visible development progress in a new rapid diagnostic tool for detection of biowarfare agents in military industry [76].

In medical sectors, a new glucose monitoring device will be still attractive for growth of the biosensor market in the future. The development in this sector is going in the direction of implantology. There is also a continuous need to develop medical biosensor based devices that are used for Point-of-Care testing or devices that monitor vital symptoms related to the daily clinical application.

Large amounts of money are also invested in the development of a DNA microarray technology and gene or DNA chips. Affymetrix is the leading company in that field, but there are some other companies that are starting to work on this technology [77]. In the future, it may result in new technology development and applications.

The progress in microfluids fields and semiconductor micro-fabrication technology has been resulting in the development of a Lab-on-chip technique. It is a concept of integration of all laboratory task on a miniaturized, easy to handle portable chip. Caliper Life Science is the leading company in the microfluid LabChip technology [78]. Agilent licenses the Caliper's technology to develop diagnostic systems leading to personalized medical applications [79]. The future market scope for lab-on-chip devices is vast and an attractive pricing model can be still established.

1.5.2   Baselt and magnetoresistive biosensor

An interesting solution for future technology requirements and markets needs has been proposed in 1998 by Baselt and other researchers from Naval Research Laboratory in USA [80]. This technology was based on magnetoresistive effect, previously used in computer memory technology. It provides fully automatical and inexpensive devices, characterized by higher sensitivities [81].

Today, the magnetoresistive biosensor technology based on the giant magnetoresistive effect is well established [81]. The development of magnetoresistive sensors in research laboratories is going in two direction. Some of the research group are focussing on the development of large area sensors for detection of single DNA spots [75]. Others are concentrating on the development of micro-sized sensors for single magnetic molecule detection and investigation of binding forces [82,83]. Prototypes of large area magnetoresistive sensors will find application in medical diagnostic or as a point of care testing device. Actually, the concept of magnetoresistive biosensors used for detection of low concentrations of targets in body fluids for diagnostics is developed by Philips Reseach Laboratory in Eindhoven. One can expect that a commercialized device will come in the near future [84]. The concept of the small area sensors for detection of single magnetic molecule has been mainly developed and investigated in research laboratories. There are only few research group that concentrate on this subject. One of them is a group from IBM Standford laboratory that is focussing on detection of single magnetic particle with aim of eventually detecting a single DNA fragment. Since 2002 our research group at the University of Bielefeld is also focussing on the development of small area sensors for the detection of single magnetic particles /molecule. This is one subject of the presented PhD thesis [83].

Parallel to the magnetoresistive technology there are also investigations on manipulation systems that can be integrated together with magnetoresisitive biosensor to build an on-chip laboratory. Such devices can find many possible applications, e.g. examination of protein-DNA interaction, measurement of binding forces of typical bonds or examination of proteins by unfolding them [85].

The future of the magnetoresistive based biosensor technology lies in the fabrication of highly sensitive devices for the detection of single magnetic nanoparticles.

2. Magnetic particle and biosystem

Since 1980s, magnetic particles have been used in biological assay. They found application in many areas of bioscience and medicine, especially for biomolecule/cell separation, drug delivery and-targeting, nucleic acid sequencing and medical therapy [86-90]. Actually they are produced commercially by many companies and their sized varies from a few micrometer down to a few nanometers [91-95]. The terminology used in literature to describe magnetic particles can sometimes be inconsistent and confusing to many readers. Essentially, the term magnetic microparticle refers to particles with a diameter larger than 1 µm. In many research application a term magnetic nanoparticle is used, that refers to particles with size below ~100nm. Magnetic microparticles are mainly used to separate cells from blood, bone marrow, core blood and prepared samples such as buffy coat and mononucleare cells and tissue digests. These particles have found application for the isolation of T cells, B cells, stem cells, cancer cells and proteins [88]. Magnetic nanoparticles are very attractive for biomedicine, because their size is comparable to a virus (20-450nm), a protein (5-50nm) or gene (2nm wide and 10-100 nm long) [86, 87, and 90]. There are also many other factors that make magnetic nanoparticle favorable for material science, medicine and chemical industry. This chapter presents an overview of magnetic particle application in biotechnology.

2.1 Basic concept

Microparticle technology has been developed by professor John Ugelstad from the University of Trondheim [92]. In 1980, he licensed the technology for making monosized polymer particles. In 1982 together with Amersham Biosciences in Upssala, they developed new method for separation of proteins and peptides using non-magnetic polystyrene particle. The magnetic particle technology was introduced a few years later and based the development of Dynal Biotech, the first company that produces commercial magnetic microparticles [92]. Since then, many biotechnology companies develop magnetic particle technologies for isolation of cells, proteins and nucleic acids. Some of them are listed below (see Figure 2.2).
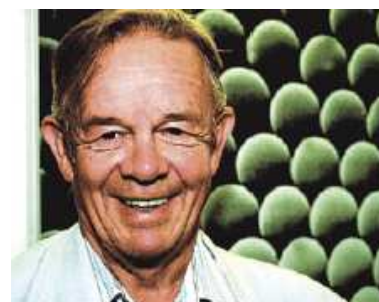
Figure 2.1 In 1976, professor John Ungelstad from University of Trondheim, for the first time, made uniform polystyrene spherical particles of exactly the same size [96].

COMPANY	WEB SITE	MAGNETIC PARTICLE
Agowa GmbH	www.agowa.de	AGOWA mag Particles Size <53µm, Composition: polymer with iron oxide, Iron Oxide Content (%) –80% Shape: irregular Properties: superparamagnetic
Bangs Lab.	www.bangslabs.com	COMPEL™ particle – Size :3, 6, and 8 µm Composition :functionalized polymer impregnated with iron oxide, Iron Oxide Content (%) 4 – 12 Shape: Spherical, BioMag® Diameters Size~1.5µm, Composition: silanized iron oxide, Iron Oxide Content (%) > 90, Shape: cluster
Dynal Inc.	www.dynal.no	Dynabeads® * Size :2,8µm, and 1 µm * for more information see the website
Micromod	www.micromod.de	Magnetic particles with the matrix types: latex ,polymer , biopolymer, biodegradable and silica Iron oxide particles* monodisperse iron oxide aggregates with a diameter of 200 nm * for more information see the website
Spherotech	www.spherotech.com	SPHERO™ * Size>0.1µm Composition: iron oxide, Iron Oxide Content (%) 10-15 Shape: spherical * for more information see the website

Figure 2.2 Suppliers of Magnetic Particles.

2.1.2 Classification

Magnetic particles can be classified depending on the size, composition, and shape [97]. According to their size, they are divided in three groups:

- large particles 1.5-100 µm,
- small particles 0.7-1.5µm,
- nanoparticles <0.7µm

When classified on the basis of the magnetic components they contain, magnetic particles can be divided into:

- iron-oxide and
- pure transition metal particles, such as Fe, Ni and Co.

Most of the commercialized magnetic particles are produced with spherical shape, but there are research groups, which fabricate ferromagnetic nanowires in the length from 100nm to several tens of microns [97,98] (See Figure 2.3). It is possible to classify magnetic particles according to their shape into:

- spherical particles (magnetic beads) and
- nanowires.
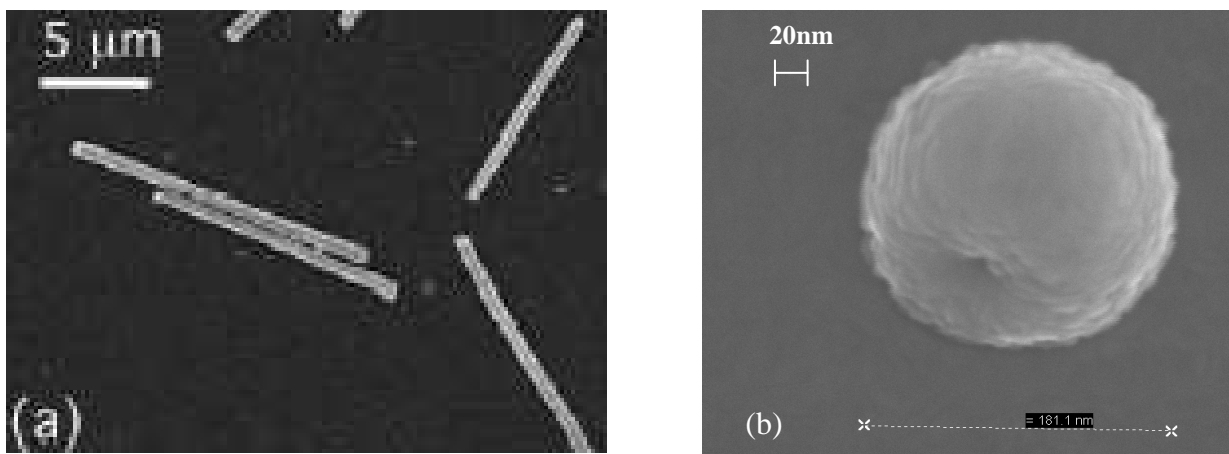
Figure 2.3 (a) SEM micrograph of nickel nanowires of 350nm in diameter [99].

(b) SEM micrograph of spherical, magnetic particle of 180 nm, made at the University of Bielefeld by the author.

2.1.3 Structure and properties of magnetic particles

Iron oxide particles such as magnetite (Fe_3O_4) or it's oxidized form maghemite (γ-Fe_2O_3) are the most common by used particles for biomedical or biosensor application. They exhibit superparamagnetism behavior: magnetizing strongly under an applied magnetic field and retaining no permanent magnetism once the field is removed. The structure of an iron oxide containing particle is shown in figure 2.4.

(a)

Small
superparamagnetic
magnetite-particle
(Fe_3O_4)

Magnetic
particles can
be coated with
Streptavidin,
Biotin, various
antibodies

Polystyrene
core

(b)

Mag = 122.77 K X   100nm   EHT = 20.00 kV   Signal A = InLens   Date :30 Aug 2004
                            WD = 9 mm   Time :11:51
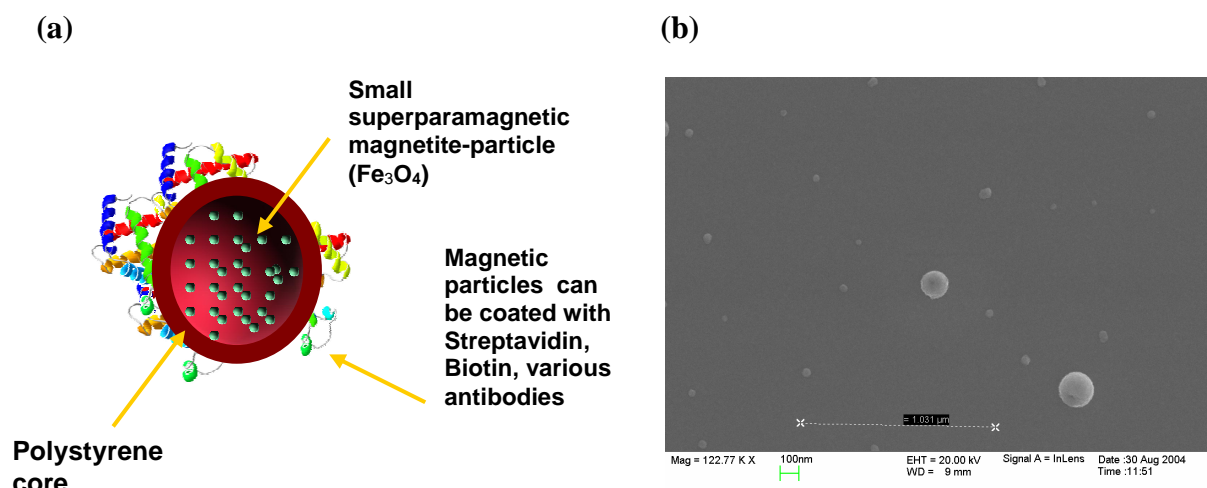
Figure 2.4 (a) Schematic diagram of a functionalized iron oxide particle
(b) SEM picture of single silica nanoparticles of 200 nm.

The iron oxide particles usually consist of a number of single domain particles (Fe_3O_4) embedding into the polymer matrix. This matrix improves the matching with organic components, reduces the susceptibility to leaching and protects the particle surface from oxidation [86]. The matrix guarantees dispersibility and chemical stability of the magnetic particle, reduces toxicity and forms a microsphere shape of the particle [86]. The surface of the particle can be also functionalized with groups such as NH2 and COOH for covalent binding of streptavidin, biotin and various antibodies for cell separation [100, 101, 102, and 93]. For example, the Proteins A and G coated magnetic particles are used for binding IgG from human, mouse and rabbit serum [102].

There are also magnetic particles coated with enzymes such as Proteinase K and RNAse A or with various reagents for a variety of applications [102].

Iron oxide particles are also available with an inorganic silica matrix [93]. This matrix has a lot of advantages. The surface silanol groups can react with alcohols and silane coupling agents to produce dispersions of the particles that are stable in non-aqueous solvent. The silica surface is also ideal for covalent bonding of biological molecules [93]. It also prevents the particles from a contact with oxidative or corrosive environment, which can damage their properties [103]. Additionally, this type of coating offers high stability of the particle exposed to the solution with changes in pH or with high electrolyte concentration [93].

Another class of magnetic particles produced from Fe, Ni, Co metals can exhibit ferromagnetic behavior [97]. These particles tend to stay magnetized to some extent after being subjected to an external magnetic field. This is the reason why these particles tend to form clusters. Ferromagnetics particles have also higher magnetic moment than the iron oxide particles. Thus they are preferred for a biosensor aplication, because they can produce a better signal than the iron oxide particles [97]. Up to now these particles are produced mainly in the research laboratory and they are not yet commercially available [104-105]. The main problem to produce the ferromagnetic nanoparticles is that they can burn when exposed to air [97]. Co particles are not reacting as strongly as Fe particles but they are still oxidizing when exposed to the air [97].

A solution of these problems is a thin Au film protective coating disposed on the magnetic particle to avoid reactions with environment. Au is also a common surface for attaching biological molecules by covalent bonds, so the surface functionalization of a gold coated particle is easier [106-109]. The main problem in the synthesis of Au coated particles is that the gold layer is too thin to prevent the agglomeration of the particles. During the synthesis, it is necessary to add a special ligand against particle agglomeration [97]. Thus the main challenges for future research are the structural integrity and the chemical stability of ferromagnetic particles (see figure 2.5) [107].
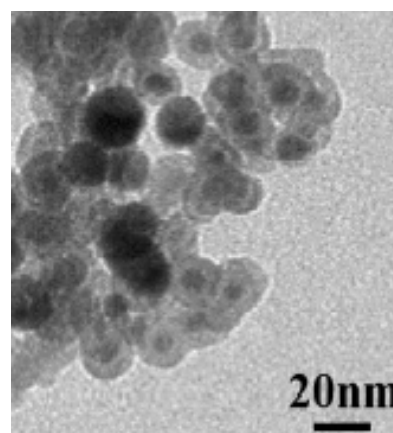
Figure 2.5 TEM image of Au-coated Fe particles [109].

2.2 Synthesis methods

2.2.1 Magnetic microparticles

Emulsion polymerization is one of the common methods used to synthetize magnetic microparticles [110,111]. The methods are based on the preparation of a mixture that contains two liquids that are non-miscible. One of this liquids is water, the second is oil, that is hydrophobic. To the mixture one can also add a surfactant, a substance that is semi-miscible with both water and oil. The surfactant is usually used to stabilize the mixture [110]. If mixed in correct ratios, this procedure results in the formation of highly organized structures depending on the ratio of the three mixed liquids. The magnetic particles can be synthesized in a similar procedure by a mix of styrene, water, sodium dodecyl sulfate, ammonium persulfate, potassium persulfate, and magnetite [110]. All these substances are important for the preparation of emulsion polymerization, only magnetite is introduced to form a magnetic type particle.

Figure 2.6 Mechanism of formation of magnetic mcioparticles by water in oil emulsion.
A-B The dispersion of magnetite nanoparticles and a water-soluble homopolymer, into droplets in an organic medium via the use of an amphiphilic block-copolymer dispersant
B-C This is followed by water distillation at a raisedtemperature from the aqueous droplets to yield polymer/magnetite particles stabilized by the blockcopolymer
C-D The structure of the particles is then locked in by a reagent being added to cross-link the homopolymer and water-soluble copolymer block [111].

2.2.2 Magnetic nanoparticles

The most common methods of synthesis of magnetic nanoparticles are precipitation from solutions and the aerosol/vapor methods. These methods are mainly used to form iron oxide nanoparticles [86].

2.2.2.1 Precipitation from a solution

The nanoparticles can be produced by precipitation from a solution. This technique is based on the precipation reaction that allows to form a particle. Parameters such as a rate, temperature and pH are controlled during the reaction that's resulting in uniform particles of spherical shape [113]. The mechanism of particle formation is quite simple; when a reaction takes place, the concentration of the iron oxide increases until the solution reaches supersaturation. At this critical point, small nuclei of iron oxide precipitate out of the solution (see Figure 2.7). In the standard mechanism, the solute concentration continuously increases until it reaches the supersaturation point, where nucleation starts. The particles continue to grow until the final size is reached (see curve I-Figure 2.6). The second possibility is similar but after the formation of the nuclei, the particles break up to form smaller particles (see curve II-Figure 2.6). There is also a possibility to form particles with multiple nucleation events (represented by the curve III). In this procedure particles with different size are formed and further each of these particles continues to grow.
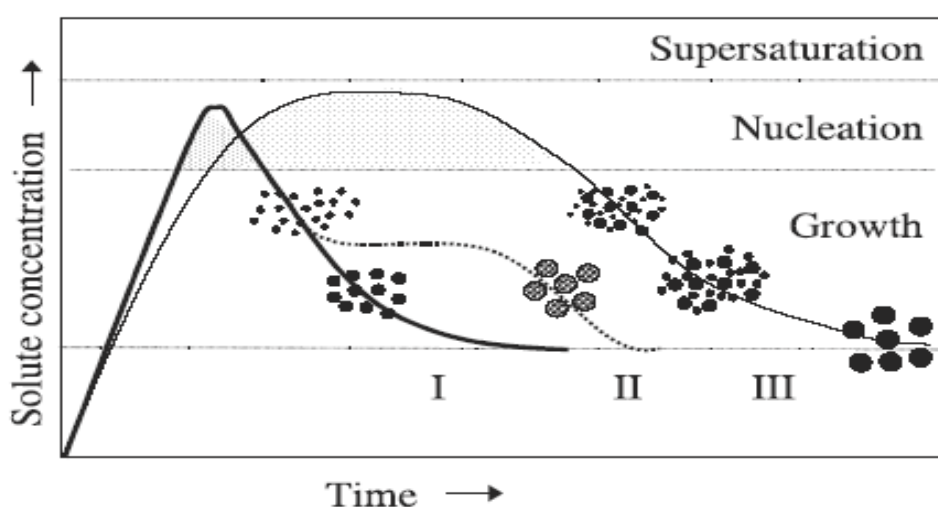
Figure 2.7 Mechanism of particle formation [86].

There are also other methods such as co-precipitation and polyol method that can be also used to form ferromagnetic particles. These methods are described in detail in reference [86].

2.2.2.2 Vapor/ Aerosol Technique

This synthesis method is based on the formation of very small droplets of a solution of an iron compound and a solvent. These are two main methods to form the particles: spray and laser pyrolysis. In the first method, the droplets of solution, which contain iron salt and a solvent are prepared. Later on the droplets are heated in a special furnace. During the heating, the process of formation of nuclei of iron oxide is started   and the solvent evaporates. In the final stage, the particles are filtered and collected in powder form. The spray pyrolisis apparatus is presented in the figure 2.8.

(a)   **(b)**
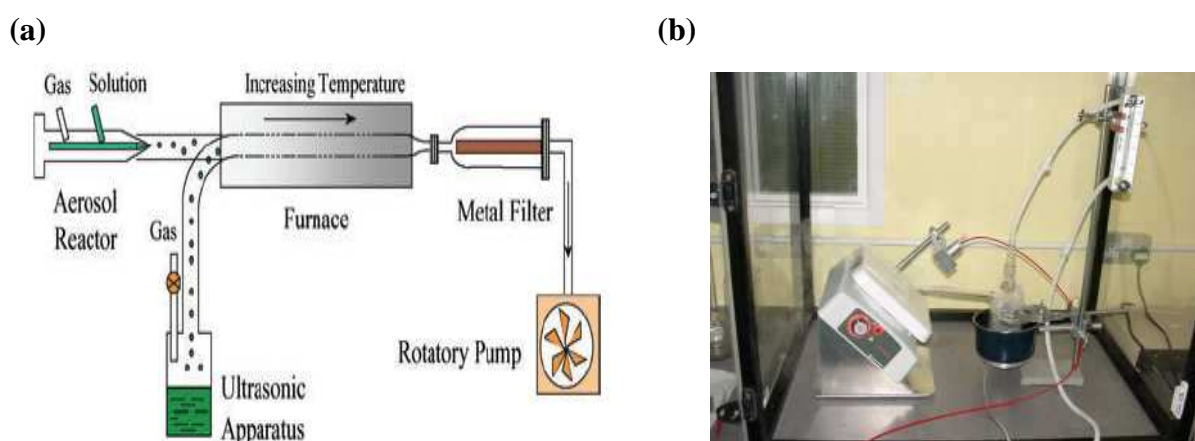
Figure 2.8: (a) Scheme of spray pyrolysis instrumentations (b) Photo of ultrasonic spray pyrolsis [86].

In the laser pyrolysis method, an iron pentacarbonyl ($Fe(CO)_5$), is heated under a laser. This results in the formation of iron and carbon monoxide. The iron oxide particles are formed by introducing   oxygen from air and are filtered out later on by an inert gas [86].

2.3 Application

2.3.1 Magnetic separation

Nanoparticles are applied in biotechnology to isolate specially "labelled" subtypes of cells or other biological entities in a process called magnetic separation. The magnetic separation with nanoparticles is a two-step process, involving the „labelling" of the desired biological entity with biocompatibly coated magnetic material, and the separation of these entities via a fluid-based magnetic separation device (see figure 2.9). Sophisticated systems enable nowadays a flexible, fast and simple magnetic cell sorting of large numbers of cells according to specific cell surface markers without affecting cell viability and proliferation [115].

Figure 2.9 Priniciple of magnetic particle separation. Functionalize magnetic particle bind to the target analyte. Magnetic particle-target complex are manipulate by external magnetic field [114].

In this process iron oxide magnetic particle of >1µm diameter or conglomerations of such particles coated with biocompatible substances such as dextran, phospholipides, polyvinyl alkohol or immunspecific agents are used. The targeted entities bind highly specific with the coated magnetic particles. In the next step the fluid with the marked objects passes through a magnetic separator; magnetic forces generate a gradient that immobilizes the magnetic particles with tagged entities. There are two methods of isolation of the nanoparticle marked objects. A permanent magnet can be applied to a test tube to cause aggregation which is followed by isolation of supernatant. As an alternative a system can be used with a spatially varying magnitude of the magnetic field gradient enabling splitting of the fluid passing through the column into the fractions according to their magnetophoretic mobility. The superparamagnetic nanoparticles are not only used to label the entities by binding to the surface antigen but also can be internalized into specific cells. This newly developed technique [116] enables for example tracking of differentiation and distribution of progenior cells by means of high resolution in vivo imaging techniques. Especially with HIV-Tat peptide derivatized iron oxide coated nanoparticles were incorporated into hematopoietic and neural progenitor cells without affecting cell viability, differentiation or proliferation of CD34+ cells. Derivatized particles were internalized into lymphocytes over 100-fold more efficiently than nonmodified particles. This technology makes it possible not only to detect the homing of the progenitor cells in the tissue sample with the magnetic separation columns
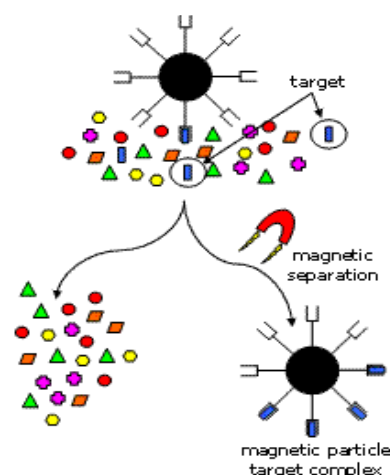
but also to track a single nanoparticle in vivo incorporated in progenitor cell by means of magnetic resonance imaging. The described method has also potential for recovering intracellularly labeled cells from organs. Very promising appears also the publication of C.Y.Wang et al. [117]. The authors report having synthesized Fe3O4/Au (GoldMag) particles with a core/shell structure by means of reduction of Au3+ with hydroxylamine in the presence of Fe3O4. The GoldMag particles need only a single step for antibody incorporating and have high binding capacity for antibodies. These advantages can improve the methods of isolating and detecting biomolecules. The magnetic separation is recognized as a method with a wide spectrum of applications in biotechnology. This technique is used to detect with very high sensitivity the tumor cells in organism, to sense parasites, in cell counting in immunology, oncology and hematology and as a pre-processing technology for polymerase chain reaction. Since magnetic nanoparticles are attracted to a high magnetic flux density, magnetic force and MCLs were used to construct multilayered cell structures and a heterotypic layered 3D coculture system. Thus, the applications of these functionalized magnetic nanoparticles with their unique features will further improve medical techniques.

2.3.2 Biomedical Application

2.3.2.1 Drug delivery

Drug delivery means a targeted distribution of a medicine within a specific tissue thereby diminishing the side effects on the rest of the organism. This technique enables to lower the dose of medicine being administered into the organism- see fig 2.10. Targeted delivery of cytotoxic drugs used in oncology is the foremost point of interest of biotechnology [118-119]. The drug molecules are bound with a biocomptible magnetic nanoparticle [118-119]. The biocompatible ferrofluid is than injected into the patients circulatory system and directed by means of high-gradient magnetic field into the targeted body part. When the drug concentration in the targeted tissue reaches the desired level the drug can be released by enzymatic activity or a change of the pH, osmolality or the temperature in the tissue. There are many factors influencing the effectiveness of this method – the way of drug administration, the hemodynamic status of the patient, the dimensions of the targeted tumor and the physical properties of the applied magnetic molecules. A magnetic molecule carrier is formed of a magnetic particle or a conglomerate of magnetic particles (usually magnetite or maghemite) coated with a biocompatible polymer, non-organic substance or noble metal layer [86]. There are also alternative magnetic particle cores under research: iron, nickel, and cobalt [86,97]. Although the drug delivery is a promising technique there are some limitations in this

method such as toxic reactions with magnetic particles, lack of possibility to influence the drug distribution after release from the carrier, danger of arterial embolization by ferrofluid overload [120-121].
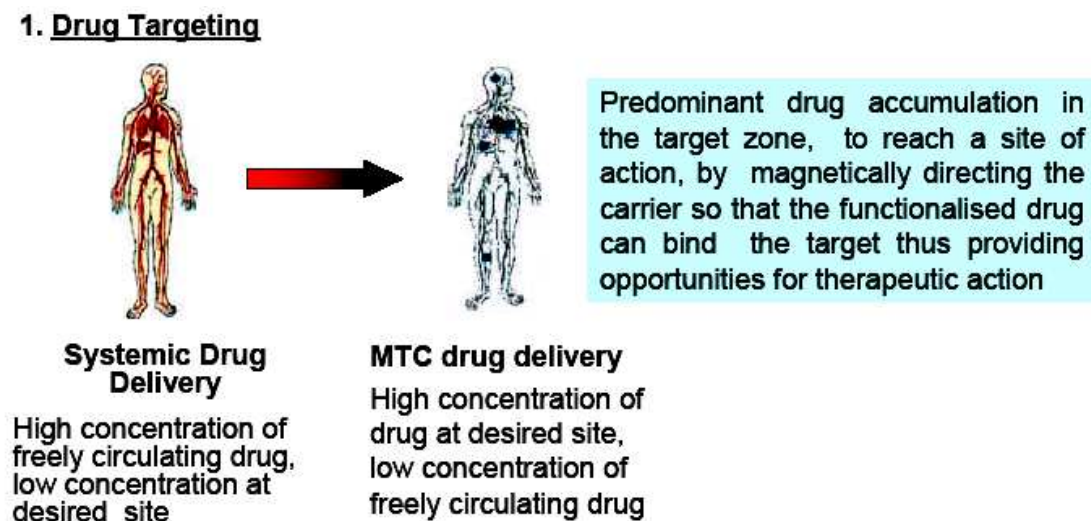
Figure 2.10 The concept of superparamagnetic particle application in drug delivery [122].

Another group of medicine that can be delivered with nanoparticles are radiopharmaka-radionuclides applied in medicine, mainly in tumor therapy. In opposite to cytotoxic drugs they do not have to be incorporated to the targeted cells and they stay coupled to the carrier [123]. The use of drug delivery is also a matter of research in the case of gene therapy, where the therapeutic gene is carried by a vector. The vector's role is to make it possible for a gene to be incorporated by a cell nucleus. The application of a magnetic drug delivery according to experimental studies should increase the probability that such a therapeutic gene will be expressed by a host organism [124].

The complexity of nanoparticles applied in biotechnology is presented in figure 2.11.
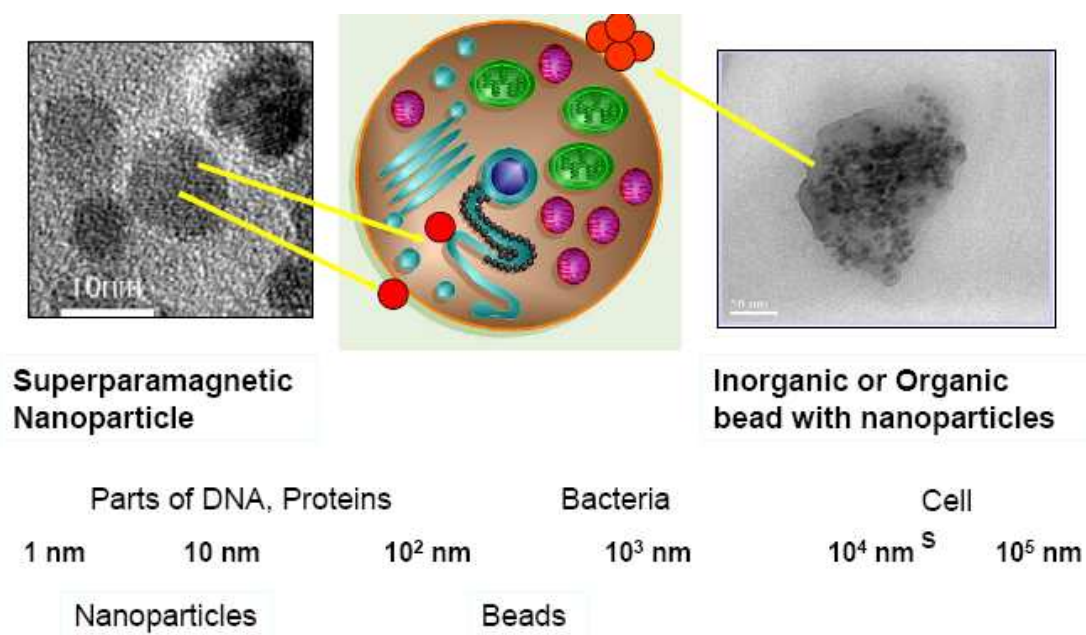
Figure 2.11 The dimensions of supraparamagnetic particles in biomedical application [122].

2.3.2.2 Hyperthermia

Another application of magnetic molecules is the treatment of tumors by hyperthermia [86, 87,125]. In this method the nanoparticles are directed into and dispersed within the target tissue. In the next step AC magnetic field cause this particles to heat. If the temperature is constantly raised above a threshold, this destroys the tumor [86-87]. Magnetic particles can generate heat by hysteretic loss under an alternating magnetic field (AMF).

This technology is up to date not easy to apply in humans as a high frequency and strong external magnetic field causes deleterious effects on organism [126]. Up to date there are no studies with hyperthermia on humans, however the newest animal experiments such as application of magnetite cationic liposomes (MCLs) in immunotherapy of mouse EL4 T-lymphoma (a sort of cancer) are very promising [126]. The particles have a positive surface charge and generate heat in an alternating magnetic field (AMF) due to hysteresis loss. Authors assume that hyperthermia using magnetic nanoparticles induces antitumor immunity. MCLs can be also used as carriers to introduce magnetite nanoparticles into target cells since their positively charged surface interacts with the negatively charged cell surface. There are also other types of nanoparticles used in hyperthermia -magnetite nanoparticles conjugated with antibodies (antibody-conjugated magnetoliposomes, AMLs) [127]. Ito et al. describe an animal-model of melanoma (very malignant sort of cancer) in which MCLs were used to

incorporate "heat shock proteins (HSPs)" into immunologic cells. (HSPs) are acknowledged as important participants in immune reactions. Expression of HSP70 in reaction to hyperthermia, produced with (MCLs), induces antitumor resistance. 24 hours after the incorporation of the hsp70 gene, MCLs were administered into melanoma nodules in melanoma mice and subjected to AMF for 30 minutes. The temperature at the cancer reached 43 degrees C and was maintained by regulation of the magnetic field intensity. The joint therapy strongly slowed the tumor expansion over a 30-day time. Complete regression of melanom due to systemic antitumor immunity was found in 30% of mice [127]. Another technology uses ferrimagnetic microspheres 20-30 micron in diameter as thermoseeds for inducing hyperthermia in tumors, especially for cancers located deep inside the body. The microspheres are blocked in the capillary bed of the tumors when they flow through blood vessels and produce heat locally by their hysteresis loss when placed under an alternating magnetic field.

2.3.2.3 Magnetic resonance imaging (MRI)

Magnetic resonance imaging (MRI)- also called tomography (MRT) - is a technique of obtaining images of internal organs in living organisms. MRI determines the amount of bound water and is applied also in the geology [128].The most important use of it is to present internal pathological lesions in living organisms. Nowadays it is a commonly used technique of medical imaging. Apart of medical application MRI is also used for example to determine rock permeability to hydrocarbons and timber quality [128]. Medical MRI usually relies on the relaxation features of excited hydrogen nuclei. The spins of the atomic nuclei with non-zero spin numbers within the tissue align in magnetic field parallel or antiparallel. Because of quantum mechanical reasons the nuclei are set off at an angle from the direction of the static magnetic field. The magnetic dipole moment of the nuclei precesses around the axial field with the Larmor frequency. Applying a time-varying magnetic field B_0 tuned to the Larmor precession frequency $\omega_0 = \gamma B_0$ of the protons causes some of the magnetically aligned hydrogen nuclei to assume a temporary non-aligned high-energy state. The γ is the gyromagnetic ratio, a nuclear constant. For hydrogen, $\gamma/2\pi$=4258 Hz/Gauss. The relaxation of the coherent response is measured from the time that the radio frequency pulse is turned off by means of induced currents in pick-up coils in the scanner. The signal is amplified by a factor of ca 50–100. To selectively picture the singular voxels (3-D pixels) of the tissue three orthogonal magnetic gradients are applied. The first is the slice selection, which is set during

the RF pulse, then the phase encoding and finally the frequency encoding gradient, during which the tissue is imaged. The realignment of the nuclei with the magnetic field is called longitudinal relaxation and the time necessary for the tissue nuclei to realign is termed "Time 1" or T1. This is the rule of T1-weighted imaging. T2-weighted imaging is based on local dephasing of spins subsequent to the transverse energy pulse; the transverse relaxation time is called "Time 2" or T2. Both T1- and T2- images are used in most medical examinations. T1 and T2 can be shortened with a magnetic contrast agent. Frequently, a paramagnetic contrast- a gadolinium is administered, and both pre-contrast T1- images and post-contrast T1- images are obtained. The usual medical resolution is about 1 mm^3, while in investigation models it can exceed 1 µm^3. The most widespread contrast agents are gadolinium ion complexes. Contrasts based on SPM nanoparticles also are available- here with iron oxide nanoparticles. Dextran layered iron oxides are biocompatible and are excreted by the liver after the scanning. The base of the contrast imaging is their property of being taken up by the reticuloendothelial system, a complex of cells coating blood vessels whose role is to take out antigenic substances from the bloodstream. MRI contrast agents are characterized by different uptakes in different tissues. The contrast agent with a smaller molecular mass has a longer half-life in the blood stream and thus is collected by reticuloendothelial system throughout the body. That is why this agents have been used to image the vasculature and central nerve system. SPIO particles in comparison to other contrast agents have however the broadest potential of application in MRI. SPIO molecules can be produced with various particle sizes and surface layers. Large SPIO media (50-150 nm) principally produce a signal decline or T2 -reduction and are applied as contrast for MRI of the liver and spleen. They have a high accuracy, particularly in detecting liver metastases. Smaller molecules (about 20 nm in diameter) are characterized by a diverse tissue allocation and have a potential for enhancement of noninvasive lymph node estimation or characterizing susceptible atherosclerotic plaques. Particles with an optimized T1-relaxivity and long-lasting intravascular flow time can be applied as contrast media for MR angiography. Small SPIO particles can be used in MRI of the bone marrow and the measurement of perfusion parameters in tumours or myocardium. Molecules up to 20 nm in length have different features in the body depending on their dimension [129]. Though these molecules have similar chemical characteristics, small alterations in size can greatly influence their pharmacokinetics. A modification in molecular size up to 15 nm changed permeability across the vascular wall, elimination course, and identification by the reticuloendothelial system.

Smaller sized polyamidoamine (PAMAM) dendrimer-based contrast agents, i.e., less than 3 nm in diameter, easily diffuse across the vascular wall resulting in rapid perfusion throughout the body. Molecules of 3-6 nm in length are fast excreted through the kidney indicative of their suitability as a renal contrast agents. Particles of 7-12 nm do not diffuse from the circulation and are thus suggestive of their potential application as blood pool contrast agents. Hydrophobic variants SPIO shaped with polypropylenimine diaminobutane (DAB) dendrimer layers quickly gather in the liver, enabling their use as liver contrast agents. Larger hydrophilic agents have proper features for lymphatic visualisation. Agents bound with monoclonal antibodies are capable to be utilized as tumor-specific contrast agents. SPIO particles with an adapted coat-layer can be used in molecular imaging, such as receptor-directed scanning, cell tagging for in-vivo monitoring of stem cell migration. SPIO applications range from diagnostic imaging to molecular medicine. Specially manufactured SPIO molecules- AMLs make it possible by means of antibody –antigene reaction to accomplish tumor-specific contrast enhancement in MRI via systemic administration- see Figure 2.12. It is also possible to manipulate cells tagged with magnetic nanoparticles using magnets; this feature has been also applied in tissue engineering.
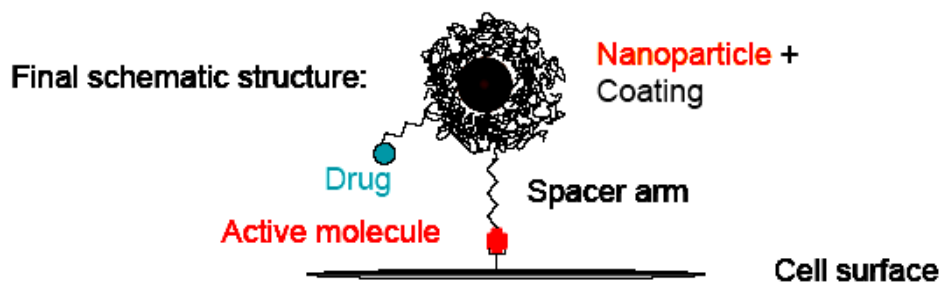
Figure 2.12 SPIO molecule application in tumor-specific contrast enhancement in MRT [122].

2.3.3 Smart sensor/remote control

2.3.3.1 Detection of DNA fragment

The magnetic particles also found application in biosensor research especially for detection of DNA. Conventional detection methods use fluorescent labels that were attached to biological targets and external laser for detection. These methods are presented in Figure 2.13.

1)

Immobilized
probe DNA

Spacer molecule

Surface silinization

2) Traget DNA
+ fluorescent tag
Insert on chip

3) Target DNA
hybridised with probe

4) Light scanner
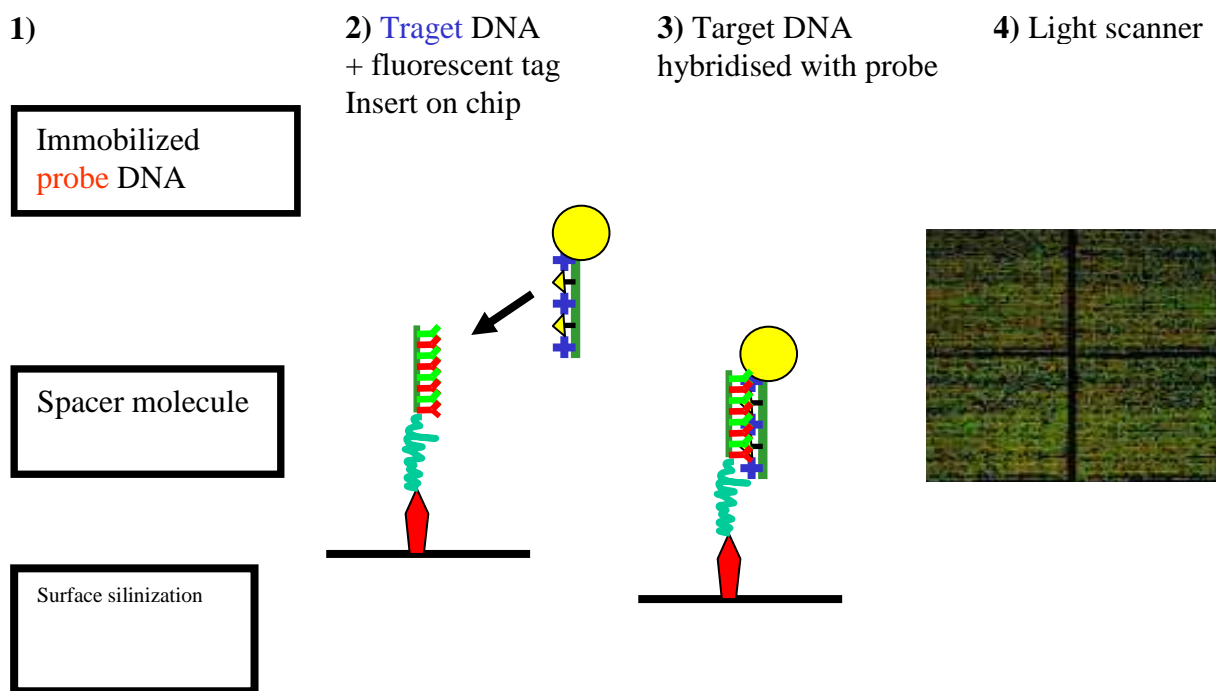
Figure 2.13 Conventional hybridisation detection using fluorescent labels attached to biological targets [130].

In standard fluorescent methods the probe of a DNA is immobilized on the surface of a chip. The surface must be specially prepared (surface silinization, spacer molecule). In the next step a target DNA together with a fluorescent tag are inserted into a chip. Finally, the target DNA hybridizes with the probe and then a light scanner is used for detection. The fluorescent method is sensitive enough for detection of specific probes of a DNA.

The biosensors involved in the magnetoresistive detection method are presented in Figure 2.14.
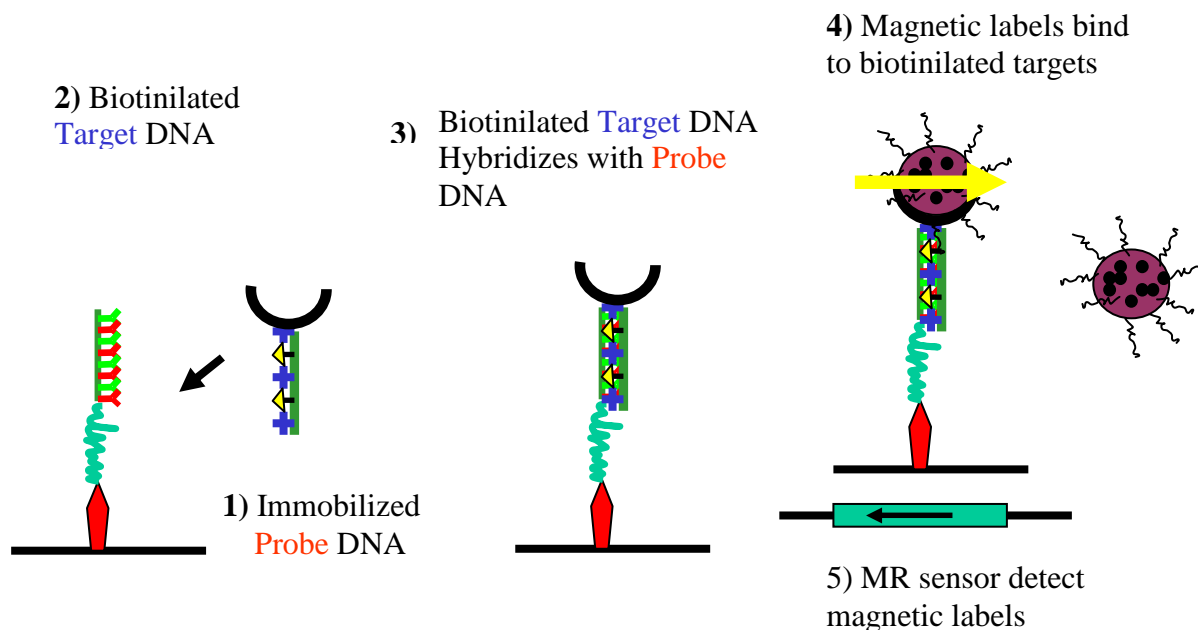
Figure 2.14 Magnetoresistive-based hybridisation detection using magnetic labels, and an integrated magnetoresistive sensor array for detection. [130].

In this method, first the probes of DNA are immobilized on the sensor surface. In the next step biotinilated target DNA hybridizes with probes of DNA. Finally, functionalized magnetic particles are bound to biotinilated targets and the magnetic sensor detects the presence of magnetic particles and DNA probes. In the PhD work from J. Schotter (University of Bielefeld) it is possible to find a comparison of these two detection methods. Fig. 2.15 shows relative sensitivities of the magnetic biosensor and fluorescent chips in the presence of DNA spots [75].
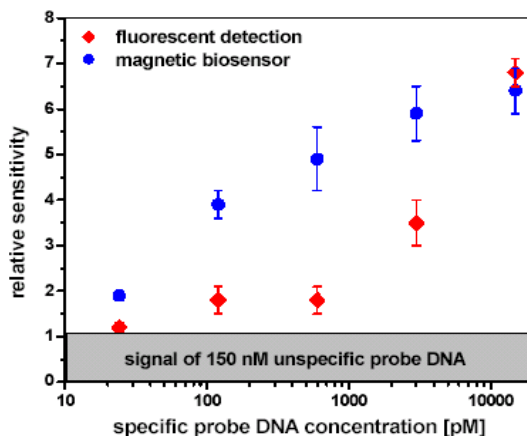
Figure 2.15 Relative sensitivities of the magnetoresitive biosensors and the fluorescent chips [75].

In this experiment the sensitivity of the magnetic biosensor was superior to the fluorescent detection at low concentrations of a probe DNA, for example by a factor of 2.7 at 600 pg/µl. Therefore, the magnetic biosensors are devices for the detection units of the future medical diagnostic [75].

3. Magnetoresistive sensor

The history of magnetoresistive technology started with the discovery of magnetoresistance effect by William Thomson (Lord Kelvin) in 1865. He found that the resistance of a ferromagnetic metal changes in the presence of magnetic field. The amounts of changes in the resistance were defined as the magnetoresistance ratio MR that is characterized as the quotient of the difference between maximum and minimum resistance values and the minimum resistance value. Actually MR is usually given in dimensionless units of percent. The effect reported by Thomson is today hence dubbed anisotropic magnetoresistance (AMR) [131]. In 1988, Peter Grünberg et.al of the Jülich Research Center and Albert Fert et.al of the University of Paris-Sud independently discovered a larger magnetoresistive effect known as giant magnetoresistive effect (GMR effect). The GMR effect was observed in a magnetic multilayers stack: ferromagnetic, non ferromagnetic metallic and ferromagnetic layer. This discovery is considered as the beginning of a new class of electronic devices based on the spin degree of freedom of the electron [132,133]. Peter Grünberg and Albert Fert have received a number of prestigious prizes and awards for their discovery and contributions to the field of spintronics. The most recent is the Nobel Prize 2007.

Today, a class of magnetic field sensors such as magnetoresistive sensor is of great interest for industry due to a small size, low-cost and low-power consumption (see Figure 3.1) [134,135,136].
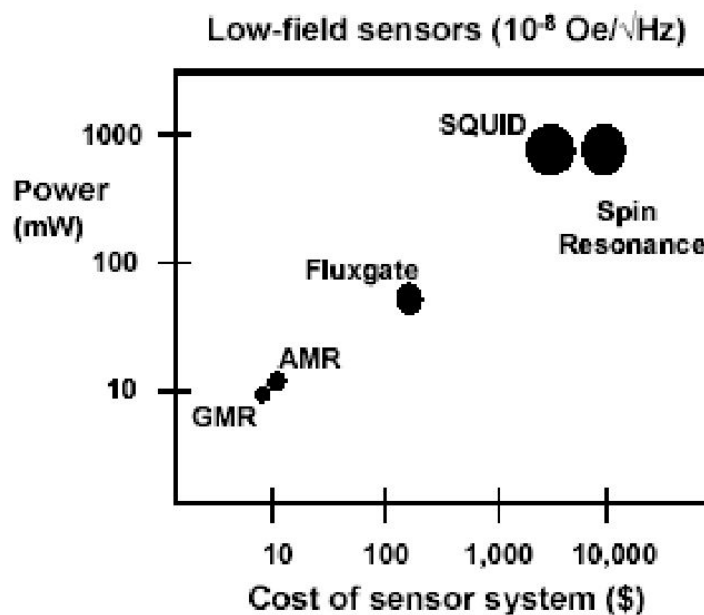
Figure 3.1 The costs of various low field magnetic sensor systems

vs power consumption [137].

The magnetoresisitive sensors are much more sensitive than for example Hall sensors and are applied for e.g., the detection of magnetic particles associated with biomolecules, where a low field sensing is required [138]. The class of magnetoresistive sensors depends on the type of sensing. The mostly used sensors are anisotropic and giant magnetoresistance type sensors (AMR and GMR sensors). A new type of sensors, investigated mainly in academic activities, is based on the tunneling magnetoresistance effect and is characterized by higher sensitivity. Recently, many research activities are focused on the new magnetoresistive effect called colossal magnetoresitance. It is described as colossal since it is a much larger effect than had ever been previously seen in metals. The mechanism of this effect is not clearly understood yet and still some investigation has to be done on it [131].

In this chapter an overview is given on the state of the art in the magnetoresistive biosensors technology.

3.1 Magnetoresistive transducer

A magnetoresistive transducer is a resistor with a resistance value that depends on an external magnetic field, $R = R(H)$. The first magnetoresistive transducers were based on the anisotropic magnetoresistance (AMR).

3.1.1 Anisotropic magnetoresistance (AMR)

The anisotropic magnetoresistance effect measures the changes in the resistance from the current passing through the ferromagnetic layer, when the magnetization is changing from parallel to perpendicular to the current [139]. The resistivity of the ferromagnetic metal depends on the angle θ between the magnetization direction and the current density [140].

The AMR effect is physically based on spin orbit coupling [131]. When the magnetization direction are oriented perpendicular to the current, then the electron orbits are oriented in plane to the current. There is a small cross-section of electrons for scattering, that results in a low resistance. For magnetic field applied parallel to the current, the electron orbits are oriented perpendicular to the current, and the cross-section for scattering of electrons is larger, that gives a much higher resistance [131].

The AMR effect was often investigated in permalloy and $Ni_{1-x}Co_x$ structures [140]. At room temperature, the highest effect was discover for $Ni_{1-x}Co_x$ and the magnetoresistance ratio was about 6%. For permalloy, the AMR effect depends on the layer thickness and the deposition conditions. For a 30nm permalloy film, the AMR ratio was about 2.5% [140]. Detailed description of AMR effect can be found in the references [131,141,142].

3.1.2 Giant magnetoresistance (GMR)

The giant magnetoresistance effect was discovered in 1988 by two researchers working independently: Peter Grünberg et al. of the KFA Research Institute in Jülich and Albert Fert et al. of the University of Paris South [132,133]. They observed a very large magenetoresistive effect (larger than the AMR discovered by Thomson) in multilayer stacks consisting of two magnetic layers separated by a non-magnetic metallic layer [132,133]. The discovery of this effect was a kind of sensation in research and the beginning of a new paradigm of electronics called spin-electronics. Since then, many companies were interested to commercialize GMR multilayers. The first company institute that started to work with GMR materials was IBM's Almaden Resarch Center, San Jose [143]. The first IBM's multilayers were made by Stuart Parkin and Kevin P. Roche. The GMR stacks were produced using common process, known in disk-drive technology: sputtering [143]. To better understand the GMR mechanism, different variations of multilayers were produced. It was discovered that the relative orientation of the magnetic moments of two magnetic layers depends on thickness of the non-magnetic layer [143]. If the thickness of the non-magnetic layer increases, then the strength of magnetic coupling decreases. Doing this experiment they discovered that the magnetic moments of the magnetic layers oscillate between parallel (ferromagnetic) and anti-parallel (antiferromagnetic) orientation as a function of the non-magnetic layer thickness [144].This is called a oscillatory exchange coupling [144]. Additionally they discovered, that resistance is relatively low when the layers are in parallel alignment and relatively high when in anti-parallel alignment (see figure 3.2) .
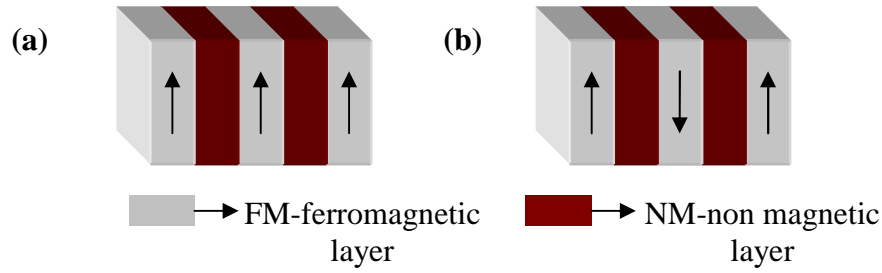
Figure 3.2 The GMR composition of magnetic multilayers (a) ferromagnetic configuration (b) antiferromagnetic configuration [145].

For sensor purposes, the thickness of the non-magnetic layer in GMR structure is chosen in a way that the orientation of the magnetic layers is antiferromagnetic [144]. After application of magnetic field, the magnetic configuration is changing from antiferromagentic to ferromagnetic configuration causing a change in the resistance [144]. The magnetoresistance ratio MR is defined in two ways as a "optimistic " magnetoresistance ratio:

$$(\Delta R/R = (R^{\uparrow\downarrow} - R^{\uparrow\uparrow})/R^{\uparrow\uparrow} \tag{3.1}$$

where $R^{\uparrow\downarrow}$ and $R^{\uparrow\uparrow}$- are the resistance of the magnetic multilayer in its antiparallel (zero field) and parallel (saturation field) magnetic configuration and as a "pessimistic" ratio:

$$(\Delta R/R = (R^{\uparrow\downarrow} - R^{\uparrow\uparrow})/R^{\uparrow\downarrow} \tag{3.2}$$

The pessimistic ratio is never greater than one [144].

For the investigation on GMR multilayers, Stuart Parkin won the European Physical Society's prestigious Hewlett-Packard Europhysics Prize in 1997. Further GMR structure was developed by Bruce Gurney and other colleague also from IBM's. It was named spin valve and found application as a disk-driver sensor that operates at a low magnetic field [143]. In 2007 the group leaders P. Grünberg and A.Fert were awarded the Nobel Prize in physics for the discovery of the GMR effect.

3.1.2.1 The GMR geometries

The GMR effect can be observed in two different types of geometries [144]. One of them is termed the Current IN Plane (CIP) and other is called the Current Perpendicular to Plane (CPP) geometry [144]. The two different types are presented in Figure 3.3.
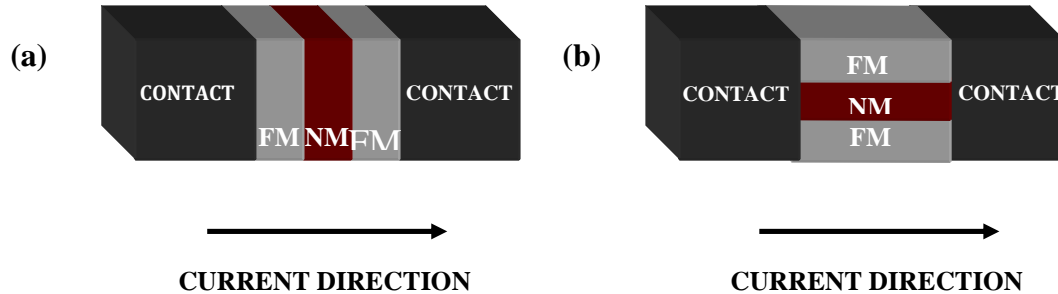
Figure 3.3 Two GMR geometries: a) CIP and b) CPP [145].

The CIP is the well known configuration for measuring the GMR effect of magnetic alloys and is easy to arrange experimentally. The resistance of the CPP geometry is low and it is difficult to measure the voltage drop across the sample [144]. The difference between the CIP and CPP geometries of GMR can be explained through microscopic theory of spin dependent scattering [144].

3.1.2.2 Resistor model of GMR

The GMR effect is based on the fact that spin is conserved over distances of up to several hundreds of nanometers, i.e. much more then the thickness of the non-magnetic layer in GMR structures [144].Based on this fact, it is possible to assume that electric currents in GMR layers are flowing in two channels: one corresponding to the electrons with spin up $\uparrow$ and the second to the electrons with spin down $\downarrow$. These two channels are separated, because the spin is conserved, and can be taken as two conductors, which are connected in parallel [144].

The other fact is that electrons with different spin orientation (parrallel and antiparallel to the magnetization of the ferromagnetic layer) are scattered at different rates in a ferromagnetic layer. This is termed as spin dependent scattering [144].

The GMR structure usually consists of two ferromagnetic layers separated by a non-magnetic layer. In a parallel configuration the magnetizations of the ferromagnetic layers are aligned in one direction.

In this ferromagnetic configuration, the electrons with spin- up ↑are weakly scattered in both ferromagnetic layers. On   the   other hand, electrons   with spin-down ↓ are scattered more strongly. This situation is presented in the figure 3.4.
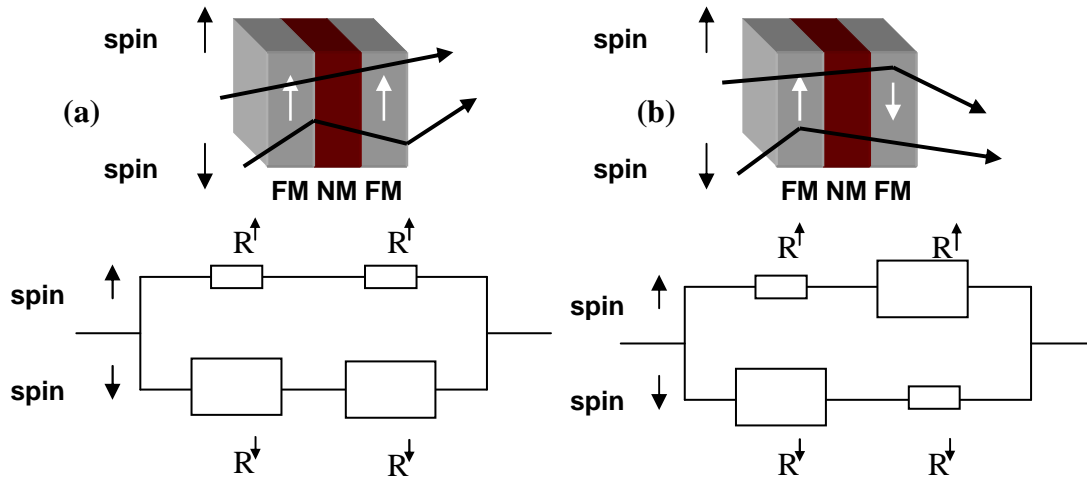
Figure 3.4 a and b parallel and anti-parallel
configuration of GMR layer with resistor model [145].

The small resistors correspond to the electrons with spin up that are weakly scattering in both ferromagnetic layers. The big resistors are corresponding to the scattering of electrons with spin down. Because the electrons with spin up and spin down represent two channels that are connected in parallel, the total resistance of three layers is determined by the low resistance of the spin up ↑ channel, which shorts the high-resistance of the spin down ↓ channel (see figure 3.4). In conclusion, the parallel configuration of the GMR structure corresponds to the low resistance [144]. In the opposite situation, where two ferromagnetic layers are aligned anti-parallel (anti-ferromagnetic configuration), the total resistance is much higher then in the previous configuration. This can be also explained using the resistor model. The spin up ↑ electrons are weakly scattering in the first ferromagnetic layer, but strongly in the second ferromagnetic layer. A different situation is for the electrons with spin down ↓. First, the electrons are strongly scattered in the first ferromagnetic layer and weakly scattered in the second ferromagnetic layer [144]. The big resistors are corresponding to the electrons with spin up and down that are strongly scattering in to the ferromagnetic layer and small resistors are representing the weakly scattering electrons (see figure 3.4).

This simple model presented here describes the GMR effect but if doesn't explain the differences between two geometrical configurations: CIP and CPP. For further explanation of the GMR effect a quantitative theory has to be used [144].

3.1.2.2 Spin dependent scattering of electrons in GMR structure.

The term spin dependent scattering means that, the spin of electrons is conserved, but the electrons with spin orientation up and down are scattered with different rates in ferromagnetic layers. According to Pauli's principles, the electrons can scatter from impurities to a quantum state, which is not occupied by other electron. At zero temperature, only the states with energy higher then the Fermi energy ($E > E_F$) are empty. The scattering of electrons from impurities is elastic, so electrons at the Fermi level can only scatter to the immediate vicinity of the Fermi level [144]. This means, that the scattering probability is proportional to the number of states available for scattering at E_F, i.e. depends from on density of states $D(E_F)$. For example in the case of cooper, the Fermi level intersects the conduction band and the density of states is relatively low (see Figure 3.5). The probability of scattering is therefore, also very low. This is the reason why cooper is a good conductor [144]. In cases of transition metals, the Fermi level intersects the conductions band and the d band [144]. Atomic waves of d levels are more localized then those for s levels, that means that the d band is narrow and the density of state is high. In this case the electrons have higher probability to scatter into the d bands. For this reason, the transition metals are poor conductors in comparison to, e.g., cooper. In case of magnetic transition metals, the d bands for spin-up ↑ and spin-down ↓ electrons are split by exchange interaction [144]. This resulting in a rigid shift of the spin-up ↑ and spin-down ↓ d bands, which can be clearly identified by measuring densities of states of Fe and Co in the figure 3.5 [144]. The density of state at E_F of cobalt is very low for the spin-up ↑ d bands and much higher for the spin-down ↓ d bands. In case of iron, the density of state at E_F is higher for spin-up ↑ electrons than for spin-down ↓ electrons. The spin asymmetry in the density of state is also larger for cobalt than for iron, resulting in different scattering rates for spin up ↑ and spin down ↓ electrons (bulk spin dependent scattering).

_____
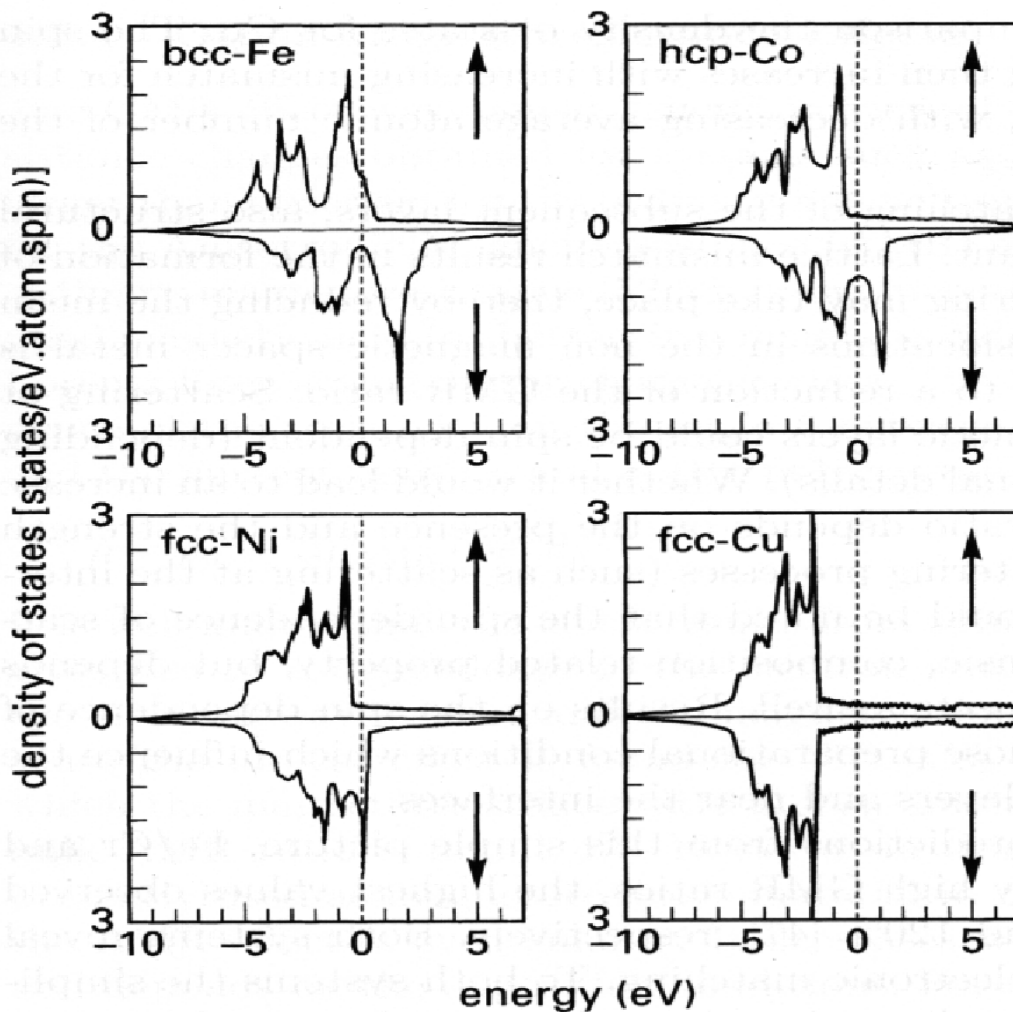
Figure 3.5 Spin-polarized densities of states for the metals: Fe, hcp-Co, Ni and Cu.
The broken line shows the position of the Fermi level [145].

The difference between CIP and CPP geometry can be explained by a spin dependent scattering mechanism, which is specific for the multilayers. Electrons coming from non-magnetic layer to the ferromagnetic layer meet a spin dependent potential barrier, which differently reflects electrons with spin up and spin down. In the CPP geometry, this is a stronger spin dependent scattering, than for CIP [144].

The spin dependent scattering based on spin dependence of the scattering potentials takes only place at the ferromagnetic/non-magnet interface and is called interfacial spin dependent scattering [144]. Typical interfaces in GMR structures are Co/Cu and Fe/Cr. The interfacial spin dependent scattering can be clearly understood using a band structure, for example for cobalt and cooper. The band structure is shown in the figure 3.6 . It is possible to see, that there is a very good matching between the Cu band structure and the majority spin of Co band [144]. The spin-up ↑ electrons crossing the interface have a weak scattering on that interface and it stays so also in cases when the Cu and Co atoms are intermixed [144]. In case of the Cu band structure and the Co minority band structure, there is a large mismatch and the spin-down electrons are strongly scattered at the Cu/Co interface [144].
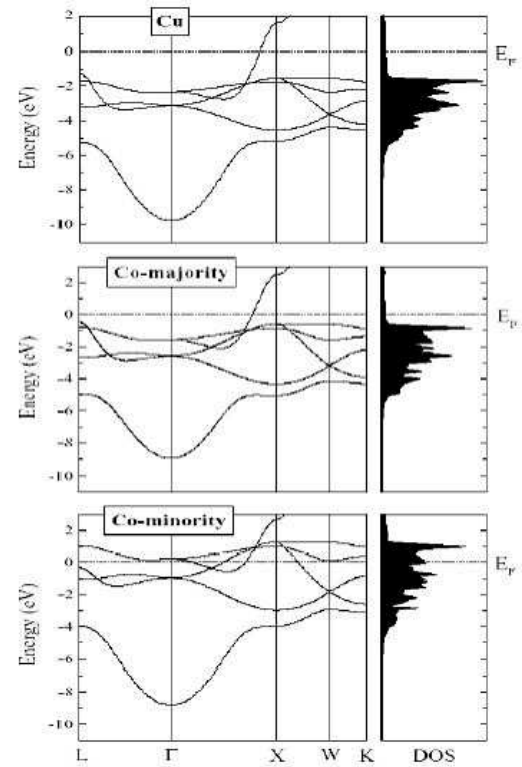
Figure 3.6 Band structure of cobalt and cooper [146].

Generally, one can conclude that the maximum GMR effect can be measured in a configuration of magnetic and non-magnetic interface layers, where a good match is observed for one of spin channel (for example a majority channel) and a large mismatch is observed in the second spin channel (for example minority channel) [144].

3.1.2.3 Magnetic superlattice and GMR effect

Magnetic superlattice consists of a number of alternating non-magnetic and magnetic layers. The whole superlattice is usually built of identical blocks. To calculate the GMR, the superlattice is divided to units cells. The magnetic cell is defined as two magnetic layers and two non-magnetic layers with length L and width W [144] (see Figure 3.7).

The superlattice unit cell has three different regions with local resistivities: resistivities of the non-magnetic spacer layer-ρ_{NM} , which doesn't depends on the spin orientation and the high and low resistivities for different spin orientation in the ferromagnet (ρ_{FM}^{H} and ρ_{FM}^{L}) [144].
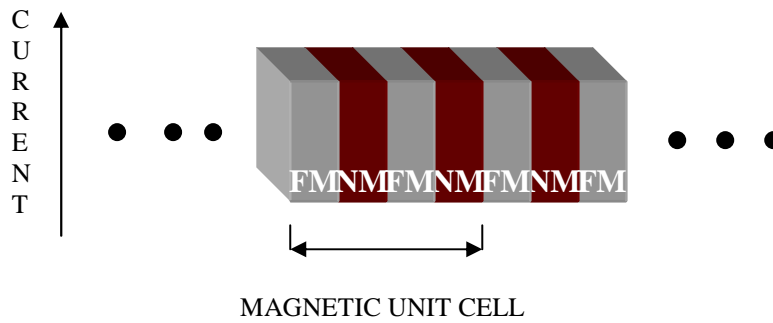
Figure 3.7 Definition of magnetic superlattice unit cell [147].

The total resistivities of the unit cells are modeled by a system of eight resistors; four resistors for each channel (see figure 3.8) [144].
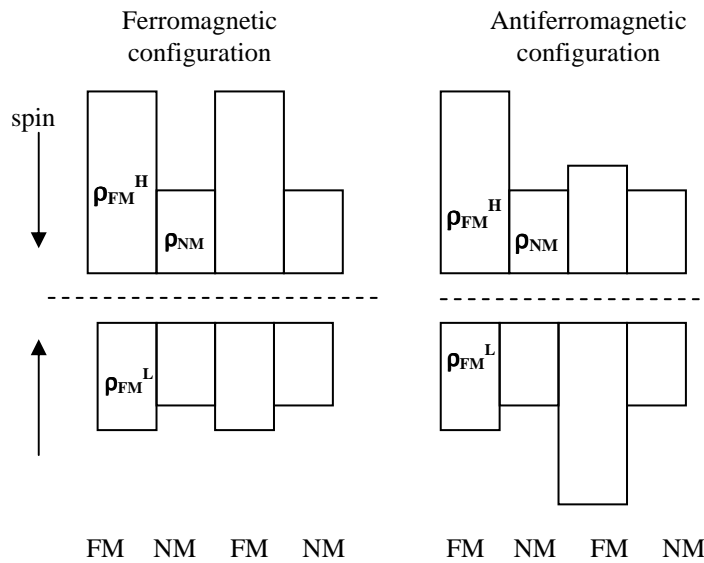
Figure 3.8 Model of eight resistors for distribution of resistivities
in a magnetic unit cell [148].

The total resistance for ferromagnetic and antiferromagnetic configurations is then calculated from the equation:

$$\frac{1}{R\uparrow\uparrow} = \left(\frac{1}{R\uparrow} + \frac{1}{R\downarrow}\right)_{\uparrow\uparrow} \quad ; \quad \frac{1}{R\uparrow\downarrow} = \left(\frac{1}{R\uparrow} + \frac{1}{R\downarrow}\right)_{\uparrow\downarrow} \qquad (3.3)$$

The are two rules according to which the total resistance can be calculated in the superlattice.

If the mean free path in each superlattice is shorter then the thickness of the layer, only few electron can travel to the next layers. The electrons from each layer are then flowing separate channels and don't mix. The total resistance in this case can be calculated as a conventional resistor network. According to figure 3.8 there are the same numbers of resistors for antiferomagnetic and ferromagnetic configuration. In these cases the $R_{\uparrow\uparrow}$ is equal to $R_{\uparrow\downarrow}$ and there is no magnetoresistance [144].

When the mean free path in each layer is much longer then the thickness of the layer, the traveling electrons will sample the layers with low and high resistivities, so the average resistivities have to be calculated. The average resistivity ρ_{av} for the superlattice consisting of N components with resistivity ρ_N and the layer thickness t_n is given by:

$$\rho_{av} = \frac{t_1\rho_1 + t_2\rho_2 + ... + t_N\rho_N}{t_1 + t_2 + ... + t_N} \tag{3.4}$$

The mean free paths in metals are often of the order of tens to hundreds of interatomic distances. This means that a multilayer with layers thickness in the nanometers range will exhibit the GMR effect, because the mean free paths are longer than the thickness of the layer. The resistance for different spin orientation for two configurations is expressed in the ferromagnetic configuration by:

$$R_{\downarrow} = \frac{L}{2(t_{FM}+t_{NM})W} \frac{2t_{FM}\rho_{FM}{}^{H} + 2t_{NM}\rho_{NM}}{2(t_{FM}+t_{NM})}$$

$$\tag{3.5}$$

$$R_{\uparrow} = \frac{L}{2(t_{FM}+t_{NM})W} \frac{2t_{FM}\rho_{FM}{}^{L} + 2t_{NM}\rho_{NM}}{2(t_{FM}+t_{NM})}$$

and for spin- down and spin-up electrons in antiferomagnetic configuration by:

$$R_{\uparrow} = R_{\uparrow} = \frac{L}{2(t_{FM}+t_{NM})W} \frac{2t_{FM}\rho_{FM}{}^{L} + 2t_{FM}\rho_{FM}{}^{H} + 2t_{NM}\rho_{NM}}{2(t_{FM}+t_{NM})} \tag{3.6}$$

If the two channels are considered independently, then the total resistance is calculated in parallel by:

$$R_{\uparrow\uparrow} = \frac{R_{\uparrow\uparrow}^{\downarrow} R_{\uparrow\uparrow}^{\uparrow}}{R_{\uparrow\uparrow}^{\downarrow} + R_{\uparrow\uparrow}^{\uparrow}} = \frac{L}{2(t_{FM}+t_{NM})^2 W} \; \frac{(t_{FM}\rho_{FM}^{L} + t_{NM}\rho_{NM})}{(t_{FM}\rho_{FM}^{L} + t_{FM}\rho_{FM}^{H} + 2\, t_{NM}\rho_{NM})} \tag{3.7}$$

in ferromagnetic configuration and

$$R_{\uparrow\downarrow} = \frac{1}{2}R_{\uparrow\downarrow} = \frac{1}{2} R_{\uparrow\downarrow}^{\uparrow} = \frac{L}{8(t_{FM}+t_{NM})^2 W} \; (t_{FM}\rho_{FM}^{L} + t_{FM}\rho_{FM}^{H} + 2\, t_{NM}\rho_{NM}) \tag{3.8}$$

in antiferomagnetic configuration, where L and W are a length and width of the unit cell respectively, t_{FM} is a thickness of the ferromagnetic layer and t_{NM} is a thickness of the non-magnetic layer, ρ_{NM} is the resistivity of the non-magnetic layer and ρ_{FM}^{H}, ρ_{FM}^{L} are the high and low resistivity in the ferromagnetic layers.

The GMR ratio is defined as:

$$GMR = \frac{R_{\uparrow\downarrow} - R_{\uparrow\uparrow}}{R_{\uparrow\uparrow}} = \frac{(\alpha-\beta)^2}{4\,(\alpha + \frac{t_{NM}}{t_{FM}})\,(\beta + \frac{t_{NM}}{t_{FM}})} \tag{3.9}$$

where $\alpha = \rho_{FM}^{H}/\rho_{NM}$ and $\beta = \rho_{FM}^{L}/\rho_{NM}$

The GMR amplitude is increasing by a strong spin asymmetry ratio that is defined as $\alpha/\beta = \rho_{FM}^{H}/\rho_{FM}^{L}$ and is decreasing with increasing the thickness of the spacer and the ferromagentic layer [144].

3.1.3 Tunneling magneto resistance

The tunneling magneto resistance effect was for the first time observed at tunnel junctions where two ferromagnetic layers are separated by a thin insulating layer (barrier) [139]. Electrons are tunneling between the electrodes and the spin is conserved during the tunneling process [139]. The tunneling probability is different for majority and minority spin electrons. There are different values of the tunnel resistance for parallel configuration and antiparallel configuration, leading to a TMR value $\neq 0$. For different coercive fields of the two electrodes the magnetic configuration goes from parallell to antiparallel state and then is back

to parallel state in a varying magnetic field. A typical TMR measurement is shown in the Figure 3.9 [139].
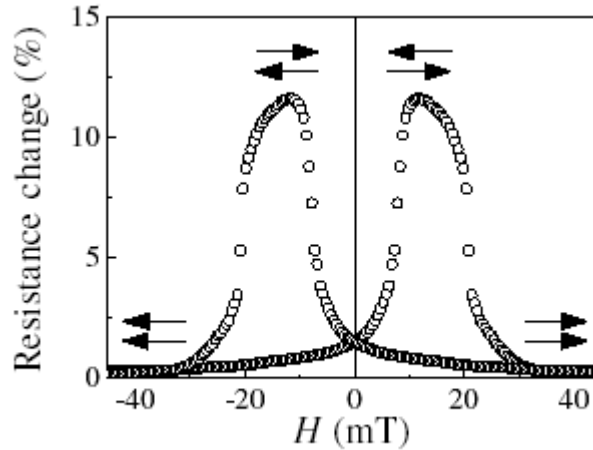
Figure 3.9 TMR effect observed in CoFe/Al$_2$O$_3$/Co MTJ. The arrows indicate the relative magnetization orientation in the CoFe and Co layers [150].

The TMR is a consequence of spin-dependent tunneling, an imbalance in the electric current carried by up- and down-spin electrons tunneling from a ferromagnet through the tunneling barrier [149]. The origin of this phenomenon can be explained by the fact that the probability for an electron to tunnel through the barrier depends on its wave vector. In a ferromagnet, the electronic bands are exchange split, which implies different wave vectors for the up- and down-spin electrons and consequently a tunneling probability that depends on the spin [149].

3.1.3.1 Julliere's experiments and model

For the first time, the TMR was measured in 1975 by Julliere in a ferromagnetic/insulator/ferromagnetic tunnel junction [151]. He observed that the tunneling current depends on the orientation of the two ferromagnetic electrodes, giving rise to a TMR amplitude. For the experiments, he used Co and Fe as ferromagnets with different coercivity fields and a Ge barrier layer. The experiment was done at 4.2 K. He observed a maximum amplitude of about 14% at low temperature, which decreased with increasing bias voltage due to spin-flip scattering at the ferromagnet/barrier interfaces [149]. Juliere tried to explain his results by a simple model, which was based on two assumptions: the spin of the electrons is conserved in the tunneling process

57

and the tunneling of up- and down-spin electrons are two independent processes, so the conductance occurs in the two independent spin channels [149] .

Such a two-current model was also previously used to understand GMR phenomena. Based on this assumption, electrons from one spin state of the first ferromagnet can move to unfilled states of the same spin of the second ferromagnet [149]. When the two ferromagnetic films are magnetized parallel, the minority spins tunnel to the minority states and the majority spins tunnel to the majority states. For antiparallel magnetizations the majority spins of the first magnetic layer tunnel to the minority states of the second magnetic layer and vice versa. Julliere also assumed that the conductance for each spin orientation is proportional to the product of the tunneling rate of the two ferromagnetic electrodes [149]. The conductance for the parallel and antiparallel alignment, G_P and G_{AP}, can be given by:

$$G_p \; \alpha \quad \rho_1^{\uparrow}\rho_2^{\uparrow}+\rho_1^{\downarrow}\rho_2^{\downarrow} \tag{3.10}$$

$$G_{AP}\alpha\rho_1^{\uparrow}\rho_2^{\downarrow}+\rho_1^{\downarrow}\rho_2^{\uparrow} \tag{3.11}$$

where $\rho_i^{\uparrow}$ and $\rho_i^{\downarrow}$ are the tunneling DOS (DOS-density of state, the tunneling DOS is understood for itinerant electrons with spin of the ferromagnetic electrodes for different spin orientation. [149] According to these two equations, the parallel and antiparallel configuration has different conduction, which gives a TMR value different from zero. When the orientation of the two ferromagnetic layers is changing from parallel to antiparallel configuration, the TMR is given as :

$$TMR=(R_{AP}-R_P)/R_P \tag{3.12}$$

where R_P and R_{AP} are the resistances for the magnetizations of the electrodes parallel and antiparallel. The TMR can be also expressed by the polarization of the electrodes with respect to spin :

$$TMR=2P_1P_2/(1-P_1P_2) \tag{3.13}$$

where P_1 and P_2 are the spin polarization of two ferromagnetic electrodes [149].

3.1.3.2 Slonczewski 's model

The first true theoretical model of TMR was given by Slonczewski [149]. This model was based on the assumption that electrons tunnel through a rectangular potential barrier. The ferromagnet was described with two parabolic bands shifted to each other to model the

exchange splitting of the spin bands [149]. His calculations were based on the one-electron Hamiltonian within the free electron approximation. He considered a perfect junction with translation symmetry along the layers and with wave functions of the electrons across the junction [149]. His consideration started from the Schrödinger equation and he calculated the conductance as a function of the relative magnetizations of the two ferromagnetic layers. Slonczewski assumed that the external voltage is small and the potential is zero in the electrodes and V_0 in the barrier. He found that the conductance is a linear function of the cosine of   the angle θ between the magnetic moments of the two ferromagnetic layer.:

$$G(\theta) = G_0 (1 + P^2 \cos \theta) \tag{3.14}$$

where P is the spin polarization of tunneling electrons expressed by:

$$P \quad = \frac{k^\uparrow - k^\downarrow}{k^\uparrow + k^\downarrow} \quad \frac{k^2 - k^\uparrow k^\downarrow}{k^2 + k^\uparrow k^\downarrow} \tag{3.15}$$

where k is the constant of the decay of the wave function into the barrier and is dependent on the potential of the barrier height U: $k = [(2m/\hbar^2)(U - E_F)]^{1/2}$ [149].

The magnitude of the TMR decreases with decreasing U and changes sign for a very thin barrier [149].

3.2 Spin Valve

Spin valves where the first time introduced in 1991 [152]. They usually consist of two ferromagnetic layer, separated by a Cu spacer. One of the magnetic layer has pinned magnetization and the other can free by rotate. The free layer is usually built from $Co_{90}Fe_{10}$ or a $Ni_{80}Fe_{20}/Co$ or $Ni_{80}Fe_{20}$ bilayer [153]. The pinned ferromagnetic layer is coupled by exchange to an antiferromagnet. The MR value for the first spin valve was in the range from 6 to 10% [153]. A typical exchange –biased spin valve layer structure is $Ni_{80}Fe_{20}/Cu/Ni_{80}Fe_{20}/Fe_{50}Mn_{50}$. The upper permalloy layer is exchange biased to an antiferomagnetic layer of $Fe_{50}Mn_{50}$. An example of a magnetization loop in Figure 3.10 shows that the pinned layer switches far from zero field due to the exchange bias. The free layers usually are switched around zero field [154]. A small offset due to coupling to the pinned layer to the free layer can be observed (see Figure 3.10).
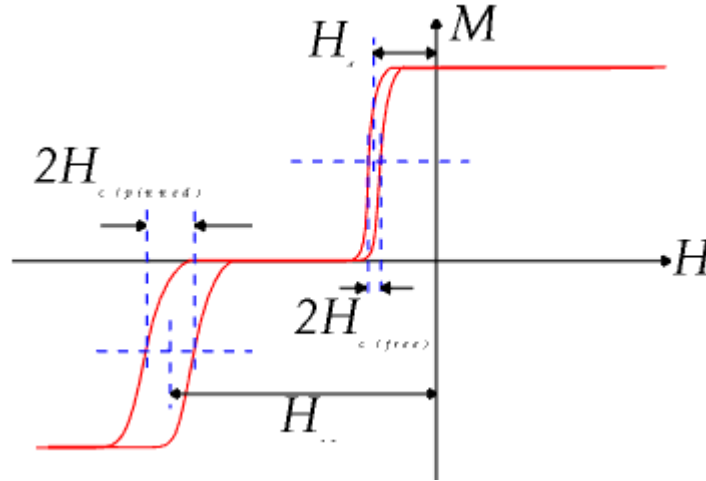
Figure 3.10 A schematic of the magnetization loop for
spin valve structure [155].

There are different configurations of spin valves such as bottom spin valve and symmetric spin valve [154]. In the first spin valve structure the biased layer is added in the bottom of structure. This type of design usually introduces a growth problem, because the biasing antiferomagnetic layer is not deposited on the magnetically saturated film and the magnetic structure of the antiferomagnetic layer is random [154]. Examples of magnetoresistance measurements for a bottom spin valve structure with a NiFe seed layer and for asymteric spin valve structure are presented in Figure 3.11.

(a)   **(b)**
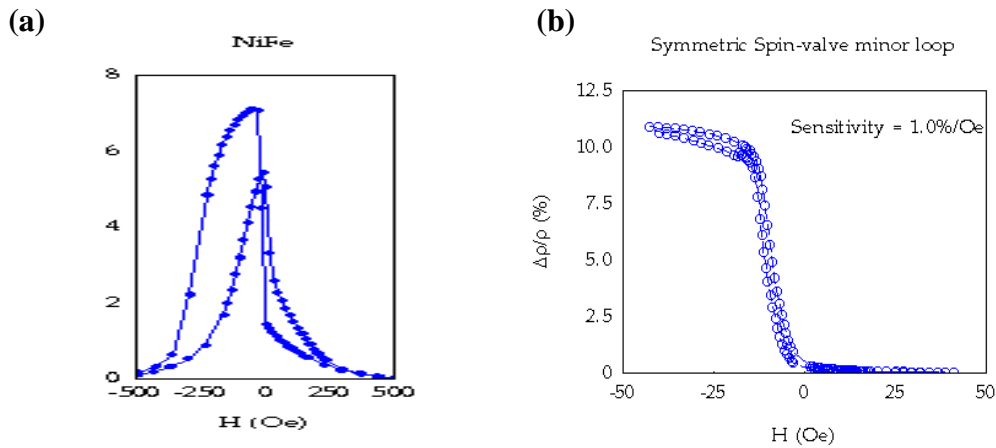
Figure 3.11 Magnetoresistive response for different Spin Valve structures
(a) bottom structure and (b) asymmetric structure [155].

The asymmetric spin valve structures are built up from three magnetic layers, and two Cu spacer layers. The top and bottom layers are pinned by an antiferomagnet. The magnetic field is applied in the pinning direction and the free layer is swept in hard axis direction [154]. The sensor shows reduced hysteresis and linear response. This type of sensor is more recommended for biosensor industry due to the linear response.

3.3 Magnetic Tunnel Junction

A magnetic tunnel junction (MTJ) consists of two ferromagnetic thin films separated by a thin insulating barrier. The insulating layer thickness is in the range of few nanometers or less so that electrons can tunnel through the barrier if a bias voltage is applied between the two electrodes across the insulator. The tunneling current depends on the relative orientation of the magnetizations of the two ferromagnetic layers, which can be changed by an applied magnetic field [156]. When a voltage V is applied to the structure, the Fermi level of one of the electrodes shifts by eV with respect to the other one [156] (Figure3.12). The electron can tunnel in both direction: from the left to the right electrode and from the right to the left. To calculate the total tunneling current, one has first to calculate the current from the left electrode (L) to the right electrode (R) [156]. The current depends on the density of states at a given energy in the left electrode, $\rho_L(E)$, the density of states at the same energy in the right electrode, $\rho_R(E+eV)$, the probability of transmission through the barrier expressed as the square of a matrix element $\left|M\right|^2$ and also on the probabilities that the states in the left electrode are occupied and the states in the right electrode are empty [156]. These probabilities are determined by the Fermi-Dirac function as f(E) and [1-f(E+eV)] [156]. The tunneling current from the left electrode to the right electrode is calculated as,

$$I_{l\rightarrow r}(V)=\int_{-\infty}^{+\infty} \rho_l(E)\rho_r(E+eV)\ |M|^2\ f(E)[1\text{-}f(E+eV)]dE \tag{3.16}$$

and the total current is given by $\mathbf{I_{Total=}}\boldsymbol{I}_{\mathbf{L\text{-}R}}\boldsymbol{-}\boldsymbol{I}_{\mathbf{R\text{-}L}}\boldsymbol{.}$
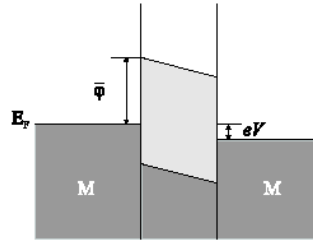
Figure 3.12 Diagram for a Metal/Insulator/Metal structure with an applied bias eV [157].

In a magnetic tunnel junction, due to the ferromagnetic nature of the electrodes, the tunneling is spin dependent giving rise to a magnetoresistance effect: the junction resistance depends on the relative orientation of the magnetization in the top and the bottom layer [149]. The magnetoresistance of a tunnel junction can be measured only if the magnetization directions of the top and the bottom layer can be switched from a parallel orientation to an antiparallel orientation [149]. An antiparallel alignment can be obtained by using materials with different coercive fields (a soft-hard system) or by exchange coupling one of the layers to an antiferromagnet (exchange biasing) [149]. A typical MTJ major loop and a minor loop is presented in the figure 3.13.
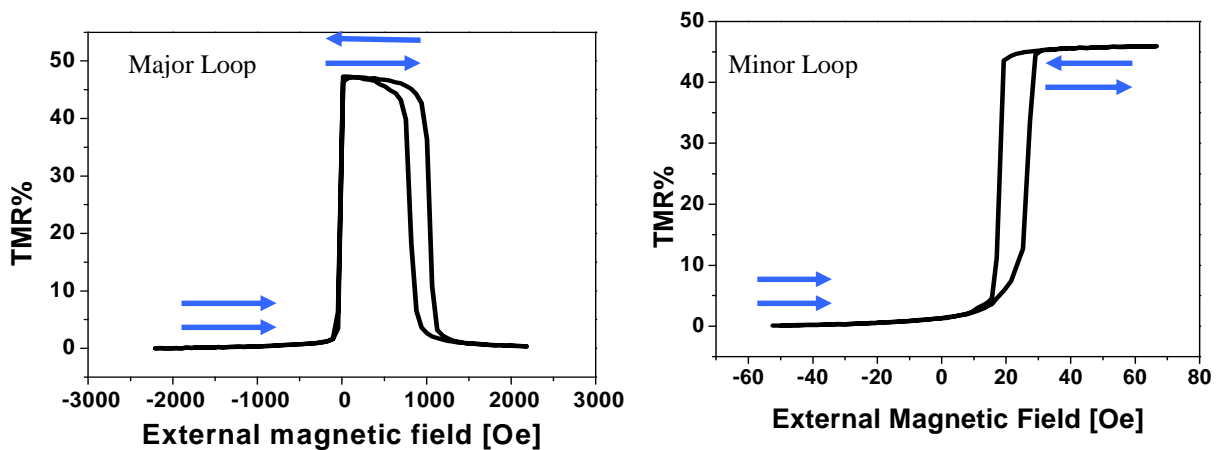
Figure 3.13 Magneto-resistance response of the MTJ sensor composed of
$Ta_{6.5nm}/Cu_{30nm}/Ta_{19nm}/Py_{4nm}/Co_{3nm}/$ $Mn_{83}Ir_{17\ (15nm)}/$ $Al_{1.4nm}/Ni_{80}Fe_{20\ (5nm)}/$ $Ta_{6.5nm}$
The resistance changes by 47 % in a field range of 10 Oe, resulting in a high sensitivity of about 5 %/Oe.

The changes from parallel configuration to antiparallel configuration state cause the changes in resistance by ~50% at room temperature. The resistance changes in a field range of 10 Oe, that results in a high mean sensitivity of about 5%/Oe.

3.3.1 Exchange bias

The exchange bias was reported for the first time for Co particles by Meiklejohn and Bean in 1956 [158]. This phenomenon is based on the exchange interaction between the antiferromagnet and ferromagnet at their interface [159] and found applications in information storage technology. Meiklejohn and Bean observed that hysteresis loops below room temperature of Co nanoparticles are shifted along the field axis after cooling in an applied field [159]. The explanation was based on the theory that the particles shells have been oxidized to CoO, which is an antiferromagnet. Then the particle was considered as a complex of a ferromagnetic Co core and an antiferromagnetic CoO shell. In their publications they described how the exchange interaction can produce a shift in the hysteresis loop of a ferromagnetic [159]. Figure 3.14 shows this mechanism of exchange bias.
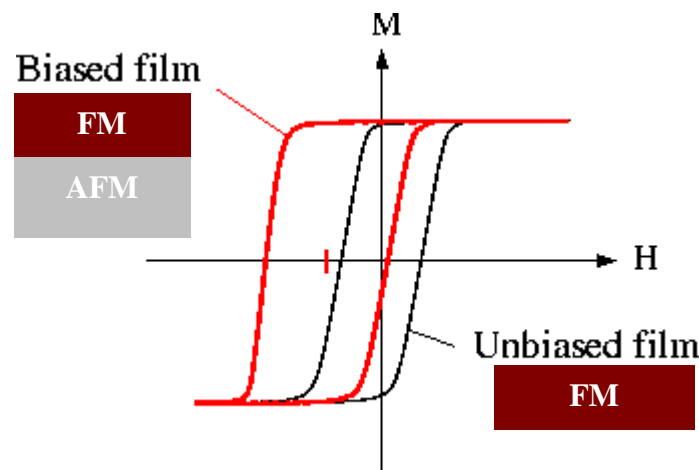
Figure 3.14 Mechanism of exchange bias [160].

In the case, when the Curie temperature of the ferromagnet is larger then the Neel temperature of the antiferomagent $T_C > T_N$ then the ferromagnetic magnetization will align in the field direction, while the AFM spins will remain paramagnetic for $T > T_N$. If the temperature T is lowered below T_N, the net localized AFM spins will couple to the aligned FM spins [159]. The hysteresis loop is usually shifted along the field axis in the opposite direction (negative) to the cooling field. The loop shift is termed exchange bias [159]. The hysteresis loop of the ferromagnet has also an increased coercivity, H_C, after the field cool procedure [159]. The exchange bias can be better understood using a scheme presented in a figure 3.15.
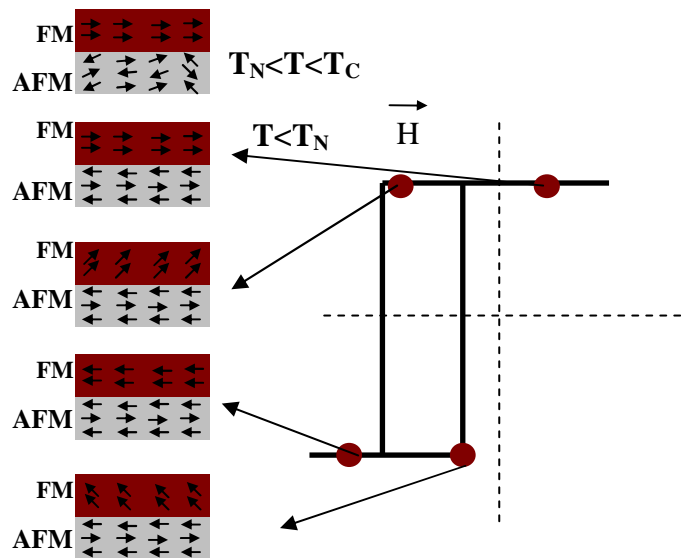
Figure 3.15 Diagram of the spin configuration for the structure FM-AFM [159].

In an initial step, when the temperature stays in the range $T_N < T < T_C$ the ferromagnetic spins line up according to the applied magnetic field, but the AFM spins stay random. After cooling to a temperature $T < T_N$, in the presence of the magnetic field, the AFM aligns ferromagnetically due to interaction at the interface [159]. In the case, when the temperature T $> T_N$, the FM spins starts to rotate and the AFM spin stays in the same configuration [159].

The interfacial interaction between the FM-AFM causes ferromagnetically alignment of FM spins with the AFM spins at the interface. One can say that FM spins have one single stable configuration, so the anisotropy is unidirectional [159].

When the field is rotated and it's back to the previous direction, the FM spins start rotating at small field due to interactions with the AFM spins. The material sees an additional biasing field that causes the shift in the FM hysteresis loop in the field axis, the so-called exchange bias [159].

3.3.2 Orange peel coupling

In 1962, Neel studied the ferromagnetic coupling between two magnetic layers with in-plane magnetization separated by a non magnetic layer [162,163]. This phenomenon was termed orange peel coupling and occurs when the interface shows correlated in-phase waviness. It decreases exponentially with spacer layer thickness [162]. The concept of orange peel

coupling was previously developed for the thick layers and adopted to the thin films technology by Kools et al. in 1999 [162].

For a magnetic layer system the dipolar coupling field is expressed by:

$$H_d = \frac{\pi^2 h^2 M_H}{\sqrt{2}\lambda t_s} \exp(-2\pi\sqrt{2}d/\lambda) \times [1-\exp(-2\pi\sqrt{2}t_s/\lambda)] \times [1-\exp(-2\pi\sqrt{2}t_H/\lambda)]$$

(3.17)

where λ and h are the correlation length and the height of the film roughness, d is the interlayer thickness, t_S and t_H are the thickness of the hard and soft magnetic films and M_H the magnetization of the hard magnetic layer. The model presented here was based on the assumption that there is no phase, amplitude, or correlation length difference in the topology of the various layer surface [162]. Based on equation 3.17, one has noticed that film and interfacial roughness cause a ferromagnetic coupling in a multilayer system. The ferromagnetic coupling field weakens an antiparallel magnetization orientation. For this reason the antiparallel configuration can become unstable or there is no antiparallel state [162].

3.4 Experiments with magnetoresistive biosensors

A magnetoresistive biosensor was demonstrated for the first time by Baselt *et al*. in 1998 [164] (see Figure 3.16).

	1st public.	Sensor type
NVL/NV	**1998**	GMR
Universität Bielefeld	02/2004	GMR/MTJ
IMEC, Leuven,	**2002**	Spin Valve
INESC,Lisbon, Portugal	**2002**	Spin Valve
Stanford/IBM	**2003**	Spin Valve
Philips Reasearch Labs	**2004**	Spin Valve

Figure 3.16 Magnetic biosensor evaluation [165].

In their experiment they measured the stray fields of the magnetic particles.The sensors were fabricated using magnetoresistive computer memory technology.

The experiment was performed with 2.8 µm Dynabeads M-280 on $80\times5µm^2$ GMR strips. They obtained an optimal signal-to-noise ratio corresponding to a detection limit of about one bead per strip [164]. Further, this idea was developed in a Bead Array Counter termed BARC, that uses DNA hybridization to detect biological warfare agents [80,84] (see figure 3.17a).
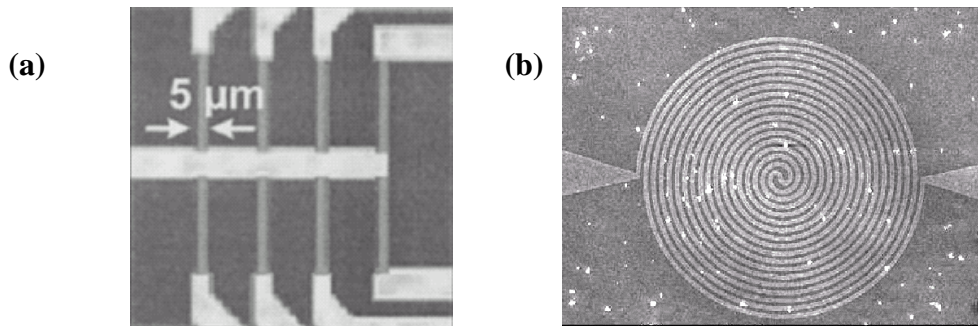
Figure 3.17 Different concepts of magnetic biosensors: (a) BARC II from Naval Research Laboratory (USA, Washington)(b) large area sensor from University of Bielefeld [165].

Further magnetoresistive biosensors were developed by a number of groups with different types of sensors and with different aims of detection (see Figure 3.16) [84]. Recently, in our group from the University of Bielefeld we developed similar sensors, but with a larger area and spiral-shaped lines (see figure 3.17). Each sensor element was in the size of a probe DNA spot. The sensor has a 75 µm diameter spiral shape that is ideal for pen spotted or injected DNA probes (see figure 3.17). We also focused on the detection of smaller magnetic particles, down to 0.35 µm diameter [75,84]. The new BARC-III biosensor from the Naval research group has also circular spots, 200 µm in diameter, including GMR strips connected in series [164].

3.5 Single magnetic particle detection

Since 2002 we are developing a small area MTJs sensor for the detection of single magnetic particles/molecules and this is a subject of the presented PhD thesis. In 2003, the group of Wang et al. at IBM Stanford also focused on detection of a single bead, with the aim of

detecting a single DNA fragment [82,84]. They used small area sensor with a width 1 to 3µm of the spin valve type with magnetoresistance (MR) of 10.3% (See figure 3.18).

Single beads 2.8µm
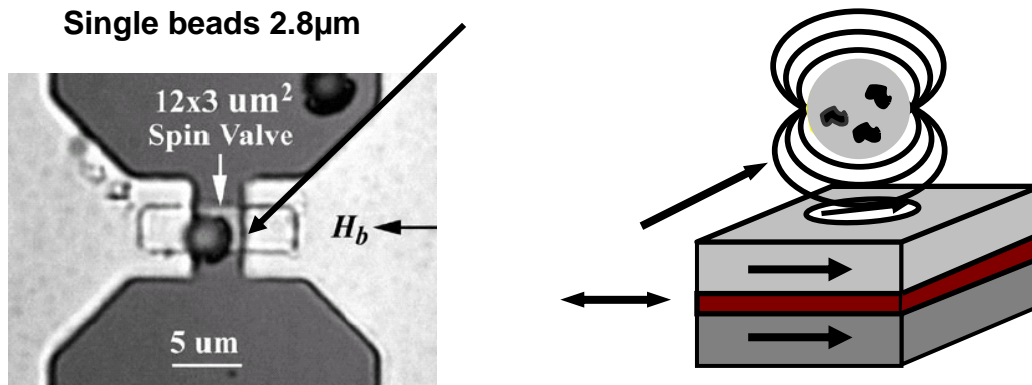
Figure 3.18 Detection of single magnetic particle using spin valve type sensor. The highest sensitivity for single detection is achieved when the size of the sensor matches the particle size [165].

In this experiment they demonstrated that the detection of a single 2.8 µm Dynal particle is possible with a spin valve type sensor [82,84]. In addition to the experiments a micromagnetic simulation was performed [82]. Simulation and experiment suggest that this type of sensor would be able to detect few 11 nm Co and other nanoparticles and make the identification of a single DNA fragment possible [82,84].

In our case we developed MTJ sensor that is much more sensitive that the spin valve sensor and the aim is to detect small sized magnetic particles with diameters up to 250 nm. Spin valve sensors and GMR sensors are the most common biosensor types; MTJs sensor and detection of single magnetic nanoparticles are still very novel.

4. Magnetic tunnel junction sensor (MTJ sensor)

From an experimental point of view, producing a high quality magnetic tunnel junction sensor is a complex task. One has to prepare a stable sensor with high MR amplitude and small area. In the following chapter a detailed description of the techniques used to design and fabricate (MTJ) sensors such as: magnetron sputtering, optical/e-beam lithography and ion beam etching are reported. A short overview on thin film analysis methods and characterization tools for MTJ sensor, as used in this work, is also presented.

4.1 Fabrication of MTJ sensor

In this section, the fundamentals of MTJ sensor fabrication will be discussed and the major steps of the process will be described. It is critical that all the magnetic tunnel junction elements operate with nearly identical characteristics. For this reason, this part will focus on the general outline of the process and on the interaction of various processing steps, which determine the quality and the performance of the sensor.

4.1.1 Silicon substrate

The device fabrication usually begins with the choice of the substrate. Magnetic tunnel junctions are fabricated on a silicon wafers that are often used as substrates in magnetoresistive technology due to their low roughness. For our experiments, thermally oxidized silicon wafers from CrysTec with an amorphous silicon oxide layer of approximately 50 nm thickness were used. Native oxide silicon wafers are not used in the fabrication process, because the substrate shorts the devices electrically at room temperature. The deposition of the magnetic tunnel junction structure starts with the substrate preparation. Depending on the experiments, complete wafers are used or the substrates are cut into proper dimensions.

Figure 4.1 Silicon wafers.

_____

In the next step, the wafers are cleaned from organic materials and any particles by using compressed dry N_2. Additionally, the substrates can be also ultrasonically cleaned by acetone and ethanol for 2 minutes in each solution and then dried using compressed dry nitrogen. When the cleaning procedure is finished, the substrate is ready for deposition.

4.1.2 Magnetic Tunnel Junction deposition

MTJs structures are deposited in a magnetron sputtering ClAB 600 systems from Leybold Vakuum GmBH [166]. It is a fully automatic system that consists of a sputter chamber with six four inch magnetron sputter cathodes: two RF and four DC magnetron sputter cathodes, a substrate rotating table and a central robot handling system [166]. Additionally the system consists of an oxidation chamber with an electron cyclotron resonance (ECR) oxygen plasma source from Roth & Rau GmbH, which is used to produce the Al2O3 tunneling barrier of the MTJs structures .
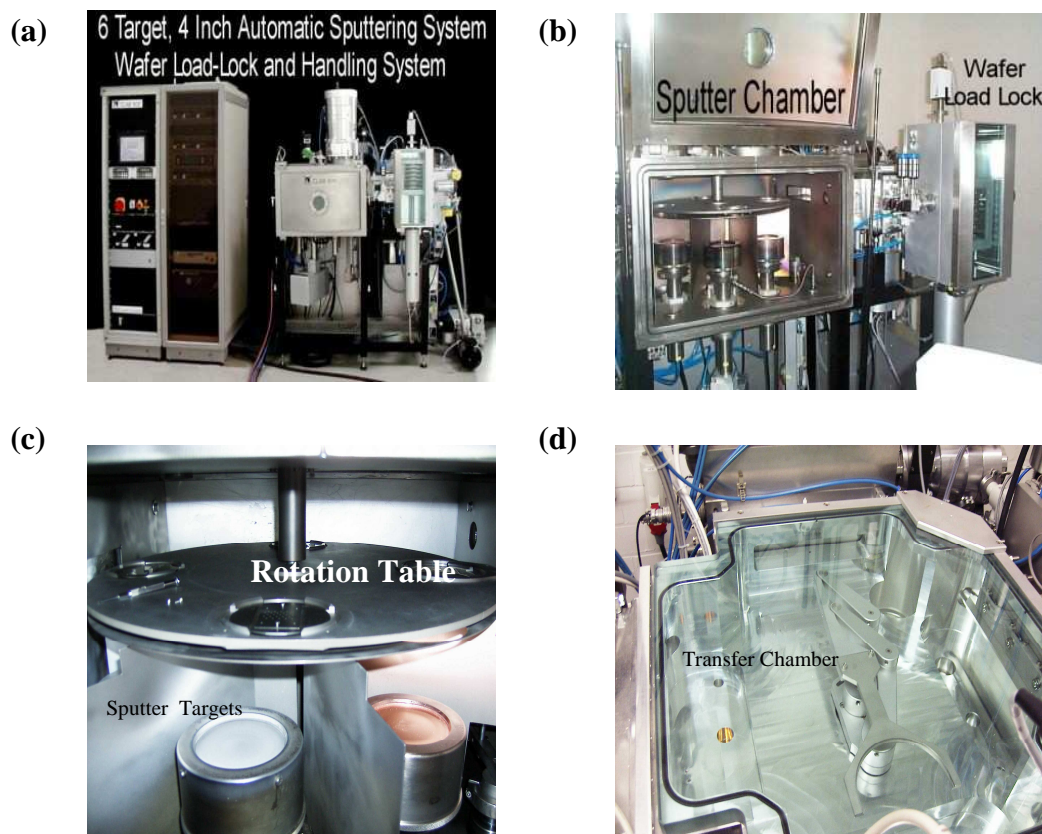
Figure 4.2 (a) CLAB 600 deposition system from Leybold Vakumm Gmbh, as used in this work to fabricate MTJ sensor (b) and (c) deposition chamber with six sputtering targets (d) transfer chamber between load lock, sputter chamber and oxidation chamber.

A more detailed description of the major components of CLAB systems can be found in the reference [167].

4.1.2.1 The physical principles of the process

Magnetron sputtering is a vacuum process used to deposit high quality thin films on substrates. The materials used in the process are usually in the form of   plates called targets. The target is fixed in a chamber, which is filled with argon gas usually at a pressure in the raugh some militorr. The substrate to be coated is mounted facing the target [168] .

The simplest sputtering process is called DC or diode sputtering. It is a process, where a negative external potential is applied to charge the target. When argon is introduced to the vacuum chamber, the high negative potential ionizes the gas and creates a plasma. The positively charged argon ions are then accelerated towards the target, striking the target atoms and transferring their momentum to them [169]. The target is thus bombarded by high energetic ions that lead to the sputtering of the target atoms and to the formation of thin films on the substrate (see figure 4.3). This process is also called diode sputtering, because the target is usually placed at the cathode side (negative potential) and the substrate is at the anode side [168].
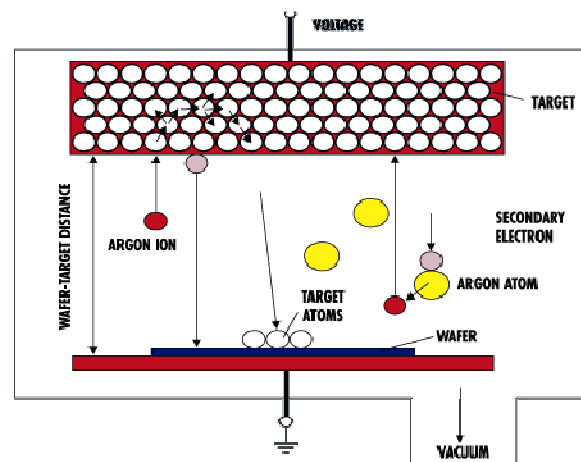
Figure 4.3 Material deposition of thin films through the DC sputtering [170].

In magnetron sputtering, a permanent magnet is used to generate a magnetic field that traps electrons from the plasma near the target in order to increase the ionization of the gas atoms and the deposition rate [168]. From the physical point of view, the magnetic field is used in the process to control the motion of electrons. According to Lorentz's law, the force F on particle with a charge of q and a velocity v in a magnetic field B is given by:

$$F = q\vec{v} \times \vec{B} \tag{4.1}$$

Thus a magnetic field applied to a plasma causes the charged particles to move in helical paths with a radius r of:

$$r = \frac{mv_{\perp}}{qB} \tag{4.2}$$

m is the mass of the charged particle, q is the charge of the particle and $v_{\perp}$ the component of the particle's velocity normal to the applied magnetic field B [169]. The radius of the helix in equation (4.2) is proportional to the mass of the charged particle. Because electrons are much lighter than ions, only electrons are affected by the magnetic field. The movement of the electrons in the helical paths ionizes the gas molecules through collision. The plasma density is increased at the target surface and this increases the sputtering rate from the target. The sputtered target atoms are neutrally charged, so that they are not affected by the magnetic field and can move in the direction of the substrate to form a coating layer [168]. The magnetron sputtering requires a minimum field of about 15.9 kA/m for most non magnetic sputter targets. For other targets such us permalloy the magnetron has to produce a much higher field, because the target shunts the magnetron field [169].

4.1.2.2 The growth procedure

The procedure of growing magnetic tunnel junctions is as follows: first the sample is fixed onto the sample holder by using a small drop of silver paste and cleaned with compressed dry nitrogen. When this procedures are finished, the sample is transferred into a Load Lock chamber. The whole system is then pumped until the pressure reaches a value of $< 3 \times 10^{-7}$. Then the sample is automatically transported to the sputter chamber, where it is placed on the rotation stage. For growing the film stacks for the magnetic tunnel junctions,

different types of sputter targets are used such as Aluminium (Al), Tantalum (Ta), Coper (Cu), Manganese Iridium (MnIr), Cobalt Iron (CoFe) and Permalloy (NiFe). The sample is rotated automatically inside chamber over the sputter targets, where the argon plasma is ignited. The thicknesses of the sputtered layers depend on the growth conditions, i.e. deposition rate and time:

.

$$d = C \; x \; (\; t \; + 0.55 \; s) \tag{4.3}$$

Where d is the thickness of the growing layer in nm, C is the deposition rate in nm/s and t is the deposition time in s. The constant time (0.55s) corresponds to the opening of the shutter. The necessary deposition rate of the sputter materials are verified experimentally using X-ray diffraction or atomic force microscopy (AFM) [167].

The deposition time is calculated from the equation (4.3). Further, these data together with other sputter parameters such as argon flow are transferred to the computer.

The layers are sputtered at a power of 115 W with an argon flow of $1.3x10^{-3}$ mbar. The deposition process of an MTJ stack is divided into three parts. First the seed layer together with the bottom electrode and the barrier material are deposited. When the process is finished, the sample is automatically transported to the chamber, where the oxidation process of the barrier material takes place. The   layer is oxidized for 100 sec at an oxygen pressure of 3×10^{-3} mbar and a microwave power of 275 W with a DC bias voltage at the sample of –10 V. After the Al-oxide layer is formed, the sample is transported again to the sputter chamber, where the upper electrode together with protection layers are deposited. When the process is finished the sample comes back to the Load Lock chamber. The complete sputtering process including sample preparation takes about 50 minutes.

4.1.3   Vacuum furnace

The MTJ films are transported as deposited to a vacuum furnace to enhance the exchange biasing and to improve the magneto resistance amplitude. The procedure is as follows: the samples are heated to 275° (over the Néel temperature) at a pressure below 1×10^{-7} mbar and are kept at this temperature for 10 minutes. Further, the samples are cooled down to a room temperature in about 30 minutes in a homogeneous magnetic field of 80 kA/m to define the direction of the unidirectional exchange anisotropy [75] (see figure 4.4). In case where the two ferromagnetic layers require different directions, the exchange bias is introduced by depositing the ferromagnetic layer in two different magnetic masks.
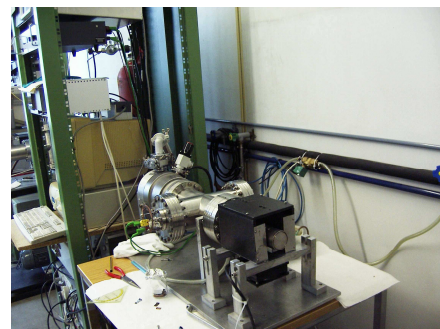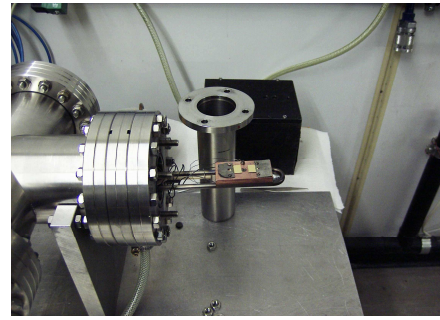
Figure 4.4 Vacumm furniture as used in this work.

4.1.4   Lithography

In this work, different types of lithography are used to pattern submicron elements such as UV, E-beam, and Laser lithography. Generally, the lithography process can be divided in six steps: sample or wafer cleaning, photoresist coating, baking, exposure, development, Lift Off or etching. This section provides a short introduction to the pattering processes including specific considerations of the e-beam lithography, which is the favored tool for the fabrication of magnetic tunnel junction elements.

4.1.4.1 Sample or wafer cleaning

The procedure of sample cleaning is the same as in the deposition process. The samples are cleaned with compressed dry nitrogen N_2. The samples can also be ultrasonically cleaned by acetone and ethanol for 2 minutes in each solution and dried by using compressed dry nitrogen. This additional procedure is preferred if, for instance, many particles adhere to the surface. This can occur, e.g., when the wafer is cut to required dimensions. These particles are

_____

not easily removed by blowing with dry nitrogen. The surface of the sample is checked before the lithography process is started, for example using optical microscope.

4.1.4.2 Photoresist coating

The lithography process starts with the choice of a photosensitive material. This material is usually called resist or photoresist. In definition, a photosensitive material is a material which changes its physical properties upon being exposed to radiation [171]. When the resist is exposed for example through a mask, the pattern of the mask is transferred (see the figure 4.5). The properties of the exposed resist are different from those of the unexposed resist [171]. This means, that exposure increases or decreases the solubility in a solvent called developer. The resist itself is made from polymer materials and can be classified in two groups: positive and negative. This relies on the

The propeties of resist are changing in place of exposure

Figure 4.5 Transmission of pattern.

response of the resist to the exposure. Figure 4.5 shows the photolithography process with negative and positive resist. When the positive resist is developed in a solution, the exposed regions of the material are removed; for a negative resist, after developing procedure, the unexposed region is removed [171] (see figure 4.6).

Radiation

Mask

Resist

Substrate

The propeties of resist are changing in place of exposure

Substrate

Sample in developer solution

Substrate

After development with

Positive resist

Negative resist

Substrate

Substrate

Figure 4.6 A scheme presenting the photolithography
with positive and negative resists [172].

In our lithography process, different types of resists- positive and negative are used. They are
supplied by ALLRESIST Gmbh [173]. The positive resist (AR-P 610.03) is suitable for e-
beam lithography.

It is chemically composed from copolymers, which have a high sensitivity to electron irradiation. This type of resist adheres to glass, silicon or metals and is suitable for nanolithography down to 30 nm [173].

To simplify the photolithography process in the fabrication of the sensor, the negative AR-N 7500.13 is used. This resist gives a good resolution (< 80 nm) and can be applied to pattern nanometer structures. It has also other advantages such as a good plasma etching stability. The resists contains novolak resins, naphthochinondiazides and cross linking compounds in solvents (propylene glycol methyl ether acetate). Additionally, it can be adapted for UV exposure with a wavelength range between 310 - 450 nm. The resist layer can be developed in an aqueous alkaline developer [173].

For a one step processes, the laser lithography or UV lithography is used. The positive resist adequate for this kind of lithography is AR P 535. This resist is used to produce a so called undercut profile; this means that it is used in the lithography process involving deposition, baking, exposure and development without any further procedure. It is a high sensitive resist and adheres very well to metal or oxide surfaces [173].

The deposition of all resists takes place in the clean room, because the photoresists are sensitive to white light. The resist is deposited on the surface by spin coating technique. This procedure usually has three steps. In the first step the resist is spread onto the wafer surface. Further, the wafer is accelerated to the correct rotational speed, which depends on the type of resist and the desired thickness. Finally, the resist is spinning at constant speed and allowed to dry for a few second. The spin coating parameters for the resist used in this work are presented in the table 4.1.

RESIST NUMBER	TYPE OF RESIST	SPIN COATING PARAMETERS	
		SPEED [RPM]	TIME [S]
AR P 610.03	positive	4000	60
AR P 535	positive	4000	30
AR N 750.12	negative	4000	30

Table 4.1 Spin coating parameters as used in this work for different photoresists.

4.1.4.3 Baking

After the spin coating procedure, a baking of the resist is necessary. The wafers are heated on a hot plate from the reverse side. The bake temperature depends upon the type of resist. The positive AR P 610.03 resist is baked at 150 °C for 30 minutes. The time of baking for the negative AR N 7500.13 takes only 3 min at 85 °C. The optical positive AR P 535 resist requires baking at 95 °C for 30 min. During the baking process the solvent is removed, the resist adhesion is increased and the stress between the resist and the substrate is decreased [169].

4.1.4.4 Exposure with electron beam lithography

Electron beam lithography is the main procedure used for magnetic tunnel junction element pattering. Here a LEO series 1530 field emission electron microscope with Raith Elphy Plus lithography system is employed [174,175]. This type of microscope is a fully computer controlled tool. The commands are transported to the electronic system using fibre-optical cables. The sample stage is controlled by a joystick and additionally by the

Figure 4.7 Photograph of the scanning electron microscope Leo 1530.

operation panel [176]. The sample coated with the resist is placed in the vacuum chamber on the microscope stage. The beam is produced by a thermic field emission cathode, Schottky emitter (ZrO/W cathode) [176]. When the sample is placed in the microscope vacuum chamber, the whole system is pumped until it reaches a vacuum of 8-9 x10^{-7} mbar; then the acceleration voltage appears on the display. The accelerating voltage for the Leo1530 microscope can be varied between 100V and 30 kV. The exposure of the resist structure is done in this work at an accelerating voltage of 20 kV [176].

There are some important parameters that have to be adjusted during the exposure such as magnification, focus, stigmator and beam alignment.

In the first step it is necessary to adjust the magnification. The structures are usually not in focus in the X and Y direction. After this procedure, the image is correctly focused [176]. For a small magnetic tunnel junction element, the focus adjustment is very important. It is recommended to

focus onto a very small object with a size below the future pattering and then onto the whole image.

To fabricate a high quality pattern, it is essential to adjust the apertures. In the Leo 1530 system, different types of apertures can be chosen. The standard one is a 30µm aperture used for most microscopy work such as imaging. For highest resolution and lithography purposes the apertures 20µm, 10µm and 7.5µm are used. In this work, the patterns were prepared with the aperture of 20µm. The apertures are usually adjusted by clicking "Aperture Alignment" and moving the mouse to the left or the right for X alignment and up or down for Y alignment. It is also possible to align the aperture by activating the control box with Focus Wobble. The drift of the image during the focussing signalises that the beam is not passing through the aperture centre. In this case the alignment can be corrected by moving the image in the X or Y direction. When the aperture and magnification parameters are adjustment the sample is ready for exposure [176].

In e-beam lithography not only the adjustment of the parameters is significant. It is also necessary to chose an accurate dose to change the properties of the resist during exposure. Every photoresists has different sensitivities to different electron energies. The dose for the chosen photoresist is constant for patterns with equal size. In many cases, this value may change for example with the resist thickness or due to a highly reflective layer below the resist [171]. For positive photoresist, an incorrect value of dosage may produce a pattern with eroded edges, decreased size and/or with less sharpness on the corners (see figure 4.8) [171]. In the case of negative resist, patterns with an incorrect dosage become larger than the designed structure. The sample may also have low sharpness at the corners [171].
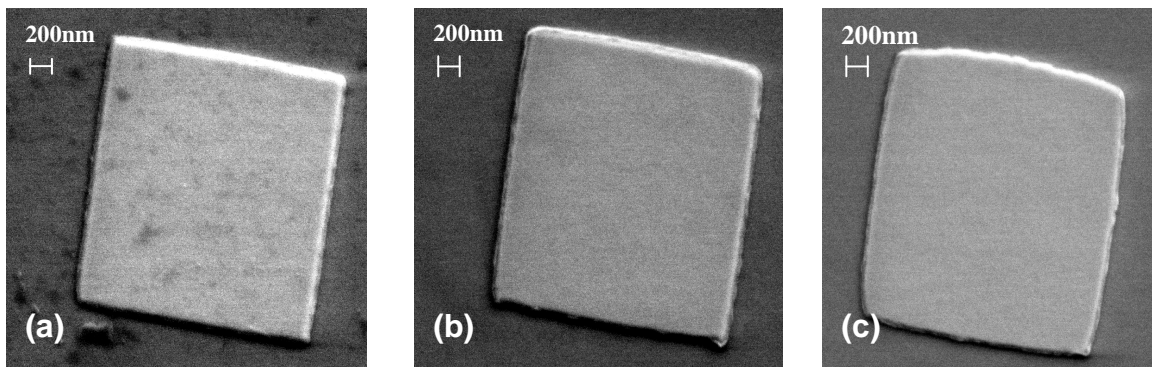
Figure 4.8 Exposure of positive resist with different dosage value:
a-1.0 µC/cm², b-1.6 µC/cm², c-2.07 µC/cm² at accelerating voltage of 20kV.

There are several steps during pattering of magnetic tunnel junction elements. Each step consists of deposition of resist, baking, exposure, developing in a solution and etching. The number of steps depends on the element design and the type of the resist used. It is very important that various patterns of different lithography steps are aligned to each other, as they consequently make one complete structure. The alignment can be achieved by introducing a special mark in the structure design (see figure 4.9). It is important that marks are introduced in every lithography step, as they are reference points for future positioning and localization of previously exposed structures [171]. The precise alignment of the patterns has influence on the quality of the fabricated devices.
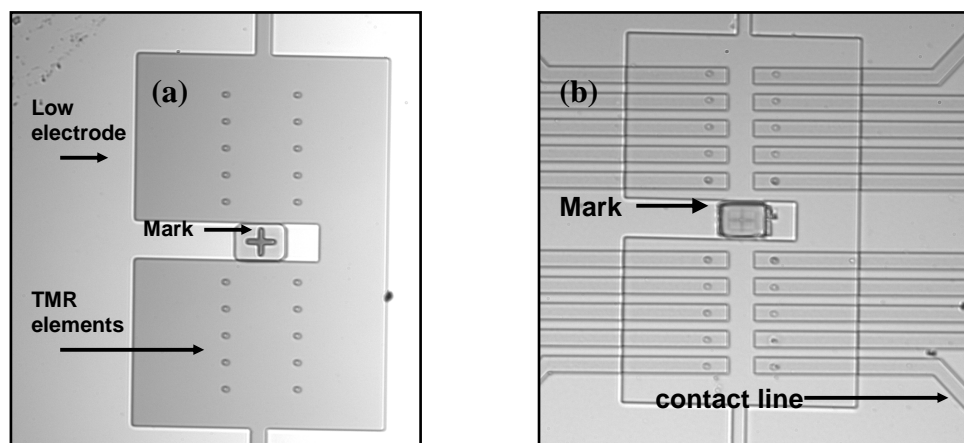
Figure 4.9 Optical microscope photo of sensor elements with contact lines;
(a) and (b) alignment marks used for exposure of TMR elements on the low electrode and for positioning of contact lines.

4.1.4.5 Exposure with UV and Laser Lithography

The UV and Laser lithography system is used in this work for patterns requiring only one step of lithography such as the exposure of simple TMR elements. Such TMR structures have to be fabricated for the measurement of the MR amplitude and the resistance area product of the film systems. The test on simple TMR structures to be carried out before the pattering of complex magnetic tunnel junction structures is started. It can take one weak to finish complete a lithography process used for the fabrication of magnetic tunnel junction sensors. First, one therefore has to check that the quality of the film stack is acceptable before starting a complicated exposure process.

The UV lithography system is an easy way to produce structures larger than about 5µm. For this experiment the UV-mask lithography system from Thermo Oriel has been used [177]. The mask was made from tantalum on glass by Laser Lithography. During the exposure the mask is placed on the top of the sample and an appropriate UV exposure is performed. The whole process takes about 3 to 5sec. Figure 4.10 shows the mask design used for the UV-exposure [85]. The patterned TMR elements have an area size: $90000\mu m^2$, $40000\mu m^2$, $10000\mu m^2$, $506.25\mu m^2$ and $56,25\mu m^2$ [85].
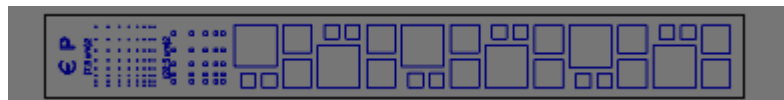
Figure 4.10 Mask used in the UV-photolithography exposure [85].

DWL 66 Laser Lithography system from Heidelberg Instruments GmbH is a high resolution direct writing system used in this work [178]. It is used to pattern on silicon substrates and also for mask making. A photograph of the apparatus is presented in the Figure 4.11. The system is equipped with a 4 mm write head and a camera for alignment of the patterns.

The resolution of the instrumentation is 40nm. The system can fabricate patterns with a minimum size of 1.2µm.

Figure 4.11 DWL 66 from Heidelberg Instrumentation GmbH [178].

This direct writing system uses a laser as a radiation source (laser from Melles Griot) with an output power of 90 mW at a wavelength of 442 nm [75].

4.1.4.6 Etching

The etching process is responsible for the correct transformation of the designed patterns in the metal [179]. This section will introduce the Ion Beam Etching procedure used in this work.

During the IBE process, the wafer is placed in a vacuum chamber, and exposed to an ion beam [179]. The ion beam is produced by an Ar gas, which is fed into the source chamber and ionised by electron bombardment. The ions erode the target and etch away the areas not covered by the photoresist.

In this work, two different systems have been used for pattern transformation. The TMR elements are etched using the UniLab system from Roth&Rau AG [180]. The system works with the base pressure of $5 \cdot 10^{-5}$ mbarr. The etching process is started at an Ar pressure of $1.2 \cdot 10^{-3}$ mbarr. The ion source operates at a discharge voltage of 55 V, a beam voltage of 400 V, an accelerator voltage of 30 V and a beam current of 7 mA. To create the circularly homogeneous etching area, the sample is tilted at an angle of 30° and rotates slowly inside a vacuum chamber. The electric current through the sample holder measures the ion dosage [75].

For a multi-step lithography, the etching apparatus built up at the Bielefeld University has been used. During this step of the process, a quadrupole mass spectrometer is employed for monitoring the etching procedure [85]. The sample is placed in a vacuum chamber with a base pressure of $2 \cdot 10^{-8}$ mbar and an argon pressure of $4 \cdot 10^{-4}$ mbar. Here the discharge voltage is 50V, the beam voltage is 400V, the accelerator voltage is 30V and the beam current is 6mA. Before the etching process is started, the sample is tilted to 35° and the rotation is initiated. The etching rate is controlled by measuring the sample current, which has to be kept at around 400µA during the process [85]. The advantage of this method is that the end point for etching can be easily identified by the mass spectrometer.

4.1.4.7 Lift-off procedure

Lift-off is a simply procedure of remove undesired parts from the sample. There are different lift off procedures for positive and negative resist. The negative resist is removed in a N-methyl-2pyrolidinone (NMP) remover for 60 minutes at 80°C in an ultrasonic bath. The positive resist is removed in AR-300-70 solution for 15 minutes and the temperature is less important. The solution is dried from the sample using compressed dry N_2. Small patterns require longer time in the remover than predicted by the standard parameters. When the procedure is finished, the structures have to be scrutinized in the optical microscope. In case of small patterns it is difficult to remove negative resist completely at the edges of the structure.

4.2 Characterization tool for an MTJ sensor

4.2.1 Energy dispersive X-ray sensor (EDX)

Additionally, the LEO 1530 field emission scanning electron microscope is equipped with an EDX (Energy dispersive X-ray) system from OXFORD Instruments [181]. This tool is not only useful for the elemental surface analysis, but the X-rays can penetrate the sample to a depth of about 2 μm [75]. We used the EDX mainly to define the end point of the etching processes. The typical detector used in EDX is a Lithium drifted Silicon detector. It works at liquid nitrogen temperature. The beam energy used for the EDX is 20 keV.

During the EDX measurement, the incident beam penetrates the sample and creates secondary electrons. Thus, there are a lot of atoms with holes in the electrons shells. Then, the atoms will be stabilized by dropping electrons from the outer shells. This generates radiation in the form of X-rays. The X-rays strike the detector, generating photoelectrons within the silicon. The photoelectrons move through the silicon to generate electron-hole pairs. The electrons and holes are collected at the end of the detector by a strong electric field. This generates a current pulse that depends on the number of electron-hole paires created and thus on the incoming X-ray energy. Based on this it is possible to obtain information about the elemental composition of the analysed materials [182].

4.2.2 Magneto-optical Kerr effect (MOKE)

The Magneto-optical Kerr effect is used in this work to characterize the magnetic state of the samples. The system is a home built apparatus made at Bielefeld University [183]. The magneto-optical Kerr effect is a change in the intensity or polarization state of light reflected from a magnetic material. These changes are proportional to the magnetization of the sample. When the magnetic field is varied, it is possible to measure a hysteresis loop that characterizes the magnetic state of the sample [184].

In particular, the MOKE apparatus built-up in our laboratory utilizes as light source a red laser working at 0.5 mW. Two polarisers are used to define the polarization of the incoming beam, and to analyse the beam after reflection at the sample. The beam from the polarizer is transmitted to the detector (photodiode) which is connected to a Keithley K2000 multimeter [183]. The magnetic field H is produced by Ferrite rod coils and the H- sweep is controlled by the computer. The coils produced a maximum field of 3500 Oe with a 36V- 12A power supply. A more detailed description of the apparatus can be found in the reference [183].

4.2.3 Optical microscope

An Axiotech Vario microscope from Zeiss is used for microscopic observation and analysis of the sample [185]. The microscope consist of 3 Epiplan objectives, with magnification of 10x, 20x, 50x and 100x. The sample is placed on top of a micro precision positioning table from Parker. A CCD camera is attached to the microscope with a special software available for visualising, analysing and processing of digital images [185].

Figure 4.12 Photo of optical microscope as used in this work [186].

4.2.4 Computerized Film Thickness Measurement System

The NanoSpec 210 is a Computerized Film Thickness Measurement System used for measurement of small areas samples [187]. This tool is used in this work to measure the

thickness of the SiO_2 on the Si wafers. The SiO_2 layer is necessary for the fabrication of a MTJ sensor. The Nanospec system consists of an optical microscope and a personal computer [187]. The optical microscope has a mechanical spectrophotometer head, which measures the illuminating light wavelength from the sample surface in a range of 370 to 800 nm. The microscope has three objective lenses: 5X, 10X, 15X and 50X magnifications [187]. It measures the thickness of SiO_2 layer down to 50 nm with an accuracy of 0.2 nm [75].

4.3 Transport measurement

The transport measurements are carried out by conventional 2 probe DC measurements technique and are recorded by a computer. During the measurement, a voltage is applied to the sample in the range from –2 to +2 V. The current is measured by an electrometer and the signal is transmitted through six amplifier settings in the range from 1µa to 100mA [75, 183]. The output of the electrometer is measured by a Keithley Model 2000 digital multimeter [183]. A homogeneous magnetic field is produced by two coils with a ferrite rod supplied with a 36V - 12A power supplies and with an error of ± 5mV [183] (see Figure 4.13). The maximum field produced by the coils is in the range of 3500Oe and is measured using a Bell 6010 Gauss/Tesla meter [183].
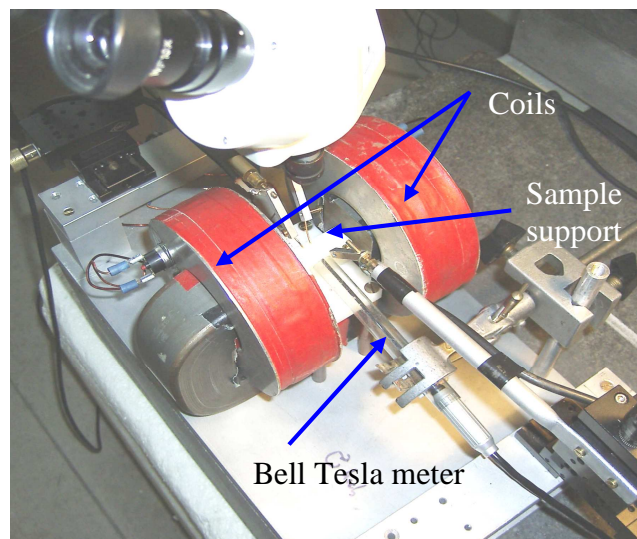
Figure 4.13 Photographs of the set up as used in this work
for transport measurement.

4.3. 1 Measurements with an Atomic Force Microscope

A conventional standard Topomterix AFM microscope is assembled into the transport measurement system with the two Helmholtz coils [188] (see Figure 4.14). Two different measurements are possible with this setup: topography of the MTJ sensor and a magnetoresistance map at constant magnetic field (for details of this experiments see chapter 6.4).

Figure 4.14 (a) and (b) Photos of Topometrix AFM microscope as used in this work for topography and magnetoresistance map measurement.

An AFM usually consist of a sensing probe (a tip), piezoelectric ceramics for positioning the probe, an electronic unit and a computer for controlling the scan parameters, which can be also used to generate an image [189].

4.3. 1.1 Basic of atomic force microscope

The AFM can operate in contact and non-contact scanning mode. In the contact AFM mode, a tip is scanned across the sample surface with "direct" physical contact with the sample. During scanning, the topographic features of the sample cause a deflection of the tip and cantilever. A light beam is bounced off of the cantilever and reflected onto a four-section photodector. The force applied to the tip (amount of deflection) is calculated from the difference in the light intensity on the sectors of the photodetector [189].

In non-contact AFM, the cantilever oscillates at its resonance frequency. In this mode, the force gradients between the tip and sample are detected. When the probe is close to the sample surface, the force gradient causes a change in the oscillating frequency, amplitude and phase of the vibrating cantilever. These changes are detected by the feedback-control loop [189].

4.3. 1.2 Topometrix Instrumentation

A Topometrix is an easy to handle microscope that consist of TrueMetrix^{TM} scanner system and an open-loop software scanner linearization system [189]. There are two scanners used with the Topometrix: tube and tripod. The tripod scanners are built up from separate X,Y, and Z piezoelectric components. The tube scanners are constructed from cylindric piezo ceramics with an outside surface divided into quadrants. Each quadrant is attached to a separate voltage source. The inner surface forms a continuous electrode. When a voltage is applied to the correct piezo quadrants the probes scans in X or Y direction. If the voltage is applied to all quadrants, the scanner is moved in the Z direction. The piezo scanner´s movements are controled by the TrueMetrix closed-loop scan linearizer [189] .

Additionally the microscope consist of the Electronic Control Unit (ECU-Plus) system that is built up from 16-bit scanner controls in the X,Y, and Z directions. ECU-Plus provides an electronic signal that controls the scanner, position of the device and an amplifier in the microscope. It is directly connected to the computer, connectors and power supplies by mother boards. The rear of the ECU has various input/output lines that allow to customize the instruments configuration. Thus the output of an electrometer can be directly connected to the rear and the recording of magnetoresistance map is possible. The system is also equipped with a CCD video camera for viewing the tip and the sample at a 45° angle [189].

4.3. 1.3 Procedure for use of Topometrix Explorer AFM

The procedure of using the Topometrix AFM starts with the tip mounting. The tip is mounted on the holder using a drop of a nail lack . It dries completely in 24 hours. In the same time, a sample can be mounted on the microscope stage. After preparation, the AFM can be placed on the microscope stage.

An important procedure in Topometrix operation is the beam alignment. Every time when a new cantilever is mounted or the adjustments are altered, this procedure has to be repeated. Three components play a significant role in AFM microscope beam alignment: the laser, mirror and photodetector. The principle of the alignment procedure is to maximize the signal at the photodetector and to equalize the amounts of light hitting each quadrant. The beam alignment can be done using a software program.

The program is started with the scanner selection. Later on, the voltage is applied to the head of the microscope and the laser is set on the high intensity. The cantilever tip is lowered by using an icon. It is important to put attention to the tip shadow. This is a reference, which give information how high above the sample the tip is. When the photodetector and the mirror are correctly aligned, the laser signal is cantered on the photodiode quadrants. The final adjustment has to be done by enter the Sum mode, where the laser signal can be maximized. The initial scan parameters can be found in the reference [189].

The tip approach is starting with a setting of usually 50 nA. The tip is automatically approaching. The scanning with the microscope can be started by clicking on the Instant Scan button [189].

In the experiment a Olympus probes were used with resonance frequencies of approximately 70 kHz, and typical forces constant 2 N∕m.

5. Magnetic particle detection with MTJ sensors

The conventional detection of magnetic particles or molecules is based on fluorescent techniques. A new detection method based on magnetoresistive technology has been developed to address these shortcomings of the conventional technique [See section 3.4] .

In this chapter, the detection of particles using the principles of magnetic tunnel junction are discussed. A magnetoresistive transducer is built using electron beam lithography and ion beam etching technique. The sensor is coated with 1.5µm diameter iron oxide particles and magnetized perpendicular to the sensor plane. The signal response of sensor elements with and without magnetic particles is measured. This chapter concludes with comments and recommendations concerning the detection of single magnetic particles.

5.1 Principle of detection

Iron oxide particles, encapsulated in a polymer matrix, are the most common particles used in magnetoresistive biosensors. They exhibit superparamagnetic behavior with zero remanence. An external magnetic field must be applied to magnetize the particles and to obtain a detectable magnetic stray field. In principle, two different configurations are possible: the magnetizing field could be applied perpendicular or parallel to the film plane of the magnetoresistive sensor (See Figure 5.1).

(a)   **(b)**
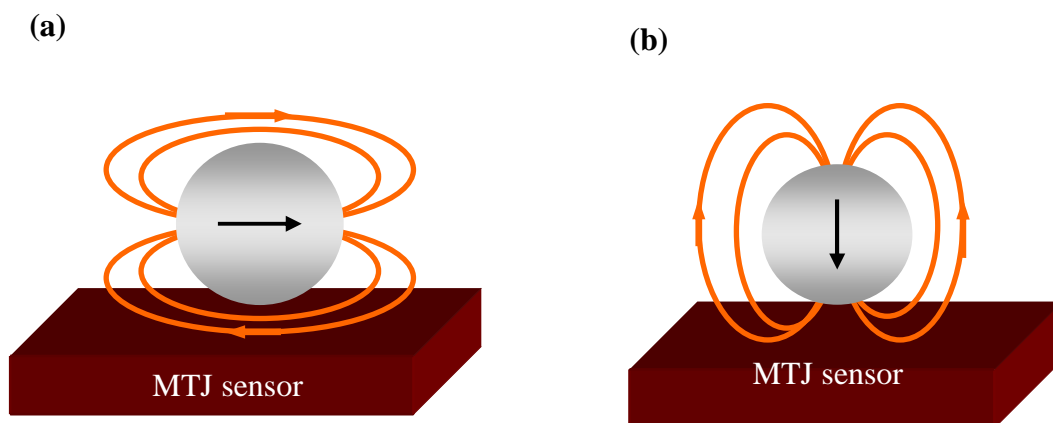
Figure 5.1 Magnetic particle magnetization
(a) parallel to plane and (b) perpendicular to plane.

The sensitivity of the sensor should not be affected by the magnetization field of the particles [75]. The MTJ sensor usually contains a very thin magnetic layer in nanometer range. Demagnetizing the field in the perpendicular to the plane of the ferromagnet can be expressed as:

$$H_d = N_d \cdot M \cong M$$ (5.1)

where H_d is the demagnetizing field and N_d is the demagnetizing factor [75].

For a very thin layer, N_d is approximately equal to $\cong 1$ and the demagnetizing field is in the range of the saturation magnetization of the layer. In MTJ sensors, a magnetic sense layer is formed by Py. At room temperature, the saturation magnetization of the Py is equal to 860 kA/m. According to Equation (5.1), a demagnetizing field will have approximately the same magnitude [75]. In these cases, it is possible to apply a large field in the out-of-plane orientation of the magnetoresistive sensor without affecting the sensor [75]. The out-of-plane configuration also has other advantages. The magnetic moment of the particle can be switched off and on by changing the magnitude of the magnetizing field. It is also possible to use the same sensor element as a reference and compare the signal response with and without the presence of the stray field of the particle [75].

In the case of in-plane configuration of the sensor, the experiments require a sensor with sensitive regions at large in-plane fields of ferromagnetic markers. To date, ferromagnetic particles are not commercialized and the magnetic moment of iron oxide particles is not large enough to produce a stray field that can be detected by the sensor. The advantage of this set up is that this type of particle will always display the same magnetic moment in the sensitive field range of the sensor, so that many measurements can be taken [75].

In both configurations, the in-plane components of the particle stray field have an influence on the relevant resistance variation in the sensor. Figure 5.2 shows the magnitude and direction of the particle stray field for both configurations. The magnitude of the stray field in the out- of- plane configuration is lower than that of in-plane configuration [190]. The patterns in this geometry are radially symmetric. This decreases the influence of the particle on the sense layer. From an experimental point of view, the in-plane configuration is preferred over the out-of-plane configuration, but the experimental arrangement is rather difficult in this geometry.

(a)   **(b)**
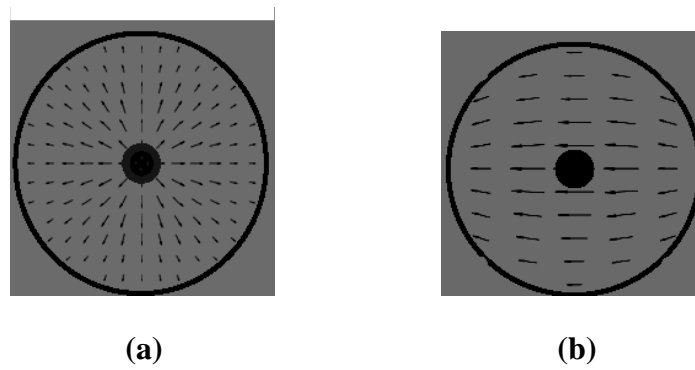
Figure 5.2 This diagram shows the in-plan components of the particle magnetic stray field for both configurations: (a) in plane and (b) out-of-plane [190].

In the present work, the magnetizing field is always applied in the out- of-plane direction.

5.2 Sensor fabrication and characterization

A magnetic tunnel junction sensor consists of two ferromagnetic layers separated by a thin layer of insulator. MTJ films are typically deposited on insulating substrates in a vacuum deposition system by dc magnetron sputtering. The lower magnetic layer is comprised of a 3nm $Co_{70}Fe_{30}$ exchange coupled with a 15 nm thick layer of the antiferromagnet $Mn_{83}Ir_{17}$. The upper magnetic layer is composed of a 5 nm thick $Ni_{80}Fe_{20}$. An insulating tunnel barrier is formed from a 1.4 nm thick Al layer which is oxidized to amorphous Al_2O_3 in an electron cyclotron resonance (ECR) oxygen plasma source (RR 160 PQE from Roth & Rau GmbH Germany).
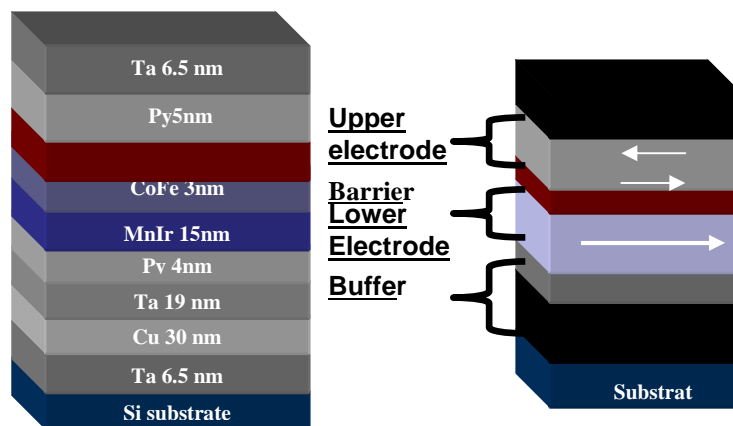
Figure 5.3 Magnetic tunnel junction layer stack as used in this experiments.

Other layers are added as conductors, seed layers, or stopping layers for the Ar ion etching technique [191]. The individual thicknesses of the layers are shown Figure 5.3.

Patterning of the films to rectangular sensor elements with dimension of $10x10\mu m^2$ was done with electron beam lithography and ion etching. The sensor fabrication is carried out with a negative photolithography process.

5.2.1 Sensor fabrication with a negative lithography

Three steps of e-beam lithography are needed to fabricate a magnetic tunnel junction sensor with a negative resist, but the whole procedure is divided into several stages. In the first stage, the MTJ films are deposited on the silicon wafers. After deposition, the wafer is cut into the correct dimensions. Usually, a Si- wafer substrate of 15x20mm is used. After preparation, the sample is annealed in a vacuum furnace at 270°C for 10 min to enhance exchange bias (For a detailed description of this process, see Section 4.1.3). The typical temperature profile of the vacuum furnace is presented in Figure 5.4.
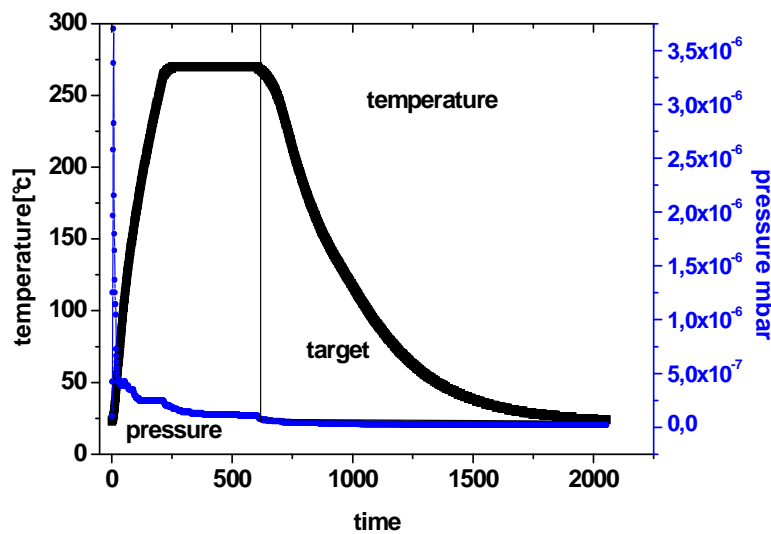
Figure 5.4 Typical temperature profile of the vacuum furnace.
The sample is annealed for a 10 min at 270°C (10' @270°C).

The magnetic properties of the MTJ stack are measured by the Magneto Optical Kerr Effect (MOKE). In Figure 5.5 MOKE, measurement is presented, for the annealed samples.
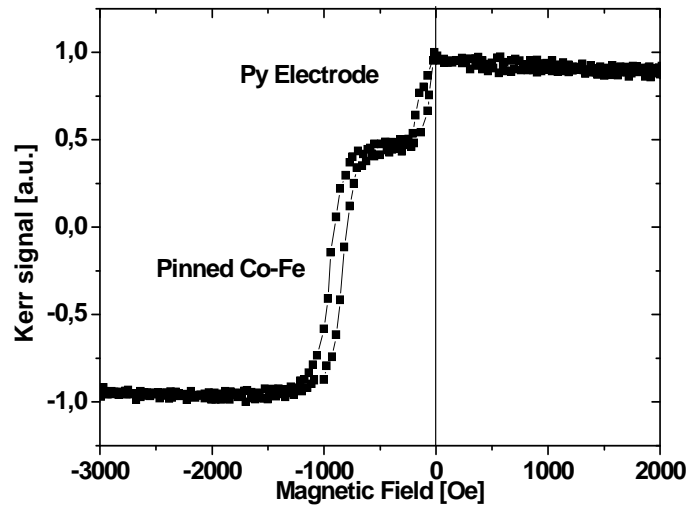
Figure 5.5 MOKE measurement of $Ta_{6.5nm}/Cu_{30nm}/Ta_{19nm}/Py_{4nm}/MnIr_{15nm}/CoFe_{3nm}$ /$Al_{1.4nm}/Py_{5nm}/Ta_{6.5nm}$ annealed at 270°C for 10 minutes in a magnetic field of 1000 Oe.

Here, a Py-free layer switches around zero field. A shift with respect to H=0 is observed due to coupling to the pinned layer. The pinned Co-Fe layer switches far from H=0 due to the exchange bias.

5.2.1.1 Sensor fabrication procedure

The stages involved in MTJ stack pattering are schematically presented in Figure 5.6. The first lithography step is the exposure of the lower electrode. This step requires a negative photolithography resist AR N 7500.13. The resist is deposited on the substrate and the sample is spun at a typical speed of 4000 RPM for 30 s (For more information, see Section 4.1.4.2). Exposure is performed with the e-beam lithography system (section 4.1.4.4). Typical parameters for e-beam lithography are: an acceleration voltage of 20KV, a working distance of 9mm and an aperture of 120µm.

The resist has a sensitivity value equal to $170\mu As/cm^2$ and a dosage factor equal to $1\mu C/cm^2$. The beam current is measured during every exposure and the values are entered in the "exposure " menu to calculate the dweltime ($>375ns$). After exposure, the sample is developed for 3 min in developer AR 300-47. In the next step, a sample is transported to etching chamber. The etching process is controlled by a secondary ion mass spectrometer (See Section 4.1.4.6). The resist is removed in an ultra–sonic-bath in a remover NMP at 80°C for approximately 60min.

The second lithography step is the pattering of the MTJ-elements and the paths to the future contact line. The parameters of acceleration voltage and working distance are the same as in the previous exposure. The elements are exposed with an aperture of 20µm, but the paths are exposed with the aperture of 120µm. The resist has a sensitivity of $170\mu As/cm^2$ and a dosage factor that varies from 0.8 to 1 for an element and a factor 1 for the paths. The structure is aligned to the cross mark of the previous exposure (For more details see Section 4.1.4.4). After developing, the sample is put into the spectrometer chamber and the etching process begins. Directly after etching, the sample is placed into the home made UHV chamber for sputtering the SiO2 layer. It is used to isolate the bottom and the top contact lines. The SiO_2 layer has to be 100nm thick as an isolation material. When the sputtering process is complete the sample is placed into the NMP remover for 90 minutes.

The third lithography step is the pattering of the contact lines. First, a sandwich layer of Ta_{5nm}/Au_{45nm} is sputtered in the UHV chamber on top of the sample. The tantalum layer is used as an adhesive between the SiO_2 and Au layer. After metal deposition, the sample is placed in a clean room for spin coating a negative resist AR N 7500.13. The contact lines are exposed with the aperture of 120µm. The resist sensitivity is $170\mu As/cm^2$ and the pattern required dosage factor equal to 1.0. The structure is also aligned to the cross of the previous exposure. Pattering with a negative resist can be simplified to two step lithography. In that case, the sample is a pattern without a lower electrode.

The micrograph of the sensor is presented in Figure 5.6. The MTJ sensor prototypes consist of 20 sensor elements with an area 10µmx10µm. The two point measurement of the single MTJ elements is carried out between the upper and lower electrode.

I First Lithography Step :
Lower electrode

(1) Resist deposition:
   Negative e-beam
resist   AR N 7500.13
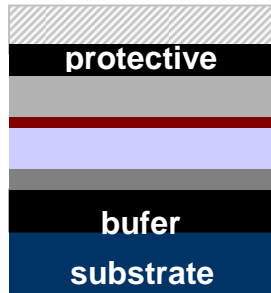
(2)Exposure: Lower
electrode exposure
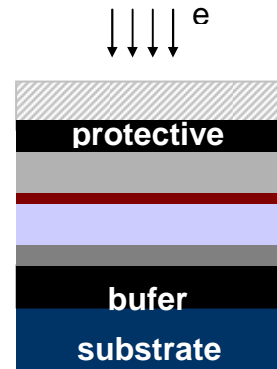
(3) Resist
development
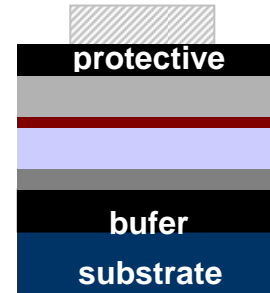
SEM pictures of
profile view
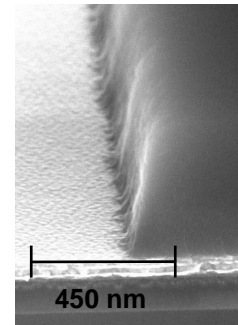
(5) Ar$^+$ - ion beam
etching
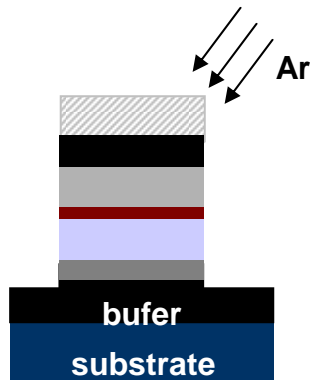
SEM pictures of
etching profiles view
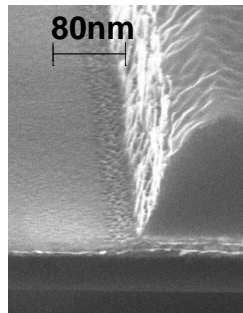
(6) Lift off of
the resist
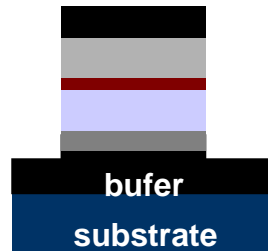
SEM photo of lower electrode
with introducing contact pads
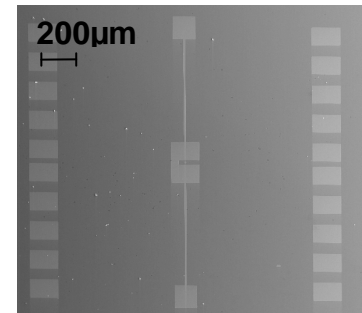
II Second Lithography Step : MTJ
Elements

(1) Resist deposition:
   Negative e-beam
 resist   AR N 7500.13
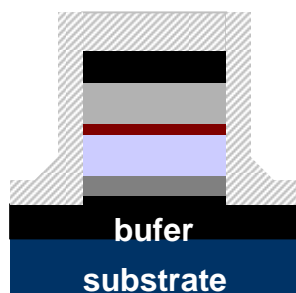
(2) Resist exposure and
    development: MTJ
    elements and paths

(3) Etching

(4) SiO$_2$ sputtering

SEM photo; SiO$_2$
thickness: 140nm
at the edges less

(5) Lift off of the
negative resist

80nm

III Third Lithography Step : Contact Line

(1) Sandich metal layer deposition
Ta$_{5nm}$/Cu$_{30nm}$/Au45nm

(2) Resist deposition

(3)Resist exposure and development

(4) Etching

Micrograph of a sensor prototype

Close up of a single sensor element

200μm

10μm

Active area
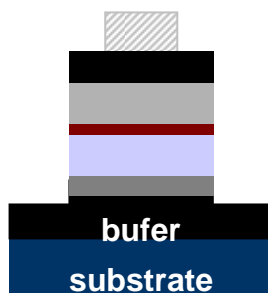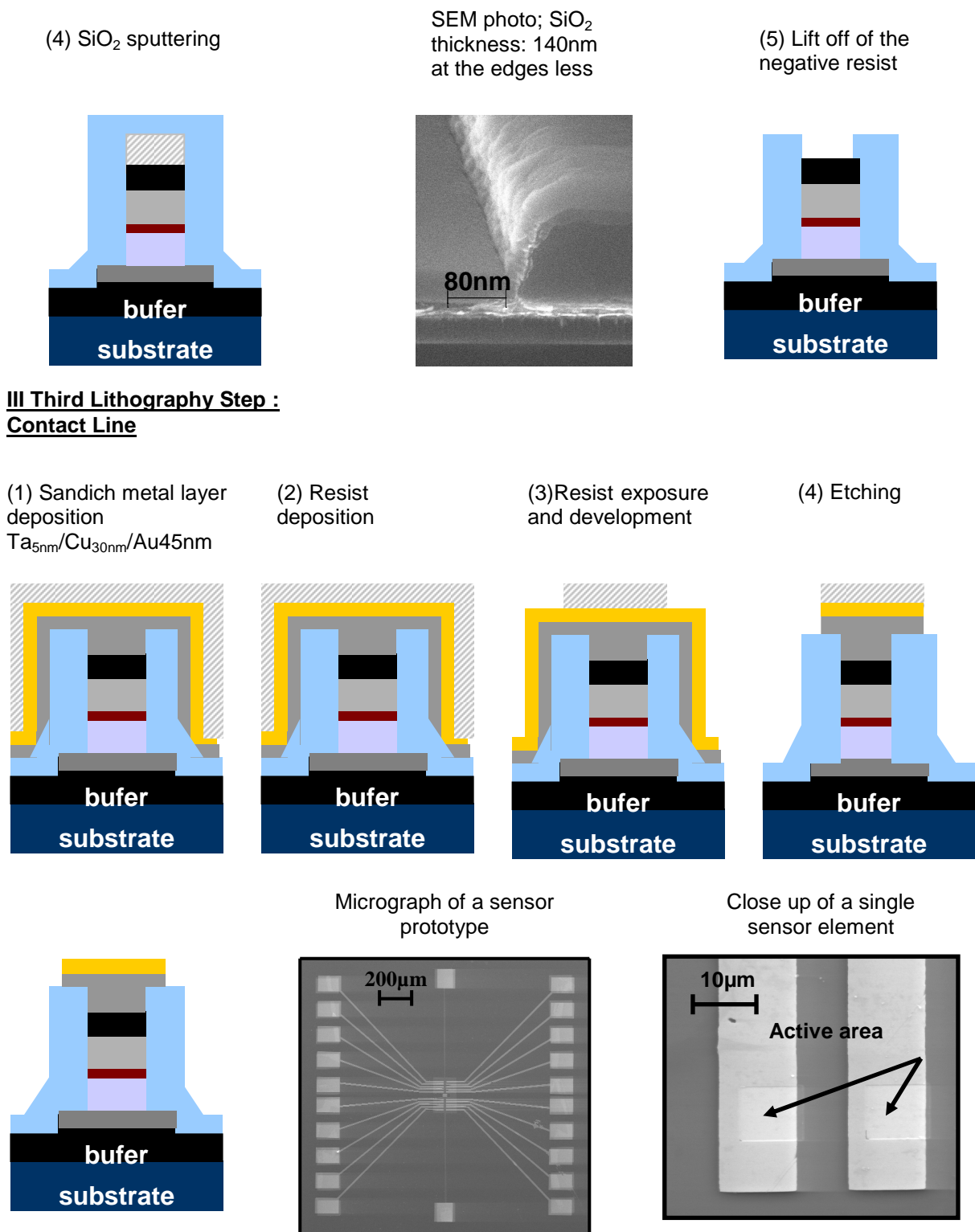
Figure 5.6 The stages involved in the pattering of MTJ sensor with
a negative resist.

5.2.2 Sensor characteristic

To characterizes the MTJ elements three measurements are carried out:

- major loop
- minor loop
- IV curve (electrical characterization of the tunneling barrier)

Figure 5.7 shows an example of the major loop and minor loops of the individual sensor elements.
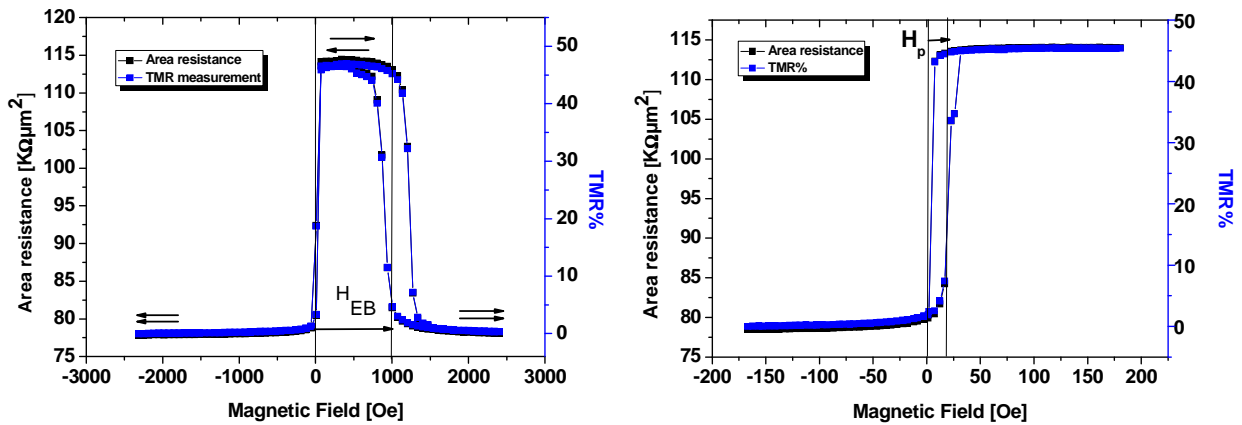
Figure 5.7 Electric measurements on TMR elements with an area of 10x10 μm^2 composed of $Ta_{6.5nm}/Cu_{30nm}/Ta_{19nm}/Py_{4nm}Co_{3nm}/ Mn_{83}Ir_{17\ (15nm)}{}^{/} Al_{1.4nm}/Ni_{80}Fe_{20\ (5nm)}/ Ta_{6.5nm.}$ (a) Major loop measurement (b) Minor loop measurement of deposit stack.

The major loop measurement in the Figure 5.7 (a) illustrates the changing magnetization of both magnetic layers. The Py layer switched its magnetization around zero field. The Co-Fe layer was pinned to an antiferomagnet and its hysteresis loop is shifted due to the exchange bias (for more details, see section 3.3.1). A large magnitude of the exchange bias field H_{EB} is necessary to obtain a good antiparallel alignment of the magnetic layers in an MTJ. In the investigated sample, the exchange bias field has a magnitude of around 1000 Oe. This field is enough to stabilize the antiparallel alignment of the magnetic layers. The switching between parallel and antiparallel orientations (magnetization of the layer indicated by narrows in Fig.5.7a) gives a maximal TMR ratio of 47% and area resistance between 0.78 to 1.15 $K\Omega\mu m^2$ at a bias voltage of 50mV. Across the sensor elements, the TMR ratios vary between 44.8% and 47.1% and the area resistance range from 0.76 to 0.78 $M\Omega\mu m^2$. The calculated average of the TMR ratio and area resistance is equal 46.7% $\pm$ 0.2 and 0.771 $M\Omega\mu m^2$ ± 0.2 respectively.

The Figure 5.7 (b) presents a minor loop, where only the magnetization of the soft layer (Py) is changed. From the experimental point of view, the minor loop characteristic is more important than the major loop. In the MTJ stack, the Co-Fe layer has a fixed direction, while the Py layer switches between parallel and antiparallel state. This is called the soft magnetic or sense layer, because only this layer can be affected by the stray field of the particle.

The antiparallel magnetization state in the MTJ stack may be strongly affected by magnetic coupling phenomena (see Section 3.3.2). Magnetic coupling exists on this example between the ferromagnetic layers due to magnetic dipoles at the interface. Ferromagnetic coupling counteracts the antiparallel magnetization state of the layers and makes this configuration unstable, which influences the TMR amplitude. In the MTJ stack, the orange peel coupling causes a ferromagnetic pinning of the Py layer to the exchange biased Co-Fe layer. In the Figure 5.7(b), the pinning field H_p has a magnitude of around 25 Oe.

As previously stated, to detect a particle, one has to look at the differences displayed in minor loop measurement with and without particles. For this reason, it is favorable for a Py layer to switch close to zero magnetic field [75]. The pinning field H_p can be compensated by an in-plane bias field or by increasing the thickness of the Py layer [75].

It should also be pointed out that a particle with a high magnetic moment is preferred for detection, because this particle can produce a large stray field, which can influence the Py layer.

The ideal working TMR elements should also have a thin insulating barrier. This barrier is characterized by the measurement of the conductance dependence on the applied bias voltage. Figure 5.8 (a) presents the area-specific current for parallel alignment of the magnetizations of the two ferromagnetic layers. This I/V curve is measured at an in-plane field of 2000 Oe and shows an ohmic behavior with a slight deviation from linearity.

The parameters for barrier height and thickness are determined in an indirect way using the BRINKMAN fit to the differentiated I/V plot [205].

Brinkam's models are based on two theoretical assumptions: the barrier has a trapezoidal structure and the boundaries between the metals and the barrier are assumed to be sharp.

The conductance G of the barrier is calculated by applying the Wenzel-Kramer –Brillouin Model (WKB). For a low voltage, the differential conductivity is express as a 2nd order polynominal:

$$G = \frac{dI_{total}}{dU} = A(\overline{\varphi}, d)U^2 + B(\overline{\varphi}, \Delta\varphi)U + C(\overline{\varphi}, d) \tag{5.1}$$

where $\overline{\varphi}, d, \Delta\varphi$ are the height of the barrier, the barrier thickness, and the asymmetry, respectively. The constant A,B, C parameters are determined experimentally from differentiated I/V plot fitted with the BRINKMAN formula (Figure 5.8 b).
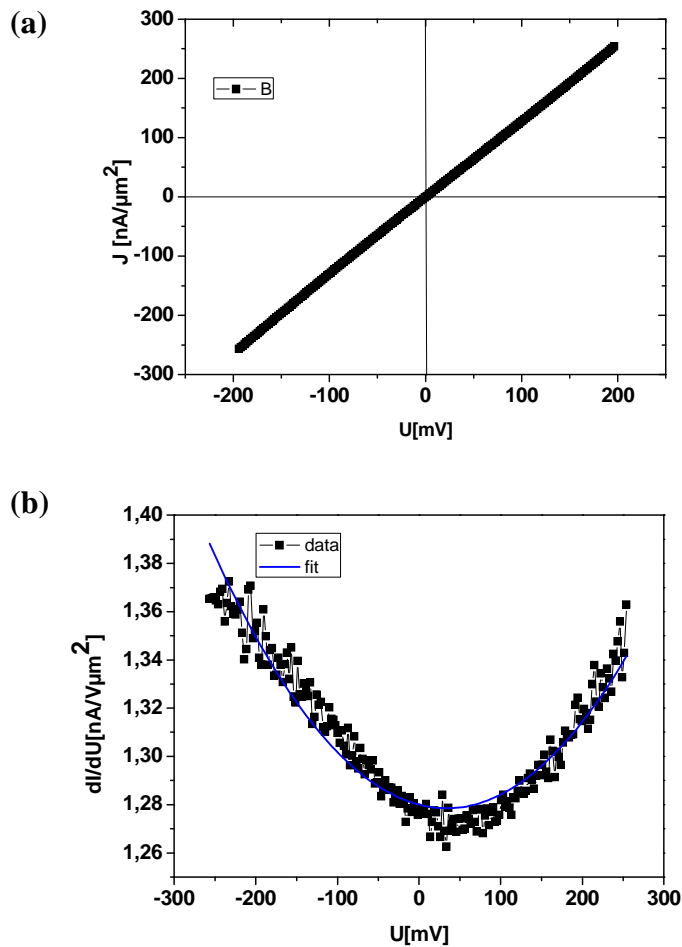
Figure 5.8 Electrical characterization of the tunneling barrier: (a) the IV curve (b) differentiated I/V plot.

The barrier parameters ($\overline{\varphi}, d, \Delta\varphi$) are calculated from the follow equations:

$$\varphi^2 = \frac{e^2 C}{32A}\left[\ln\left(\frac{h^3}{\sqrt{2}\pi e^3 m_{eff}} \cdot \sqrt{AC}\right)\right] \tag{5.2}$$

99

$$\text{d}= -\frac{\hbar}{8\sqrt{\varphi}m_{eff}} \cdot \ln\left(\frac{\hbar^3}{\sqrt{2}\pi e^3 m_{eff}}\right) \tag{5.3}$$

$$\Delta\varphi = -\frac{12\hbar\overline{\varphi}^{-\frac{2}{3}}B}{\sqrt{2m_{eff}}\,edC} \tag{5.4}$$

where m_{eff} is the effective electron mass ($m_{eff} = 0.4 \cdot m_e$) for the Al-barrier. For the curve presented in Figure 5.8 (b) the experimental $\overline{\varphi}, d, \Delta\varphi$ are verified:

$$\overline{\varphi} = 2.20 eV \pm 0.03$$

$$d = 1.708 nm \pm 0.009$$

$$\Delta\varphi = 0.68 eV \pm 0.02$$

The thickness of the barrier obtained from the Brinkman fit is equal to 1.708 nm. In the deposited MTJ stack, the Al film has a thickness of 1.4nm. After oxidization to amorphous Al_2O_3, the thickness of the barrier should increase to about 1.8nm. The experimental value 2.20 eV reaches around 51% of the maximum of the band gap of Al_2O_3 (4.35 eV). The asymmetry $\Delta\varphi$ is equal to 0.68 eV.

5.3 Detection Method

The detection capability of the magnetic tunnel junction sensor is tested with superparamagnetic particles with a diameter of 1.5µm from Micromod. The particles that are used in the experiments are silica particles (sicastar® -M), produced by hydrolysis of orthosilicates in the presence of magnetite. The properties of the particles are presented in Table 5.1.

DATA	Sicastar® -M
Prod.-Nr.	39-00-153
Prod.Name	sicastar® -M
Surface	-SH
Size	1.5µm
Solid Cont.	50mg/ml
Quantity	10ml
Shape	spherical
Density	2.5g/ccm

Table 5.1 Properties of 1.5µm sicastar® -M magnetic particles [192].

They exhibit a homogeneous distribution of magnetite in the silica matrix [192]. For the purposes of this experiment, the suspension of particles is diluted with DI water and distributed over the sensor surface (See figure 5.9).

(a)   **(b)**   **(c)**
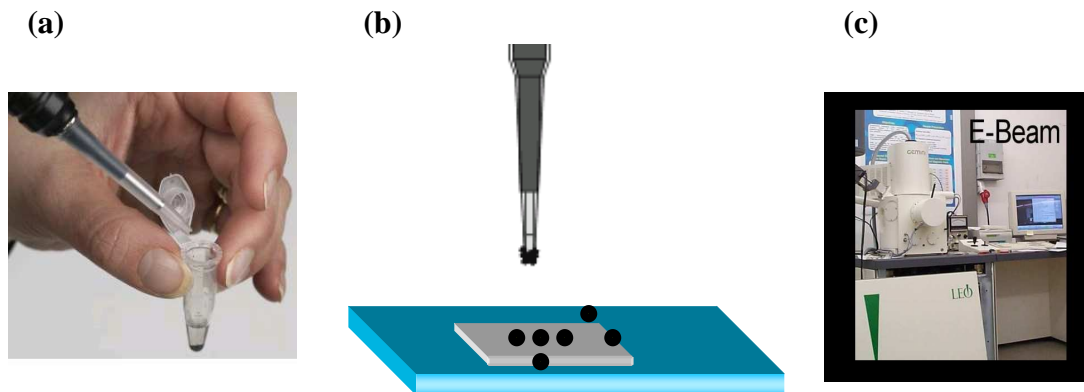
Figure 5.9 Magnetic particle distribution over the sensor surface:
- the particle solution are diluted in DI water
- particle are distributed over the sensor surface using micropipet
- the distribution of the particle on the sensor element is controlled using Scanning Electron Microscopy

Illustrations in figures (a) and (b) taken from [193].

When the water is evaporated, the particles agglomerate and form clusters on top of the sensor elements and around the contact lines (see Figure 5.10).
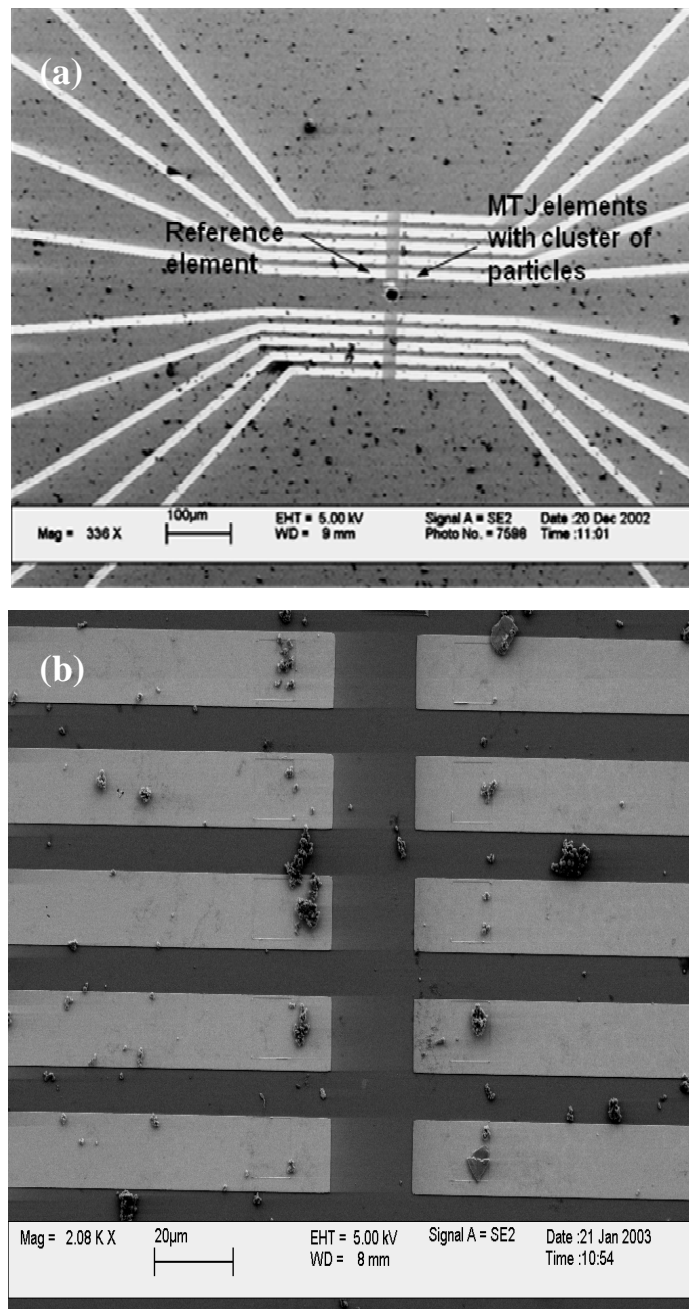
Figure 5.10 (a) SEM photo of the sensors with superparamagnetic particle 1.5µm
(b) Close- up of the sensor elements.

Even if the suspension of the particles is diluted to a different concentration, the particles display a tendency to cluster. The scanning electron microscope images shows that it is easier

to identify a cluster of magnetic particles than to find a single particle in the active area of the sensor. The SEM image is presented in the Figure 5.11.
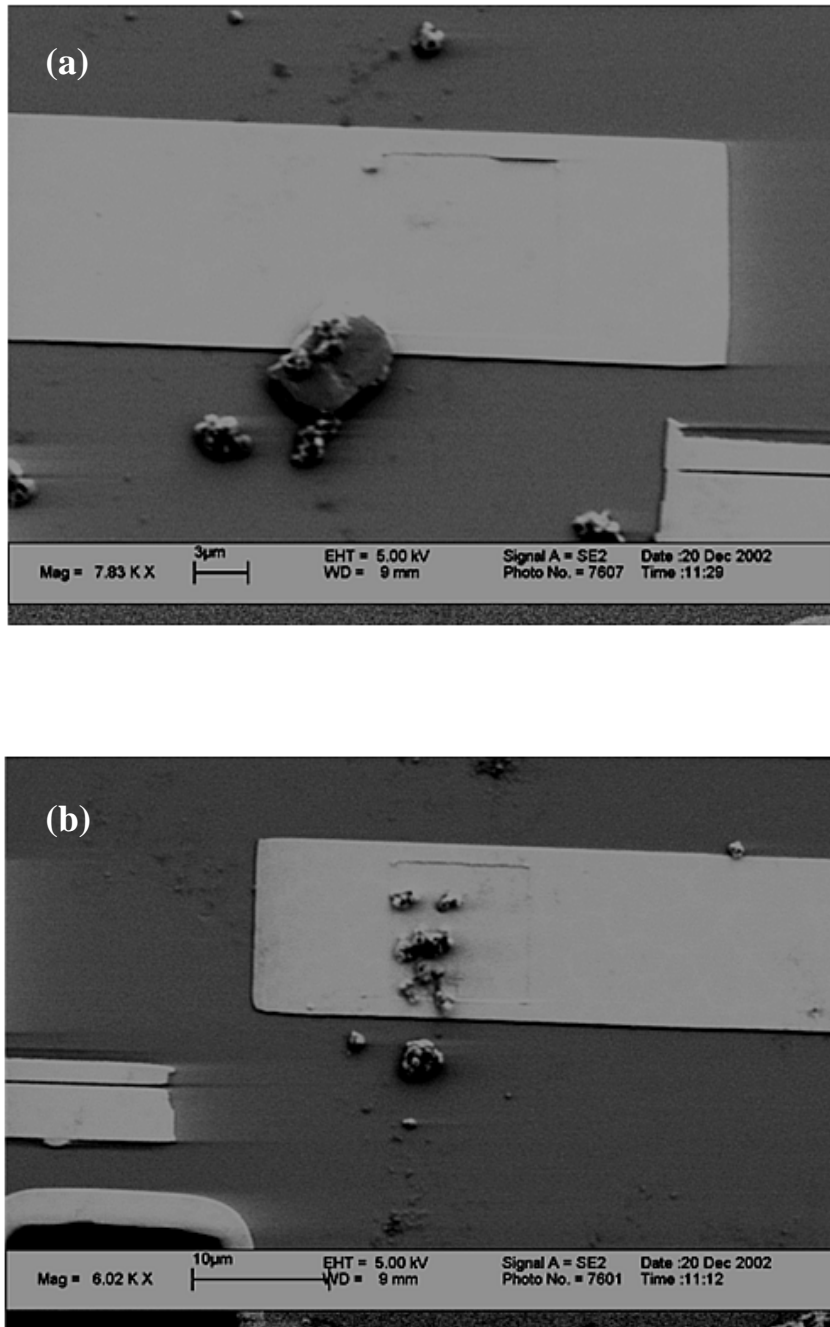
Figure 5.11 (a) SEM image of reference sensor elements ($10\times10\mu m^2$) without   magnetic particles. (b) SEM photo of a $10\times10\mu m^2$ MTJ sensor element with clusters of 1.5 µm particles (Micromod- Sicastar® -M).

An element without magnetic particles (Figure 5.11a) is also imaged under the SEM positioned on the same line as the sensor with clusters of particles (Figure 5.11 (b)).

The mentioned neighborhood of the elements is used to test the detection capabilities of the MTJ sensor.

After analysis under a microscope, the sample is placed in the set-up for TMR measurements. A description of apparatus can be found in Section 4.3, an illustration of the method used to detect the particles is presented in Figure 5.12.
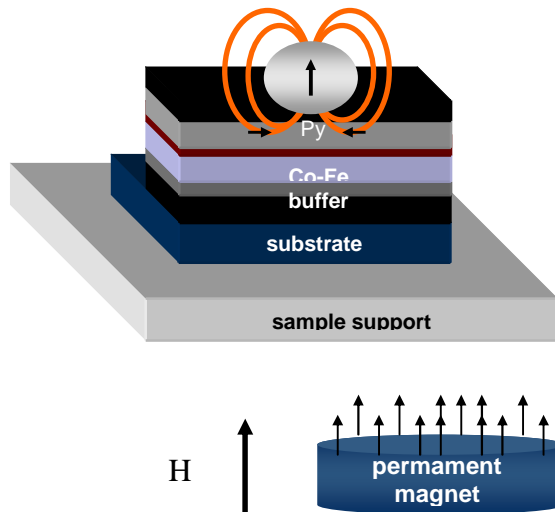
Figure 5.12 A method used to detect magnetic particles; an external magnetic field H is applied perpendicular to the surface plain, to magnetize the particles. The field is produced by a permanent magnet, which is placed directly under sample support.

To magnetize the particles, a constant magnetic field of 50 Oe is applied perpendicular to the sensor plane.

5.4 Experimental results

Figure 5.13 (a) shows a minor loop characteristic obtained for the reference sensor elements, presented in Figure 5.11 (a) i.e.without magnetic particles. The sensor shows that the TMR ratio is equal to 42.8% at room temperature at voltage of 50mV. The magnetic field is shifted along x-direction for a around 30 Oe due to the applied perpendicular field of 50 Oe (For comparison see the minor loop measurement of other sensor elements obtained without perpendicular field and presented in the figure 5.7).

Because the suspension of magnetic particles can destroy the sensor elements, the minor loops characteristic is also measured after coating. Figures 5.13 (b) and 5.14(c) show this measurement.

(a)
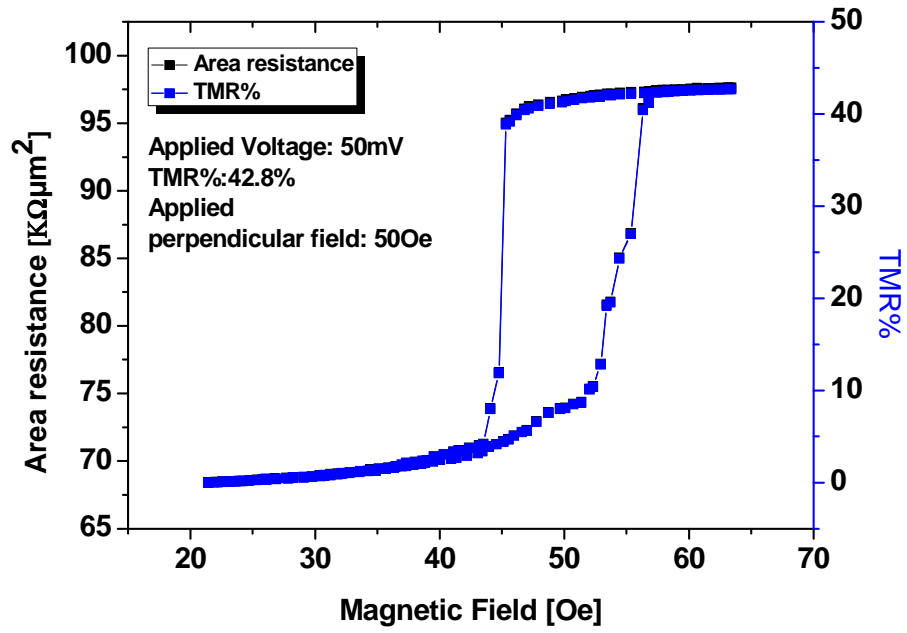
(b)
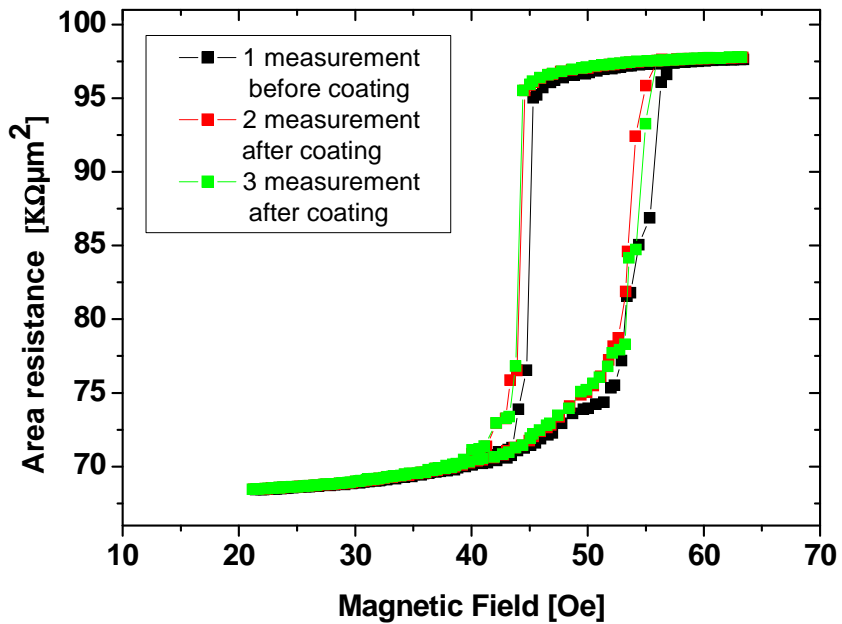
(c)
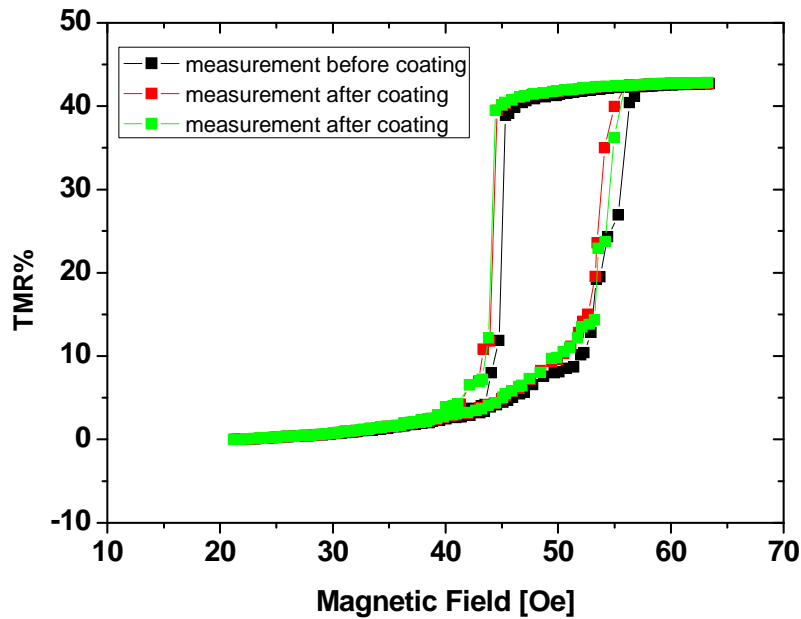
Figure 5.13 (a) Minor loop measurement without magnetic particles-reference measurement (b) and (c) series of minor loop measurement taken before and after coating of the MTJ reference sensor element. The magnetic field is shifted along x-direction for a around 30 Oe due to the applied perpendicular field of 50 Oe.

As shown in Figure 5.13 (b) and (c), the reference sensor elements display the same characteristic and maintain a high magnetoresistance. Small differences are visible in the minor loops. The same situation is observed for an MTJ sensor element with cluster of magnetic particles presented in Figure 5.11(b). Figure 5.14 shows the minor loop characteristic for this element before and after coating with a drop of magnetic particles.

(a)
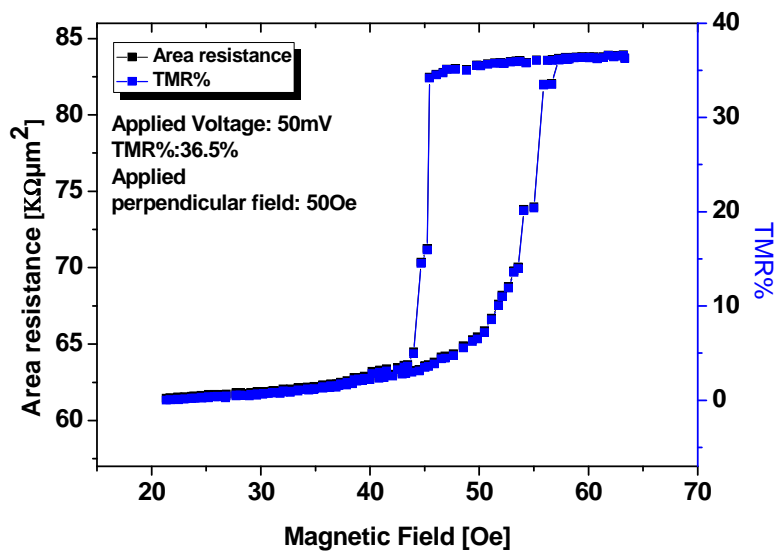
(b)
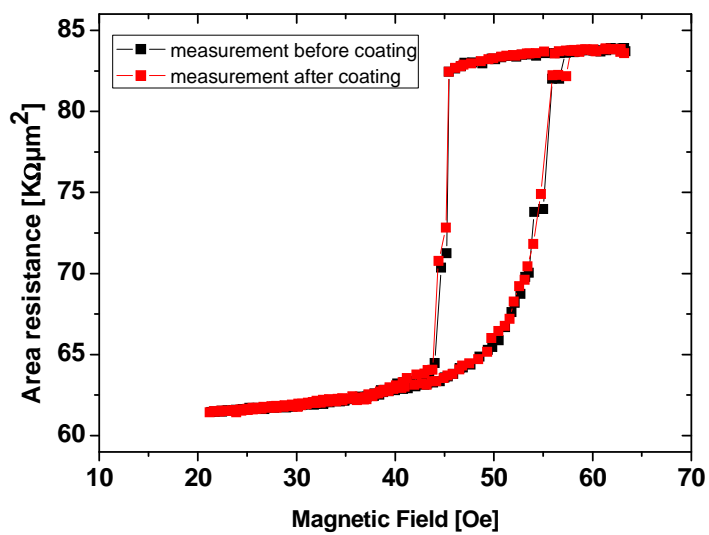
(c)
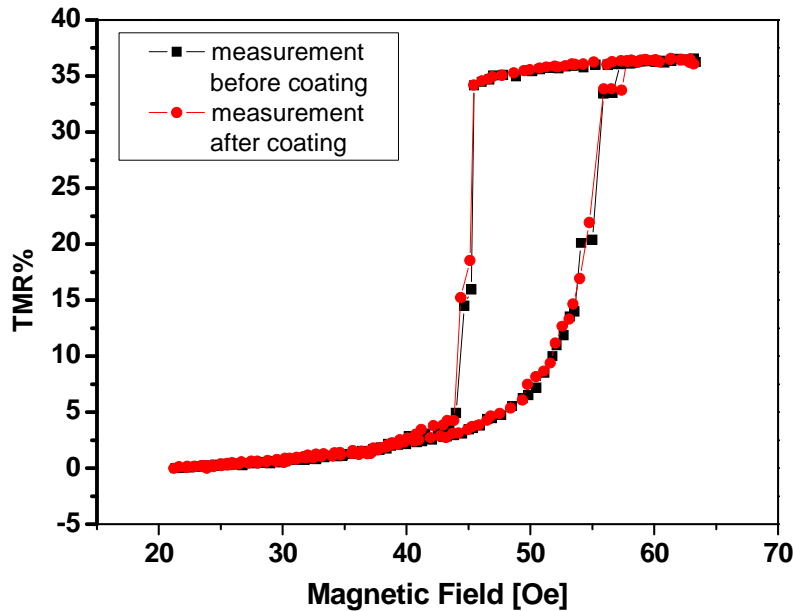
Figure 5.14 (a) minor loop measurement for sensor element with clusters of magnetic particles. The measurement is taken before coating.(b) and (c) Series of minor loop measurements taken before and after coating of the MTJ sensor element.

In this case, no differences were observed in the transport measurement. The suspension of magnetic particles did not influence the sensor characteristic. The differences in the minor loops domain were very small in comparison to the measurement presented in Figure 5.13. The TMR ratio is equal 36.5%, which was smaller than that of the reference element presented in Figure 5.13 (a). The average TMR ratio among the elements in a wafer is about 42%. The observed reduction of the TMR ratio can be due to the sample impurity, for example remaining resist.

The minor loop measurements for the reference elements and for the elements with magnetic particles are normalized and compared in Figure 5.15.
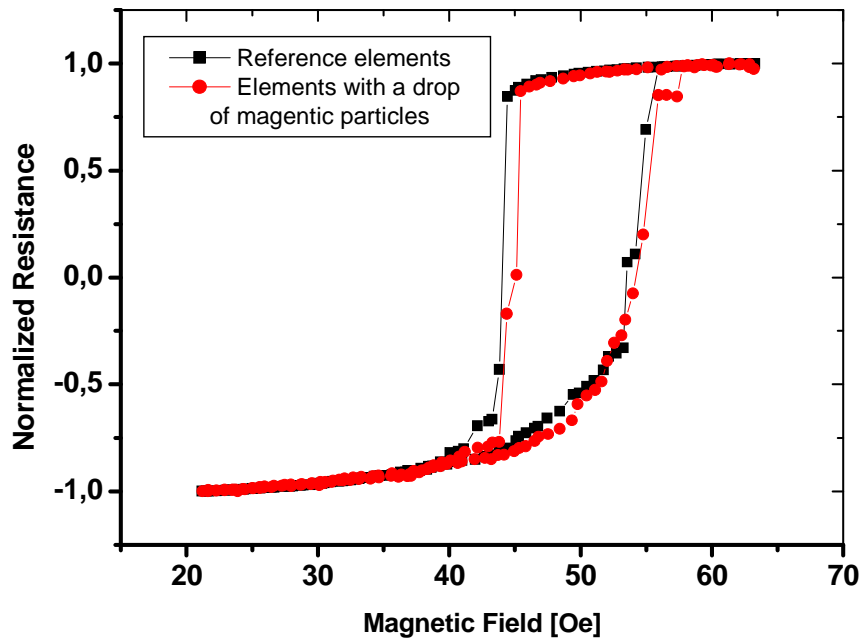
Figure 5.15 Normalized minor loops characteristic of the two sensor elements.

As shown, there are nearly no differences in the transport measurement. The reference elements and the sensor element display nearly the same minor loop characteristics. Only small differences are observed close to the switching fields. The switching field and saturation field are nearly the same for both minor loop characteristic.

5.5 Discussion and conclusion

This chapter describes a quantitative method used for single magnetic particle detection. A suspension of magnetic particles is dispersed over the sensor surface with a position control using a scanning electron microscopy (SEM).

Several problems arise when attempting to use this method of magnetic particle detection. As shown in the experiments, even if the particles are 1.5µm and are being classified as large particles, it is difficult to isolate a single magnetic particle, which is precisely positioned on top of the sensor elements.

The particles show a strong tendency to agglomerate and to form clusters. This occurs in response to interparticle magnetic dipole interactions.

The magnetization of the particles presents another problem. In these experiments we did not observe any influence of the stray field of magnetic particles on the sensor characteristics. The ideal magnetic particles for sensor application are single-domain ferromagnetic nanoparticles with a large magnetic moment, which are stable in aqueous solution and do not aggregate [75]. These particles are not available commercially and are thus produced primarily for research proposes [194].

This quantitative method of single particle detection did not deliver reproducible results. The particles will never be positioned exactly in the same location on top of the sensor elements. This exact positioning can only be achieved when the size of the sensor element matches the size of the particle. But this would also create a problem with particle positioning and agglomeration.

In conclusion, to prove the detection sensitivity of the MTJ sensor to the level of a single magnetic particle or molecule, we need a method for exactly positioning the particles in specific predefined locations, with the magnetic particle having a high magnetic moment. Such particles are not produced commercially and therefore the behavior of these particles needs to be modeled, as is described in the next chapter.

6. Model experiments for single magnetic particle detection

This chapter presents model experiments that are carried out in order to understand the behavior of MTJ sensors in the presence of a single magnetic marker. The magnetic particle is modeled by a magnetic tip of an atomic force microscope. The tips are coated by a hard magnetic stack (Ta/CoCr/Co/Ta) and magnetized perpendicular to the sensor plane prior to the measurements. The advantage of this model setup is that the tip can be placed onto any site of the MTJ element with nanometer accuracy. While the tip position onto the top of the sensor is varied, the sensor clearly indicated different responses. The experimental results are compared to micromagnetic simulation.

6.1 Sensor fabrication

MTJ sensors are fabricated with a hard and soft architecture. The hard magnetic electrode consist of a 3nm thick Co layer which is exchange biased to a 15 nm thick layer of the antiferromagnet $Mn_{83}Ir_{17}$. The soft magnetic electrode is the single 5nm thick layer of Py. The insulating barrier consists of a plasma-oxidized Al layer, 1.4nm thick. A buffer layer $Ta_{6.5nm}/Cu_{30nm}/Ta_{19nm}/Py_{4nm}$ is underneath the hard magnetic electrode, which is used as a seed layer and as an etch stop for lithography purposes. The soft magnetic electrode is covered by a 6.5 nm thick Ta protection layer and a 30nm Cu for line connection. All layers are deposited by magnetron sputtering onto Si-wafer substrates with a 100nm thick thermal oxide in a HV-chamber (Leybold CLAB 600) at a base pressure below $3x10^{-7}$mbarr. The samples are annealed in a high vacuum chamber with a base pressure below $1x10^{-7}$mbar up to 270°C for 10 minutes in an external magnetic field (1000 Oe) to setup the exchange bias. More details concerning the preparation process can be found in the chapter 4.

The layer stack is patterned to 10 µm x 10µm sized square elements using e-beam lithography and Ar ion etching. The layout with the conduction line on the top and bottom contact of the sensor elements is presented in Figure 6.1.
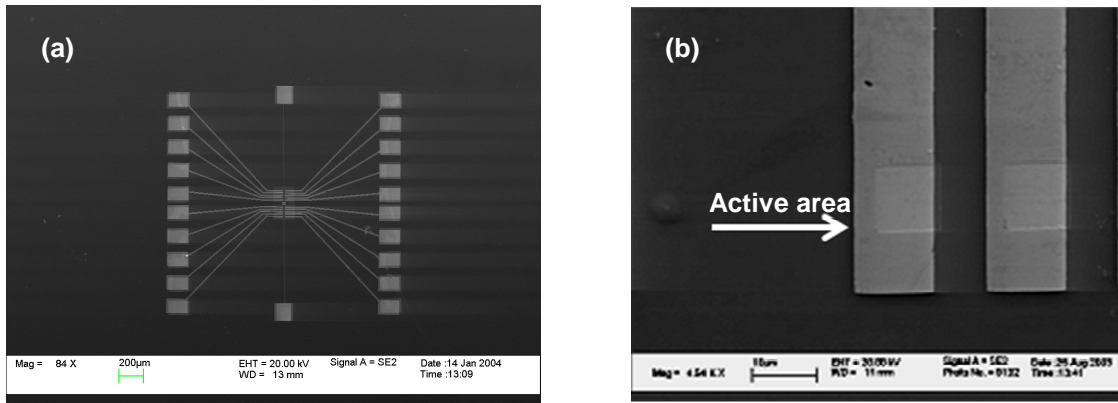
Figure 6.1 (a) Micrograph of a sensor prototype, which consists of 20 sensor element.

(b) Close up of single sensor elements with conducting lines.

Prior to the measurement the fabricated sample is glued with two components glue to a homemade non-magnetic socket. The commercially available sockets are usually magnetic, thus they cannot be used for the experiments with MFM tips. The contact pads of the sensor are wire bonded to the pads of the socket.

The socket pads required an additional preparation procedure. They are fabricated using mask- lithography. The mask is made from 1mm thick aluminum and is fixed on the silicon wafer using double stick tape. The Ta_{5nm}/Au_{200nm} sandwich layer for the contact pads is deposited through the mask onto the substrate in a UVH homemade chamber. When the sputtering process is finished, the sample is cut in to the correct dimension and glued on the socket using two components glue. The pads are contacted to the socket using copper wire. The whole procedure is illustrated in Figure 6.2.
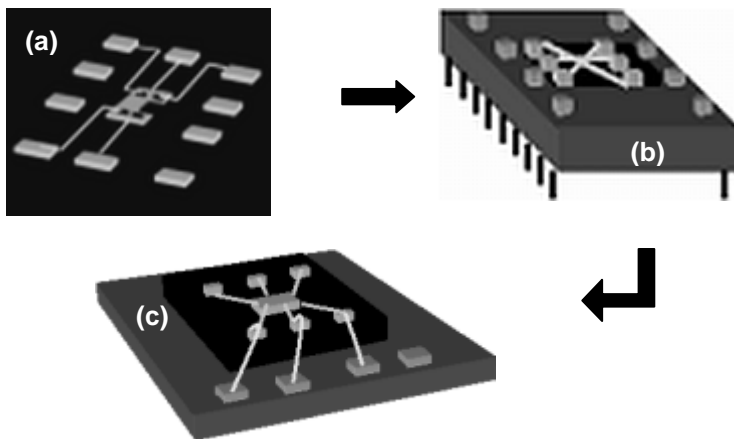
Figure 6.2 Sample preparation
- (a) the sample with sensor array is cut in correct dimension
- (b) the sample is fixed with two components glue on the home-made socket
- (c) the contact pads of the sensor are wire bonded to the socket pads

6.2 Sensor characterization

After preparation, the socket with the sample is placed in a measurement set-up. During the measurement, BNC cables of the amplifier are attached to the socket. The output of the sensor is measured with a dc bias voltage of 10 mV in an adjustable external magnetic field generated by two orthogonal pairs of Helmholtz coils (Figure 6.3 a).
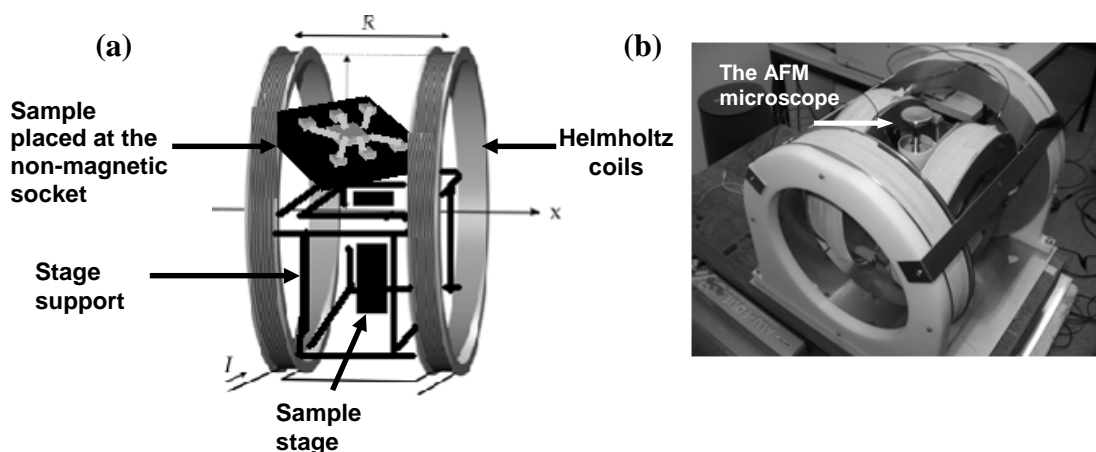
Figure 6.3 Illustration of the set-up used for the transport measurements.

        (a) the sample is placed inside the Helmholtz coils on the support

        (b) the AFM microscope is assembled in to the transport measuring system

When applying a small field in the pinning direction, the magnetization direction of the free magnetic layer switches, and the electrical resistance of the sensor increases by 30%, which is presented in Figure 6.4. Even if the TMR amplitude is lower than the expected value (50%), the fabricated sensor is sensitive enough and exhibits a reproducible characteristic.

During scanning, the current flowing through the elements is monitored by a current to voltage converter with adjustable sensitivity (1µA/V to 1nA/V).
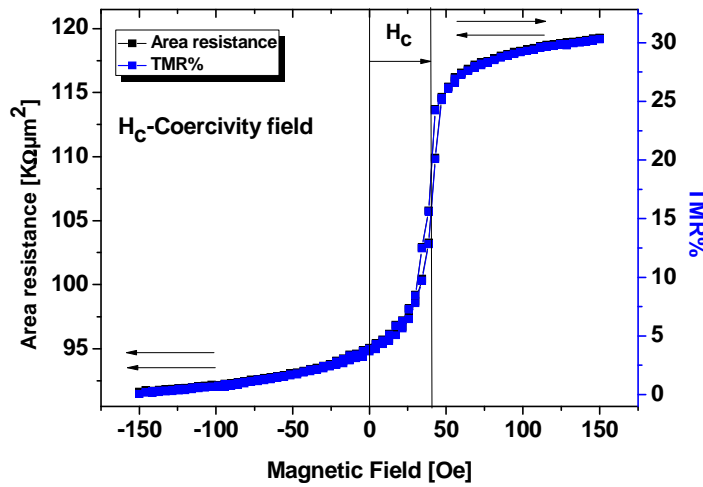
Figure 6.4 Minor loop of a 10x10µm^2 sensor element. The arrows indicate the relative magnetization orientation of the soft-bottom and hard-top magnetic layer.

6.3 Detection method and measurement

For the purposes of this experiment, an AFM tip is coated by a hard magnetic layer stack $Ta_{5nm}/CoCr_{90nm}/Co_{2nm}/Ta_{5nm}$ in a DC magnetron sputtering system and magnetized perpendicularly to the sensor plane.
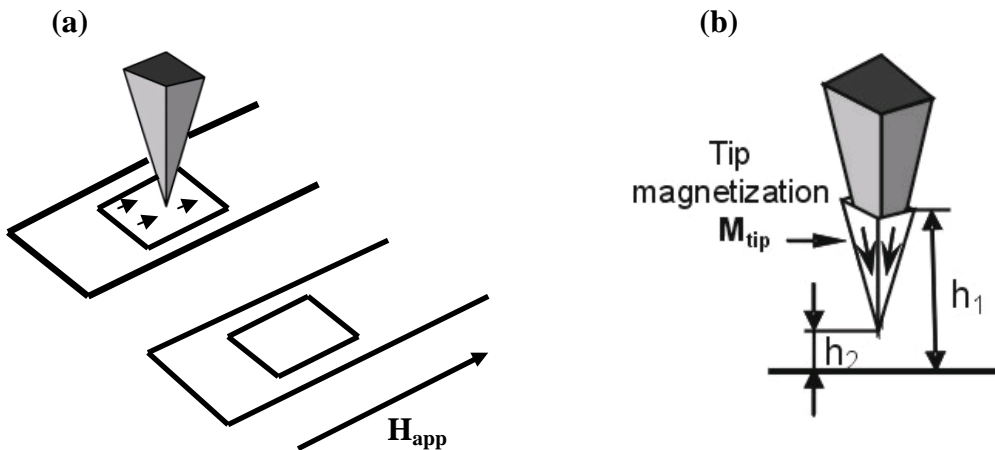
Figure 6.5 (a-b) A magnetic marker is modeled by a MFM tip. The tips are coated by the hard magnetic layer stack Ta/CoCr/Co/Ta in a DC magnetron sputtering system and magnetized perpendicular to the sensor plane. Illustration of the tip in figures (a) and (b) taken from [206].

Since magnetic cantilever tips as used in magnetic force microscopy exhibit a dipole-like magnetic stray field, this easy setup allows to model the presence of a single magnetic particle [195]. In addition, it offers the great advantage that a tip can be placed at any desired site on top of the MTJ sensor element in certain distance.

In this experiment the AFM microscope with the MFM tip is assembled into the transport measuring system with the Helmholtz coils (Figure 6.3 b) and two different measurements are carried out:

- topography and simultaneous magnetoresistance (MR) mapping at a constant magnetic field,

- MR curves at a fixed tip position with a varying magnetic field, either rotational with constant field magnitude or axial in a fixed direction.

6.3.1 Magnetoresistance (MR) map of the MTJ sensor

Figure 6.6 shows an example of the topography of two sensor elements and the simultaneous MR map of the contacted MTJ sensor. The color table represents a certain resistance range. The additional regular oblique stripe pattern is due to electronic noise, and not of interest. No external magnetic field other than the tips stray field is applied in this case. Thus, the MTJ element can be easily identified on the map. It is obvious from this measurement that the resistance of the sensor element increases under the influence of the tip.

(a)   **(b)**
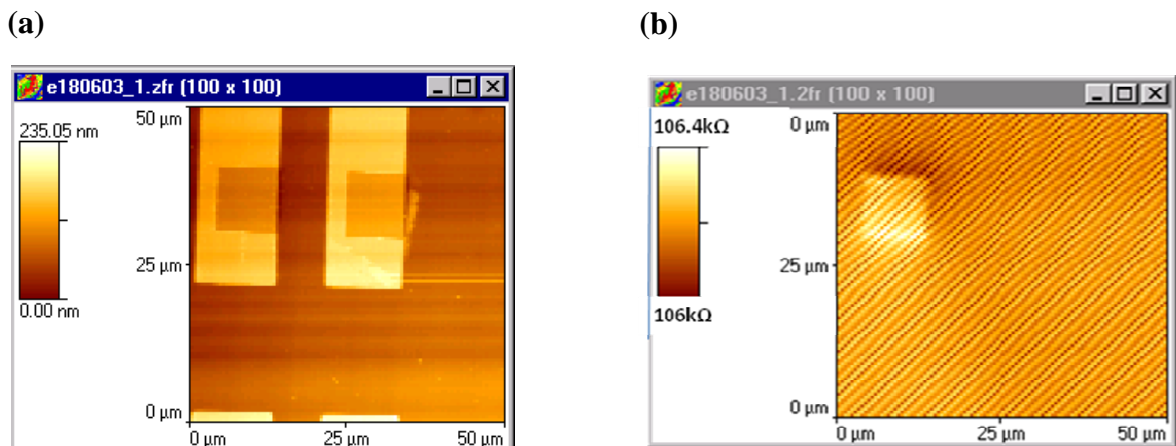
Figure 6.6 (a) Topography of two sensor elements (also showing contact lines) (b) Simultaneous resistance map of the left sensor element, which was connected, at zero external fields.

The MR maps presented in Figure 6.7 are taken at an additional homogenous magnetic field oriented to the vertical axis (in map coordinates) of the MTJ. The maps of the sensor responses are distinctly different for various fields. At field of 40 Oe, which corresponds to the coercivity field (cf. Figure 6.4), dark and bright contrasts indicate changes in the MR. The dark spots are associated with a lower resistance and the bright spots with a higher resistance. At this field, the dark and bright spots are roughly equally distributed, but in opposite corners of the sensor element. A noticeable change is also observed at fields lower ($H<H_c$) and larger ($H>H_c$) than the coercive field. At $H<H_c$, the bright spots are dominant, and the dark spots at $H>H_c$ (Figure 6.7).These facts indicate a partial, local reversal of the magnetization of the soft magnetic layer in those field ranges and at these locations.

(a)

(b)

0 Oe

(c)

(d)

10 Oe

20 Oe

(e)

(f)

30 Oe

35 Oe

(g)

(h)

40 Oe

45 Oe

(i) 50 Oe / 35 Oe

(j) 55 Oe

(k) 60 Oe

(l) 65 Oe

(m) 70 Oe

(n) 120Oe
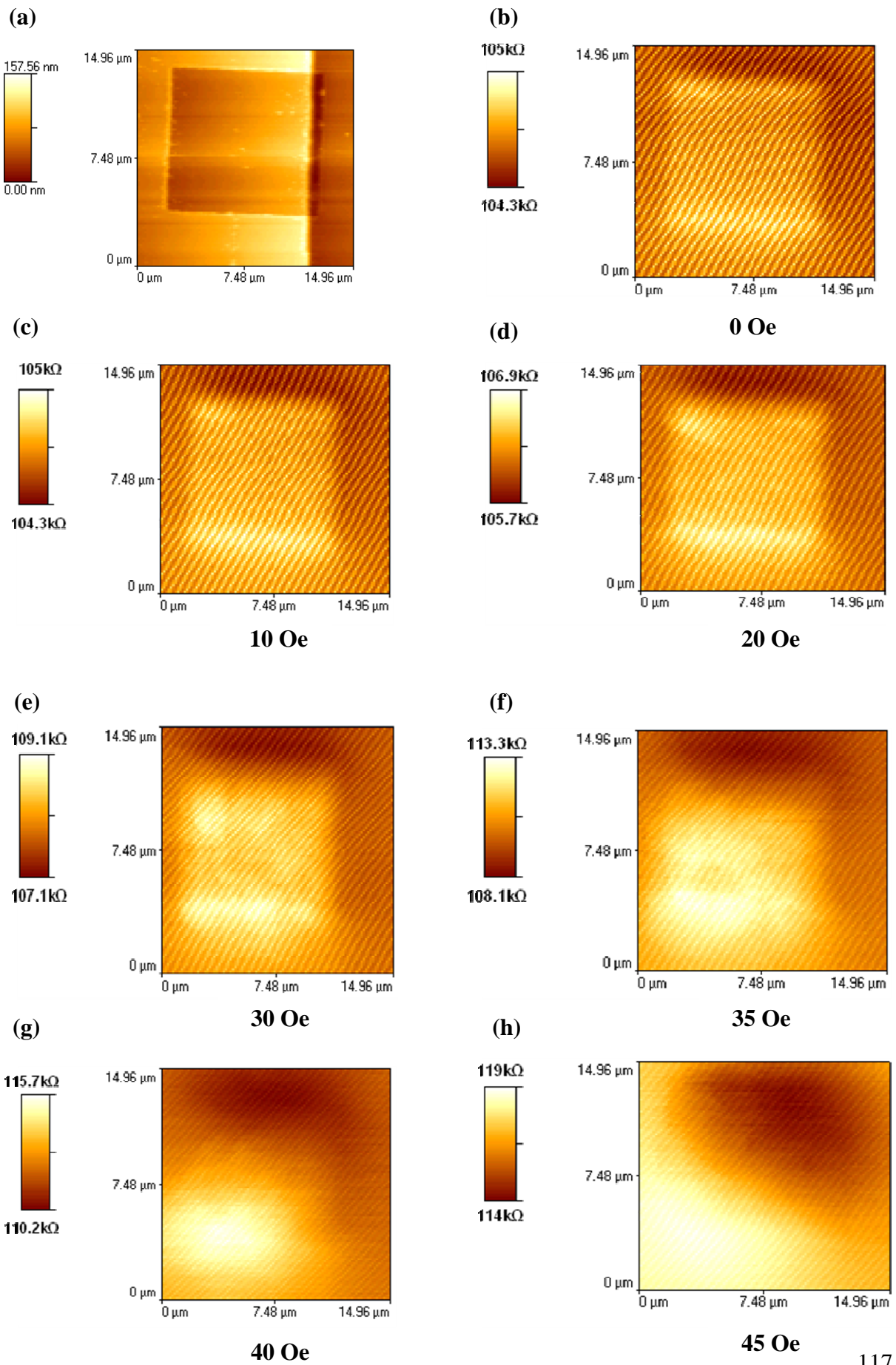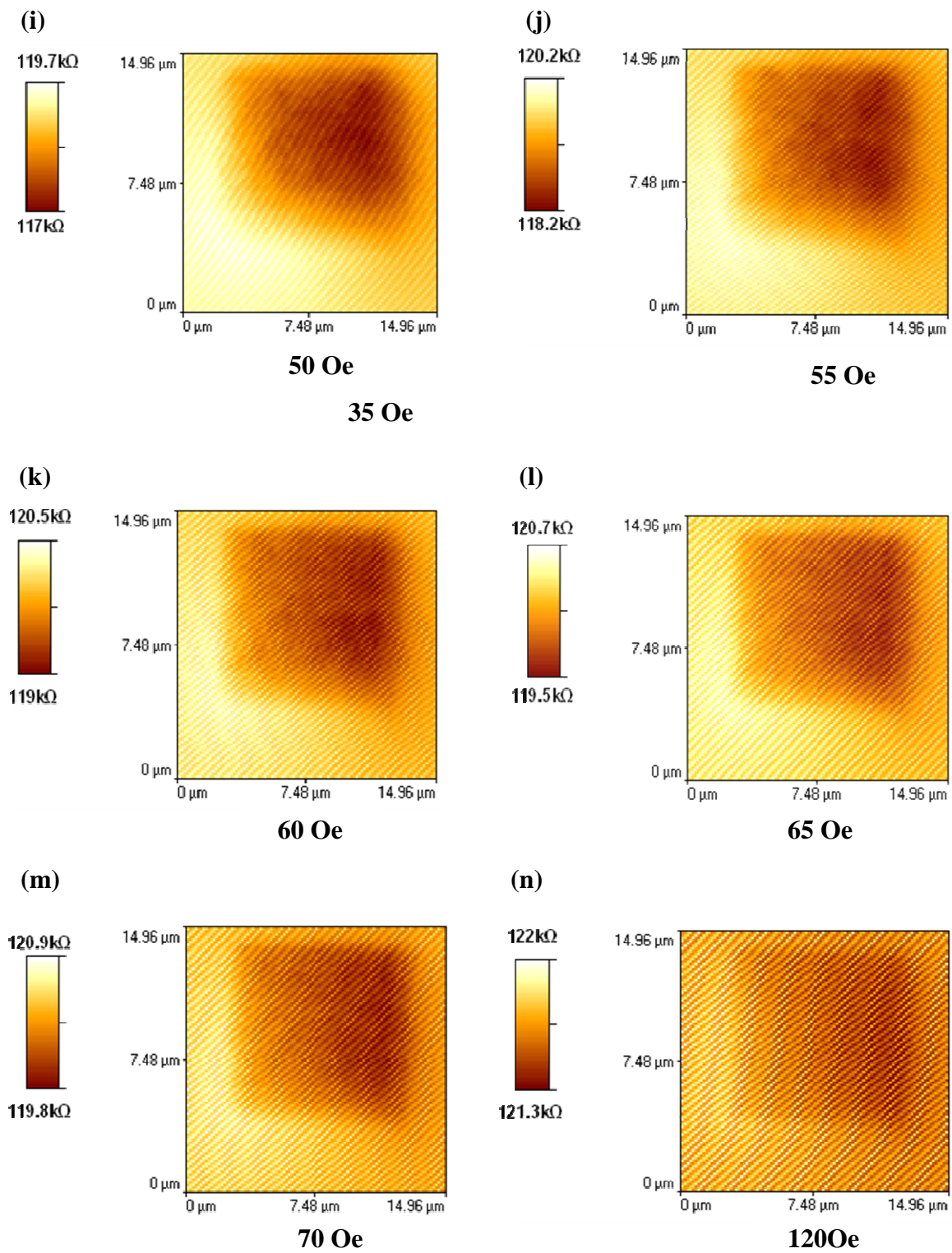
Figure 6.7(a) Topography of a single MTJs (b)-(n) Magnetoresistance map at different magnetic field; For discussion see text.

_____

Below the coercivity field, the magnetization pattern reorients locally at the tip site and turns from the parallel to the antiparallel. Therefore a higher resistance is observed in this case (bright spots). Above the coercivity field, a tendency to align in the parallel orientation is observed, and the resistance decreases (dark spots).

6.3.2 Transport measurement at fixed tip positions

The results presented in Figure 6.7 are correlated to the transport measurement at fixed tip positions. Here the tip is placed at specific positions on top of the sensor elements (Figure 6.8), and then minor loops are measured. As expected from the measurements presented in Figure 6.7, large differences in the minor loops are measured for the tip positioned in the lower left and upper right corner. In Figure 6.8, the curves b and c are obtained in the presence of the magnetic tip in the indicated positions: lower corner-position 7 and upper corner –position 19, while the reference curve a is taken in absence of the tip. The loops in case b and c are shifted with respect to the reference curve due to differences in the domain configuration. Curve (b) switches at lower fields than the reference curve. The reversed situation is observed for curve (c), where the switching field has been increased.

(a)   **(b)**

(c)
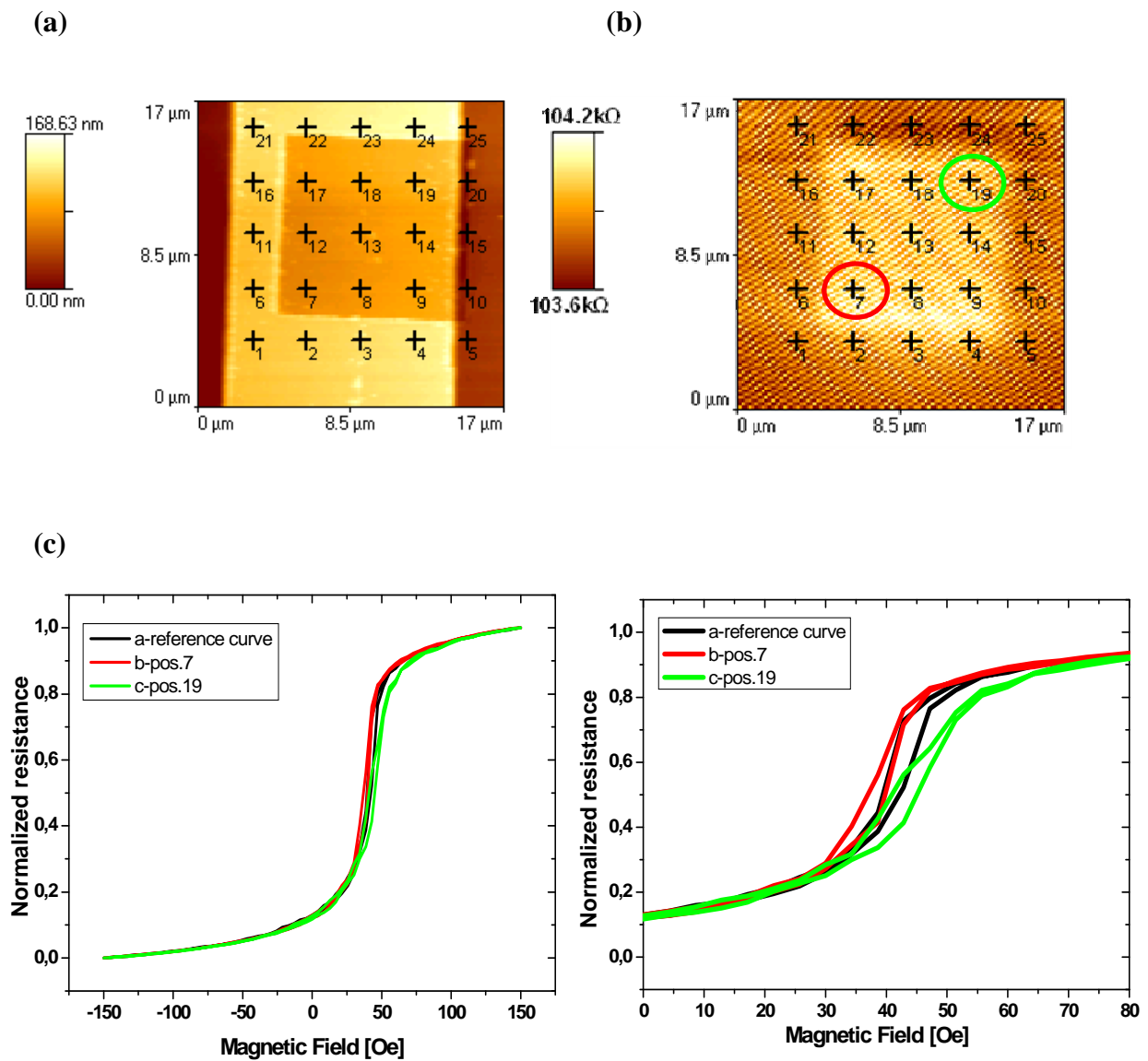
Figure 6.8 (a) Topography (top) and MR image of a sensor element with indicated positions (b) Minor loops for three positions of the magnetic tip: a- reference curve, b-at the position 7, c-at the position 19.

When the tip is located in the center of the rectangular sensor elements, the experimental curves shows a flatter slope in the presence of the magnetic tip (Figure 6.9). Although the differences are small, the tendency is distinct throughout all measurements that the slope is flatter if the tip is located centrally. This tendency is also reproduced by the simulation (Section 6.4).

(a)

(b)

(c)

(d)
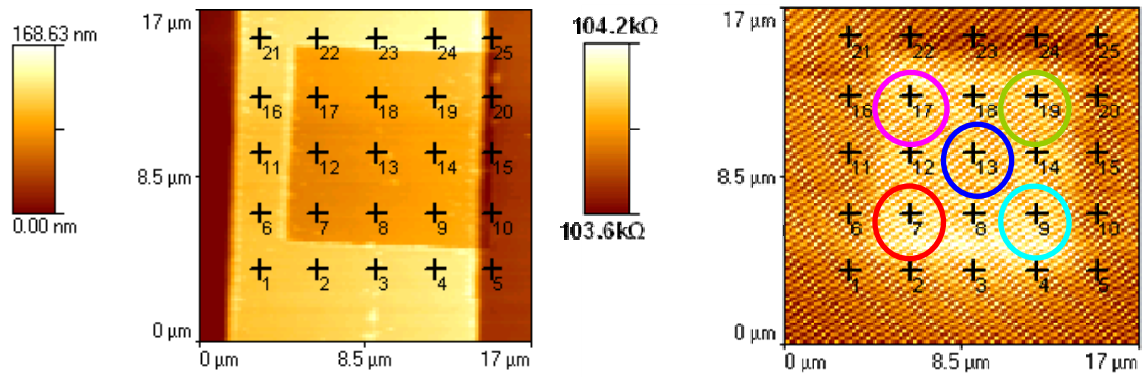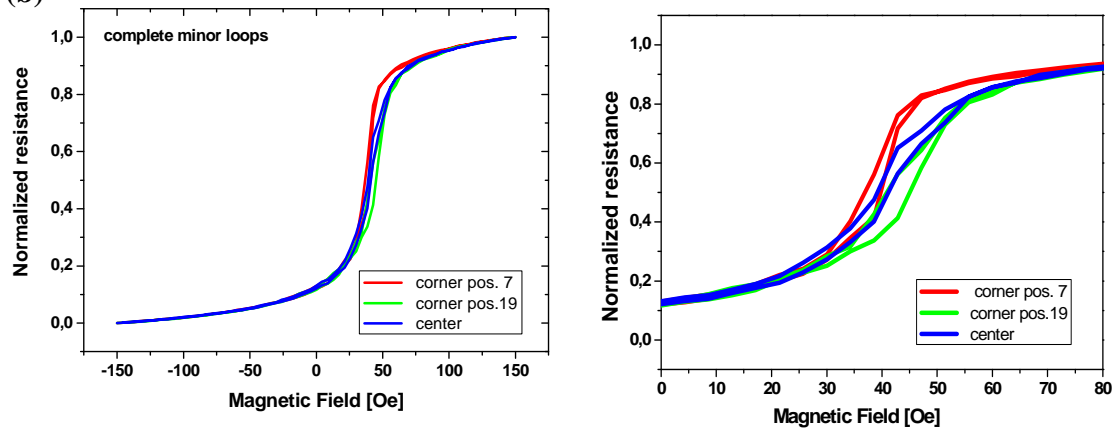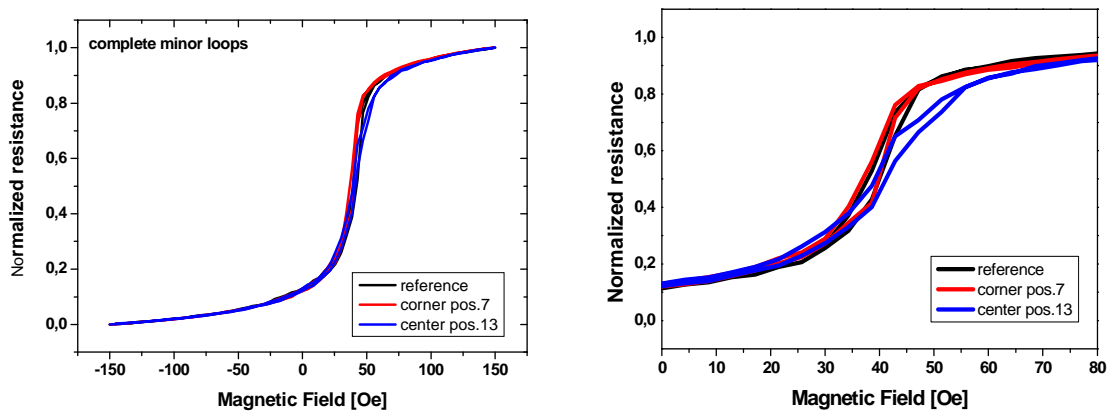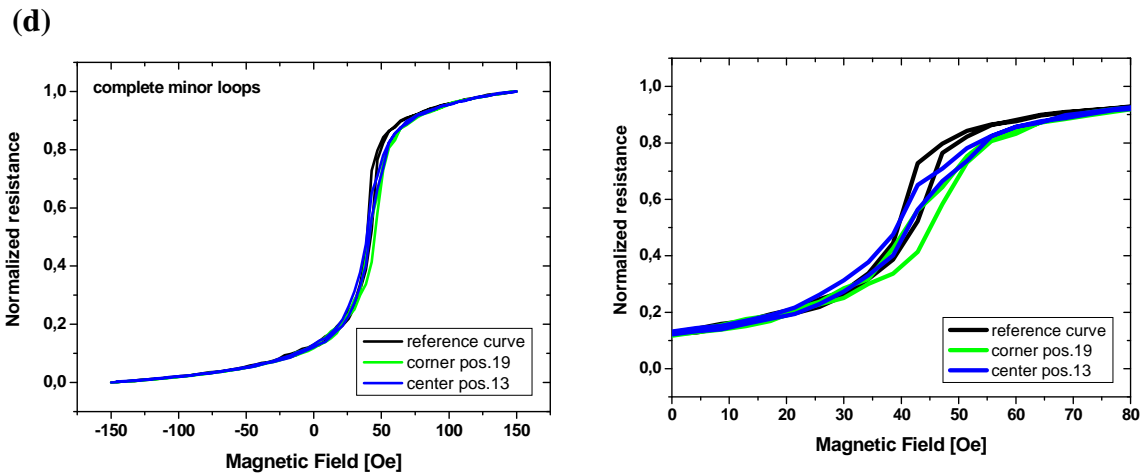
Figure 6.9 (a) Magnetoresistance map of the sensor elements with indicated position
(b-d) Experimental minor loops in presence and absence of the magnetic tip.

If the tip is placed in the corners opposite to those of Fig.6.9, indicated on the map in Figure
6.9 (a) by number 9 and 17, the differences in the minor loops are much smaller than for the
minor loops measured at the position 7 and 19 (Figure 6.10).

It is in a good agreement with MR maps presented in Figure 6.7. The position 17 and 9 are
placed on the line on the MR maps, where the differences in the measured resistance are
small. This is especially observed in the MR resistance maps measured at the coercivity field
(40Oe).

(a)

(b)
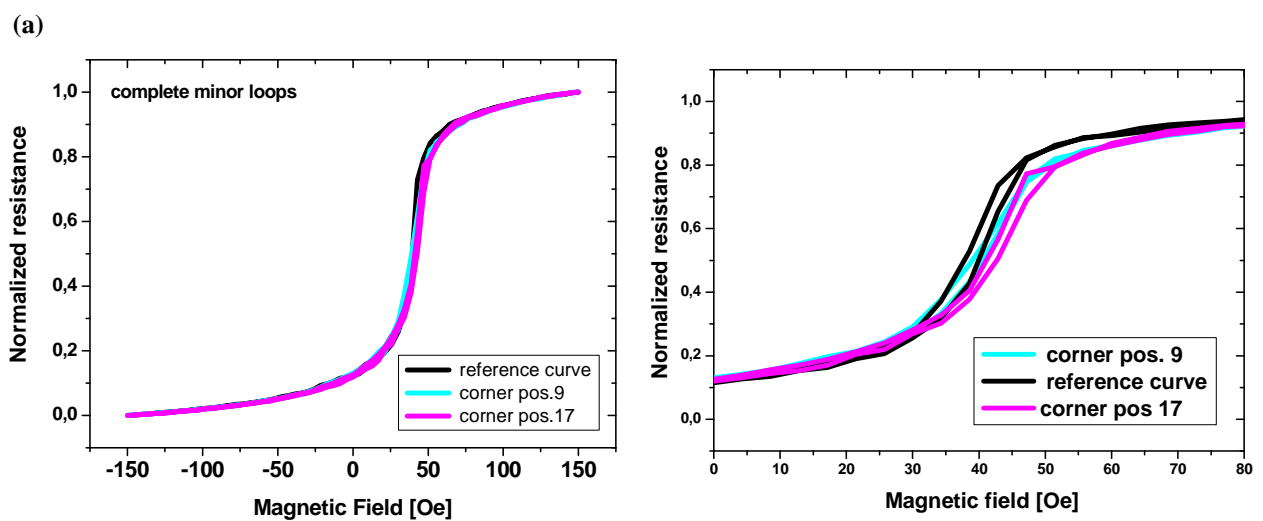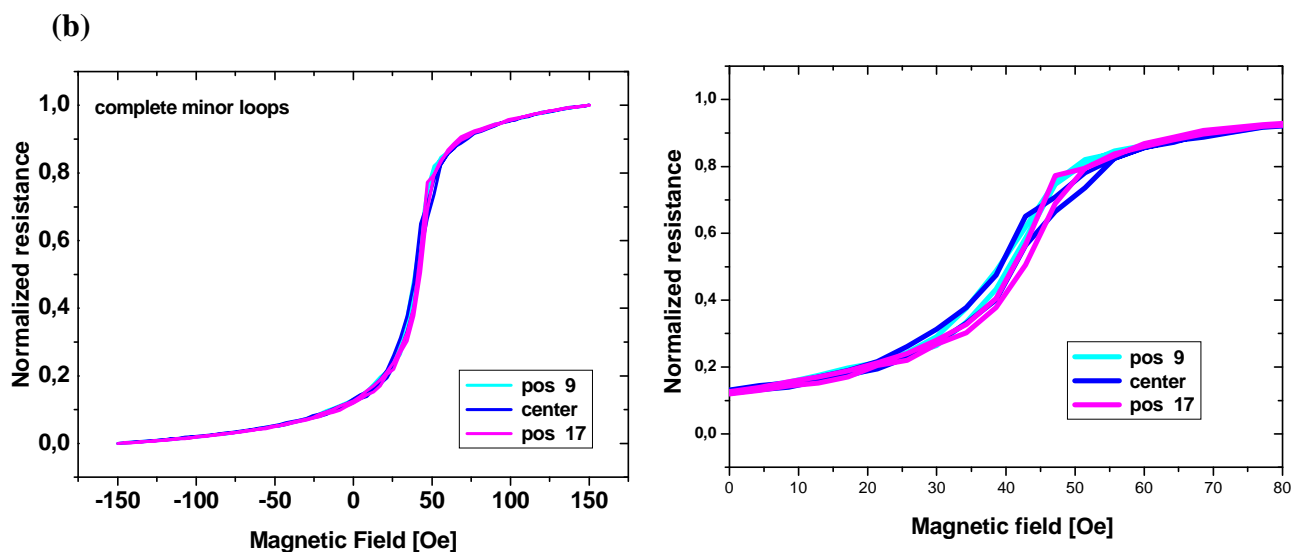
Figure 6.10 Experimental minor loops in presence and absence of the magnetic tip
at various positions of the magnetic tips: (a) lower and upper corner and without tip
(b) lower and upper corner and center

In Figure 6.10 (a), the curves corresponding to the position 9 and 17 are shifted with respect to the reference curve, but both curves in this figure show switching at large field than the reference curve. The curve corresponding to the position 9 switches earlier than the curve, plotted for the position 17. The curves show also a flatter slope if the tip is located centrally. (Figure 6.10 b), but in comparison to the Figure 6.9 b, the differences in the measurement are smaller.

Another situation is observed for the tip positions indicated by the number 8, 7, 12 and positions 18, 19, 14. The minor loops corresponding to that position are presented in Figure 6.11. Here, in Figure 6.11(c) the differences in minor loops are rather small and the same situation is for the measurement presented in Figure 6.11 (d), but the slope of the curves in Figure 6.11 (d) is more flat. The differences in minor loop are larger in the figure 6.11(e) and 6.11(f), which correspond to the position 8,9,14 and 12,17,18.

(a)

(b)

(c)

(d)

(e)

(f)
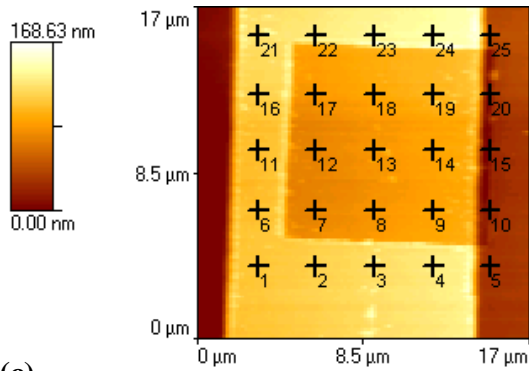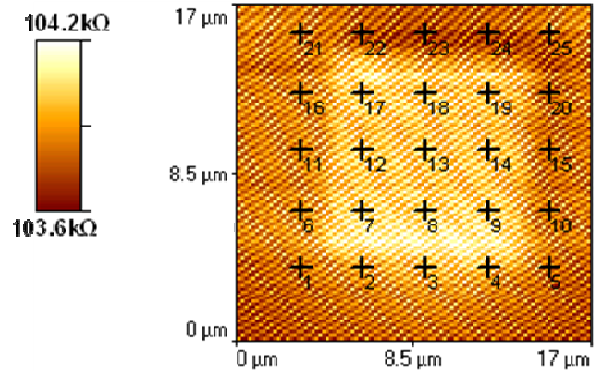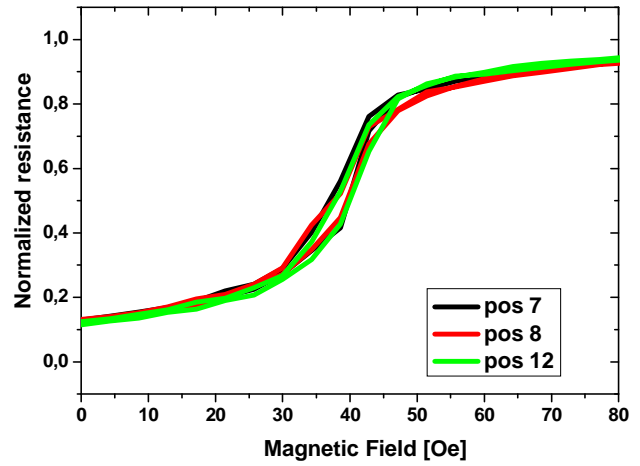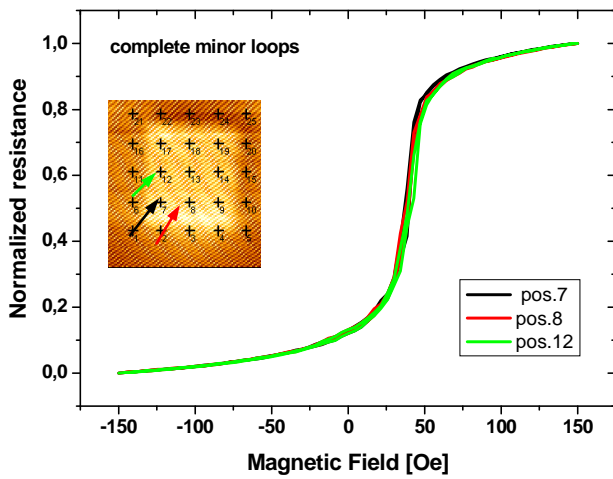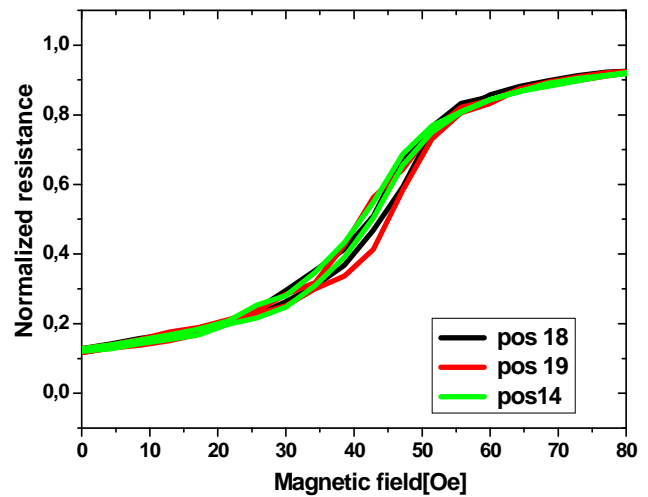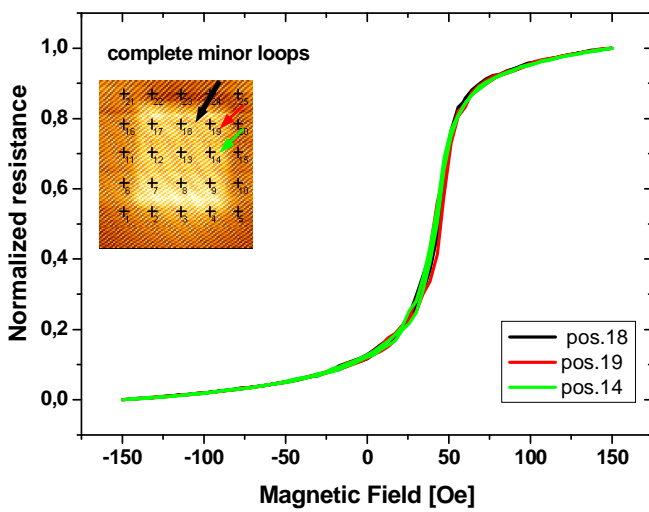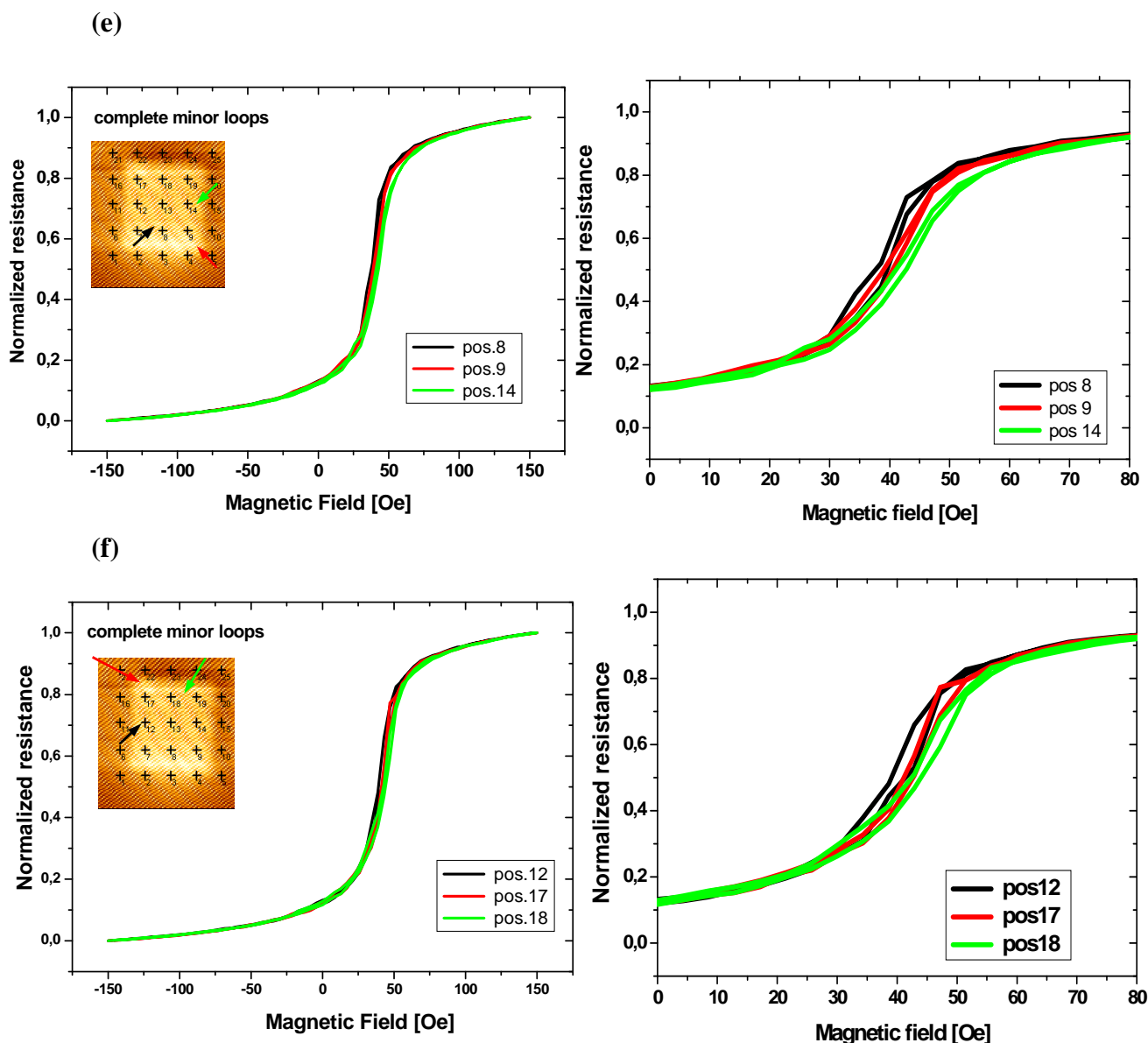
Figure 6.11 (a-b) Topography (a) and magnetoresistance map of the sensor elements with indicated position (c-f) Experimental minor loops in presence of the magnetic tip.

6.3.3 TMR measurement for different tip positions

In the model experiment, the magnetic tip is magnetized perpendicular to the sensor plane as are the superparamagnetic particles for perpendicular fields. From experiment point of view it is important that the magnetizing field of the magnetic particle/tip does not affect the sensitivity of the magnetoresistive sensor elements. Figure 6.12 shows a series of TMR measurement for different tip position.
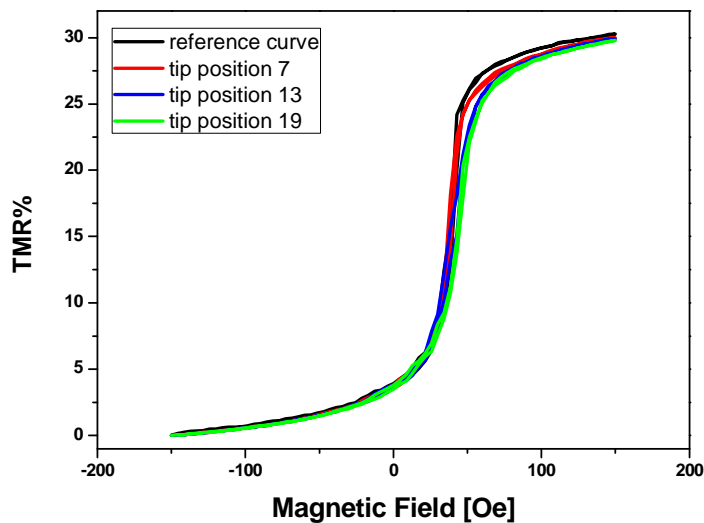
Figure 6.12 Reference curve and series of TMR measurement for

fixed tip position 7,13 and 19.

The TMR ratio in the absence of the tip is equal to 30.2 % (See the reference curve). The same value is obtained for the other characteristic. (Table 6.1). The small differences are in the probable errors range of ±0.1.

Tip position	TMR%
Reference curve	30.2%
Position 7	30%
Position 13	29.9%
Position 19	29.8%

Table 6.1 TMR ratio measurement for reference curve and the curve measure at different tip position.

It is clear from these measurements that the tip stray field didn't influence the total TMR ratio; the slope of the TMR curves, however, show changes if the tip is positioned at different locations.

6.4 Micromagnetic simulations

In addition to the experiments, three-dimensional micromagnetic simulations for the MTJ sensors are performed using the object oriented micromagnetic framework (OOMMF) software from NIST [196]. The OOMMF is freely available software used for simulation of the behavior of the domain structure in magnetic materials. The distribution of spins are modeled by solving the Landau-Lifshitz equation [196]. To model the experiment, the last version of OMMF (OMMF 1.2) including the OMMF eXtensible Solver (OXs) is used [196]. OXs can be extended with own modules and supports 3D simulations, thus the modeling of the experiment is possible.

6.4.1 Simulation parameters

Since the MTJ consists a pinned hard magnetic layer (hard–soft architecture) only the soft magnetic layer (NiFe layer) can be affected by a dipole moment of the magnetic particle. In the model, the magnetization of the sense layer is simulated with a single magnetic particle on top. The element has a total size of 1000x1000x6 nm^3 and is divided into cells of 40x40x6nm^3 for calculation.
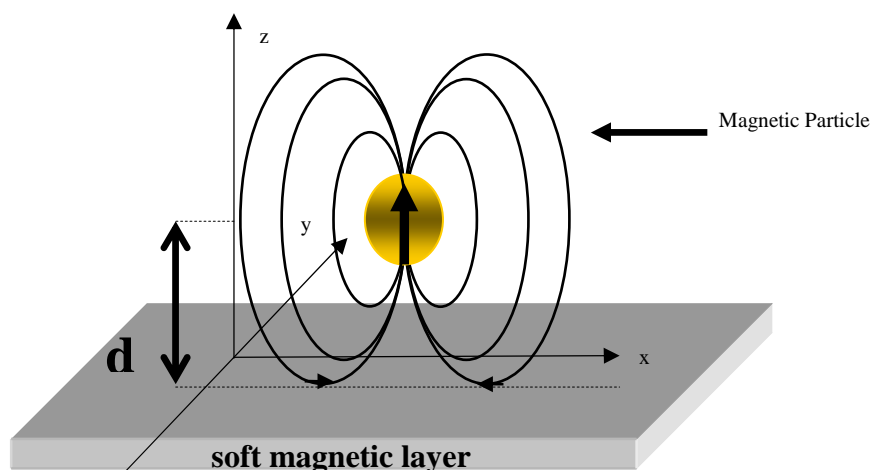
Figure 6.13   In order to understand the experimental results, the influence of a single
magnetic particle on top of the soft magnetic layer is simulated.

The following NiFe parameters are used:

- M_s=860kA/m for saturation magnetization
- A=3.3x10^{-11}J/m for the exchange constant
- The magnetic anisotropy is estimated to be 0.3 x 10^{-3}J/m^{-3}

The magnetic particle is considered as a magnetic dipole with a constant magnetization oriented perpendicular to the sensor plane (Figure 6.13). The value of the dipole moment is set to 10^{-15} Am^2 and is in the range of usual commercial magnetite particle.

Since the experimental minor loops are shifted by Néel coupling, the same shift is introduced in the simulated loops. The distance between the magnetic particle and upper sensor layer is h=80nm (distance between Ta upper sensor layer and contact layers). Figure 6.14 shows the magnetization component along the x and y axis in the NiFe free layer.
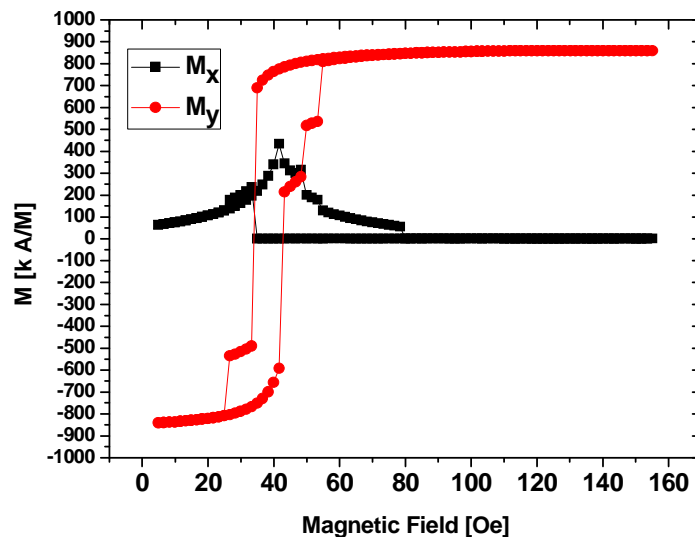
Figure 6.14 Magnetization components along the x and y axis in the NiFe layer in dependence on the magnetic field oriented parallel to pinning direction.

Figure 6.15 shows the normalized magnetization M_x/Ms as a function of applied magnetic field.
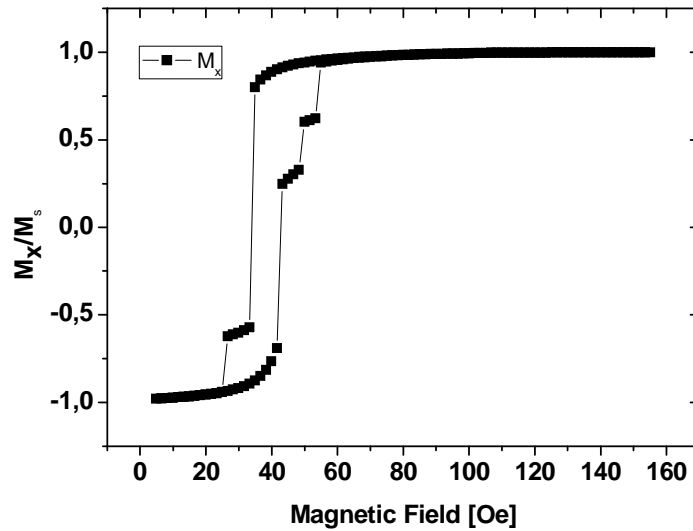
Figure 6.15 Normalized magnetization M_x/M_s as a function of the magnetic field.

To properly compare experiments and OMMF calculations, the magnetization of the NiFe free layer at every stage of the simulation has to be converted into magnetotransport data. This can be done by calculating the relative resistance of all cells given by equation 6.1 and summing over all individual resistance paths in a parallel circuit configuration [75].

$$TMR(\theta) = TMR_{max} \frac{1 - \cos\theta}{2} \qquad (6.1)$$

In the equation 6.1, TMR_{max} is the maximum differences between the antiparallel and the parallel state, normalized to the parallel resistance and Θ is the angle between the magnetizations of the two ferromagnetic layers.

According to the reference [75] , the total resistance R of a system consisting of a free magnetic layer with N cells relative to the low resistance state R_0 (magnetizations of the free and pinned magnetic layer aligned ferromagnetically) is given by:

$$\frac{R}{R_0} = N \left(\sum_{i=1}^{N} \frac{1}{1 + \frac{A}{2}\left(1 + \frac{M_x^i}{M}\right)} \right)^{-1} \tag{6.2}$$

where A is the full TMR normalized to the low resistance state, which is set to 30.2% according to the section 6.3.3, M_x^i is the magnetization component of the single cell i along the x-axis in the NiFe free layer,

Figure 6.16 shows the normalized magnetization M_x/Ms and calculated resistance as a function of applied magnetic field.
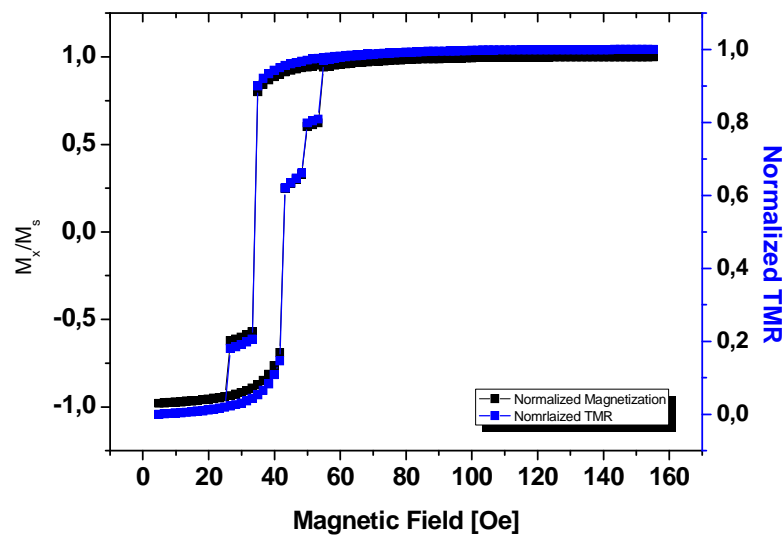
Figure 6.16 Normalized magnetization M_x/Ms (black curve) and calculated resistance (blue curve) as a function of the magnetic field.

The curves show the same shape, but there are some slight differences. These slight differences are also described in the reference [75]. However, this calculation needs to be done to compare simulation and experimental data.

6.4.2 Simulation results

Similar to the model experiments, the single magnetic particle is positioned in the upper and lower corner of the rectangular sensor element. Simulated patterns affected by the magnetic particle and hysteresis loops are presented in Figure 6.17.

(a)

(b)

(c)
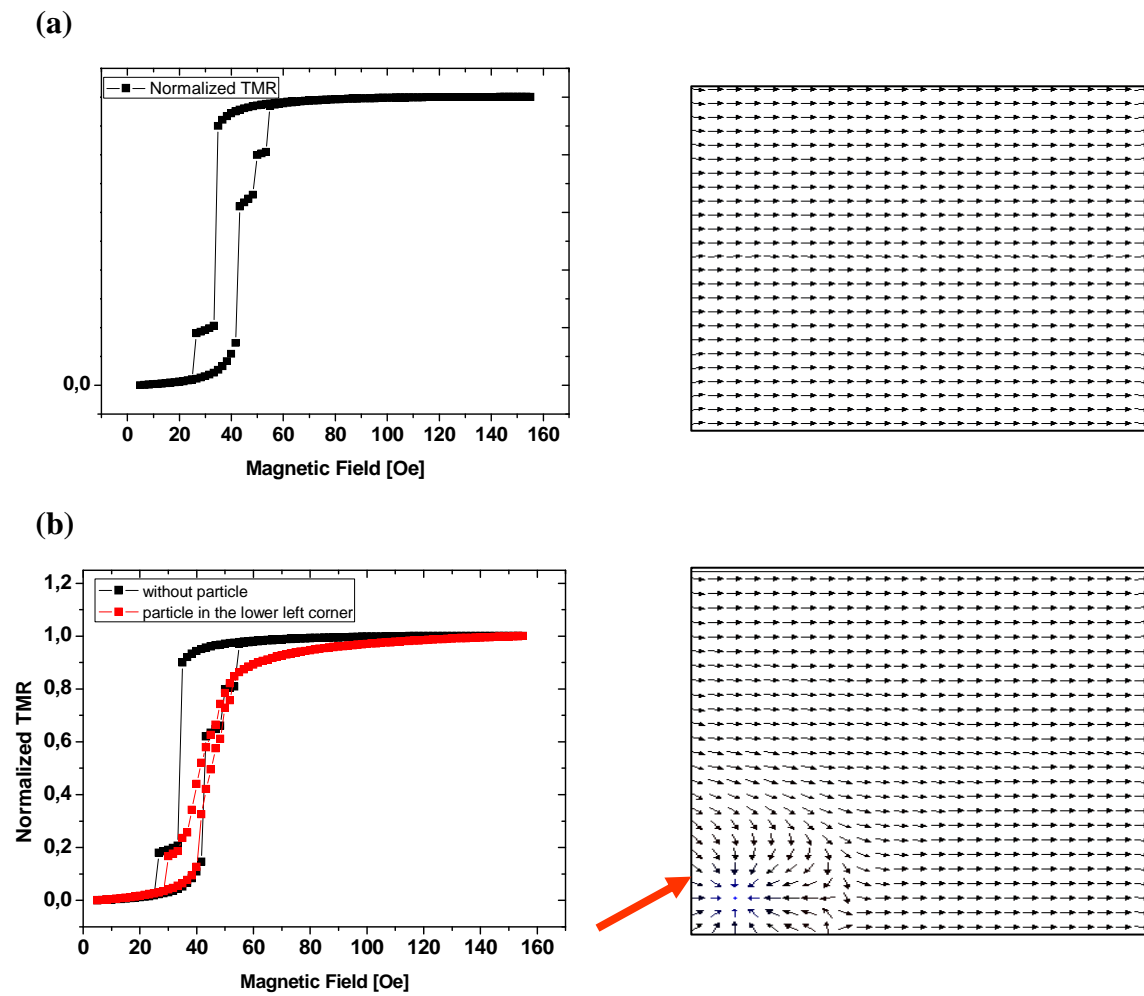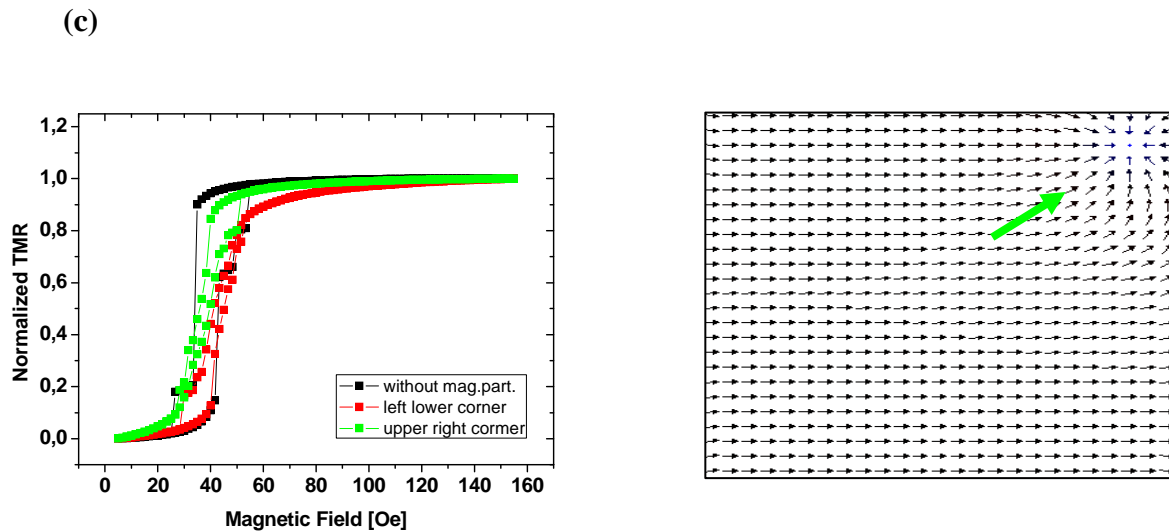
Figure 6.17 (a) Hysteresis loop and according domain structure in the NiFe layer in the absence of a particle (b) and (c). Hysteresis loop and according domain structure in the NiFe layer in the presence of the magnetic particle (particle positioned in the lower left and upper right corner).

As is shown in Figure 6.17, the local changes of the magnetization are induced by a dipole-like stray field of the simulated particle. The symmetry of the magnetization pattern and hence the sensor response are different at different positions. Figure 6.18 shows a comparison between experimental and simulated characteristic.

(a)   **(b)**
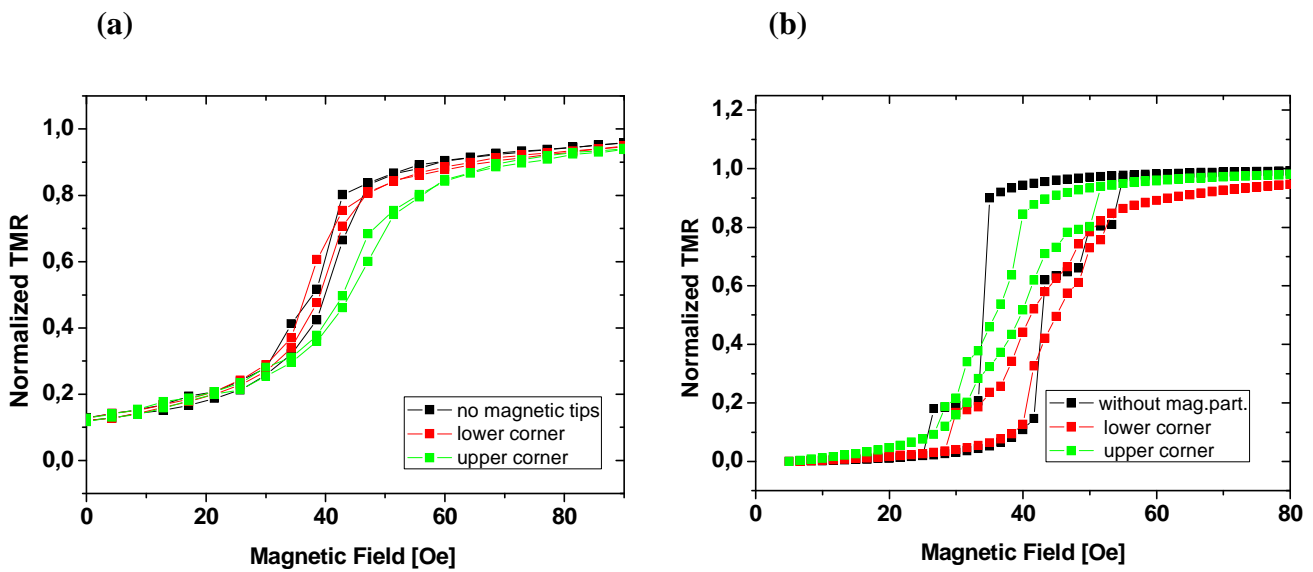
Figure 6.18 (a) Experimentally minor lops for three positions of the magnetic tip

(b) Simulated hysteresis loops in a presence and absence of a single magnetic particle.

In both cases a retarded switching and saturation field is observed. Simulated hysteresis loop in comparison to the experimental characteristic shows a larger coercivity and a larger saturation field. The differences are caused by different switching mechanisms: rotation through formation of an s-state and vortex for the simulated hysteresis and domain formation and propagation for the sensor elements (See figure 6.19). Additional jumps obtained in the simulated loops occur due to their limited size. The visible asymmetry in the simulated loop (Figure 6.18 b) is not observed experimentally.

(a)
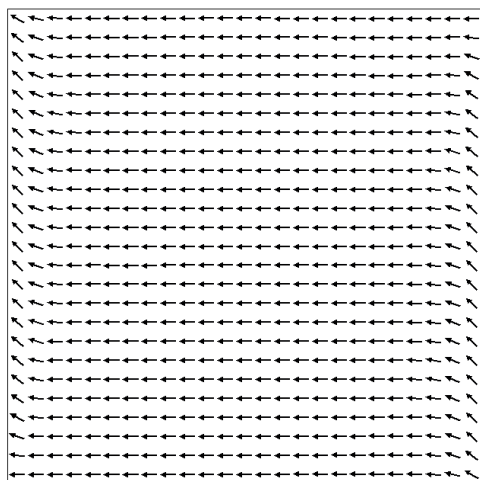
(b)
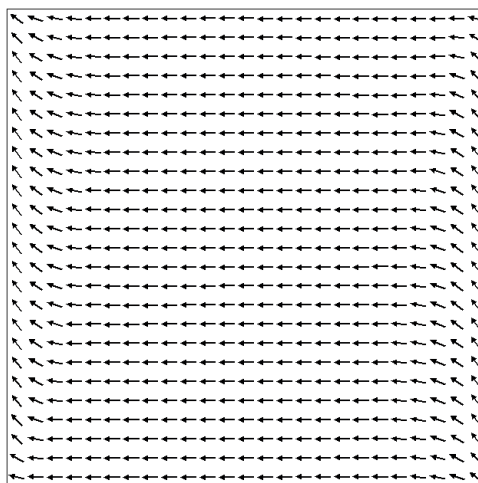
(c)   H=5 Oe

(d)   H=20 Oe
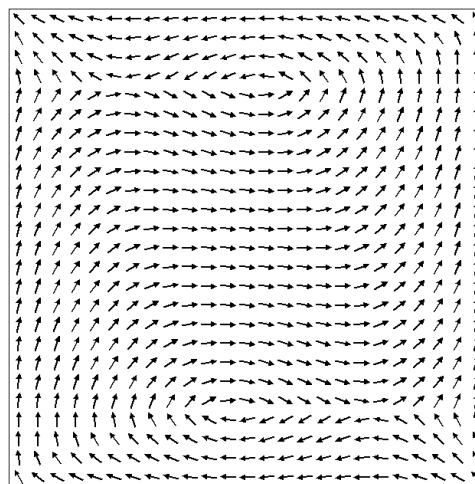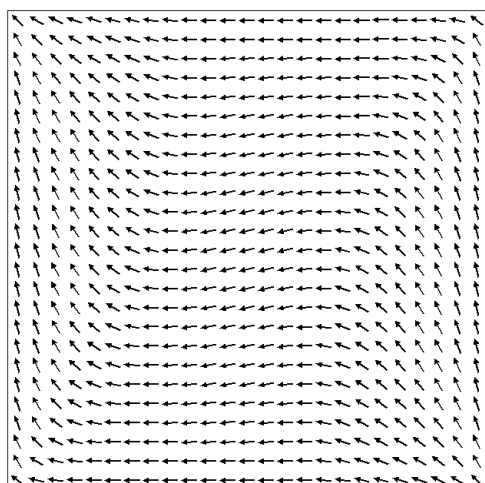
(e)   H=38 Oe

(f)   H=43 Oe
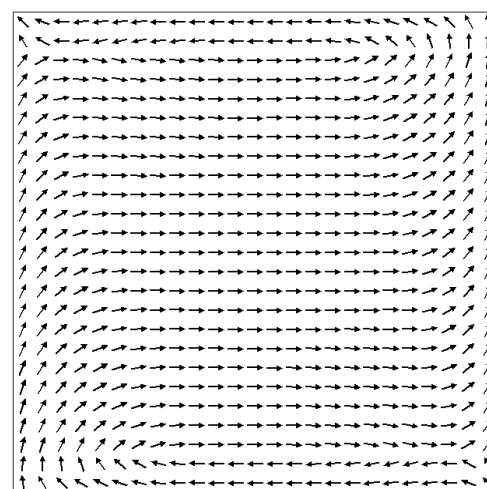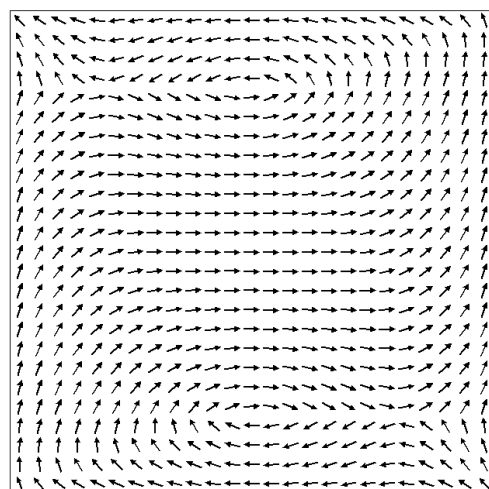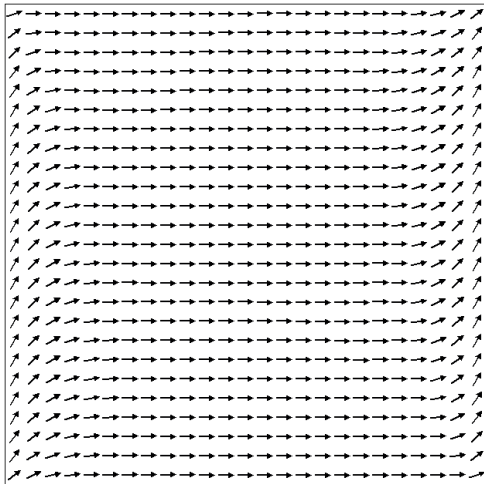
(g)　　　　　　　　　　　　　　　　　　**(h)**
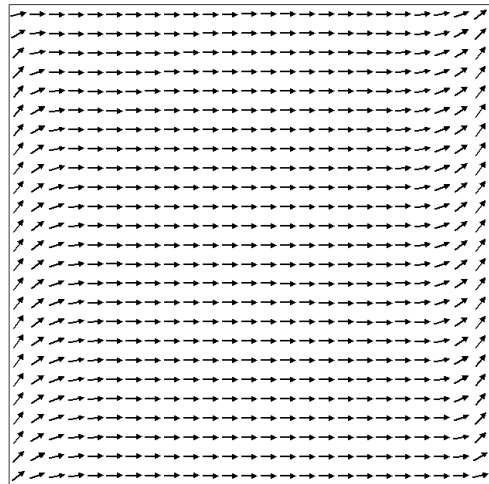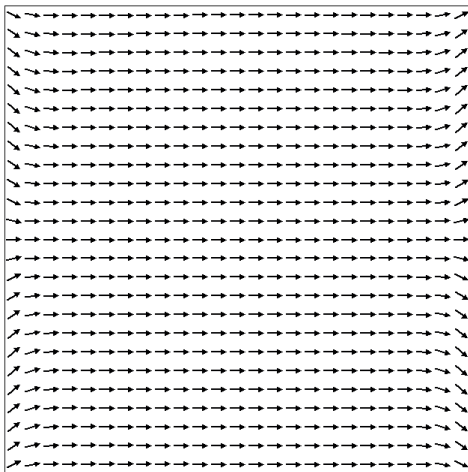
(i)　　　　H=55 Oe　　　　　　　　**(j)**　　　　H=60 Oe
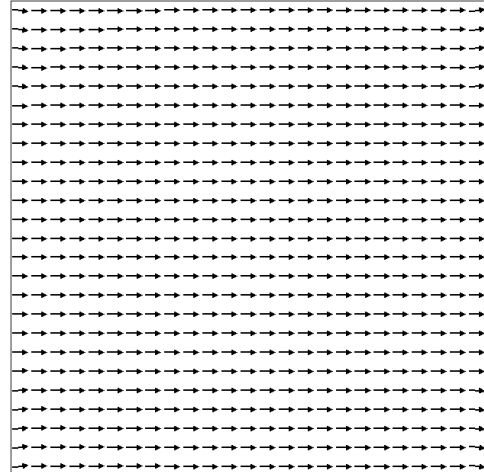
H=130 Oe　　　　　　　　　　　　　　H=155 Oe

Figure 6.19 (a-j) Domains structure in the NiFe layer in the absence of a particle at magnetic field from 0 to 160 Oe.

It is observed experimentally that the slope of the magnetization curve gets flatter if the particle is located centrally. This is also confirmed by the simulation. Figure 6.20 shows a simulated pattern for different position of the magnetic particle: from lower corner up to the center.

(a)

(b)

(c)

(d)

(e)
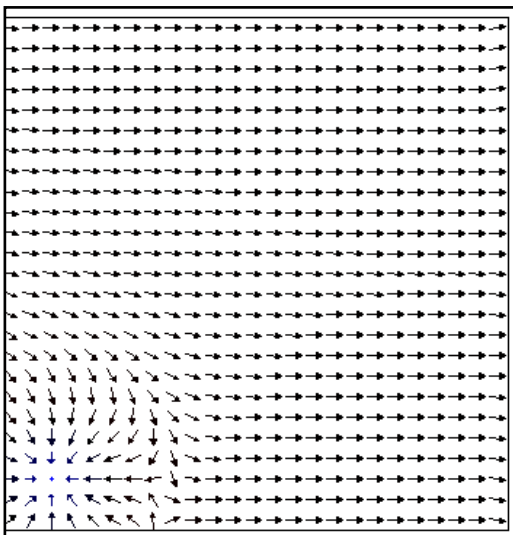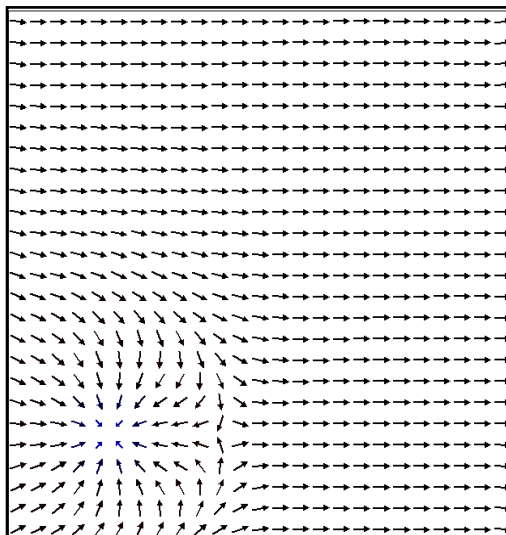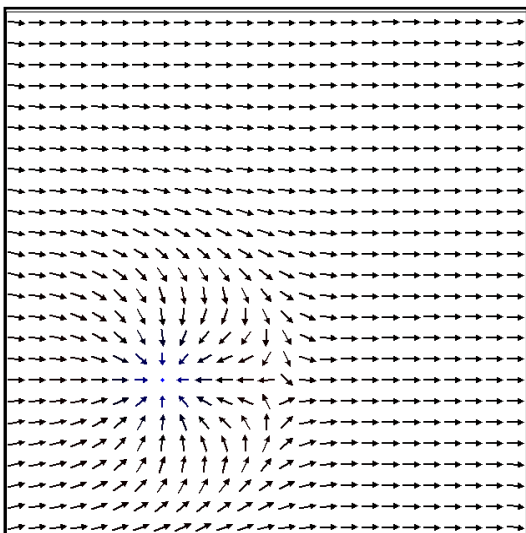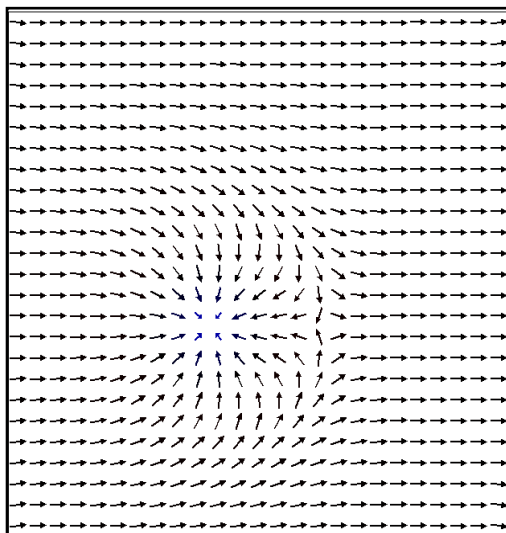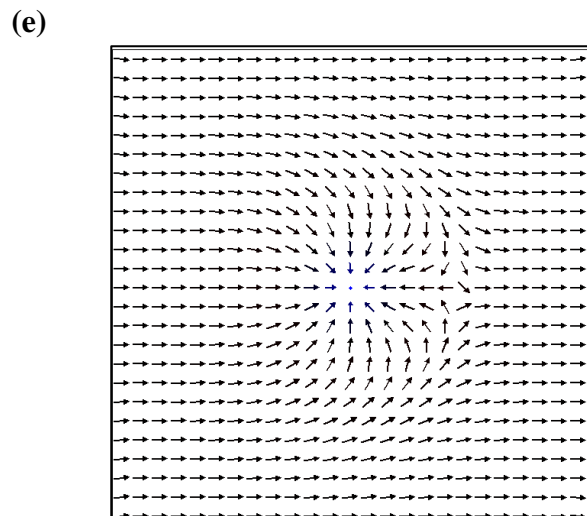
Figure 6.20 (a) – (e) Simulated magnetic pattern for different position of the magnetic
particle: from lower corner up to the center.

The corresponding simulated hysteresis loops are presented in Figure 6.21
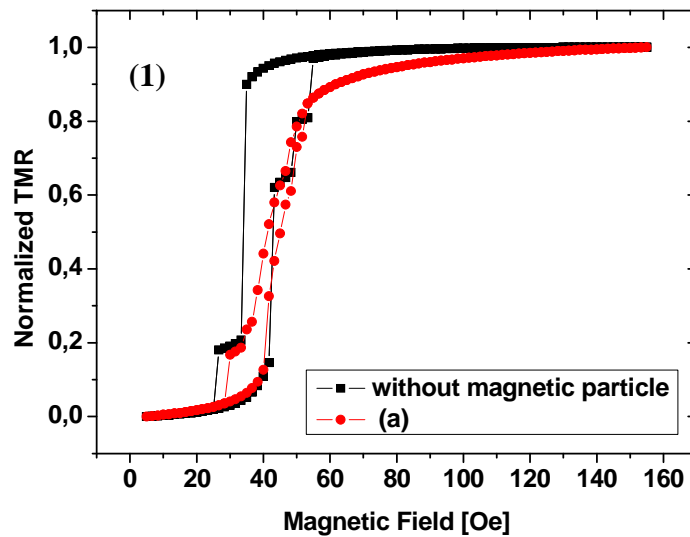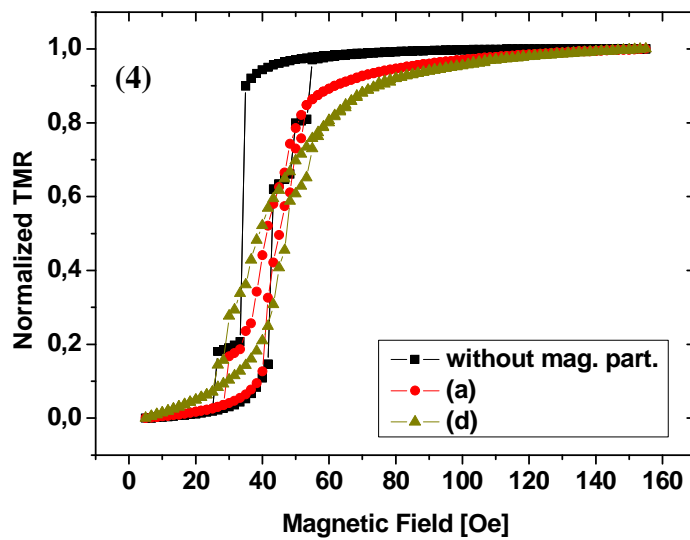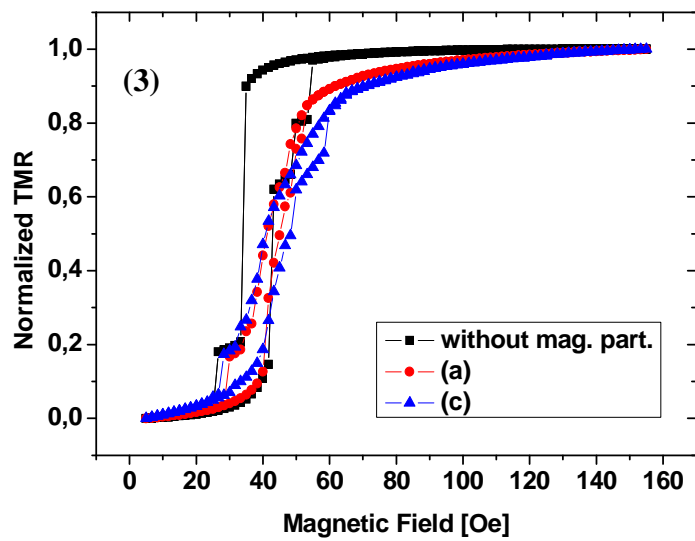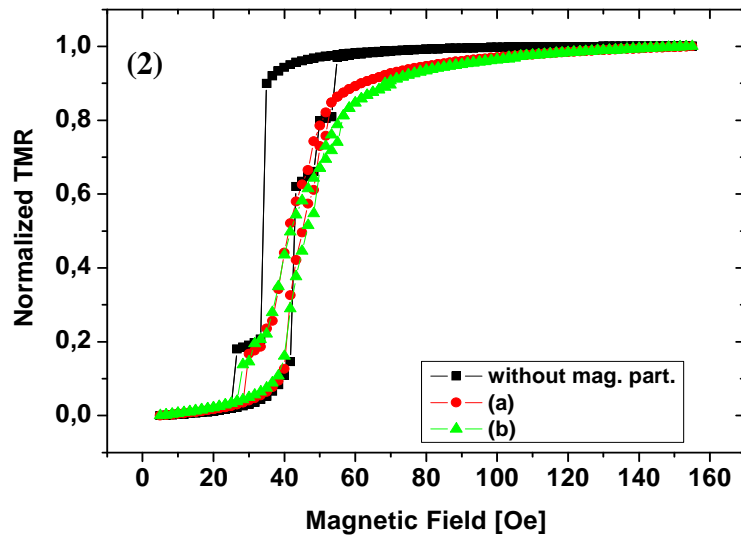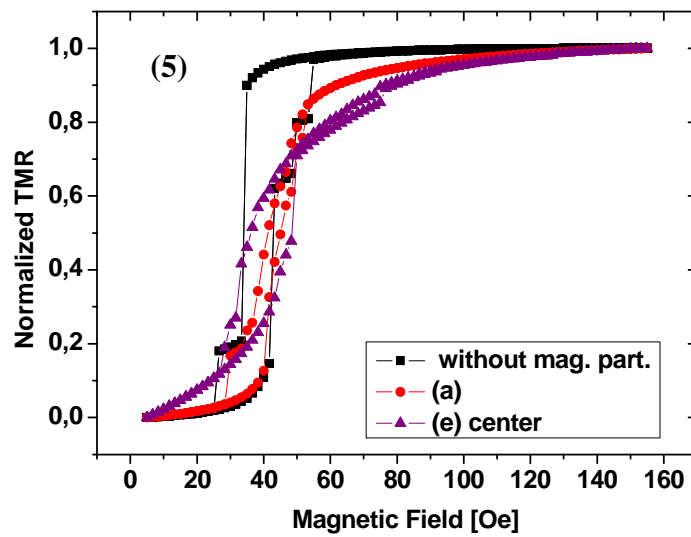
Figure 6.21 (1)-(5) Simulated hysteresis loops for different position of the magnetic particle indicated in the figure 6.20.

As is shown in Figure 6.20, a single particle causes slight, local disturbances and they are greater if the particle is located more centrally. Figure 6.22 shows a comparison between experimental and simulated characteristic. Similar to the experimental setup, single magnetic particle are positioned in the upper and lower corner and the center of the rectangular sensor element. As can be realized in the Figure 6.22 the magnetization behavior of the NiFe sense layer is strongly affected and behaves similar to the measured loops.
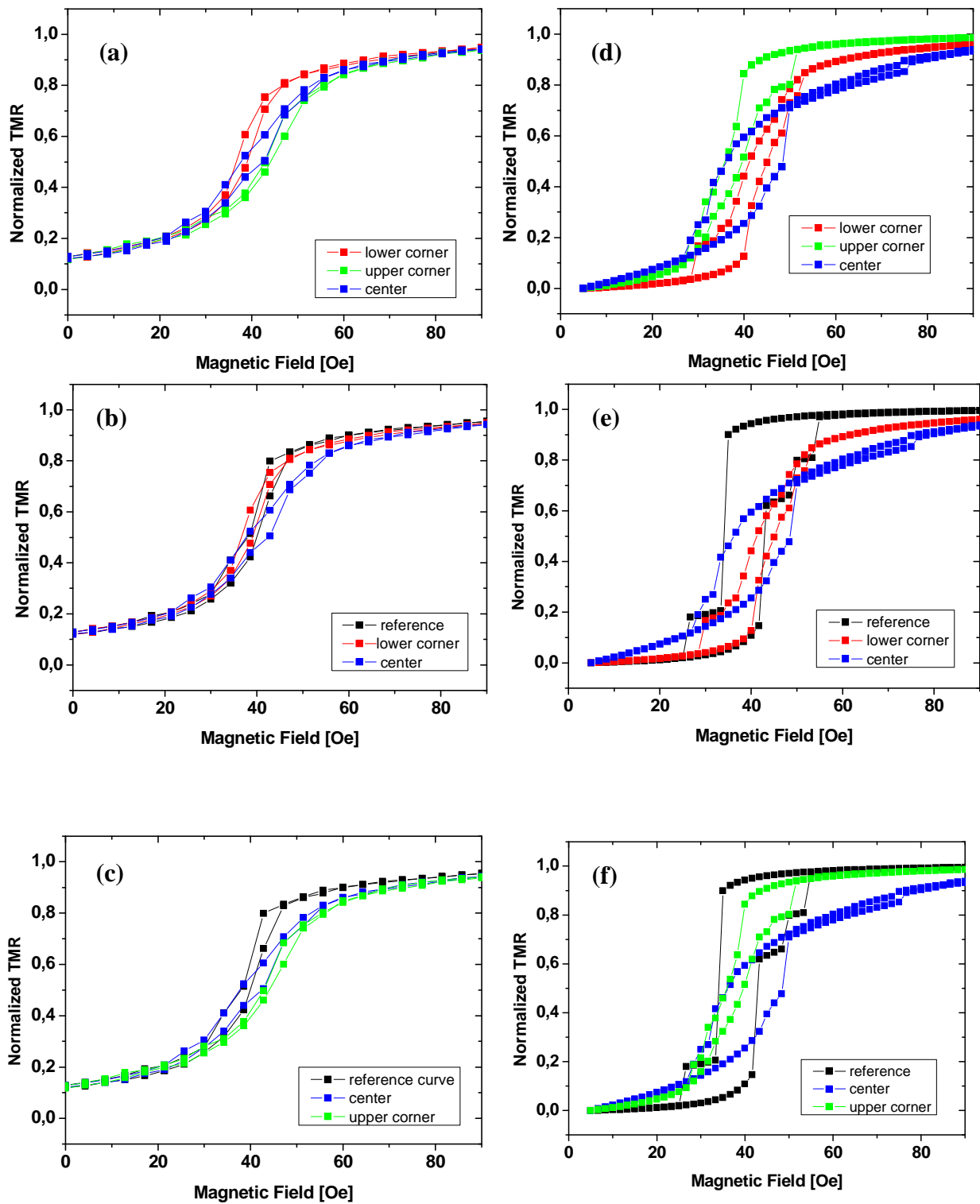
Figure 6.22 (a-c) Experimental minor loops at different positions of the magnetic tip: lower, upper corner and center and without any tip (reference curve), (d-f) Simulated minor loops at different positions of the magnetic particle: lower, upper corner and center and without particle (reference curve).

6.4.3 Conclusion

A model experiment for MTJ sensor with a magnetic particle on top is carried out by scanning with the magnetic tip across the sensor elements. Experiment and simulation confirm the detection capability of the MTJ sensor down to the single marker level. The differences in the transport measurement are strongly dependent on the tip position and the according domain configuration in the sense layer. Therefore the next chapter shows the model experiment carried out on the small sized elements with an ellipse-like shape.

7. Model experiments on elliptical shaped MTJ sensor

In this chapter, a model experiment is described for understanding the behavior of an elliptical-like shape MTJ sensor element in the presence of a single magnetic particle. The magnetic particle, as in the previous chapter, is modeled by a magnetic tip in an AFM. The focus in this chapter is on the experimental results. A detailed description of the detection method used can be found in Section 6.3.

7.1 Sensor fabrication and charcaterization

The MTJ sensor used in this experiment had a following layer structure:

$Ta_{6.5nm}/Cu_{30nm}/Ta_{19nm}/Py_{4nm}/Co_{3nm}/Mn_{38}Ir_{17\ (15nm)}/Al_{1.4nm}/Py_{5nm}/Ta_{6.5nm}/Cu_{30nm.}$ Py stands for permalloy. The sensor is patterned using E-beam lithography followed by an Ar ion-beam etching. Detailed MTJ sensor fabrication procedures are described in the previous chapter. For the experiment, the elliptical-like shape sensor is used with following dimension:

- long axis-750nm
- short axis-415nm

Figure 7.1 shows micrographs of the sensors prototype which consists of 20 sensor elements 7.1 (a) and close up of single sensor elements with contact lines 7.1 (b).
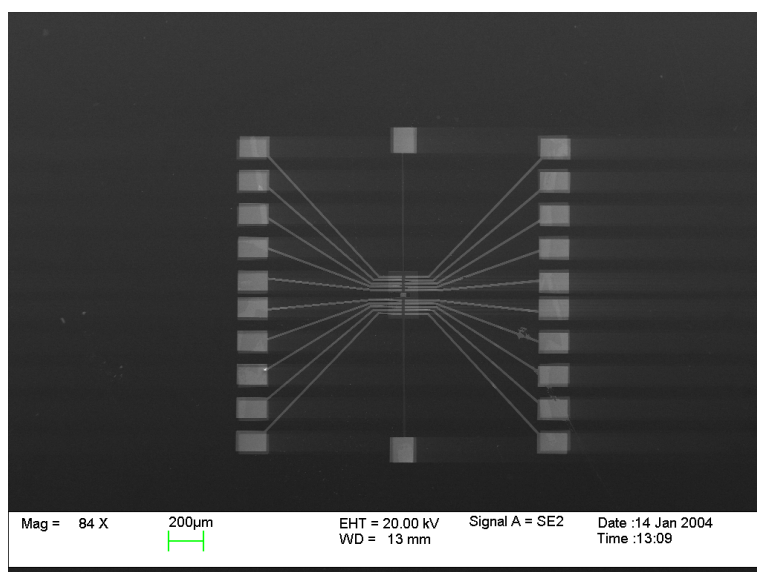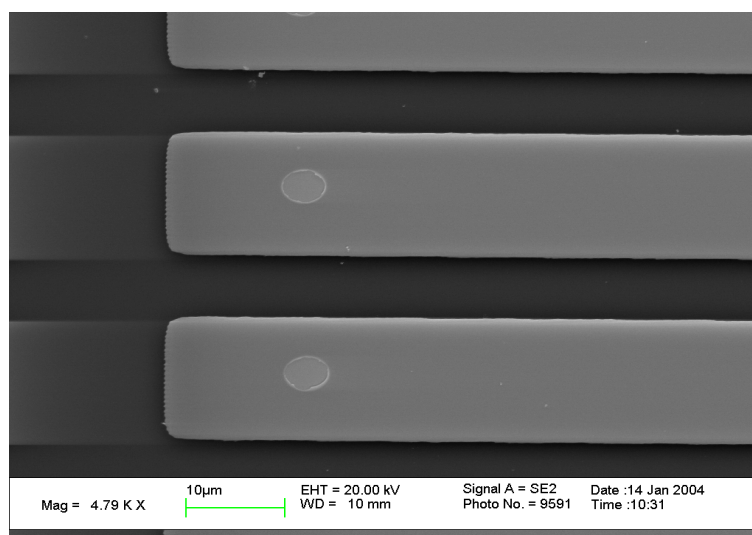
Figure 7.1 (a) Micrograph of a sensor prototype, which consists of 20 sensor elements (b) Close up of a single sensor element with contact lines. The active area of the sensor element is 2µm².

The minor loop characteristic is presented in Figure 7.2.
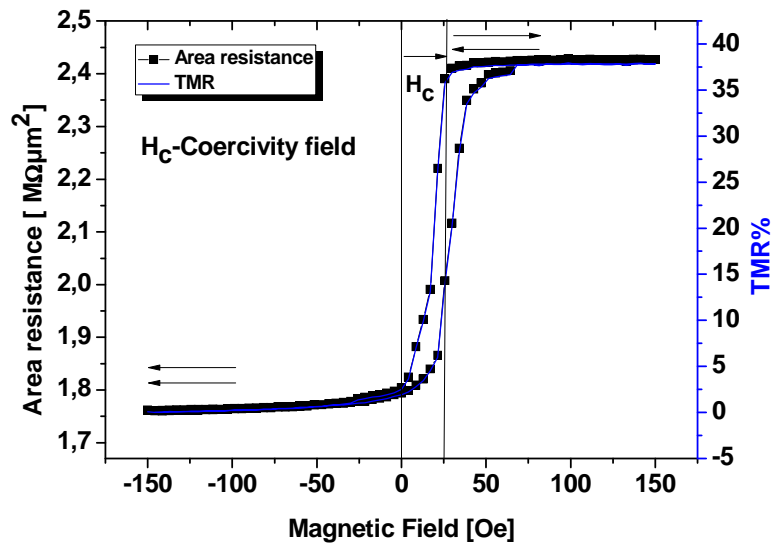
Figure 7.2 Minor loop of an elliptical shaped sensor element. The arrows indicate the relative magnetization orientation of the soft-bottom and hard-top magnetic layer.

The TMR ratio of the elements is 38% while the resistance area product is equal to 2.4 $M\Omega\mu m^2$. The resistance changes by 38 % in the field range of 12 Oe, resulting in a high sensitivity of about 3.2 %/Oe.

7.2 Experimental results

The response of the MTJ sensor elements is measured during scanning with a home-made MFM tip (Section 6.1 and 6.3). Figure 7.3 shows the topography of the sensor elements and a simultaneously recorded magnetoresistance map at constant magnetic field. Here, like in the previous chapter, the color table represents a certain resistance range and the additional regular oblique stripe pattern is due to electronic noise.

(a)   **(b)**
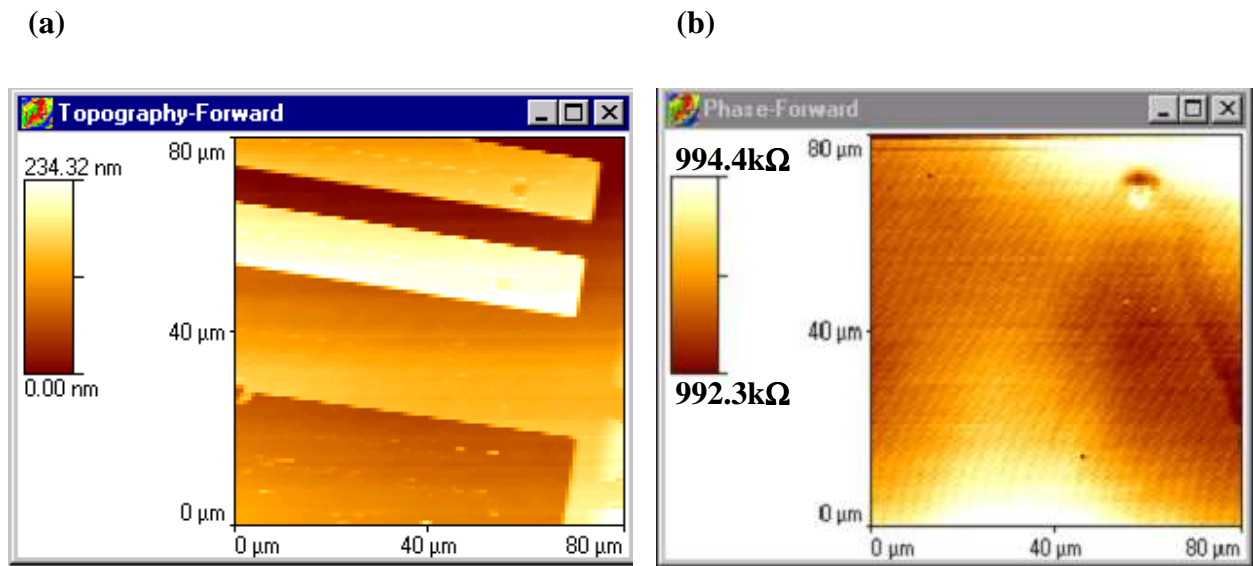
Figure 7.3 (a) Topography of two sensor elements (also showing contact lines) (b) Simultaneous resistance map of the first sensor element at the external field (25 Oe).

During measurements only the "first element" (Figure 7.3(a)) was connected via a BNC capable to the amplifier. It is obvious from the Figure 7.3 (b) that the resistance of the elements changes during imaging with a MFM tip. The situation is analogous to that presented in Section 6.3.1. The connected MTJ element can be easily identified in the MR map.

Additional MR maps taken at an additional homogenous magnetic field oriented parallel to the vertical axis (in map coordinates) of the MTJ are presented Figure 7.4.

(a)

(b)

(c)

(d)

10 Oe

20 Oe

25 Oe

(e)

(f)

30 Oe

35 Oe

(g)

(h)

40 Oe

50 Oe

(i)

(j)

60 Oe

70 Oe

(k)

(l)

100 Oe

120 Oe
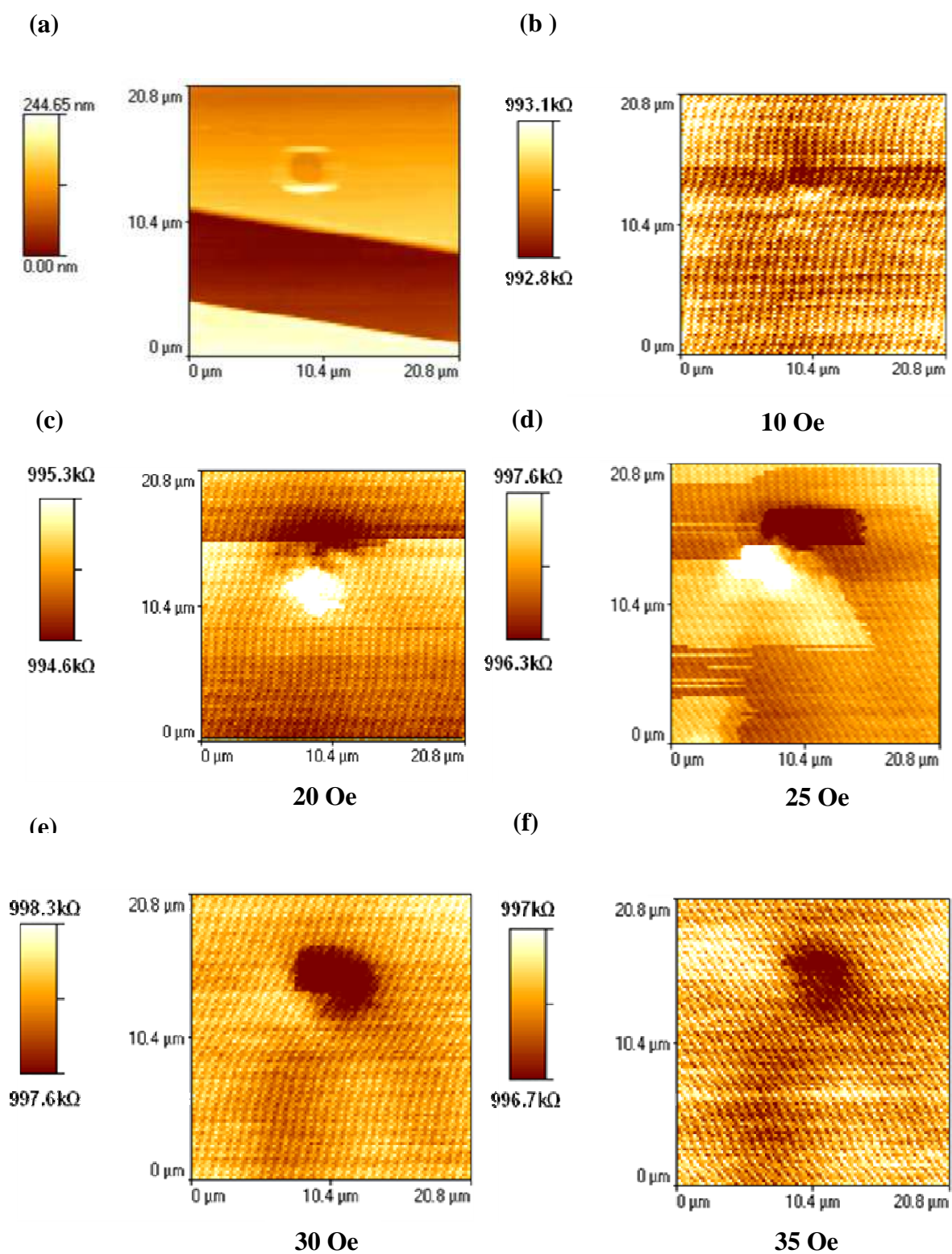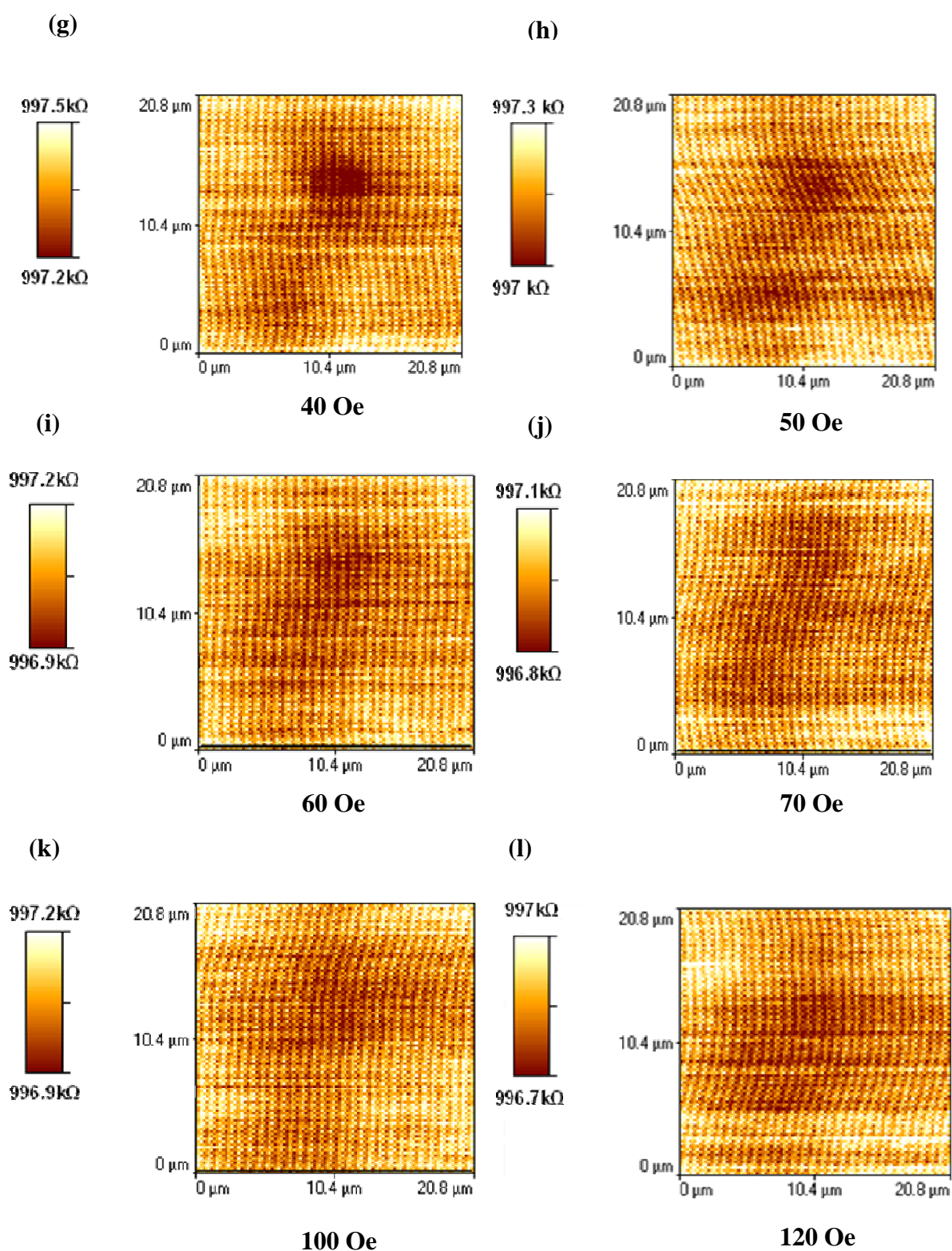
Figure 7.4 (a) Topography of a single MTJs sensor elements; (b)-(l) Magnetoresistance map at different magnetic fields. For discussion see text.

Here again, the maps of the sensor response are distinctly different for various fields. At the field of 25 Oe, which correspond to the coercivity field (Figure 7.2), dark and bright contrasts indicate changes in the MR. The situation is analogous to that described in Section 6.7. At field of 20 Oe two spots are still dominating. The situation became different at the field of 10 Oe. There is only one very small bright spot (Figure 7.4 (b)). Above the coercivity field, the dark spots dominate. At 70 Oe the elements switch completely and there is no changes in the resistance upon tip scanning. Significant differences however are observed in the transport measurement at the fixed tip position. Figure 7.5 shows the topography of a single MTJs sensor element with indicated tips positions and a series of minor loop measurements taken at the fixed tip position.

(a)
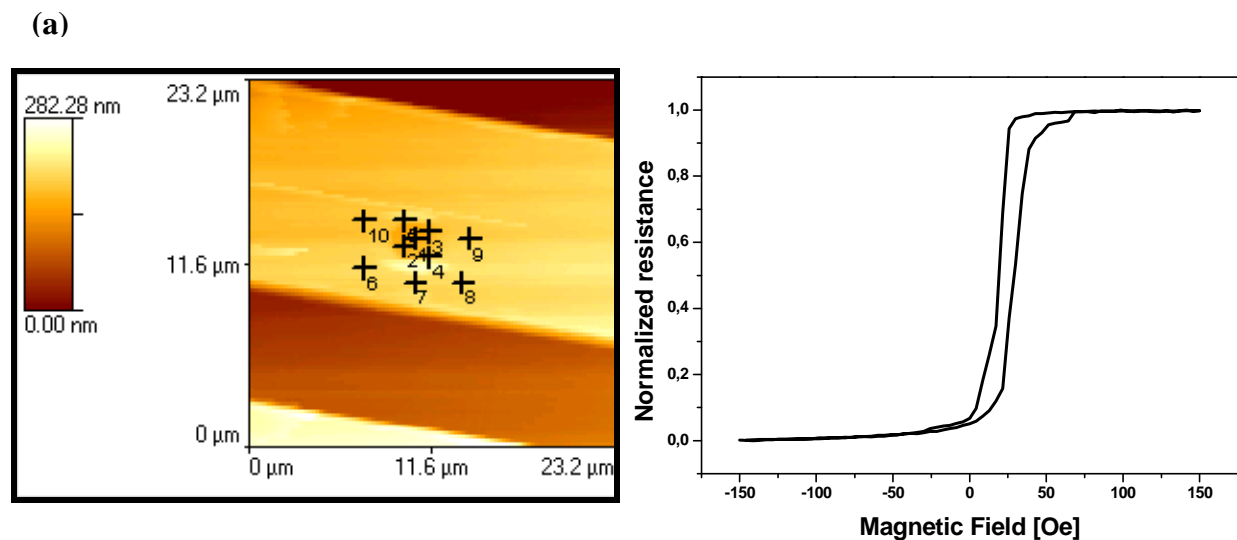
(b)
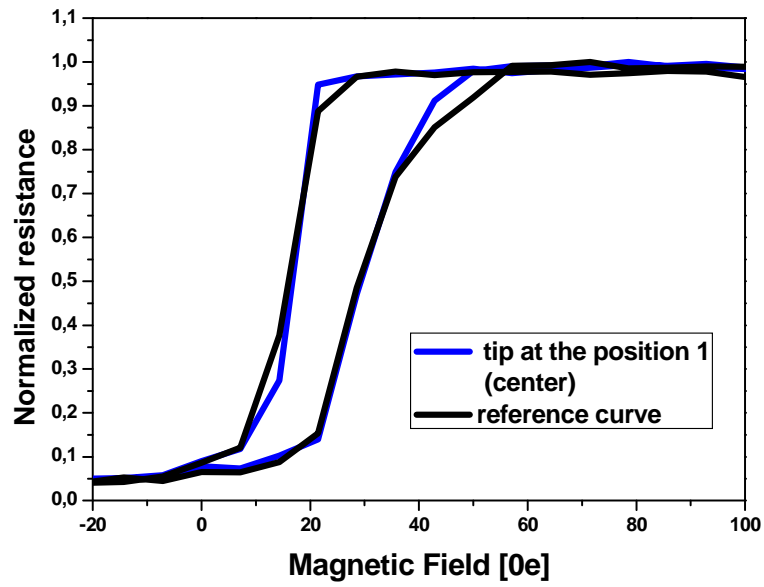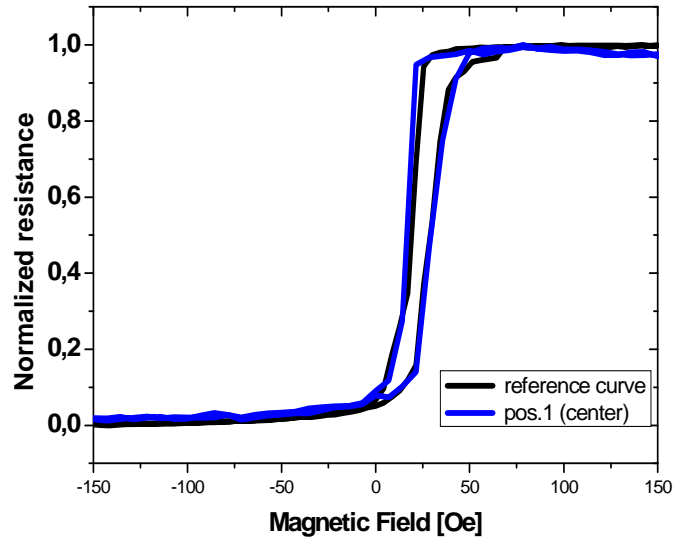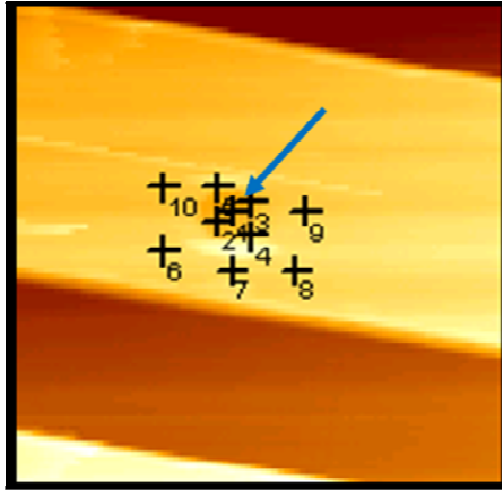
(c)
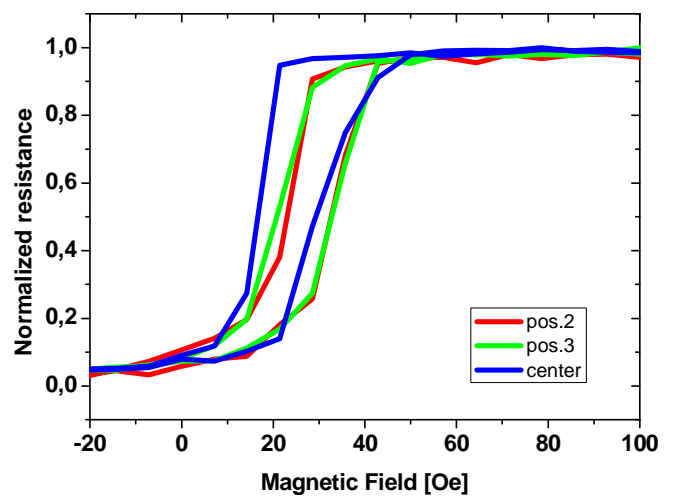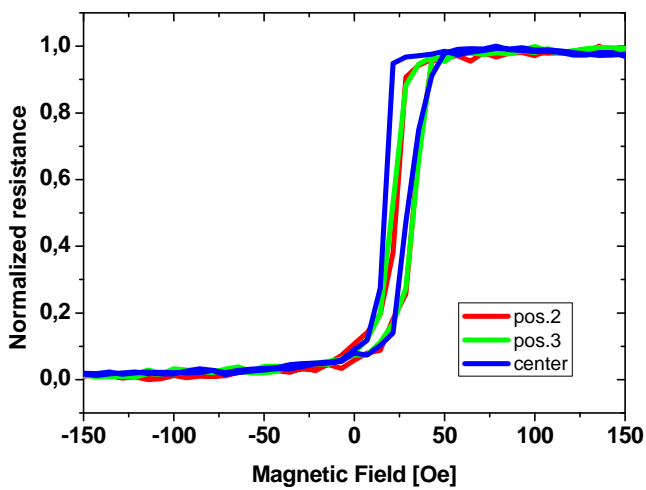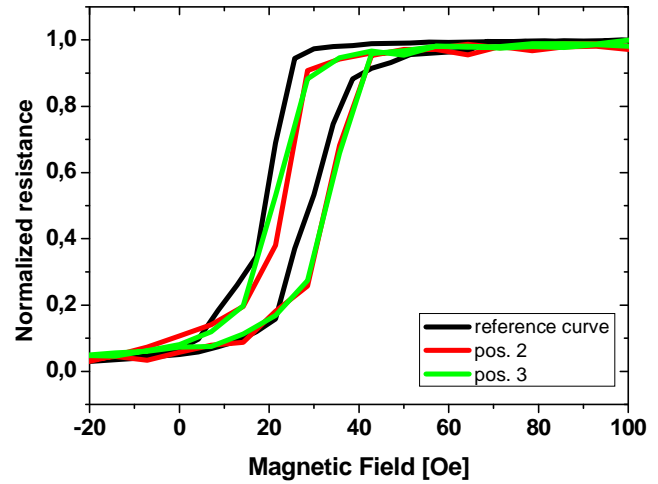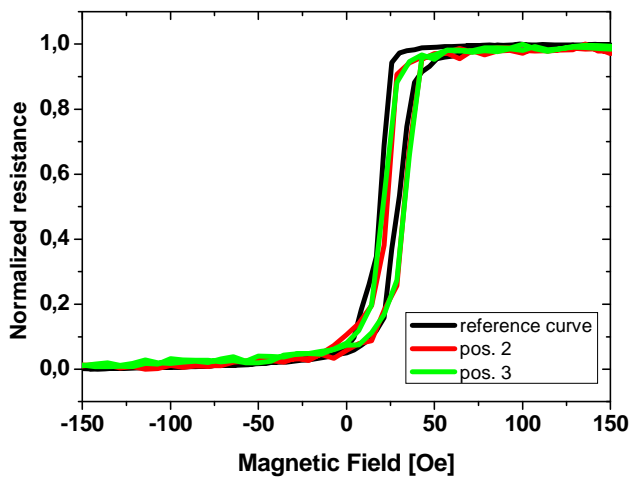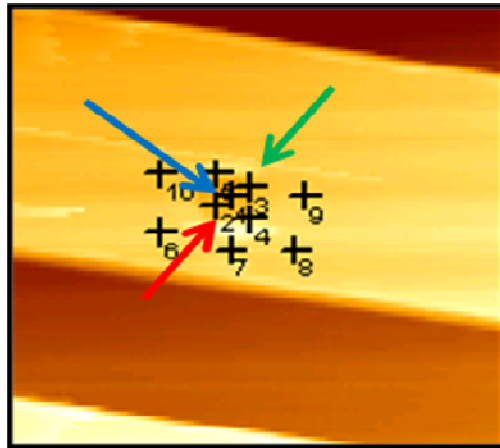
(d)
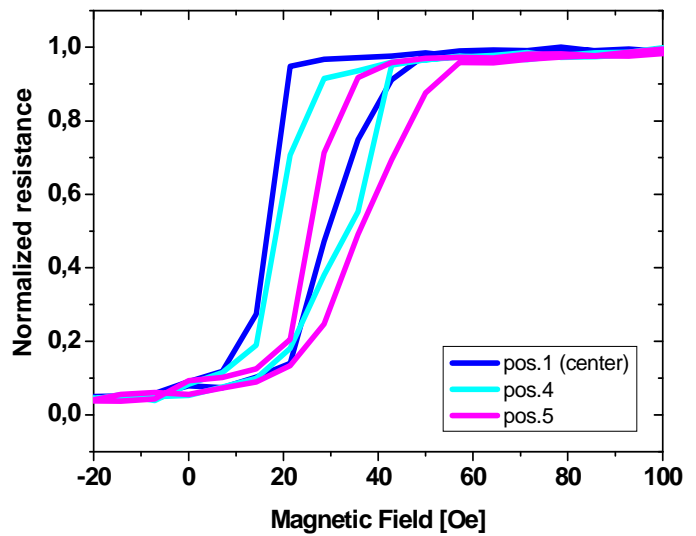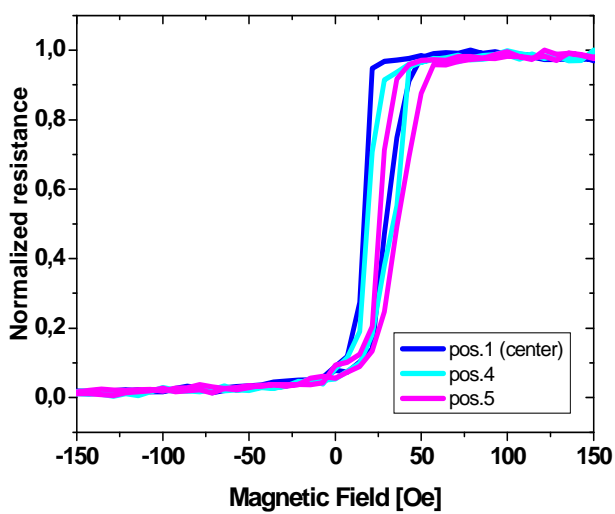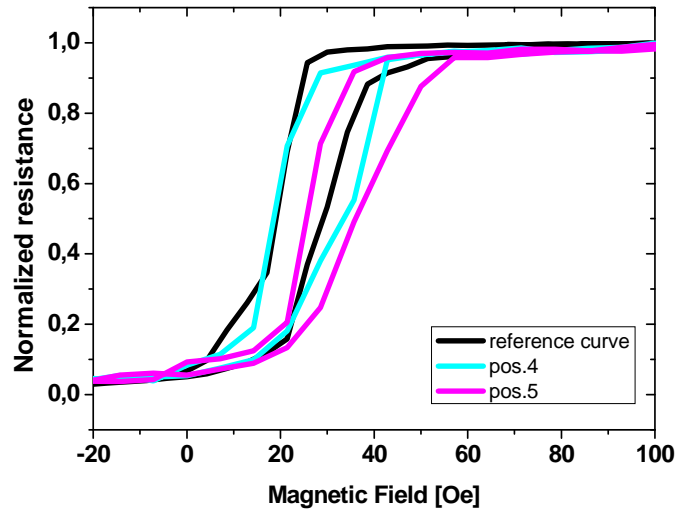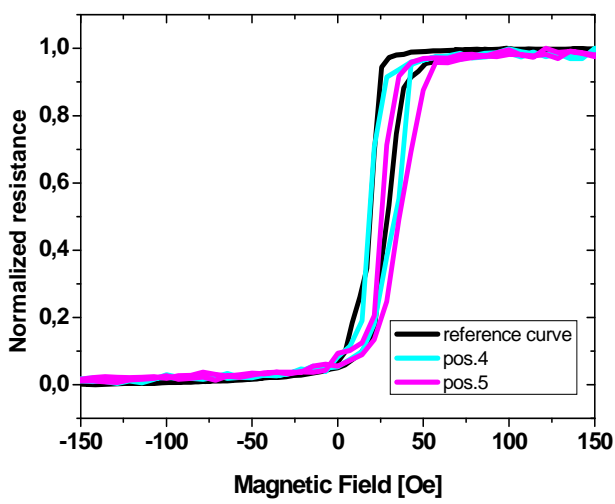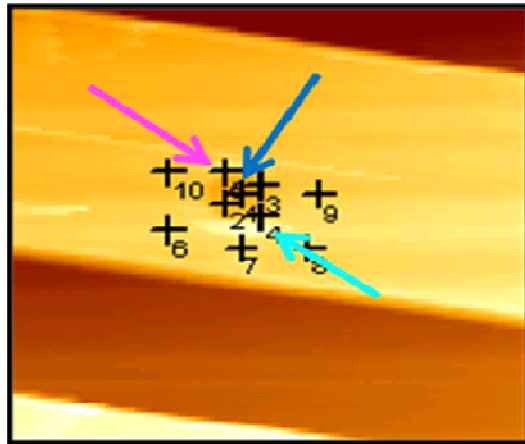
Figure 7.5 (a) Topography with indicated position

(b-d) Experimental minor loops in the presence and absence of the magnetic tip.

In Figure 7.5b, the black curve is taken in absence of the tip (reference curve), while the blue curve is measured at the center (the tip position number 1). The switching field and saturation field are the same for both measurements. Figure 7.5 c shows a minor loop measurement for the reference curve and the curve measured at the tip position 1, 2 and 3. Here, the tip locations 2 and 3 are positioned opposite with respect to the center. The two curves 2 and 3 are shifted with respect to the reference curve. A retarded switching field is observed. Another situation is presented in Figure 7.5d. Here, the curves 4 and 5 are shifted with respect to reference curve, but the curve 5 shows a large shift. Here again, a retarded switching is observed with respect to the reference curve, but the curve 4 switches below the curve 5. Figure 7.6 shows a sensor characteristic measured at the positions 6, 7, 8 and 9 that are located outside the sensor elements

(a)

(b)
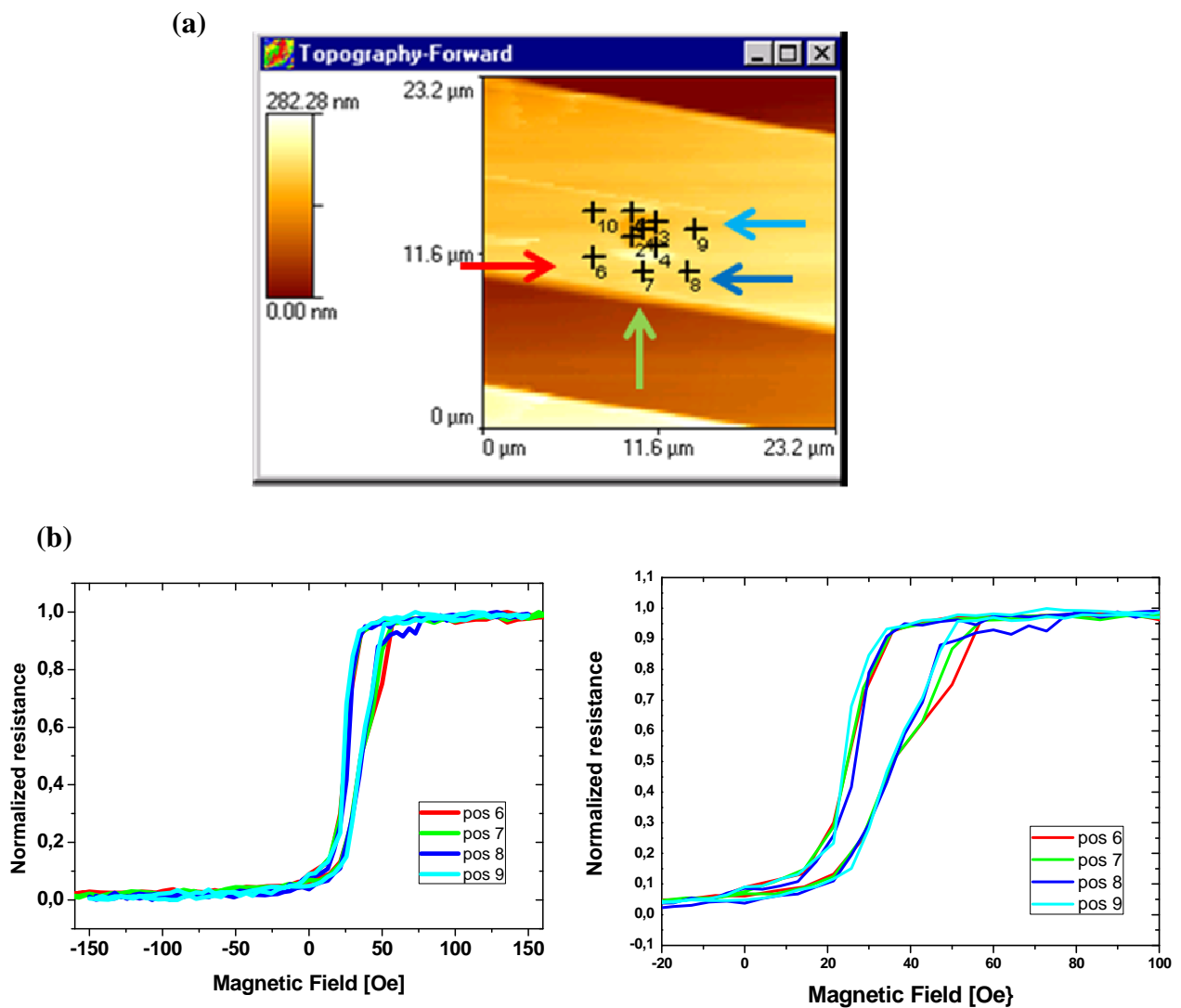
Figure 7.6 (a) Topography with indicated tip positions

(b) Experimental minor loops measured at the tip position 6, 7, 8 and 9.

153

Here, as expected, there is nearly no difference in the transport measurement for different tip positions. The switching and saturation fields are the same for all characteristic. The very small differences are observed in the field range of 25 to 50 Oe.

The most surprising results are obtained for TMR measurements. Figure 7.7 presents a TMR characteristic for different tip positions.
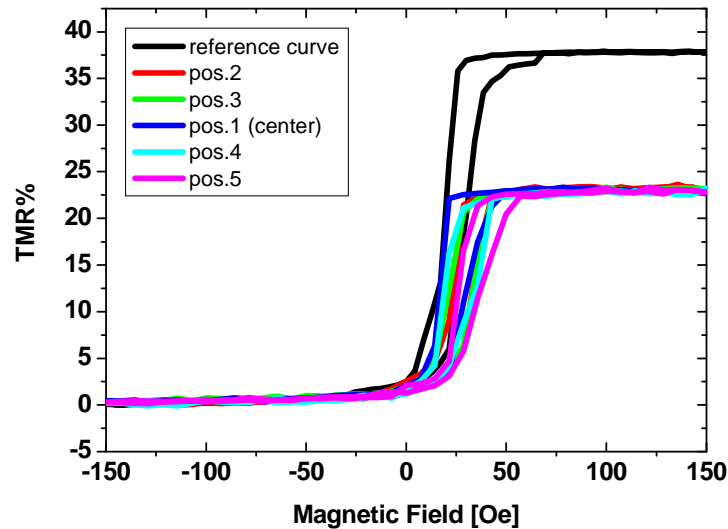
Figure 7.7 The TMR ratio measured at different tip positions.

The TMR ratio measured in the absence of the magnetic tip is equal to 38 (Figure 7.7). When the tip is close to the elements and located in certain positions on the top of the active sensor area, the TMR ratio decreases and reaches a value of around of 23.4 % . Values for TMR ratio measurements are given in Table 7.1

Tip position	TMR ratio in %
1	23.4
2	23.5
3	23.5
4	23.3
5	23.4

Table 7.1 The TMR ratio measurements for different tip positions.

It is clear from this measurement, that the stray field of the magnetic tip is too strong and influences the sensor characteristic.

154

7.3 Conclusion

In conclusion, this chapter presented a model experiment for single magnetic particle detection with elliptically shaped MTJ sensor elements. The active area of the sensors was $2\mu m^2$. The single particle, like in the previous chapter is modeled, by a MFM tip. Here again, the response of the sensitive element clearly depends on the tip position.

Additionally, the TMR ratio of the sensor element is reduced due to the stray field of the MFM tip. The results show that a too large stray field of the particle can influence the sensor characteristic and switch completely an element.

_____

8. Hysteresis-free MTJ sensor

MTJ sensors have a potential to detect single magnetic particles respectively biomolecules. This was demonstrated by a magnetic force microscope (MFM) tip, which serves as an artificial model for a magnetic particle on the top of MTJ sensor. The response of the MTJs was measured during the scanning with a MFM tip. While the tip position and height on top of sensor were varied, the sensor clearly indicates different responses. The differences in the transport measurements (See Chapter 6 and 7) were visible in the minor loops taken while the tip was positioned on top of the active sensor area. Thus, the purpose of this experiment is to produce a hysteresis-free MTJ sensor that would give a clear signal in the presence of a single magnetic particle.

8.1 Sensor fabrication

A hysteresis free-MTJ sensor was fabricated on an oxidized silicon wafer by using e-beam lithography, argon ion etching system and plasma oxidation of Al-layer. Previous experiments relied on two ferromagnetic layers (hard and soft architecture) to obtain a parallel and an anti-parallel alignment of the magnetic layers. In order to manipulate the relative orientation of the magnetic moments of the ferromagnetic layers, a new MTJ stack is fabricated. In this stack a hard magnetic layer is introduced above the soft magnetic layer to produce Neel coupling. As previously written, Neel coupling is observed when two magnetic layers are separated by non magnetic spacer and show correlated roughness; there exist an effective ferromagnetic coupling which is induced magnetostatiscally by the formation of magnetic poles at the interfaces. In the new MTJ structure, the soft magnetic layer is aligned at zero field by the upper hard magnetic layer perpendicular to the biased layer (Figure 8.1).

(a)

(b)
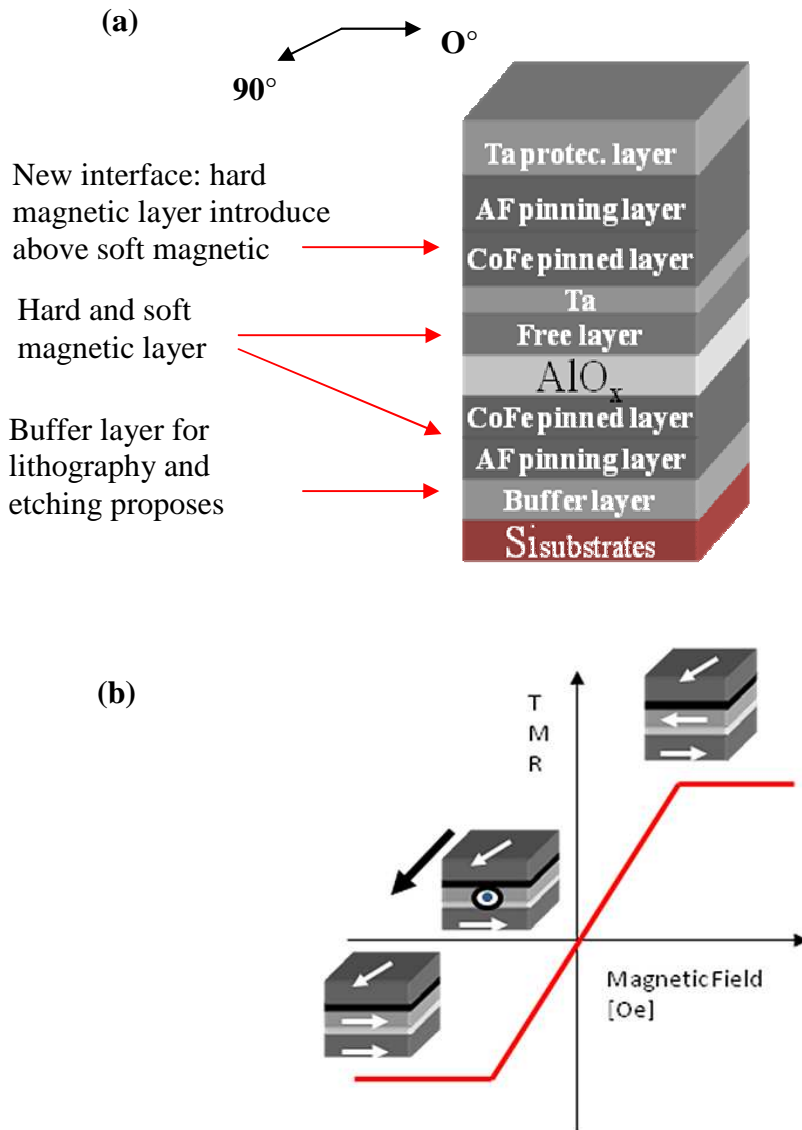
Figure 8.1 (a) Introduction of a new interface to the standard MTJs junction structure described in chapter 6 (b) Approaches: hysteresis free minor loop.

The new MTJ stack is deposited through magnetic masks that are used to align the magnetic layers. The lower layer structure including bottom layer, lower hard magnetic layer and aluminium-oxide barriers is sputtered with a " -90° magnetic mask", and the upper hard magnetic layer with a "0° magnetic mask" (See Figure 8.2).
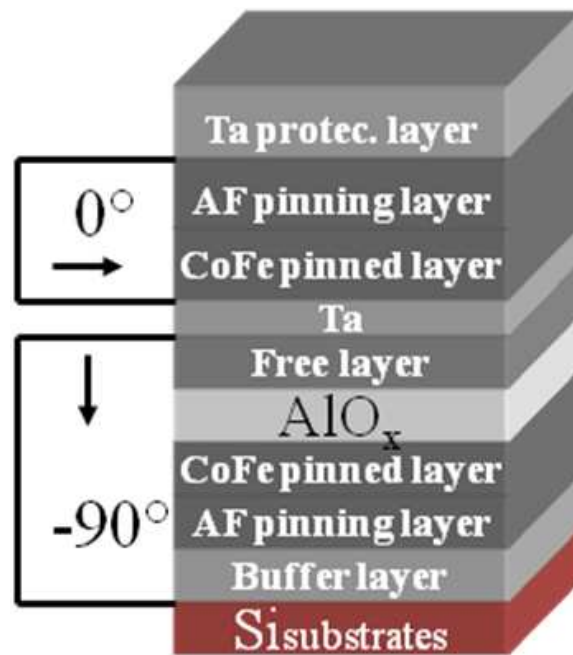
Figure 8.2 The layer stack is sputtered by using magnetic masks. The lower layers
are sputtered with a -90° magnetic mask, and the upper hard magnetic layer with a 0°
magnetic mask.

As is shown in Figure 8.1 (b), at negative field, the magnetization of the soft magnetic
layer is aligned parallel to the lower hard magnetic layer. At zero fields, the free layer is
oriented to the pinning direction. At zero field, the layer is aligned perpendicular to the
lower hard magnetic layer. These changes in the magnetization orientation of Py layer
produce a hysteresis free signal.

8.2 MOKE measurement

Prior to sensor pattering, the magnetic properties of the structures are examined using the
MOKE (See Section 4.2.2). In this experiments different types of structures are used,
where the thickness of the Py and the Ta layer (the layer between the free magnetic layer
and the upper hard magnetic layer) are varied. The final MTJ stack used in these
experiments comprised: Si/ $Ta_{6.5nm}$/Cu_{30nm}/Ta_{19nm}/ $MnIr_{15nm}$/$CoFe_{3nm}$/ $Al_{1.4nm+plas.oxid.}$/
Py_{5nm}/ Ta_{1nm}/ $CoFe_{3nm}$/$MnIr_{15nm}$/ $Ta_{6.5nm}$

The MOKE measurement for the above MTJ structure is presented in Figure 8.3. The measurement are done in two directions: 0° and 90° (See Figure 8.2).

(a)

(b)

(c)

(d)
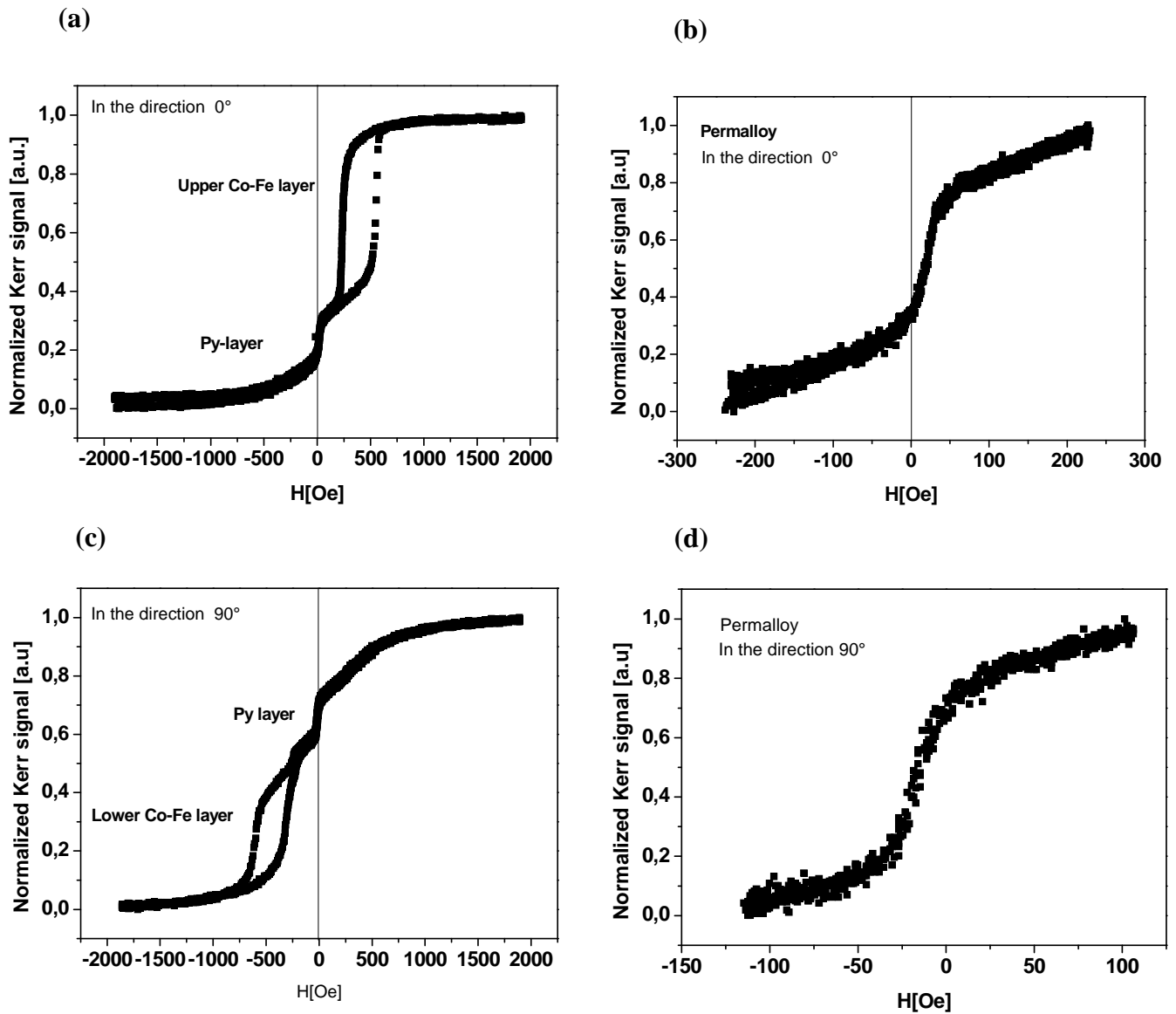
Figure 8.3 (a-d) MOKE measurements for Si/ $Ta_{6.5nm}$/Cu_{30nm}/Ta_{19nm}/ $MnIr_{15nm}$/$CoFe_{3nm}$/ $Al_{1.4nm+plas.oxid.}$/ Py_{5nm}/ Ta_{1nm}/ $CoFe_{3nm}$/$MnIr_{15nm}$/ $Ta_{6.5nm.}$ The measurement is done in two direction: 0° and 90°.

Figure 8.3(a) shows a switching of two ferromagnetic layer: the free Py magnetic layer and upper hard magnetic layer (See Figure 8.2). The Py layer switches around zero field. The pinned upper hard magnetic layers (Co-Fe layer) switches far from H=0 due to exchange bias. A similar situation is also observed in Figure 8.3 d, where the switching of the lower and the free electrode is presented. Figure 8.3 (b) and 8.3 (d) shows, that the change in the orientation of the free magnetic layer in external applied magnetic field produces a hysteresis free loop.

8.3 Transport measurement

For the experiments, several different MTJ structures are studies: rectangular and elliptical elements with different junction sizes. Figure 8.4 shows a major loop and minor loop measurement of the square MTJ elements with an active area size of $10\mu m^2$.

(a)   **(b)**

(c)
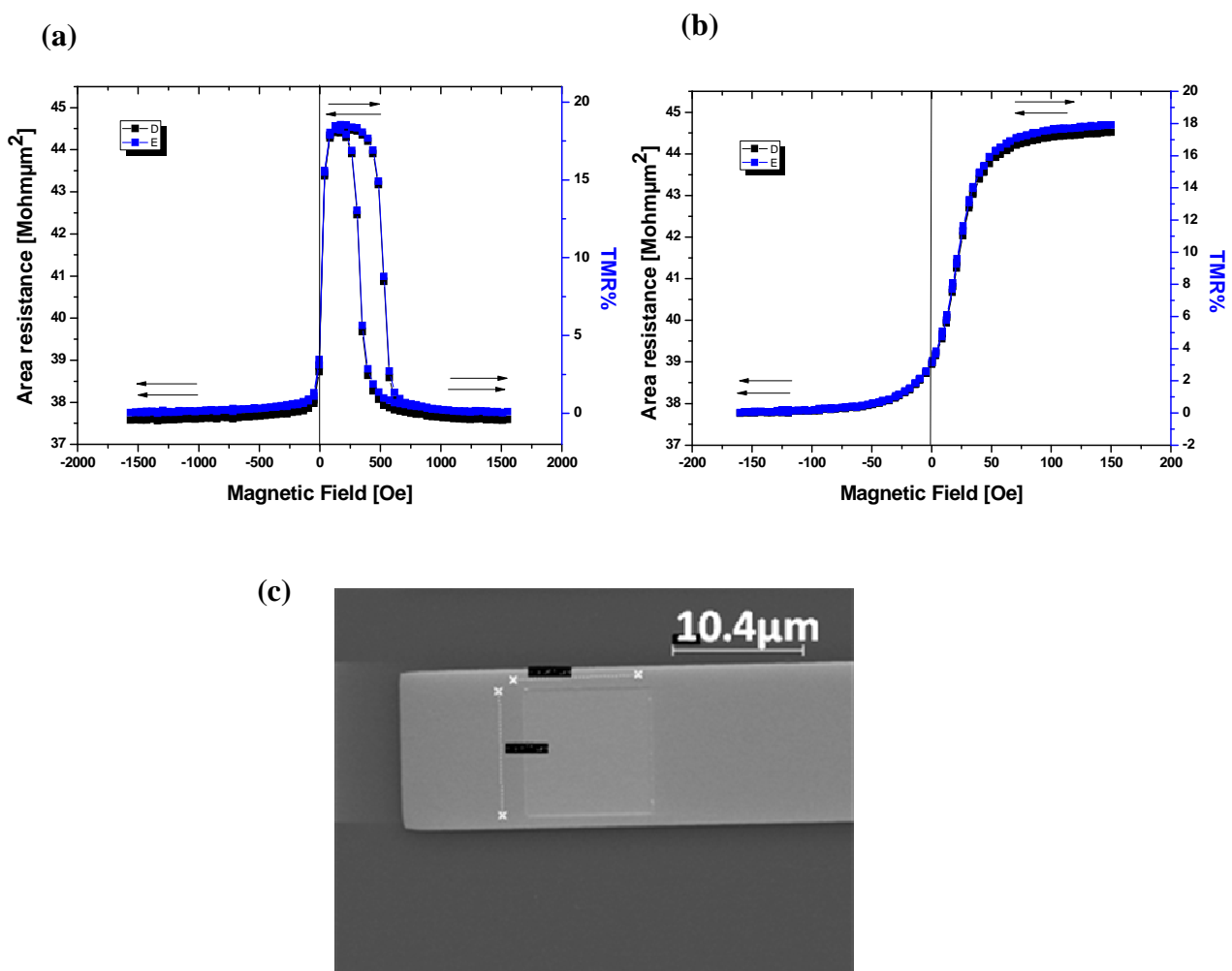
Figure 8.4 (a-b) Major loop and minor of the MTJ elements with an active area of $10\mu m^2$.

(c) SEM photo of the $10\mu m^2$ MTJ sensor element.

As shown in Figure 8.4 (a), the sensor elements exhibits TMR ratio up to 18.5% at room temperature and an area resistance product of about 37 to 46 M$\Omega\mu m^2$. The in plane magnetic field is applied parallel to the pinning of the bottom electrode. The Py magnetic layer switches around zero magnetic field and exhibits a hysteresis free loop (See Figure 8.4(b)).The I/V curve of the elements is presented in Figure 8.5.

(a)

(b)
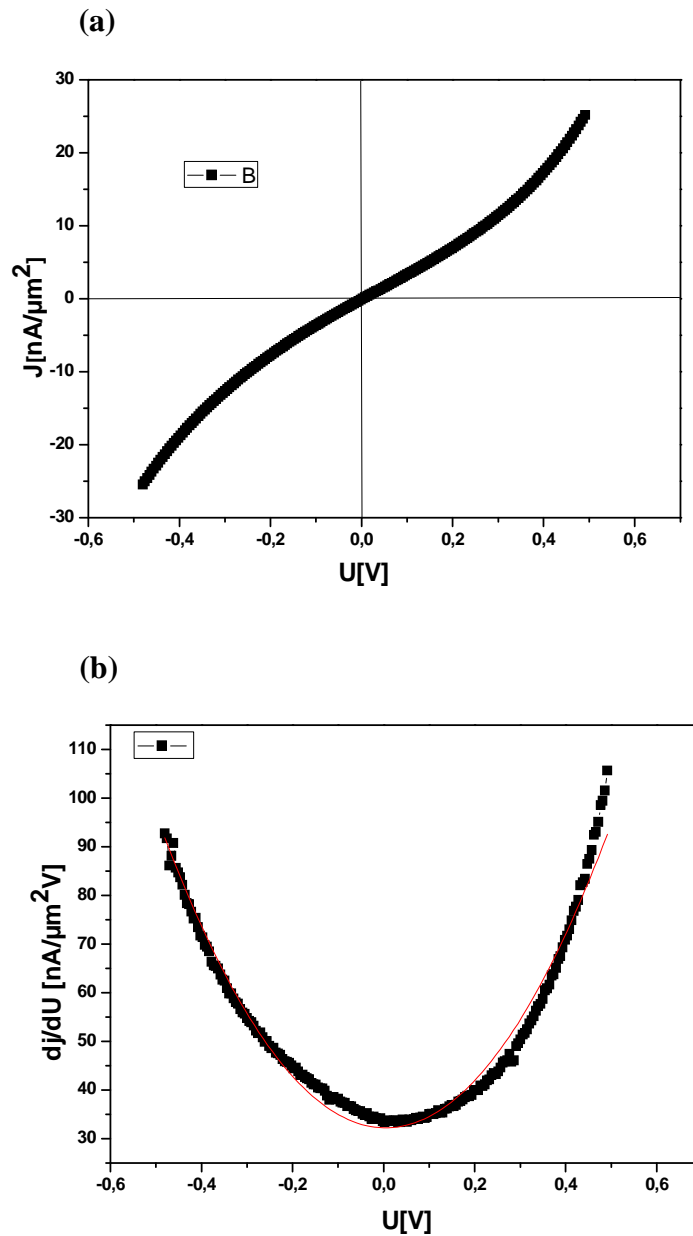
Figure 8.5 Electrical characterization of the tunneling barrier of the 10μm^2 sensor elements (a) the IV curve (b) differentiated I/V plot.

Applying the Brinkman fit to the differentiated plot in Figure 8.5 (b) gives the following barrier parameters: barrier height - $\overline{\varphi} = 1.20eV$, a barrier thickness of $d = 2.23nm$ and an asymmetry $\Delta\varphi = 0.07eV$ .The thickness of the barrier obtained from the Brinkman fit equals 2.23nm and is thicker as the expected value of 1.8nm.

Figure 8.6 shows major and minor loop measurements for an elliptical-like shaped MTJ sensor element with an active area of $2\mu m^2$. Here, again, the in plane magnetic field is applied parallel to the pinning of the bottom electrode.

(a)

(b)

(c)
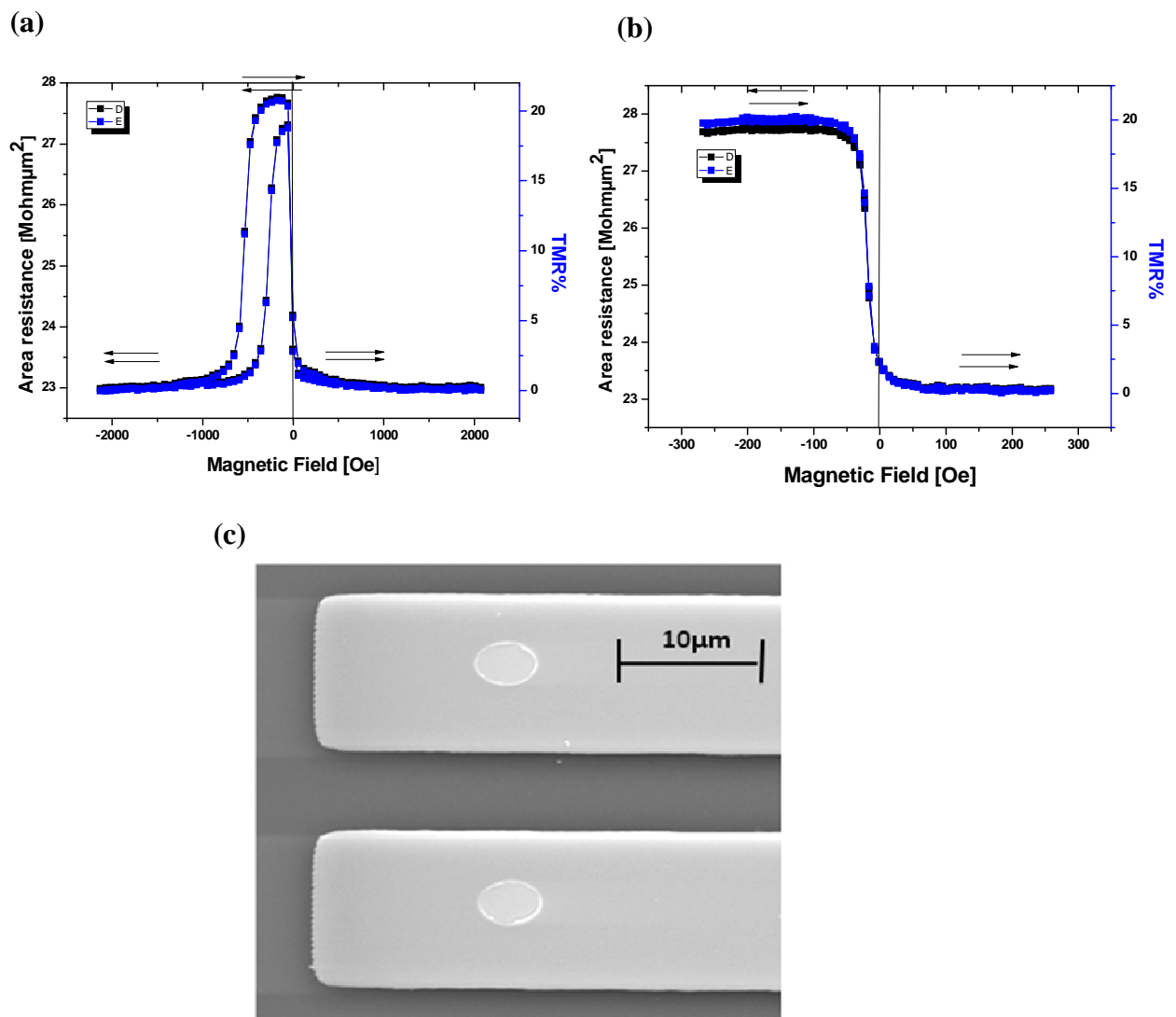
Figure 8.5 (a-b) A major loop and minor loop of an elliptical-like shaped MTJ element with an active sensor area of $2\mu m^2$. (c) SEM photo of the $2\mu m^2$ MTJ sensor elements.

At an area resistance between 23 and 28 MΩµm², the measured TMR ratio is around 21% at room temperature. The Py layer switches around zero magnetic field and produces a hysteresis-free loop. The I/V curve measurement is presented in Figure 8.6.

(a)

(b)
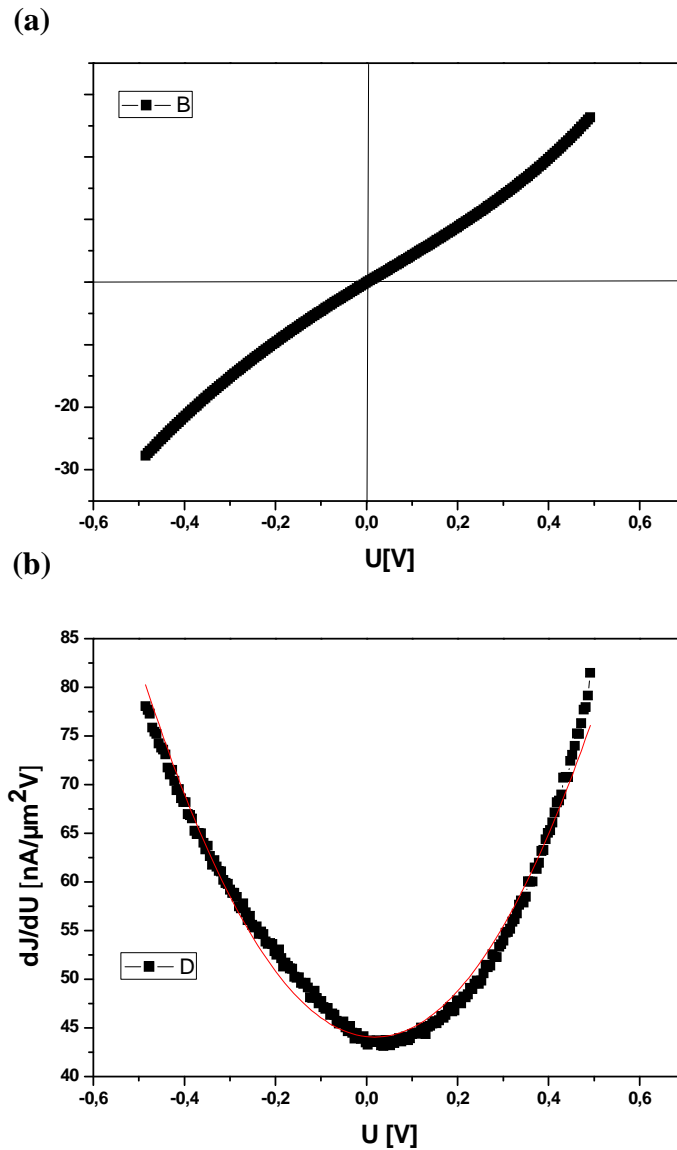
Figure 8.6 Electrical characterization of the tunneling barrier of the 2µm² sensor elements (a) the IV curve (b) differentiated I/V plot.

The barrier parameters obtained for this element are as follows: barrier height $\bar{\varphi} = 1.90eV$, barrier thickness $d = 2.18nm$ and asymmetry $\Delta\varphi = 0.52eV$.

The major and minor loop for small, elliptical elements with an area of $1\mu m^2$ are presented in Figure 8.7.

(a)

(b)

(c)
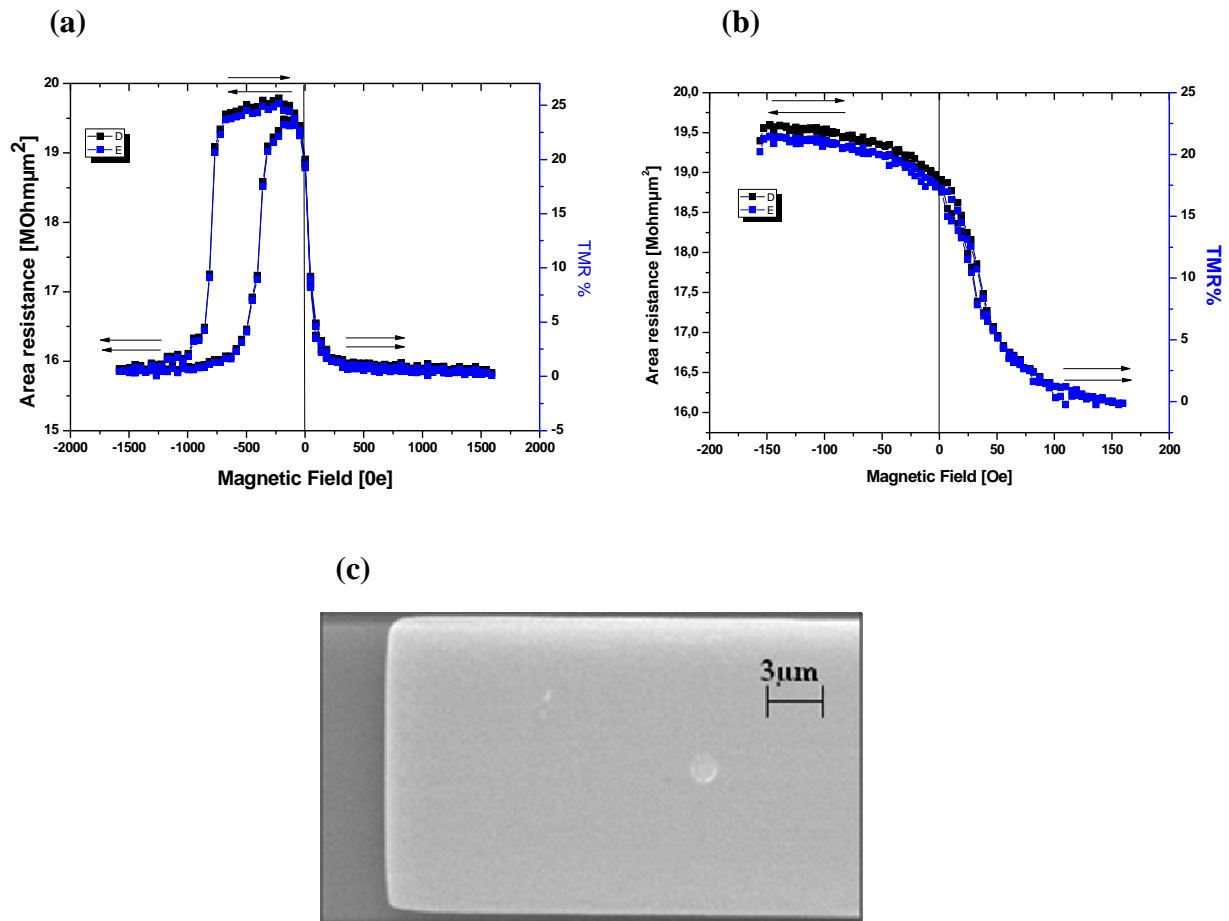
Figure 8.7 (a-b) A major loop and minor loop of an elliptical-like shape MTJ element with an active sensor area of $1\mu m^2$. (c) SEM photo SEM photo of the $1\mu m^2$ MTJ sensor elements.

The TMR elements have an area of $1\mu m^2$ and exhibit a TMR ratio of 25% and an area resistance product between 16 and 20 $M\Omega\mu m^2$. Here, again the Py layer switches around zero magnetic field and exhibits hysteresis-free loop. The IV curve of the element is presented in Figure 8.8.

(a)

(b)
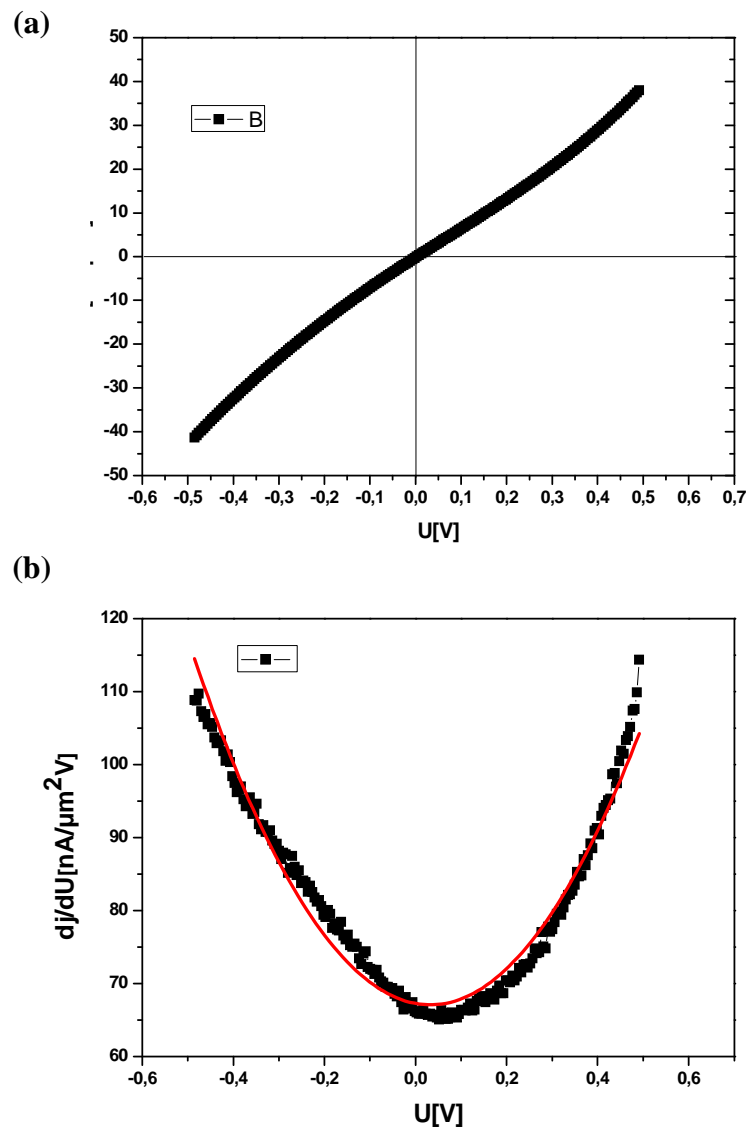
Figure 8.8 Electrical characterization of the tunneling barrier of the $1\mu m^2$ sensor elements

(a) the IV curve (b) differentiated I/V plot.

The following barrier parameters are obtained: barrier height $\overline{\varphi} = 2.09eV$, barrier thickness of $d = 2.05nm$ and asymmetry $\Delta\varphi = 0.94eV$. Here again, the thickness of barrier layer is different from the expected value of 1.8nm.

8.4 Conclusion

In this chapter, different sensors elements with elliptical and rectangular shapes are presented. In all cases the Py layers switch around zero magnetic field and exhibit hysteresis-free minor loops. The obtained TMR ratios varied between 20 and 25%. In all measurements, the barrier thickness is larger than the expected value of 1.8nm. This is due to sputtering through the mask that produces the orthogonal orientation of the free and the hard magnetic layer at zero magnetic field. The sensitivity of the new MTJ system is not very high in comparison to standard MTJ stacks and it is comparable to spin valve sensors. The aim of this experiment was, however, not to produce a high TMR ratio but to enable an exact comparison of minor loop hysteresis with reference curves by means of the MTJ sensor. For this thesis, this system is sensitive enough and can be used in model experiments with an MFM tip or in real system with ferromagnetic particles.

_____

_____

9. Single magnetic particle positioning

Several methods have been employed to position a single particle on top of the active area of the MTJ sensor. This chapter gives an overview concerning these methods and highlights particular practical aspects.

9.1 Precision attachment of a particle to the AFM cantilever

The results of the model experiments presented in chapter 6 and 7 demonstrate that differences in the transport measurements are strongly dependent on the tip position and the corresponding magnetization configuration in the sense layer. The model experiments carried out on small sized elements show, that a tip has a large magnetic moment, which strongly affects the sensitivity of the sensor elements .

Considering these results a modification of the AFM tip was proposed as a solution to the problem. An AFM tip can be modified by attaching a magnetic particle to the cantilever. A modified AFM cantilever is used in this work in order to determine the signal response of the MTJ sensor elements in the presence of tips with a precisely defined shape and dimension. Because of the pyramidal shape of the standard AFM probes, it is difficult to calculate the magnetic moment of an MFM tip; one can only check whether the probe is magnetized correctly. Another advantage of the applied method is that, a "real" single magnetic particle can be placed with the AFM cantilever at any desired site on top of the active area of the MR sensor.

In order to modify an AFM cantilever tip we applied a method, which is analogous to that presented by S.T.Huntington et.al from University of Melbourne [207]. The procedure is as follows: the first step required the selection of an AFM cantilever with a desired resonance frequency (70 kHz) and spring constant (2 N/m) OLYMPUS [208]. The actual tip parameters are presented in the figure 9.1.

	Typical value	Typical range
Tip height (um)	14	9- 19
Tip radius (nm)	6	less than 10
Tip angle (deg.)		(side) less than 35 (front) less than 35

Cantilever length L (um)	240 (±20)
Cantilever width W (um)	30 (±2)
Cantilever thickness t (um)	2.8 (±0.8)
Metal coat thickness tm (um)	Aluminum 0.1 (±0.04)
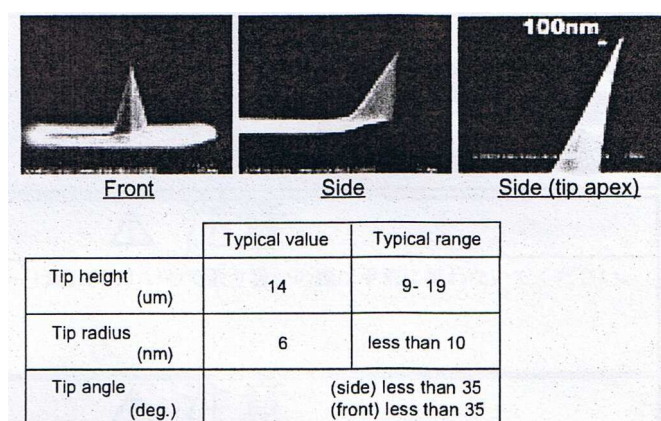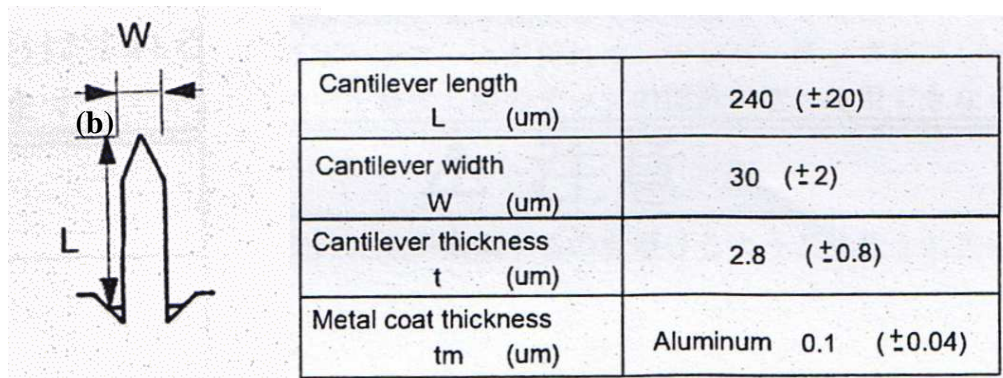
Figure 9.1 Standard AFM tip, fabricated by Olympus, used in the experiments

(a) tip dimension (b) cantilever dimension [208].

Then magnetic particles with a diameter size of 1.5 µm were used (Micromod). Since the small sensor area is ellipsoid in shape with a surface area of $12\mu m^2$, this size is suitable for testing the detection capability of the sensor and yet they are large enough to be visible under a light microscope integrated with a Scanning Force Microscope. To glue the particles to the AFM cantilever, an epoxy glue (Norland Products Nost.81) was used as this type of adhesive has a very long cure time.

To facilitate the bonding of the microparticles to cantilevers, a small quantity of the particles were dispersed onto the Si wafers ($0.5 \times 0.5\mu m^2$) and the solvent was allowed to dry. Later, the samples were mounted on the microscope stage using double sided sticky tape.

The particles are usually supplied in a solution that contains salts or other ingredients. According to the instruction from BioForce Laboratory the particles have to be washed with ddH$_2$O and dried prior to deposition. To facilitate washing of the particles, a Pick Pen tool (Bio-Nobile) was used [193]. The PickPen tip has the advantage that it can be dipped into the suspension containing magnetic particles in order to collect them. The time required for the collection of the particles depends on the amount of particles, their size and the viscosity of the suspension. When the particles are collected on the tip, they are withdrawn from the solution and transferred to the next suspension. The particles remain attached to the end of the tip due to a magnetic force, which can be switched off after transferring to the next solution (See Figure 9.2).

Figure 9.2 The PickPen method for purification of magnetic particles. Images have been taken from the reference documentation supplied by the manufacturer [193].

When the particles are released into the solution, the probes are put in an ultrasonic bath for two minutes. After this procedure, the particles are dispersed over the wafer surface.

The general setup for mounting the particles on the AFM tip is presented in Figure 9.3. The procedure for bonding the particles is as follows:
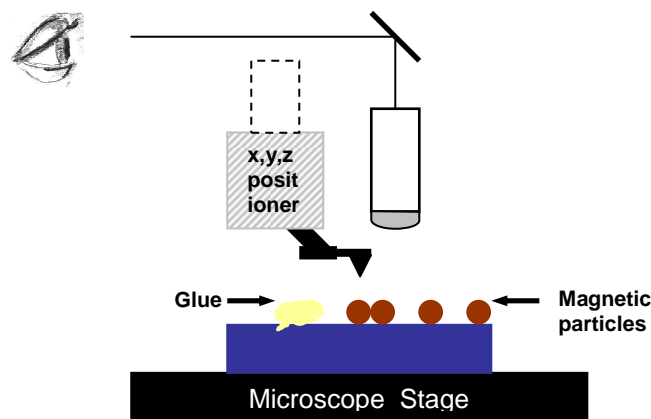
Figure 9.3 Set up for mounting the particle on the AFM cantilever.

In the first step a small amount of glue is placed within a short distance of the particles on the silicon wafer. The desired particles are then identified with the optical microscope. The AFM cantilever is then located in the center of the field of view, moved in the direction of the glue and then dipped into the drop. Next, the cantilever is moved up and shifted to the location of the desired particle and lowered to catch it .

171

When the procedure is complete, the AFM probe is taken out from cantilever support and transferred to the SEM for observation. The proximity of the SFM and SEM devices allows to test quickly, whether the particles are bound to the end of the tip or not.

While carrying out the experiments, considerable difficulties were encountered with the particles. If dried directly on to the silicon substrate the particles became charged and firmly bonded to the surface. Even if the particle were washed several times with ddH_20, they remained stuck to the wafer surface. It was very difficult to catch them without damaging the probes. The particles also have a surface charge and had a tendency to fly over when the cantilever approached them. The method for bonding the microparticles to the AFM probe appeared simple but all attempts to catch them failed. In our opinion this method can only be successfully applied to large magnetic microparticles (>2.5 µm).

9.2 Electron Beam Deposition (EBD) tips

In this section, we will present an advanced MFM probe fabrication method, based on electron beam deposition and then discuss the possibilities of the fabrication of such advanced MFM tips. This method is an alternative to that presented in section 8.1.

A technique of using electron beam deposition (EBD) was first applied to STM probes by T. Fujii et al. in 1990 who fabricated long and sharp tips onto the V shaped Si_3N_4 cantilevers (See Figure 9.4) [197].
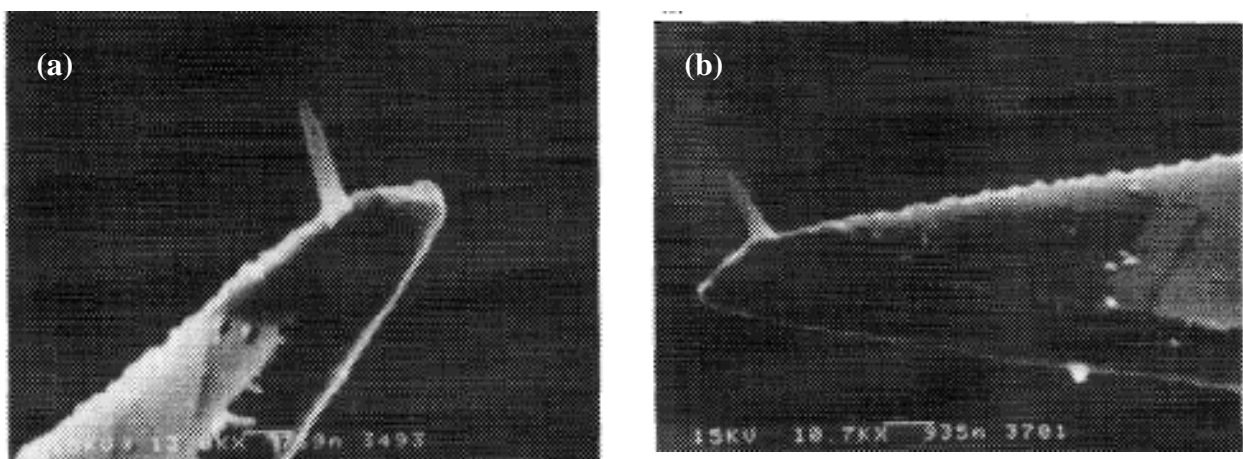
Figure 9.4 (a) EBD tip before and after (b) the measurement of the microfabricated V shaped Si_3N_4 cantilever by T. Fujii [197].

The EBD presented in figure 9.4 was made using 5 min irradiation with a 15-kV electron beam with an emission current of 100µA. The tip was 2µm in length, had a 50nm tip radius and diameter 100nm below the apex of 200nm.

A similar method to that presented by T. Fuji has been used to fabricate advanced MFM probes [198].The experimental results presented by the University of Saarland shows that an advanced probe allows high-resolution imaging of fine magnetic structures within thin-film Py elements without perturbing them [198]. A schematic diagram for the fabrication such tips is presented in figure 9.5.
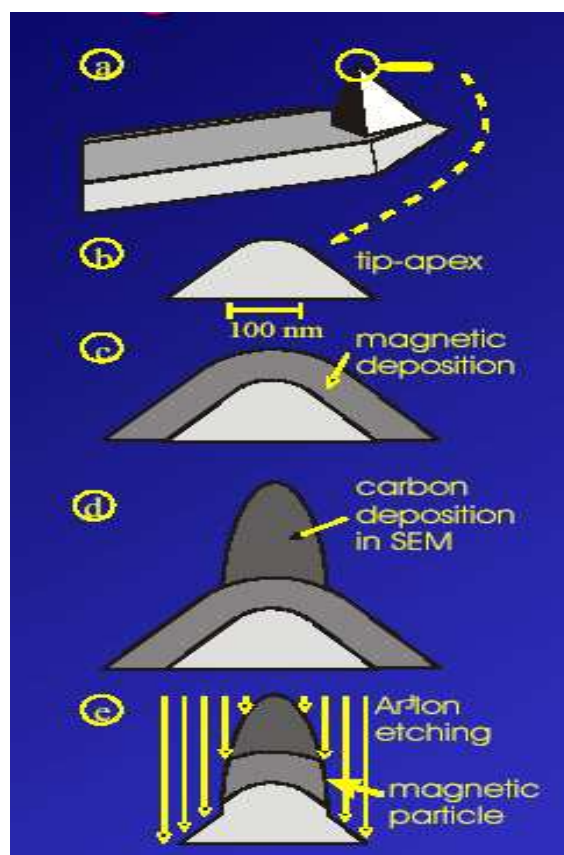
Figure 9.5 A schematic representation of the processing steps in the fabrication of advanced MFM probes - University of the Saarlanad [198].

In the methodology reported by the University of Saarlanad, a standard cantilever tip is coated of the front with a 50-100nm magnetic film of CoCr (see figure (b) and (c)). In the next step the tip is placed into the SEM and the electron beam focused onto the tip apex for 10-15min. The electron beam deposits a tiny carbon tip right at the apex of the cantilever tip [198].

The carbon tip is used as an etch mask in Ar^+- ion milling of the front side of the cantilever. This results in a cantilever with a tiny magnetic particle exposed at the probe apex [198] (See Figure 9.5 c).

In our experiments we wanted to develop a modified MFM probe and test the response of the MTJ sensor element in the presence of such a well defined magnetic particle. The method used to fabricate the EBD tips is presented in Figure 9.6.

(1)   Tip-apex

(2) Metal deposition $Ta_{5nm}/CoCr_{90nm}/Co_{2nm}/Ta_{5nm}/Au_{45nm}$

(4) Carbon deposition in SEM

(3)   Droplet aceton/parafin oil
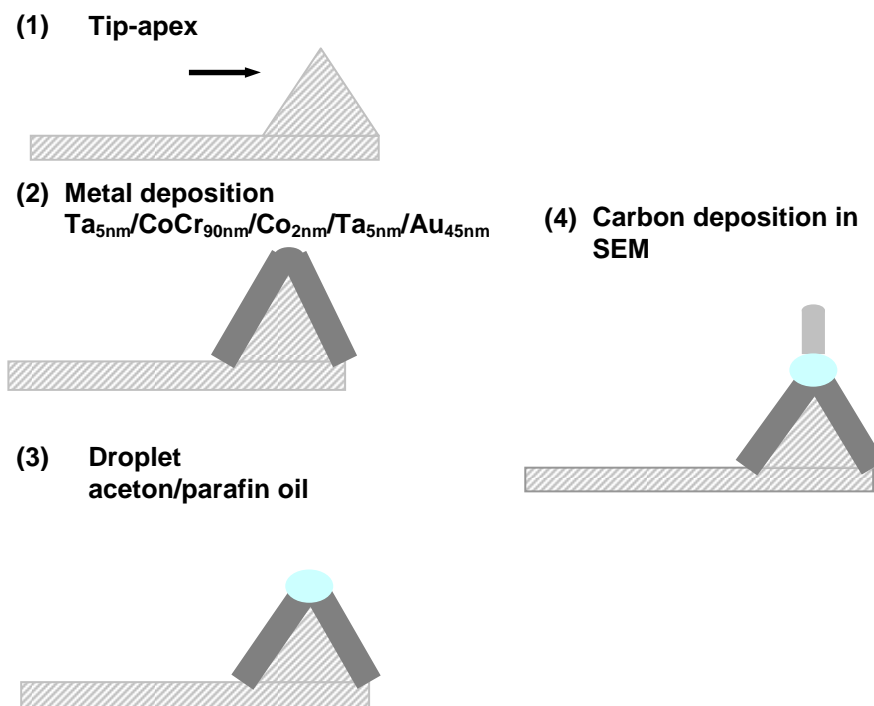
Figure 9.6 Schematic of the methods used for EBD tips deposition.

An EBD tips were fabricated using a standard AFM probe from Olympus [208]. The parameters of the tips are tabulated in Figure 9.1. After magnetic coating, the tip was placed in a UVH chamber for gold deposition (45nm). When a layer was sputtered on the tip's apex, the sample was removed and fixed onto a silicon wafer. Double-sided sticky tape was used to fix the tip on the wafer. In the next step a droplet of a mixture of acetone /paraffin oil was dispersed on the tip apex. After preparation, the probes were left to air dry for 24 hrs before being placed under a scanning electron microscope. In the last step, the tip was transferred under the microscope and the electron beam focused onto the tip apex for 1-2min.

_____

In the first step an EBD tip was deposited onto the silicon wafer. The experimental results are shown in Figure 9.7. The EBD tip was grown under 30 s focusing with a 20 kV electron beam. The tip was 950 nm in length and had a radius of approximately 50 nm.
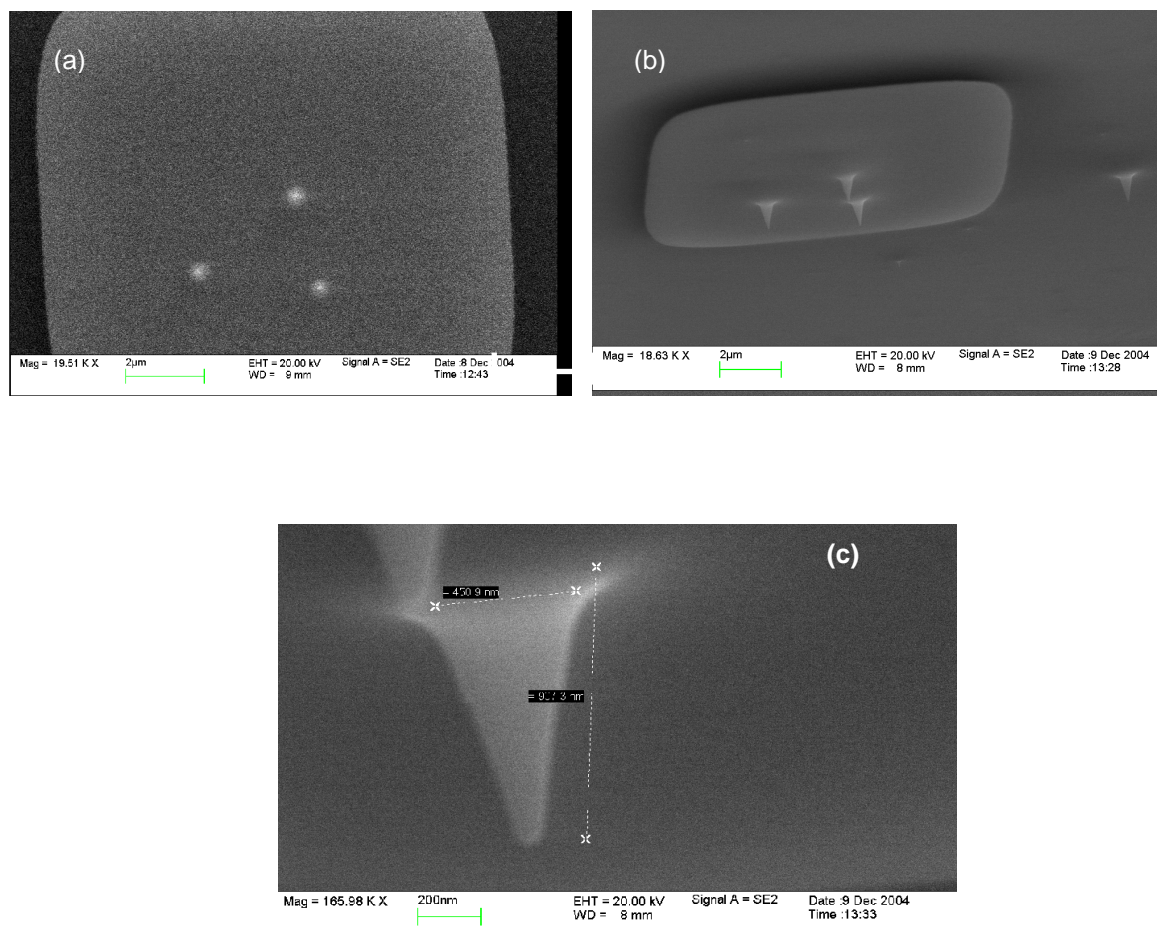
Figure 9.7 SEM micrograph of the deposited EBD tip on a silicon wafer
(exposure time 30s by 20 kV, 200-220 nm –tip radius)
(a) carbon spots, (b) and (c) a close-up view of a tip.

The height and the base diameter of the EBD tip depend on the focusing condition and the exposure time. When the electron beam is focused onto the wafers for a duration of 1min, a carbon tip with a length of ~550 nm and radius ~200nm is deposited. If the exposure time is set to 2 mins, the length and radius of the tip increases to ~950 and ~400nm respectively (See Figure 9.8).
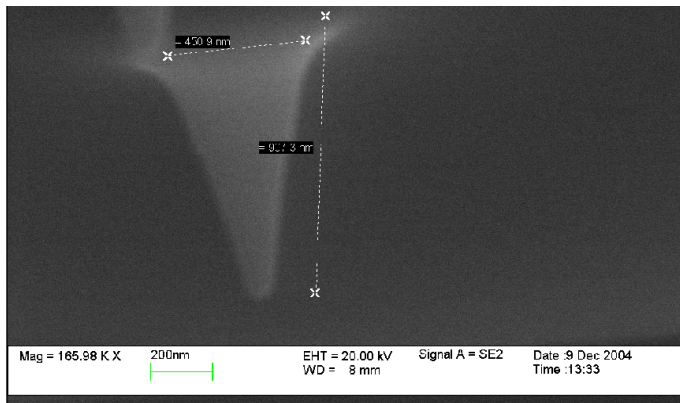
Exposure time 2min
Tips length:800-950nm
Tips radius:~50nm
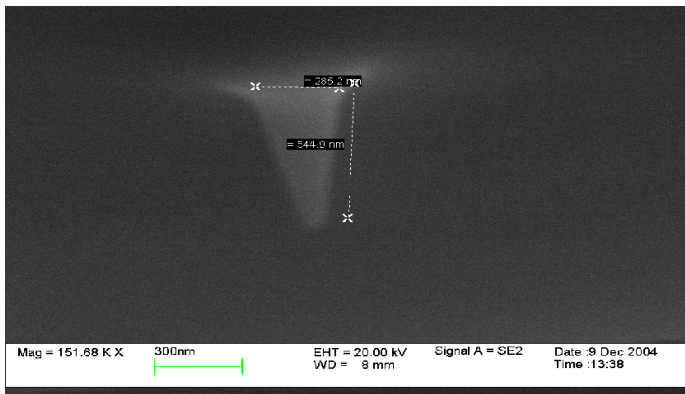
Exposure time 1min
Tips length:~500nm
Tips radius:~30nm

Figure 9.8 SEM micrograph of the deposited EBD tip on a silicon wafer.
(exposure time 1 and 2 min by 20 kV, 400 and 950 nm –tip radius).

By employing sharpened AFM tips, the fabrication of e-beam deposited (EBD) tips on top of the apex became problematic. Prior to deposition, the tip was coated with a hard magnetic layer stack $Ta_{5nm}/CoCr_{90nm}/Co_{2nm}/Ta_{5nm}$ and 45nm of Au layer. Then the AFM tips was transferred to the microscope and the EBD tips deposited by e-beam focusing onto the apex for 30 seconds with a 20kV. Figure 9.9 shows a SEM photo of an AFM probe after EBD deposition.
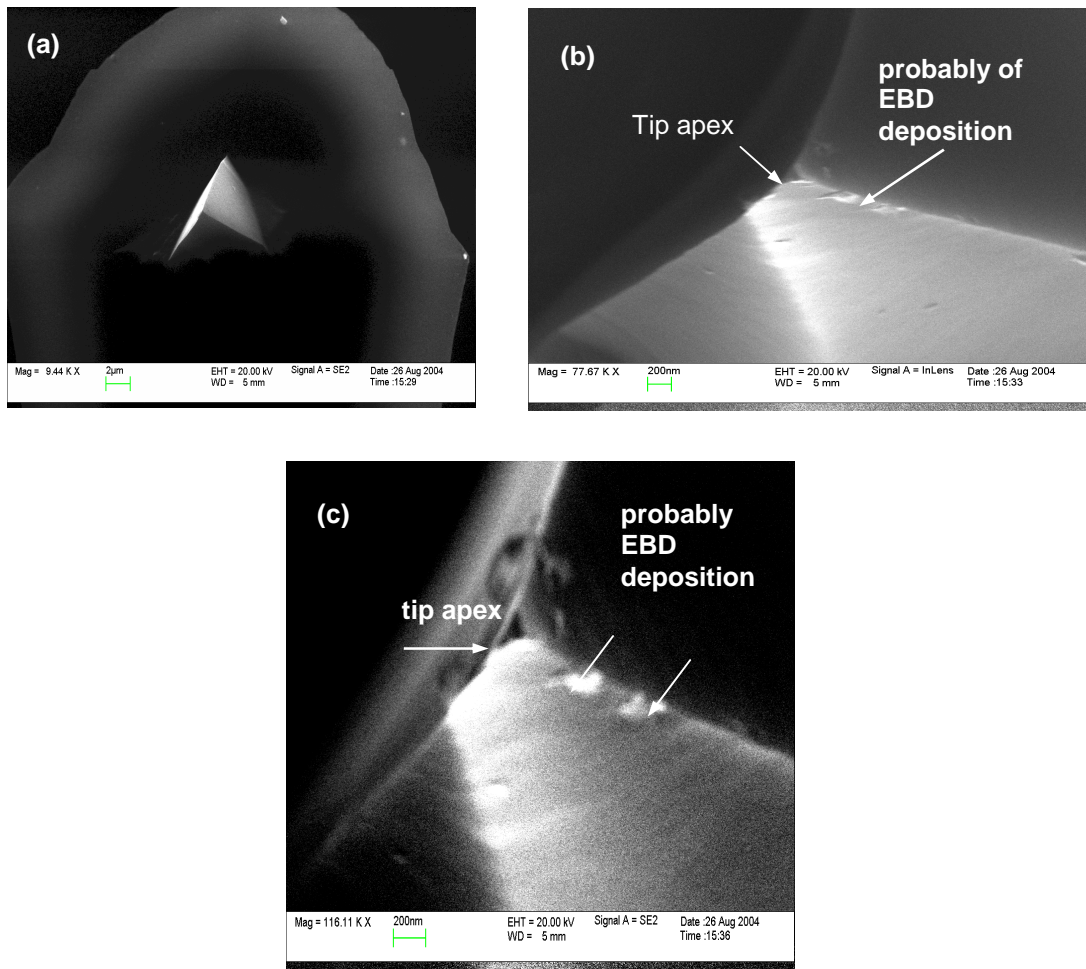
Figure 9.9 (a) Standard AFM tip used for EBD deposition in SEM

(b) and (c) Close up –AFM tip apex after EBD deposition.

Focusing at the tip apex causes a charging effect which results in the deflection of the electron beam. For this reason it is difficult to deposit an EBD tip directly onto the apex of an insulating AFM probe. After deposition, it was easy to locate the EBD spot on the silicon wafer. In the case of the AFM tip, the identification of the EBD tip on the tip's apex was problematic (for more details see Figure 9.9 (b) and (c)).

To summarize, the method used to fabricate EBD tips presented in this work is effective however all attempts to produce an EBD tip on the AFM tip apex have failed. Further work should investigate the use of a tipless cantilever. Another open question concerning the fabrication of EBD tips is the magnetization of the produced magnetic volume and the direction of the magnetiization.

9.3 Discussion

Positioning of a single magnetic particle on top of the sensor area is an integral part of the testing process.

In many experiments superparamagnetic particles are dropped over the sensor area in an aqueous solution and simply allowed to dry.

Later on, the position of the particles is identified under the microscope [75, 80, 82, 84].This method can be successfully applied to large superparamagnetic particles [82]. It can also achieve sound results in the case of small particles with a size below 1.5 µm in diameter, however, there are a few obstacles to consistent outcomes. First, the probability of finding a single particle exactly in the correct position on the sensor area is rather small. Second, sometimes this method entails the distribution of particles several times over the sensor surface until one reaches the desired position. During several probes, the particles are usually washed from the surface and this procedure can influence the sensor quality and destroy elements. Another problem is the aggregation of particles and their tendency to align in a multiple ring formation (for more details see section 9.3.2).

9.3.1 Aggregation of the particles

Even if the applied magnetic particles are superparamgentic and they are embedded into the polymer or silica matrix, they show a tendency to agglomerate and form a cluster. Figure 9.11 shows a cluster of magnetic particles with a size of 1.5 µm in diameter formed on top of an active area of a MTJ sensor.
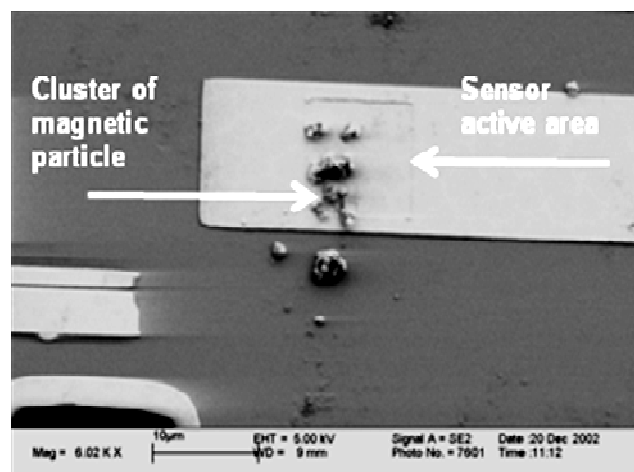
Figure 9.10 Agglomeration of magnetic particles with a size of 1.5µm in diameter on top of the sensor active area.

9.3.2 Concentric ring formation

There are a number of publications in the literature concerning the formation of two-dimensional arrays by evaporation a drop of particle containing liquid on a substrate [199]. The solution usually contains latex or metal spheres, polymer or proteins [199]. In the investigated system particles accumulate at the contact line and form ordered arrays [199]. The arrangement of particles in concentric rings within the drop was first reported by Deegan's et al. in 2000, but models describing this phenomenon were later proposed by Shmuylovich et al. in 2002 [199,200]

In the proposed model, evaporating water at the contact lines cause a flow of the particles towards a edges due to an evaporatively driven convective flow [199]. But not every particle reaches the contact lines, some of them become pinned to the substrate (see Figure 9.11).
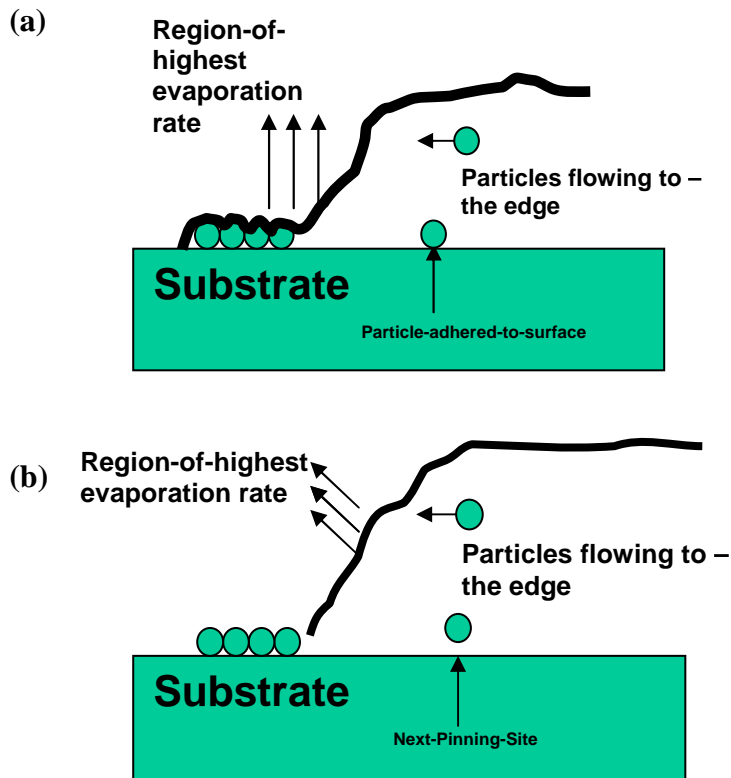
Figure 9.11 (a) Formation of the pinned line (b) Movement of the contact line to the particle and formation of the next pinned line [199].

The contact line exhibited also stick-slip motion as the water evaporated [199]. When the contact line slips the agglomerate particles at the edges it keeps moving until it reach the

next particle and the pining may start again [199]. This stick-slip motion of the contact line causes a formation of the multiple rings [199].

The agglomeration of particles at the line edges has also been observed in solutions which contain magnetic particles. Figure 9.13 displays a close-up view of the ring observed in a drop consisting of 250nm silica particles dispersed on the silicon wafer.
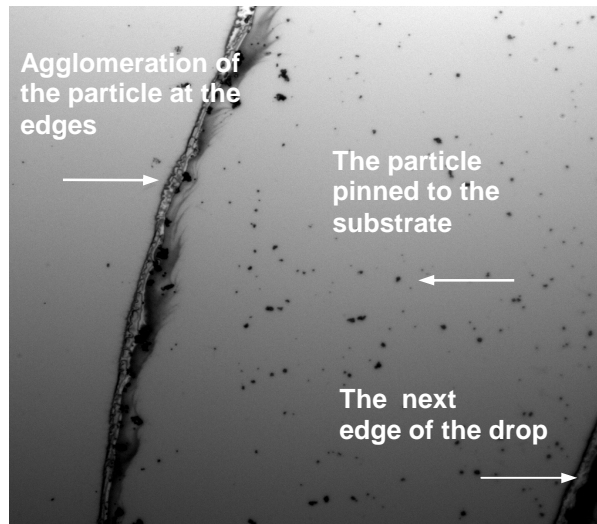
Figure 9.13 An optical image photo (50 x magnifications) of a dry drop comprising 250nm diameter magnetic particles. The image shows the edge of the contact line with the magnetic particles aggregated at the edges.

9.4 Conclusion

This chapter presents two methods for the positioning of a single magnetic particle on top of the active area of the MTJ sensor. One example described how the particle can be bound to the end of AFM probes and positioned precisely with the cantilever on top of an active area of the sensor. It is also possible to modify a MFM probes by electron beam deposition and produce a small magnetic particle at the end of the apex. In the first method, all attempts to catch the small particle (1.5µm) were unsuccessful. In the second methods, we succeeded in fabricating an EBD tip on the silicon wafer, but we failed to produce such an EBD spot on the apex of the MFM tip.

In our opinion, the most effective methods is the positioning and transport of small particles using a conducting line. This method was developed in our research group, by another researcher, and is described in detail in [85].

Summary and Outlook

Today, biosensors have found many applications in different fields including medicine, healthcare, environmental protection, biotechnology and the military. Significant developments have been made in the medicine, health care and the military because of their greater financial support. Many projects have involved significant investments in the development of a small portable device that is easy to use, inexpensive, miniaturized, and highly sensitive. This small device, so called a 'lab-on-a-chip', integrates one or more laboratory tasks on a single chip with an area of a few micrometers up to a few millimeters. Within these small devices fluorescence and electrochemical methods are commonly used for detection. In 1998, Baselt et al. presented a new concept in biological labeling that combines magnetoresistive sensors with magnetic particles [80]. This type of sensor is more sensitive than fluorescence types and has the added benefits that it can be miniaturized to the nanoscale and produced cheaply. This work presents an overview of magnetic particles and their application in this progressive and exciting field and includes the introduction and description of different types of magnetoresistive transducers.

Since 1998 many groups have followed the idea presented by Baselt. In our research group this concept has been further developed [80]. In the first thesis on the biosensor, the signaling of the GMR and TMR types of sensor is analyzed systematically under various conditions and the results compared to simulations. In this experiment a spiral-like shaped GMR sensor with an area comparable to a DNA spot was used for the first time. Here, the sensitivity of the GMR sensor was compared to a standard fluorescent detection method and was found to be higher than the sensitivity of fluorescence sensor [75].

This work describes the development of magnetic tunnel junction sensors for the detection of a single magnetic particle. Here, for the first time, the sensitivity of the magnetic tunnel junction sensor (MTJ) is proved down to the single magnetic particle level.

MTJ sensors are fabricated using an E-beam lithography technique combined with Ar ion-beam etching. A detailed description of the fabrication procedures is presented.

Two different detection methods are used to prove the detection capability of the MTJ sensor. In the first method, a suspension of magnetic particles is dispersed over the sensor surface and the position of magnetic particles is controlled using scanning electron beam lithography (SEM). In the second method, a model experiment is carried out, where home-made magnetic force microscope tips serve as an artificial magnetic particle on top of the sensor element. Two different types of sensor element (rectangular and elliptical) are examined.

The experimental results are compared with micromagnetic simulation.

Further, to enable a better analysis of the differences in transport measurement a hysteresis free magnetic tunnel junction sensor is presented. The sensor is fabricated by introducing a new interface above the soft magnetic layer in the standard MTJ stack used in this work. The TMR amplitude of the new MTJ sensor is around 20% which is comparable to a commercial spin valve sensor. The sensor is sufficiently sensitive to be used in a model experiment or in real system with micromagnetic particles. Parallel to this experiment, different methods for positioning of single particles on top of an active area are studied. The particles can be boound to the end of AFM probes and positioned precisely with the cantilever on top of the active area of the sensor. It is also possible to modify MFM probes by electron beam deposition to produce a small magnetic particle at the end of the apex. Our research group has also developed a third method where the single particle can be positioned and transported with a conducting line which is the subject of another thesis [85]. The third method is probably the most effective method that can be used for the transport and positioning of a single magnetic particle.

During the writing of this thesis there has been a recent development in the field of single magnetic particle detection. In 2005, Gang Xio's group from Brown University also began focusing on single magnetic detection and MTJ sensors [201]. In their experiment, the MTJ sensor is integrated into a microfluidic channel, and they were able to detect the presence of moving superparamagnetic particles. In 2007, the Philips Research Laboratories in Eindhoven demonstrated the detection of a 2.8μm single particle using a $100 \times 3 \mu m^2$ giant magnetoresistive sensor [202].

The experiment carried out by the Philips research group is similar to the model experiment presented in this thesis, but in contrast to us, they glued their 2,8μm particles to the tip of an atomic force microscope and magnetized the particle using conducting wires integrated in the sensor [202]. In their experiment, similar to us, they observed the influence of the single magnetic particle on the sensor strip (for comparison see section 6.3 and reference). They also observed a transition between "bright and dark bands"close to the center of the sensor [202]. Their experiments led to conclusion that by using this type of sensor it is possible to detect a single 300nm superpraramagnetic particle [202].

In our group CoFe ferromagnetic particles are fabricated and the manipulation of the magnetic nanoparticles with stray field of ferromagnetic layers was demonstrated [203].

A new class of magnetic tunnel junction structure is developed comprising a crystalline MgO tunnel barrier. This new MTJ exhibits a very large room-temperature magnetoresistive effect (over 200%) [204]. With very high sensitivities this new magnetic tunnel junction can be applied in biosensor technology and currently researches in our group are moving in this direction.

These developments have opened up many opportunities for future research and development. One interesting avenue for future work would be the investigation of the direct application and use of highly sensitive sensors in molecular diagnostics or for the detection of single nucleotide polymorphism. To facilitate this experiment, the sensor surface would have to be immobilized with an array of oligonucleotides (short nucleic acid polymer, 15 to 25 bases in length). The genomic DNA of interest will be multiplied using polymerase chain reaction (PCR) methodology and the PCR product will be labeled by a functionalized magnetic particle. Later the labeled PCR product will be spotted on the sensor surface. Then the sensor will be left for hybridization and the signal output analyzed in an external magnetic field.

Bibliography

[1] H. Nakamura and I.Karube, Current research activity in biosensor, Anal Bioanal Chem , 373:446-468, 2003

[2] A. J. Baeumer, Biosensors for enviroemntal pollutants and food contaminants, Anal Bioanal Chem, 377: 434-445, 2003

[3] A. G. Mignani, F. Baldini, Biomedical sensor using optical fibres, Reports on Progress in Physics, 59: 1-28, 1996

[4] C. B. Wilson, Sensors in medicine, British Medical Journal (BMJ), 319 : 1-3 , 1999

[5] C.L Clark and C. Lyons, Electrode system for continous monitoring in cardiovascular surgery, Ann NY Acad Sci, 102: 29-45, 1962

[6] S. J Updike and G.P Hicks, The enzyme electrode, Nature, 214:986-988, 1967

[7] G.Guilbault, J. Montalvo, Enzyme Electrode for the Substrate Urea, J Am Chem Soc,92:2533-2538, 1970

[8] T. M. Canh, Biosensors (Sensor Physics and Technology), Chaman & Hall and Masson, Masson, Paris, 1991

[9] O.S Wolbeis, Optical sensors (Industrial Enviromental and Diagnostic Application), Springer Verlag Berlin 2004

[10] F. Scheller and R.D Schmid, Biosensors : Fundamental Technologies and Application, GBF (Gesellschaft für Biotechnologische Forschung mbH), Braunschweig, 1992

[11] Engineering Science and Technology Division, Oak Ridge National Laboratory, Advanced biosensor, www.ornl.gov

[12] Wikipedia, free encyclopedia ,Biosensor, www.en.wikipedia.org

[13] Rain University, Biotechnology Lectures , Biosensors, www.rcw.raiuniversity.edu

[14] A.P.F Turner, Biosensors-Sense and Sensitivity, Science, 290: 1315- 1317, 2000

[15] M.Mehrvar, C. Bis, J.M Scharer, M.Moo-Young, J.H.Luong, Fibre-Optics Biosensors-Trends and Advances, Analytical Sciences, 16: 671-699, July 2000

[16] Images taken from the homepage of Malysia University of Science and Technology , www.must.edu.my/~ccyeo/topics/biosensors.html

[17] L.J. Kricka, Microships,microarrays,biochips and nanochips:personal laboratories for the 21st century, Clinica Chimica Acta 307: 219-223, 2001

[18] P.Dario, M. Carrozza, A. Benvenuto and A.Menciassi, Micro-systems in biomedical application, J. Micromech. Microeng, 10: 235-244, 2000

Bibliography

[19] J. Castillo, S. Gáspár , S. Leth, M. Niculescu, A. Mortari, I. Bontidean,V. Soukharev, S.A. Dorneanu,, A.D. Ryabov, E. Csöregi, Biosensors for life quality.Design, development and application, Sensors and Actuators B 102 (2004) 179–194

[20] M.P. Marco and D. Barcelo, Environmental applications of analytical biosensors et al 1996 Meas. Sci. Technol. 7, 1547-1562

[21] BM Paddle, Biosensors for chemical and biological agents of defense, Biosensors & Bioelectronics,11:1079–1113, 1996

[22] Images taken from the homapage of prof. Anthony Guiseppi-Elie from the power point presentation, Biosensors and Biochips, Lecture 27, November 26th, 2002 www.people.vcu.edu/~guiseppi/ENGR645/

[23] Images taken from the homapage of prof. Anthony Guiseppi-Elie from the power point presentation, Biosensors and Biochips, Lecture 27, November 26th, 2002 www.people.vcu.edu/~guiseppi/ENGR645/

[24] S. A Jaffari and A.P.F Turner, Recent advances in amperometric glucose biosensors for in vivo monitoring, et al 1995 Physiol. Meas 16: 1-15, 1995

[25] Aptamer-based biosensors for detection of HIV-1 Tat protein, S..Tombelli, M. Minunni, E. Luzi and M. Mascini, Bioelectrochemistry 67 (2): 135-141, 2005

[26] American Diabetes Association, All about diabetes, www.diabetes.org/about-diabetes.jsp

[27] Endocrine web's diabetes center, Diagnosing diabetes, www.endocrineweb.com/diabetes/diagnosis.html

[28] Sensor for Medicine and Science, Diabetes: Fact and Figure www.s4ms.com/glucose_facts.htm

[29] Sensor for Medicine and Science, SMSI™ Glucose Sensor Personal Glucose Monitoring www.s4ms.com/glucose_personal.htm

[30] Sensor for Medicine and Science, Planned Advantages of the SMSI™ Glucose Monitor, Planned Advantages of the SMSI™ Glucose Monitor www.s4ms.com/glucose_advantages.htm

[31] Images taken from the hompage of Sensor for Medicine and Science, www.s4ms.com

[32] A.Deisingh and M. Thompson, Biosesnor for detection of bacteria, Canadian Journal of Microbiology, 50(2): 69-77, 2004

[33] Human Genome Project Information www.ornl.gov/sci/techresources/Human_Genome/home.shtml

Bibliography

[34] C.H. Mastrangelo, M. A. Burns_ , and D. T. Burke "Microfabrizated devices for genetic diagnostics", Proc. IEEE, August Issue, 1998

[35] J. Wang, "From DNA biosensors to gene chips."Nucleic Acids Res"., vol. 28: pp. 3011-3016, 2000

[36] Lodish H.,Berk A., Zipursky S.L,Matsudaira P.,Baltimore D.,Darnell J., Molecular Cell Biology, Media Connected ,W.H. Freeman and Company 2000

[37] Darnell J.,Lodish H.,Baltimore D., Molecular Cell Biology,Scientific American Book, 1990

[38] B. Alberts, D. Bray, A. Johnson, J. Lewis, M. Raff, K. Roberts, and P. Walter, Essential Cell Biology, Garland Publishing's, 1998

[39] Images taken from the power point presentation: Biosesnors-Lecture 7 of Dr Rein V Ulijn, University of Menchester,] www.umist.ac.uk/personal/staff/R.Ulijn/biosensors/..

[40] Worthington Biochemical Corporation, Introduction to the enzymes, www.worthington-biochem.com/introBiochem/introEnzymes.html

[41] Images taken from the homepage:Worthington Biochemical Corporation, Introduction to the enzymes, www.worthington-biochem.com/introBiochem/introEnzymes.html

[42] Jeffrey D. Zahn, Ajay A. Deshmukh, Alexandros P. Papavasiliou, Albert P. Pisano and Dorian Liepmann, An Integrated Microfluidic Device for the Continuous Sampling and Analysis of Biological Fluids, Proceedings of 2001 ASME International Mechanical Engineering Congress and Exposition November 11-16, 2001, New York, NY www.bioe.psu.edu

[43] Rain University-biotechnology lectures www.rcw.raiuniversity.edu/biotechnology/Btechbiotech /biosensors

[44] Imges taken from the hompage of University of Toronto of Faculty Mechanical Mechanical &Industrial Engineering www.mie.utoronto.ca/labs/lcdlab/biopic/fig/19.6.jpg

[45] Karsten A.Fähnrich, 2002 ,Dissertation at National University of Irealand,Department of Chemistry, Development of Disposable Immunosensors for Polyaromatic Hydrocarbons (PAHs) and Development of a Novel Immunosensor System based on Electrogenerated Chemiluminescence (ECL) detection, www.karstenfaehnrich.de/

[46] Images taken from hompage of University of Colorado, Department of microbiology , www.uccs.edu/~rmelamed/

[47] Images taken from hompage of The Person Education ProductSupport, Biochemistry http://wps.prenhall.com/wps/media/objects/602/616516/

Bibliography

[48] James D. Watson and Francis HC Crick. "Molecular Structure of Nucleic Acids: A Structure for Deoxyribose Nucleic Acid", Nature 171, 737–738 ,1953

[49] Images taken from hompage of WILEY-Publischer Science, Genetics
http://www.wiley.com/legacy/products/subject/life/genetics/fig13.jpg

[50] Images taken from hompage of La Cañada Unified School District
http://www.lcusd.com/lchs/mewoldsen/abzDNA.GIF

[51] Images taken from hompgae of Physical Methods for Biochemistry - Dr. Hackert Spring 2005,
http://courses.cm.utexas.edu/mhackert/ch370/spring2005/Nucleic_acids/melt.gif

[52] Images taken from hompage of School of Biomedical Sciences, Charles Sturt University , the lectures on topics Molecular Genetics Pharmacy an Molecular Biology using figures, graphs and tables taken from Essential Cell Biology by Alberts et al. ,Garland Publishing's ,1998
http://www.csu.edu.au/faculty/health/biomed/subjects/molbol/images/10_7.jpg

[53] Fibre Optics Group Home Page,University of Menchester, Introduction to Fibre Optics
http://www.jb.man.ac.uk/research/fibre/intro2fibre.htm

[54] Wikipedia, the free encyclopedia, optical fibre,
http://en.wikipedia.org/wiki/Fibre_optics

[55] A. G. Mignani and F.Baldini, Fibre-optic sensors in health care , Phys. Med. Biol, 42: 967-979,1997

[56] Wikipedia,the free encyclopedia, Evanescent Wave
http://en.wikipedia.org/wiki/Evanescent_Wave

[57] Wikipedia, the free encyclopedia, Total Internal Reflection
http://en.wikipedia.org/wiki/Total_internal_reflection

[58] International School of Photonics, Fibre Optic Sensor, Evanescent waves
http://www.photonics.cusat.edu/Research_Fiber%20Sensors_EW.html

[59] Images taken from the hompage of University of IST Socrates, University of Berkley
http://ist-socrates.berkeley.edu/~eps2/wisc/jpeg/l2s23.jpeg

[60] Jiri Homola, Present and future of surface plasmon biosesnors, Anal. Bioanal. Chem. 377: 528-539, 2003

[61] Wikipedia, the free encyclopedia, Surface plasmon
http://en.wikipedia.org/wiki/Surface_plasmon

[62] Images taken from the hompage of The Sensor Science and Molecular Physics group from Linköpings Universitet in Sweden
http://www.ifm.liu.se/applphys/sensor/spr.html

Bibliography

[63] W. A. Clark, X. Jian, L. Chen and J K. Northup, Independent and synergistic interaction of retinal G-protein subunits with bovine rhodopsin measured by surface plasmon resonance, Biochem. J., 358: 389–397, 2001

[64] The website of Research Group of Gauglitz Optical Spectroscopy, E.Karl University of T Tübingen, http://barolo.ipc.uni-tuebingen.de/markiert.php?lang=en&show=22

[65] K.E. Sapsford, Y.S. Shubin, J.B. Delehanty, J.P. Golden, C.R. Taitt L.C. Shriver-Lakeand F.S. Ligler, Fluorescence-based array biosensors for detection of biohazards Journal of Applied Microbiology, 96:47 -58, 2004

[66] London South Bank University, Faculty of Engineering Science and The Built Enviroment, Enzyme Technology http://www.lsbu.ac.uk/biology/enztech/

[67] J.C. Johnson, S.R. Nettikadam, S.G Vengasandra, E.Henderson, Analysis of solid-phase immobilized antibodies by atomic force microscope, J. Biochem Biophys Methods, 59 (2):167-180, 2004

[68] T.Wink, S.J van Zuilen, A.Bult, W.P van Bennkom, Self-assembled monolayers for biosensor, Analyst 122(4):43R-50R, 1997

[69] Sintef Norway's Research Institute, Silanisation http://www.sintef.no/content/page1____5497.aspx

[70]] Wikipedia, the free encyclopedia, Thiol http://en.wikipedia.org/wiki/Thiol

[71] Department of Physics and Measurement Technology, Biology and Chemistry (IFM) at Linköpings Universitet in Sweden, Self-Assembled Monolayers http://www.ifm.liu.se/applphys/ftir/sams.html

[72] Images take form the hompage of the Lawrence Livermore National Laboratory, Science&Technology http://www-cms.llnl.gov/s-t/surface_images/surface-17.jpg

[73] N. Faucheuxa, R. Schweissb, K. L.utzowa, C. Wernerb, T. Grotha,Self-assembled monolayers with different terminating groups as model substrates for cell adhesion, Biomaterials, 25: 2721–2730, 2004

[74] D.R Thevenot, K.Toth, R.A. Durst and G.S. Wilson, Electrochemical biosensors: ecommended definitions and classification, Pure Appl. Chem., 71: 2333-2348, 1999

[75] J.Schotter, Development o magnetoresistive biosensor for the detection of biomolecules, Dissertation, University of Bielefeld, October 2004

[76] Nanotech Briefs, http://www.nanotechbriefs.com/auth/biz/biz_2_0205.html

Bibliography

[77] The hompage of company Affymetrix, http://www.affymetrix.com/

[78] The hompage of company Caliper Life Sciences, http://www.caliperls.com/

[79] The hompage of company Caliper Life Sciences
http://www.caliperls.com/technology_partners/licensing_opportunities.html

[80] Baselt, D.R., G.U.Lee, M.Natesan, S.W.Metzger and P.E.Sheehan , A biosensor based on magnetoresistance technology. Biosens. & Bioelectron. 13: 731–739, 1998

[81] D. L. Graham, H. A. Ferreira and P. P. Freitas, Magnetoresistive-based biosensors and biochips, Trends in Biotechnology, 22 (9): 455-462 , 2004

[82] G. Li, V. Joshi, X. Wang, et al., Detection of single microsized magnetic bead and Magnetic nanoparticles using spin valve sensors for biological application, Journal of Applied Physcis, 93, (10): 7557-7559, 2003

[83] M. Brzeska, M. Justus, et al., Development of magnetoresistive sensors for detection of single magnetic particle/molecules, Molecular Physics Reports 39:32-38, 2004

[84] M. Megens and M.Prins, Magnetic biochips: a new option for sensitive diagnostic, J. Magn. Mag. Mat, 293:702-708, 2005

[85] M.Panhorst, On-chip manipulation and positioning of biomolecules with magnetic beads, Dissertation, July 2005

[86] P. Tartaj, M. Morales, S. Veintemillas-Verdaguer, T. Gonzalez-Carreno and C.J.Serna, The preparation of magnetic nanoparticles for applications in biomedicine, J.Phys.D Appl. Phys. 36: R182-R197, 2003

[87] M. Shinkai and A. Ito, Functional Magnetic Particles for Medical Application, Adv Biochem Engin/Biotechnol. 91:191-220,2004

[88] B.Kildew, Magnetic Microparticles Used in Molecular and Cellural Isolations, Buisness Buisness Briefing: Medical Device Manufacturing &Techniology, 2002

[89] C.Jin-Woo, H.A Chong, Magnetic Separation in Lab-on-a Chip Systems for for Biotechnology Applications, Business Briefing: Future Drug Discovery, 2003

[90] U.Häfeli, M.Zborowski, Proceedings of the Fifth International Conference on Scientific and Clinical Applications of Magnetic Carriers, Journal of Magnetism and Magnetic Magnetic Materials,293(1): 294-514, 2005

[91] Bangs Laboratories, www.bangslabs.com

[92] Dynal Inc. , www.dynal.no

[93] Micromod Partikeltechnologie, ww.micromod.de

Bibliography

[94] Spherotech Inc., www.spherotech.com

[95] Agowa GmbH, www.agowa.de

[96] Images taken from the hompage of www.dynal.no

[97] P. Gould, Nanoparticles probe biosystems, Materialstoday,7(2):36-43,2004

[98] M. Tanase, E. J. Felton,D. S. Gray,A. Hultgren, C. S. Chenc and D.H. Reich., Assembly of multicellular constructs and microarrays of cells using magnetic nanowires, Lab Chip, 5: 598–605, 2005

[99] Images taken from the article in the ref.98

[100] Aureon Biosystems company http://www.aureonbio.com/Streptavidin.htm

[101] G.Kisker GbR Produkte f.d.Biotechnologie http://www.kisker-biotech.com/micro_magnetic_particles.htm

[102] Bio-Nobile Oy company http://www.bio-nobile.com/purification/purification_particles.asp

[103] K.L. Klug, V. P. Dravid, and D. L. Johnson , Silica-encapsulated magnetic nanoparticles formed by a combined arc   evaporation/chemical vapor deposition technique, J. Mater. Res., Vol. 18: 988-993, (4), 2003

[104] A.Hütten, D.Sudfeld, I.Ennen, G.Reiss, K.Wojczykowski and P.Jutzzi, Ferromagnetic FeCo nanoparticles for biotechnology, Journal of Magnetism and Magnetic Materials 293: 93-101, 2005

[105] M.L.Vadala, M.A. Zalich, D.B.Fulks,T.G.St.Pierre, J.P.Dailey and J.S.Riffle, Cobalt silica magnetic nanoparticles with functional surfaces, Journal of Magnetism and Magnetic Materials 293: 162-170, 2005

[106] E.E. Carpenter, C. Sangregorio, and C.J. O'Connor, "Effects of Shell Thickness on Blocking Temperature of Nanocomposites of Metal Particles with Gold Shells," IEEE Trans. Magn.,35:3496-3498 (1999);JMMM 225, 17 (2001).

[107] B.Ravel, E.E.Carpenter and V.G. Harris Oxidation of iron in iron/gold core/shell nanoparticles, J. Appl. Phys.,91: 8195-8197, 2002

[108] M.Chen, S.Yamamuro, D. Farrel and S.A.Majetich, Gold-coated iron nanoparticles for biomedical applications J. Appl. Phys. 93 : 7551-7553, 2003

[109] S.J. Cho, J.C.Idrobo, J.Olamit,K. Liu,N.D. Browning, S.M.Kauzlarich, Growth Mechanisms and Oxidation-Resistance of Gold-Coated Iron Nanoparticles, Chem. Mater. 17(12):3181-3186, 2005

Bibliography

[110] Binek, Sierra J.; C. Won-Suk and L. Gil,Synthesis of Magnetic Microparticles,Purdue University, https://engineering.purdue.edu/BME/REU/REU_2004/Presentations/Presentation008

[111] G. Liu, H. Yang, and J. Zhou S. Law,Q. Jiang, and G. Yang, Preparation of Magnetic Microspheres from Water-in-Oil Emulsion Stabilized by Block Copolymer Dispersant Biomacromolecules , 6:1280-1288, 2004

[112] Tartaj, Pedro, et al. "The Preparation of Magnetic Nanoparticles for Applications in Biomedicine." Journal of Physics D: Applied Physics. June 2003: 182-197.

[113] L. Theil Kuhn, A. Bojesen, L. Timmermann, M. Meedom Nielsen and S. Mørup: Structural and magnetic properties of core-shell iron – iron oxide nanoparticles. Journal of Physics: Condensed Matter. November 2002: 13551-13567.

[114] Images taken from the hompage of Nano-Structured Biopolymers research group of University of Stellenbosch http://academic.sun.ac.za/polymer/nano/projects.htm

[115] Miltenyi S, Muller W, W. Weichel W, A. Radbruch,High gradient magnetic cell separation with MACS,Cytometry, 11(2):231-238, 2005

[116] M.Lewin, N.Carlesso, CH Tung, XW Tang, D.Cory, DT Scadden and Weissleder, Tat peptide-derivatized magnetic nanoparticles allow in invitro tracking and recovery of progenitor cells, Nature Biotechnol,. 18 (4):410-414, 2000

[117] C.Y Wang, W.Hui, Z.Zhang, X.Xin, C.Chen, The synthesis of GoldMag nano-particles and their application for antibody immobilization, Biomed Microdevices, 7 (2):153-156, 2005

[118] Q.A.Pankhurst, J.Connolly,S.K.Jones and J.Dobson, Applicationsof magnetic nanoparticles in biomedicine, J.Phys. D: Appl.Phys.36: R167-R181,2003

[119] C.C.Berry, Possible exploitation of magnetic nanoparticle-cell interaction for biomedical applications, Journal of Materials Chemistry, 15 (5):543-547, 2005

[120] U.Häfeli, M.Zborowski, Evaluation of in vivo toxicity of magnetic carriers, Journal of Magnetism and Magnetic Materials 293: 277-293, 2005

[121] T.Neuberger, B.Schöpf, H.Hofmann, M.Hofmann, B. von Rechenberg, Superparamagnetic nanoparticles for biomedical applications:possibilities and limitations of a new drug delivery system, Journal of Magnetism and Magnetic Materials 293: 483-496, 2005

[122] Images taken from the homepage of Ecole Polytechnique Federale de Jausanne J.Brugger, P.Hoffmann, Nanomaterials

Bibliography

[123] C.Alexiou, R.Jurgons, RJ Schmid, C.Bergmann, J.Henke, W.Erhardt, E. Huenges, F.Parak,Magnetic drug targeting-biodistribution of the magnetic carrier and the chemotherapeutic agent mitoxantrone after locoregional cancer treatment,J Drug Target. 11(3):139-149,2003

[124] C.Plank, U.Schillinger, F.Schere, C.Bergemann, JS Remy, F.Krotz, M.Anton, J.Lausier, J.Rosenecker, The magnetofection method.using magnetic force to enhance gene delivery, Biol. Chem, 384(5):737-747,2003

[125] U.Häfeli, M.Zborowski, Hyperthemia with magnetic carriers, Journal of Magnetism and Magnetic Materials 293: 294-334, 2005

[126] K.Tanaka, A.Ito, T.Kobayashi, T.Kawamure, S.Shimada, K.Matsumoto,T.Saida, H.HondaHeat immunotherapy using magnetic nanoparticles and denritic cells for T-lymphoma,J Biosci Bioeng. 100(1): 112-115,2005

[127] A.Ito, F.Matsuoka, H.Honda,T.Kobayashi, Heat schock protein 70 gene therapy combined with hyperthemia using magnetic nanopartilces, Cancer Gene Therapy,10(12):918-925,2003

[128] Magnetic resonance imaging, wikipedia-the free encyclopedia, Magnetic Resonance Imaging,http://en.wikipedia.org/wiki/Magnetic_resonance_imaging

[129] H.Kobayashi and M.W.Brechbiel, Dendrimer-basd nanosized MRI contrast agents, Current Pharmaceutical Biotechnology, 5(6):539-549,2004

[130] Images taken from P.Freitas, H. Ferreira, et al. Magnetoresistive biochips, Europhysics News Vol. 3 (6):1-9,2003

[131] J.Nickel, Magnetoresistance Overview,Computer Peripherals Laboratory, June 14, 1995 http://www.hpl.hp.com/techreports/95/HPL-95-60.pdf

[132] Baibich M N, Broto J M, Fert A, Nguyen Van Dau F, Petroff F, Etienne P, Creuzet G, Friederich A and Chazelas, Giant Magnetoresistance of (001)Fe/(001)Cr Magnetic Superlattices, J Phys. Rev. Lett. 61: 2472-2475, 1988

[133] G. Binasch, P. Grünberg, F. Saurenbach, and W. Zinn, Enhanced magnetoresistance in layered magnetic structures with antiferromagnetic interlayer exchange, Phys. Rev. B 39 (7): 4828–4830,1989

[134] Philips semiconductors, Magnetoresistive sensors, The attractive choice. http://www.semiconductors.philips.com/acrobat_download/literature/9397/75003655.pdf

[135] C.H. Smith and R. W.Schneider, Low Field Magnetic Sensing with GMR sensors, ,Novolatile Electronics, Presented at Sensors Expo-Baltimore, May, 1999 http://www.nve.com/Downloads/lowfield.pdf

[136] C.H.Smith and R.W.Schneider, GMR and SDT Sensors and Arrays for Low-Field Magnetic Applications,1-12, Novolatile Electronics http://www.nve.com/Downloads/expo00.pdf

Bibliography

[137] Images taken from the reference [136]

[138] R.S. Popvic, P.M Drjaca, C.Schott, Briding the gap between AMR,GMR and Hall Magnetic Sensors, invited paper,Proc. 23rd Int. Conference on Microelectronics, 2002 http://www.sentron.ch/support/techpapers.htm

[139] A.Fert and C.Vouille, Magnetoresistance overview:AMR,GMR,TMR,CMR, Magnetische Schichtsysteme in Forschung und Anwendung, Vorlesungsmanuskripte des 30 IFF-Ferienkurses, Forschung Jülich GmbH, Institut für Festkörperforschung, Kurs vom 1 bis 12 März, 1999

[140] Joe Checkelsky, Anisotropic Magnetoresistance of FexCo1-xS2, Harvey Mudd College April 30, 2004 http://www2.hmc.edu/~eckert/research/JCHECKELSKY.pdf

[141] The Giant Magnetoresistive Head: A giant leap for IBM Research, IBM Research http://www.research.ibm.com/research/gmr.html

[142] M. Ziese and M.J. Thornton, Spin Electronics, Springer-Verlag Berlin Heidelberg,2001 J.Mathon, Phenomenological Theory of Giant Magnetoresistance, 71-88

[143] Images taken from the reference [142]

[144] U.Hartmann, Magnetic Multilayers and Giant Magneto-resistance, Fundamentals and Industrial Applications, Springer Verlag Berlin Heidelberg,2000 R.Coehorn, Giant Magnetoresistance in Exchange-Biased Spin Valve Layered Structure and its Application in Read Heads, 65-127

[145] Images taken from the website of Fritz Haber-Institut der Max-Planck-Gesellschaft Giant magnetoresistance, Alexey Dick,2001 http://www.fhi-berlin.mpg.de/th/VL/TFK-Sem-2001/gmr/

[146] Images taken from the website of Fritz Haber-Institut der Max-Planck-Gesellschaft Giant Magnetoresistance and Data Storage http://www.fhi-berlin.mpg.de/th/lectures/materialscience-2004/vorlesung_2004/

[147] Images taken from the reference [144]

[148] Images taken from the reference [144]

[149] E. Y. Tsymbal, O. Mryasov and P. R LeClair, Spin-dependent tunnelling in magnetic tunnel junctions, J. Phys. Condens. Matter 15: R109- R142, 2003

[150] Images taken from reference [149]

[151] M. Julliere , Tunneling between ferromagnetic films, Physics Letters A, 54:225-226 (3), 1975

Bibliography

[152] B. Dieny, V. S. Speriosu, S. S. P. Parkin, B. A. Gurney, D. R. Wilhoit, and D. Mauri, Giant magnetoresistive in soft ferromagnetic multilayers, Phys. Rev. B 43: 1297–1300, 1991

[153] M. Ziese and M.J. Thornton, Spin Electronics, Springer-Verlag Berlin Heidelberg, P.P Freitas, Spin-Valve and Spin –Tunneling Devices: Read Heads,MRAMs, Field Sensors: 463-485, 2001

[154] The hompage of Condensed Matter Research Magnetism and Superconductivity of University of Leeds, http://www.stoner.leeds.ac.uk/research/

[155] Images taken from the hompage of Condensed Matter Research Magnetism and Superconductivity of University of Leeds http://www.stoner.leeds.ac.uk/research/

[156] Dana Borsa, Nitride based insulating and magnetic thin films and multilayers, Dissertation, University of Groningen, 2004

[157] Images taken form the reference [151] http://dissertations.ub.rug.nl/FILES/faculties/science/2004/d.m.borsa/c7.pdf

[158] W.H. Meiklejohn, C.P. Bean , New Magnetic Anisotropy, Phys. Rev. 102: 1413–1414 1956

[159] A.E. Berkowitz, K.Takano, Exchange anisotropy-a review, Journal of Magnetism and Magnetic Materials 200:552-570, 1999

[160] Images taken from the hompage of Micromagnetics & Magnetic Materials Groups, Vienna University of Technology http://magnet.atp.tuwien.ac.at/gallery/exchbias/

[161] Images taken from the reference [159]

[162] S.Tegen, I. Mönch, J. Schumann, H. Vinzelberg and C.M. Schneider, Effect of Neel coupling on magnetic tunnel junctions, Journal of Applied Physics 89(12):8169-8174

[163] B.D Schrag,A. Anguelouch,S. Ingvarsson, and G.Xiao et al. Neel "Orange-peel" coupling in magnetic tunneling junction devices, Applied Physics Letters, 77(15):2373-2375, 2000

[164] R.L. Edelstein, C.R. Tamanaha, P.E.Sheehan,M.M.Miller, D.R. Baselt,L.J.Whitman, R.J.Colton, The BARC biosensor applied to the detection of biological warfare agents, Biosensors&Bioelectronics 14:805-813,2000

[165] Images taken from the reference [84]

[166] Leybold Vakuum GmBH, www.leybold.com

[167] Marc Sacher, Diploma, University of Bielefeld

Bibliography

[168] Rainer Waser (Ed.), Nanoelectronics and Information Technology, Wiley-Vch,2005

[169] A.R Elshabini, F.D. Barlow III, Thin Film Technology Book, McGraw-Hill, 1998

[170] Images take from the website of Micromagazine
www.micromagazine.com/archive/02/07/rampf.html

[171] The website of Micro-Electro-Mechanical-Systems and Nanotechnology, Processes, Lithography, www.memsnet.org/mems/processes/lithography.html

[172] Images taken from [171]

[173] Allresist, www.allresist.de

[174] LEO series 1530 field emission electron microscope, www.leo-em.co.uk

[175] Raith ELPHY Plus Lithography system, www.raith.de

[176] Software Control LEO 15XX Manual, Handbook from LEO Electron Microscopy Ltd

[177] Thermo Electron Cor., www.thermo.com

[178] Heidelberg Instruemnts GmbH, DWL 66 direct write system, www.himt.de

[179] M. Ziese and M.J. Thornton, Spin Electronics, Springer-Verlag Berlin Heidelberg, C.Fermon, Micro- and Nanofabrication Techniques, 379-396, 2001

[180] Roth&Rau AG, UniLab system ,www.roth-rau.de

[181] Oxford Instruments, Link ISIS Series 300, www.oxford-instruments.com

[182] A. Bryant, TU Nanomaterials Wokshop, Energy Dispersive X-Ray Analysis EDX, www.ens.utulsa.edu/nanomaterialsworkshop/Teacher_Reports/EDX.doc

[183] A. Thomas, Dissertation, University of Bielefeld, 2004

[184] J.A. Venables, Introduction to Surface and Thin Film Processes, Cambrige University Press, 2000

[185] Carl Zeiss, www.zeiss.com

[186] Images taken from reference [185]

[187] Nanometrics Inc.,Model 210 AFTMS, www.nanometrics.com

[188] Topometrix homepage, http://electron.mit.edu/

Bibliography

[189] Topometrix, Explorer^{TM} Instrument Operation Manual, TopoMetrix Corporation, 1996

[190] M.Brzeska, M.Panhorst, P.B. Kamp, J.Schotter, G.Reiss, A.Pühler, A.Becker, H.Brückl ,Detection and manipulation of biomolecules by magnetic carriers, Journal of Biotechnology, 112:25-33, 2004

[191] A.Thomas, H.Brückl, M.D Sacher, J.Schmalhorst, G.Reiss, Aluminium oxidation by a remote cyclotron resonance plasma in magnetic tunnel junction, J.Vacuum Sci. Technology, B 21: 2120-2122, 2003

[192] Micromod company, http://www.micromod.de/

[193] Images taken from http://www.bio-nobile.com/magnetic/magnetic_pickpen.asp

[194] A. Hütten; D. Sudfeld; I. Ennen; G. Reiss; K. Wojczykowski; P. Jutzi Ferromagnetic FeCo-nanoparticles for biotechnology , J. Magn. Magn. Magn. 293: 93-191, 2005

[195] Grütter, P., Mamin, H.J., Rugar, D., Magnetic Force Microscoopy (MFM). In: R. Wiesendanger, H.-J. Güntherodt (Eds.), Scanning Tunneling microscopy II. Springer Verlag Berlin, 152-207, 1992

[196] Object Oriented MicroMagnetic Framework, http://math.nist.gov/oommf/

[197] Fujii T., Suzuki M., Miyashita M., Yamaguchi M., Onuki T., Nakamura H., Matsubara T., Yamada H., Nakayama K., Micropattern measurement with an atomic force microscope, J.Vac. Sci. Technol. B 9 (2): 666-669,1991

[198] Koblischka M.R.1; Hartmann U., Sulzbach T. Source, Improvements of the lateral resolution of the MFM technique, Thin Solid Films,428 (1),93-97,2003

[199] L.Shmuylovich, Shen A.Q.,Stone H.S., Surface morphology of drying latex film: multiple ring formation, Langmuir, 18:3441-3445,2002

[200] Deegan R.D, Pattern formation in drying drops, Phys. Rev. E 61:475 – 485, 2000

[201] W.Shen, X.Liu, D.Mazumdar, G.Xiao, In situ detection *of* single *micron-sized* magnetic beads using magnetic tunnel junction sensors, Appl. Phys. Lett. 91, 224105 (2007)

[202] M.Megens, F. de Theije, B. de Boer, F. van Gall, Scanning probe measurements on a magnetic bead biosensor, J. Appl. Phys. 102 (1): 014507-014507-5, 2007

[203] . Ennen; V. Höink; A. Weddemann; A. Hütten; J. Schmalhorst; G. Reiss, C. Waltenberg; P. Jutzi; T. Weis; D. Engel; A. Ehresmann: (2007) Manipulation of magnetic ... strayfield of magnetically patterned ferromagnetic layers, J. Appl. Phys., 102 (1)*:* 013910.1-013910.4, 2007

Bibliography

[204] Kanak, J.; Stobiecki, T.; Thomas, A.; Schmalhorst, J.; Reiss, G, Structural and tunneling properties of magnetic tunnel junctions with Al-O and MgO barrier, Vacuum *82*:1057-1061, 2008

[205] W. F. Brinkman, R. C. Dynes, and J.M. Rowell, Tunneling conductance of asymmetrical barriers, Journal of Applied Physics, 41(5): 1915-1921, 1970

[206] Images taken from http://www.spmtips.com/library/materials_research/mfm_calibration/

[207] S. T. Huntington and S. A. Nespolo, Precision attachment of (Silica) spheres to AFM cantilever tips, Microscopy Today Issue 01-3, April, 2001

[208] Atomicforce, http://www.atomicforce.de/Olympus-Cantilever-Tip-Applications.php